UTS UNIVERSITY OF TECHNOLOGY SYDNEY

# Three-Dimensional Discrete Element Simulation of Cavity Expansion from Zero Initial Radius in Sand

**by Yang Dong**

Thesis submitted in fulfilment of the requirements for the degree of

**Doctor of Philosophy**

under the supervision of A/Prof. Behzad Fatahi and A/Prof. Hadi Khabbaz

University of Technology Sydney
Faculty of Engineering and Information Technology

January 2021

# Certificate of Original Authorship

I, *Yang Dong* declare that this thesis, is submitted in fulfilment of the requirements for the award of *the degree of Doctor of Philosophy*, in the *School of Civil and Environmental Engineering, Faculty of Engineering and Information Technology* at the University of Technology Sydney.

This thesis is wholly my own work unless otherwise referenced or acknowledged. In addition, I certify that all information sources and literature used are indicated in the thesis.

This research is supported by the Australian Government Research Training Program.

Signature:

Production Note:
Signature removed prior to publication.

Date: Jan. 2021

# Acknowledgement

I, Yang Dong, would like to express my most cordial gratitude and appreciation to those who helped me, encouraged me, guided me and accompanied me during this four-year Ph.D. study.

Firstly, I would like to particularly thank my principal supervisor, Associate Professor Behzad Fatahi for his continuous support, understanding, patience throughout this long journey, and I am particularly grateful for his encouragement during the toughest time of my life. I also appreciate my co-supervisor, Associate Professor Hadi Khabbaz for his guidance and willingness to help whenever possible.

I am appreciative to my friends, colleagues, administration staffs in the School of Civil and Environmental Engineering. I would also like to express my gratitude to Matt Gaston and Anselm Motha for their assistance in providing IT support and the facility that makes such research possible. Also, it was my honour to walk through these four years memorable time with my friends, Sienna Zhang, Navid Yeganeh and Piyush Punetha.

At this very moment, I would like to extend my heartfelt appreciation to my dearest parents, my partner Ruby who are my most powerful backing, and constantly support me spiritually at any time. Without their selfless support, I would never be able to achieve this key milestone in my life.

-Yang Dong

# List of Publications

1. Dong, Y., & Fatahi, B. (2020). Discrete element simulation of cavity expansion in lightly cemented sands considering cementation degradation. *Computers and Geotechnics*, 124, 103628.
2. Dong, Y., Fatahi, B., & Khabbaz, H. (2020). Three-dimensional discrete element simulation of cylindrical cavity expansion from zero initial radius in sand. *Computers and Geotechnics*, 117, 103230.
3. Dong, Y., Fatahi, B., Khabbaz, H., & Zhang, H. (2018). Influence of particle contact models on soil response of poorly graded sand during cavity expansion in discrete element simulation. *Journal of Rock Mechanics and Geotechnical Engineering*, 10(6), 1154-1170.
4. Dong, Y, Fatahi, B, Khabbaz, H & Hsi, J 2018, 'Impact of Initial In-Situ Stress Field on Soil Response During Cavity Expansion Using Discrete Element Simulation', *New Developments in Materials for Infrastructure Sustainability and the Contemporary Issues in Geo-environmental Engineering, GeoChina International Conference*, Springer, Hang Zhou, China, pp. 1-10.
5. Dong, Y., Fatahi, B., Khabbaz, H. & Kamruzzaman, A. 2018, 'Investigating Effects of Particle Scaling for Cavity Expansion Simulation Using Discrete Element Method', *GeoShanghai International Conference*, Springer, pp. 938-4.

# Table of Contents

# List of Figures

# List of Tables

# List of Symbols

The follow symbols are used in this thesis:

$A$: contact area of spheres in DEM ($m^2$);

$A_{cf}$: curve fitting parameter in the cavity expansion solution proposed by Collins et al. (1992);

$a$ : cavity radius (m);

$a_0$: initial cavity radius (m);

$a_f$: final cavity radius (m);

$b$ : radius of the external boundary in a cavity expansion problem (m);

$c$: radius of the plastic zone in a cavity expansion problem (kPa);

$c_c$: cohesion (kPa);

$c^p$: cohesion of the bond element in DEM (MPa);

*D:* pile diameter (m);

$D_m$: size of the prediction sphere (m);

$d$ : distance between the centres of particles 1 and 2 (m);

$d_{50}$: median particle size (m);

$d_n^p$: normal dashpot;

$d_s^p$: shear dashpot;

$d_c$: damping constant at the contact;

$E$ : Young's modulus (MPa);

$E_{mod}^*$: effective modulus of the particles in DEM (MPa);

$E_*^p$: bond effective modulus (MPa);

e: void ratio;

f: friction force acting parallel to the slipping plane (kN);

$F_n$: normal force at the contact interface between contacting particles (kN);

$F_s$: shear force at the contact interface between contacting particles (kN);

$F_n^0$: normal force between two contacting particles at the beginning of the timestep (kN);

$F_s^0$: shear force between two contacting particles at the beginning of the timestep (kN);

$F_x$: resultant force in the x direction (kN);

$F_y$: resultant force in the y direction (kN);

$F_n^H$: Hertz normal force (kN);

$F_s^H$: Hertz shear force (kN);

$F_{s_0}^H$: Hertz shear force at the beginning of the timestep (kN);

$F_s^{max}$: shear strength at the contact interface (kPa);

$F_{s_{max}}^l$: maximum shear strength of the linear frictional component (kN);

$F_{s_{max}}^p$: maximum shear strength of the parallel cementation bond component (kN);

$F(e)$: void ratio function;

$G$ : shear modulus (MPa);

$G_{ref}$: modulus number;

$g_s$: surface gap between contacing particles (m);

$g_{max}$: maximum gap between contacting particle (m);

$H$ : horizontal force appied to the particle (kN);

$K_G^e$: elastic shear modulus exponent;

$k_n$: normal stiffness of linear springs (N/m);

$k_s$: shear stiffness of linear springs (N/m);

$k_r$: rolling stiffness of linear springs (N/m);

$k^*$: stiffness ratio between normal stiffness and shear stiffness (N/m);

$k_*^l$: linear component spring stiffness ratio (normal stiffness/shear stiffness);

$k_n^l$: normal stiffness of linear springs (N/m);

$k_s^l$: shear stiffness of linear springs (N/m);

$k_n^p$: normal stiffness of bond element (N/m);

$k_s^p$: shear stiffness of bond element (N/m);

$L$: the distance between the centres of contacting particles (m);

$L_p$: the embeded length of the pile in Strain Path Method;

$l$: linear frictional components;

$M$: the slope of critical state line;

$M^p$: resultant moment (kNm);

$M_t^p$: twisting moment (kNm);

$M_b^p$: bending moment (kNm);

$M_{RR}$: rolling resistance torque (kNm);

$M_{RR}^{max}$: limiting toque of rolling resistance torque (kNm);

$N$: the normal force acting perpendicular to the slipping plane (kN);

$N_b$: total number of broken cementation bonds;

$N_c$: ratio between the total number of cementation bonds;

$ne$: modulus exponent;

$O_1$: the centre of the contact interface between balls A and B;

$O_2$: the centre of the contact interface between balls A and B';

$P_a$: cavity pressure (kPa);

$P_{e0}$: external radial stress (kPa);

$P_i$: internal radial stress/cavity pressure in cavity expansion theory (kPa);

$P_{a0}$: internal cavity pressure (kPa);

$P_r$: radial pressure (kPa);

$P_h$: hoop stress (kPa);

$P_{max}$: maximum cavity pressure (kPa);

$P\%$: the progress of the cavity expansion;

$p$: parallel cementation bond components;

$p_{ref}$: reference pressure equal to 100 kPa;

$p_r$: radial stress (kPa);

$p'$: initial mean effective stress (kPa);

$p_{lim}$: constant limiting pressure causing a continous cavity expansion (kPa);

$q$: deviatoric stress (kPa);

$R$: particle size (m);

$R_1$: radius of particle 1 (m);

$R_2$: radius of particle 2 (m);

$R_b$: number of broken cementation bonds;

$R_c$: radius of the column to be installed (m);

$R_p$: radial distances measured from the corresponding initial cavities (m);

$R_e^H$: Hertz contact model particle effective radius (m);

$r_A$: radius of the prediction sphere A (m);

$r_B$: radius of the prediction sphere B (m);

$r$ : radial distance (m);

$r_0$: initial radial distance of a soil element (m);

$s_u$ : undrained shear strength (kPa);

$V_f$ : vertical force appied to the particle (kN);

$V$ : volume of the expansion ($m^3$);

$Y$ : a model paramater used in cavity expansion theory;

$\alpha$ : a model paramater used in cavity expansion theory;

$\gamma_c$: a model paramater used in cavity expansion theory;

$Z$: a model paramater used in cavity expansion theory;

$z$: a cylindrical coorindate (e.g. z at the ground surface is 0);

$\xi$ : composite state parameter defined as a function of the speficic volume and the mean effective stress;

$\lambda$ : slope of the critical state line;

$\lambda^p$: bond radius mutiplier;

$\Gamma_1$ : the intercept on the specific volume axis when $p'/p_{ref} = 1$;

$\alpha_c$: central angle in cavity expansion simulation (degree);

$\alpha_d$: angle of the slipping plane (degree);

$\alpha^H$: Hertz contact model exponent;

$\Delta\delta_s$: shear displacement increment in a timestep (m);

$\delta_r$: radial displacement (m);

$\Delta\delta_r$: radial displacement increment in a timestep (m);

$\Delta\delta_n$: normal displacement increment in a timestep (m);

$\vartheta$ : Poisson's ratio;

$\vartheta_s$: Specific volume;

$\omega_a$: rotational velocity of particle A (rad/s);

$\omega_b$: rotational velocity of particle B (rad/s);

$\Delta t$: increment of timestep (s);

$\mu$ : friction cofficient/interparticle friction;

$\mu_r$: rolling resistance coefficient;

$\mu_{wall}$: wall friction coeffecient;

$\mu^l$: friction coefficient of the linear frictional component;

$\eta$ : a model paramater used in cavity expansion theory;

$M$ : a model paramater used in cavity expansion theory;

$\beta$ : a model paramater used in cavity expansion theory;

$\delta_{rSS}$: soil radial movement in Strain Path Method;

$\delta_{zSS}$: soil vertical movement in Strain Path Method;

$\sigma_1$: major principle stress in Mohr's circle setting (kPa);

$\sigma_3$: minor principle stress in Mohr's circle setting (kPa);

$\sigma_{r_0}$: initial radial stress (kPa);

$\sigma_r$ : cavity expansion radial stress (kPa);

$\sigma_r^e$ : radial stress in the elastic region during the cavity expansion (kPa);

$\sigma_r^p$ : radial stress in the plastic region during the cavity expansion (kPa);

$\sigma_\theta$: cavity expansion hoop stress (kPa);

$\sigma_\theta^e$: hoop stress in the elastic region during the cavity expansion (kPa);

$\sigma_\theta^p$: hoop stress in the plastic region during the cavity expansion (kPa);

$\sigma_x$: initial stress in x direction (kPa);

$\sigma_y$: initial stress in y direction (kPa);

$\sigma_f^p$: tensile strength of a cementation bond (kPa);

$\sigma_n^p$: instant normal stress of the cementation bond (kPa);

$\sigma_f^p$: tensile strength of the cementation bond (kPa);

$\tau_f^p$: shear strength of a cementation bond (kPa);

$\Delta\varphi_r$: relative rotation increment between contacting particles in a timestep (degree);

$\emptyset$ : friction angle (degree);

$\emptyset'$ : effective stress friction angle (degree);

$\emptyset_m$: moblised friction angle (degree);

$\emptyset_f$: ultimate value of the friction angle (degree);

$\emptyset'_{cv}$: critical state/constant volume friction angle (degree);

$\psi$: dilation angle (degree);

$\psi_f$: ultimate value of the dilation angle (degree);

$\psi_m$: mobilised dilation angle (degree);

$\tau$ : shear stress (kPa);

$\varepsilon_v$: volumetric strain;

$\varepsilon_\gamma$: shear strain;

$\gamma$: deviatoric strain;

$\Omega$ : cross section area in Strain Path Method;

$\chi$ : a model paramater used in cavity expansion theory;

$T$ : a model paramater used in cavity expansion theory;

$\omega$ : a model paramater used in cavity expansion theory;

$\theta$: angle of the rotation of the cementation bond due to twisting (degree);

$\beta$: angle of the rotation of the cementation bond due to bending (degree);

# Abstract

Rigid inclusions, generally made of structural concrete, are widely employed to reduce the settlement and enhance the bearing capacity of the ground by transferring loads from superstructures through weak soil layers to a firm underlying stratum. However, the installations of rigid inclusions such as driven piles and controlled modulus columns can induce irreversible changes of the soil stress - strain state, and lead to excessive lateral soil movements during the auger penetration or pile driving/hammering process.

This thesis proposes a rigorous numerical modelling to investigate the installation effects of rigid inclusions on surrounding ground via cavity expansion simulation adopting discrete element method. The benefits of adopting the discrete element method is attributed to its capability in simulating large displacements and distortions, as well as incorporating the discontinuous nature of granular materials and providing a microscopic insight into the problem. True scale three-dimensional discrete element models simulating the creation of cylindrical cavities from zero initial cavity radius in dry clean and lightly cemented sands are developed. Contact constitutive models mimicking the behaviour of dry clean granular materials and lightly cemented sands are calibrated against existing laboratory experimental results. The numerical models proposed contain up to 500,000 particles with boundary conditions carefully selected to reproduce realistic scenarios. Embedded scripting is adopted to precisely record both the local and global stress and strain variations, as well as the cementation bond breakage during the cavity expansion process.

The results confirm that the selection of arbitrary initial cavity radius could significantly influence the soil response at the earlier stages of the cavity expansion. For a given expansion volume, creating a cylindrical cavity from zero initial radius induces larger stresses in the soil compared to expanding existing cavities in the same soil medium from a nonzero given initial radius. This implicates that the estimation of the pile driving force may be largely underestimated adopting the approximation method based on the existing cavity expansion theories, requiring an assumptive initial cavity radius. In addition, the soil lateral displacements, depending on the gradation and the relative density, can reach up to 30 $R_c$ ($R_c$ is the radius of the pile) during the installation, and the loose sand in a plane strain condition can even exhibit dilation during the early stages of the cavity expansion. In the lightly cemented sands, the installation of rigid inclusions or cavity expansion can lead to significant cementation degradations. The influence zone of cementation degradation observed in cemented sand with various cement content can extend to approximately $4R_c$, in which the shear strength of the soil is significantly reduced due to the cementation bond breakage, which may lead to the reduction in axial capacity, adversely influencing the pile toe stability. Within this influence zone, the displacement induced by the installation is not sensitive to the level of cementations, while soils with higher cement content are expected to experience larger radial displacements beyond this influence zone. Hence, extra care must be taken by practicing engineers when assessing the required pile driving pressure and the installation effects of ground inclusions in the vicinity of existing structures such as pipelines and bridge abutments in both granular materials and lightly cemented sand.

# Chapter 1 – Introduction

## 1.1 General

The rapid increase in population has been triggering intensive construction activities, particularly in constructing new infrastructures such as highways, railways, retaining walls, wastewater treatment plants, and tunnels, which leads to the scarcity of good land. Hence, there has been a massive surge in demand for development of infrastructure on contaminated sites, mining sites and landfill sites, mainly alluviums containing soft soils and loose sands. However, the design, construction and maintenance of infrastructures constructed on these sites present numerous challenges for contractors and geotechnical engineers. Owing to the low strength and modulus, high compressibility, and expansive characteristics, foundations constructed on such soils can experience excessively large settlement in a long period of time (Arora 1992; Budhu 2008). Moreover, differential settlement can take place due to spatially varying loads and ground conditions, which can contribute to the foundation failure and even the collapse of the structure.

Since the excessive ground settlement and differential settlement cause adverse effects on the working conditions of the structures, ground improvement techniques are often employed to enhance the ground properties. There is a plethora of ground improvement techniques available to improve the mechanical properties of soils, such as preloading with or without vertical drains (PVD), deep soil mixing, piled foundations and controlled modulus columns (CMC).

In a driven pile installation, for instance, piles are penetrated into the ground by means of hammering or vibration. The design capacity is achieved by displacing the soil around the shaft and compacting the soils at the pile toe. In the installation of a controlled modulus column, however, an auger, powered by equipment with high static down thrust, displaces the soil laterally. The auger is penetrated into the ground to the required depth that induces changes in the density of the surrounding soils (Plomteux et al. 2004; Nguyen et al. 2019). During driven pile or CMC installations, the penetration can lead to irreversible changes of the soil stress - strain state, and one of the greatest challenges is piling adjacent to existing utilities (e.g. buried pipelines) and structures (e.g. bridge abutments), in which predicting and controlling the lateral soil deformations due to installation are essential design considerations (Budhu 2008). Indeed, many findings claimed that previously installed piles can also exhibit a certain degree of lateral movement during new pile installation, posing risks to the pile integrity and hence its lateral and axial capacities (Chow et al. 1990; Klotz et al. 2001; Lehane et al. 2005; Yang et al. 2006). Besides this, when reinforcing weakly cemented soils in supporting heavy structures (e.g. oil tanks), the installation of piles or inclusions can induce cementation degradations. This may lead to the reduction of the soil shear strength, impacting the skin friction of the inclusion and settlement of the soil between inclusions, which may contribute to catastrophic foundation failure or serviceability issues, particularly when the bearing stratum is deep and floating piles are adopted (McClelland 1974; Saxena et al. 1978; Clough et al. 1981; Acar et al. 1986; Murff 1987; Ismael 1990, 2001; Consoli et al. 2012). These issues associated with the installation of inclusions have been well

recognised since a few decades ago and there were extensive studies carried out directly and indirectly that may be adopted in assessing the installation effects of rigid inclusions in soils. These studies were mainly focusing on deriving closed form solutions or developing a rigorous modelling technique for assessing the behaviour of driven piles, studying the changes in stresses, pore water pressure and displacement fields (e.g. cavity expansion theories). Laboratory model tests and large-scale field testings, and continuum based numerical simulations were also widely conducted to investigate such installation effects (Robinsky et al. 1964; Carter et al. 1979a; Carter et al. 1979b; Poulos et al. 1980; Baligh 1985; Carter et al. 1986; Collins et al. 1992; Yu 1992; Yu 1993; Poulos 1994; Collins et al. 1996a; Sheng et al. 2005; Henke 2010; Pucker et al. 2012; Phuong et al. 2016).

## 1.2 Statement of Problem

Despite the fact that there were numerous methods developed in the past in assessing the installation effects of rigid inclusions in soils, the behaviour of piles and associated installation effects still remain main sources of design and construction uncertainties due to the lack of fundamental understanding of physical mechanisms involved (Sheng et al. 2005). The issues associated with widely adopted methods to simulate the installation effects can be generally summarised as follows:

- Analytical cavity expansion solutions can be only derived for the special cases considering simplified geometries and idealised materials based on simple constitutive

models (Carter et al. 1979b). Hence, the solutions may not well reproduce the complex yet realistic soil behaviours in practice.

- Despite numerical techniques may be adopted for solving the cavity expansion problems with more realistic soil models, the expansion generally must commence from a finite cavity radius to avoid infinite strains in circumferential direction. Due to this issue, there is lack of studies in the current literature investigating the cavity expansion from a zero-initial radius. Even if the constant volume theory may be adopted, the solution provided is largely based on the approximation, and the state of stresses and strains of the soil within the annular region remain inaccessible. Hence, a complete stress - strain response and soil displacement variations during the cavity creation process remain unknown (Carter et al. 1979b).
- Large scale field testings to assess the installation effects may not always be cost effective, since the required field instrumentations and monitoring schemes are often expensive, and the equipment may be damaged during the execution process (Nguyen et al. 2019). In addition, the results obtained may be difficult to be applied to other projects since the ground conditions may not be the same.
- Continuum based numerical studies may encounter convergence issues due to the excessively large distortion induced when simulating the installation process. Moreover, the continuum mechanics–based simulations are not capable of providing insights into the fundamentals of granular material behaviours, such as the dilatancy, particle crushing and cementation degradation (Wang et al. 2008a; Wang et al. 2008c; de Bono et al. 2015; Feng et al. 2017).

- Furthermore, there is lack of studies investigating the installation effects in lightly cemented sands. This is attributed to the fact that many existing studies on cemented sand focused on extending the understanding of static and dynamic responses based on small scale laboratory testing, even so, fundamental and inherent mechanisms such as cementation degradation, are not well understood (Yu et al. 2007; Jiang et al. 2013)

## 1.3 Research Significance

According to infrastructure Australia (2016), the population of Australia, , will increase significantly over the next 15 years. By 2031, the population is projected to reach 30 million and most of dwellers will live in the metroplex such as Sydney, which will experience about 50 percent population increase in the next 15 years. The Australian Government has been investing in land transport infrastructure in terms of duplication, upgrade or maintenance to support the rapid population growth. For instance, the 155 kilometres Pacific highway upgrade project, from Woolgoolga to Ballina, has an estimated budget of $4.9 billion. This cost only covers the construction phase of the project, the maintenance and associated rehabilitation costs can be another huge expenditure, and most importantly, there are many similar size projects (e.g. Sydney gateway connecting west and south-west Sydney to the airport) taking place in Australia needing intensive ground improvements.

However, there have been widespread concerns among design engineers, contractors and asset owners on the possibility of existing piles or underground structure (e.g. buried pipelines) being damaged or deteriorated during installation of subsequent rigid inclusion

installation in the vicinity. In addition, the current Australian Standards related to piling (e.g. AS2159 Clause 3.3) do not provide any guidelines in assessing the installation effects, and therefore the design and construction may solely rely on the limited available experience. This may lead to an uneconomical design and pose risks to the construction. Hence, there is a fundamental necessity to decrease the cost of infrastructures by enhancing the quality assurance of rigid inclusion-based ground improvement techniques and propose practical guidelines in assisting both design and constriction engineers in assessing the installation effects and predicting potential risks.

Clearly, there is a need to establish a simple prediction method as well as a comprehensive numerical simulations investigating the pile installation effects, which can consider the realistic constitutive behaviour of soil as well as obtaining complete sets of stress- strain fields, deformations, void ratio distribution and soil displacements in a microscopic level. Considering the capabilities in investigating the problem in microscopic level (e.g. cementation degradation), discrete element method (DEM) can be adopted as an effective tool to study the installation effect of the rigid inclusions in clean and cemented sands (Cundall et al. 1979; Potyondy et al. 2004).

## 1.4 Research Scope and Objectives

This study proposes a realistic 3D numerical model based on discrete element method in investigating the soil response during cavity expansion subjected to rigid inclusion installations. A typical cylindrical cavity expansion model proposed to study the installation effects subjected to driven pile installation is illustrated in Figure 1.1.

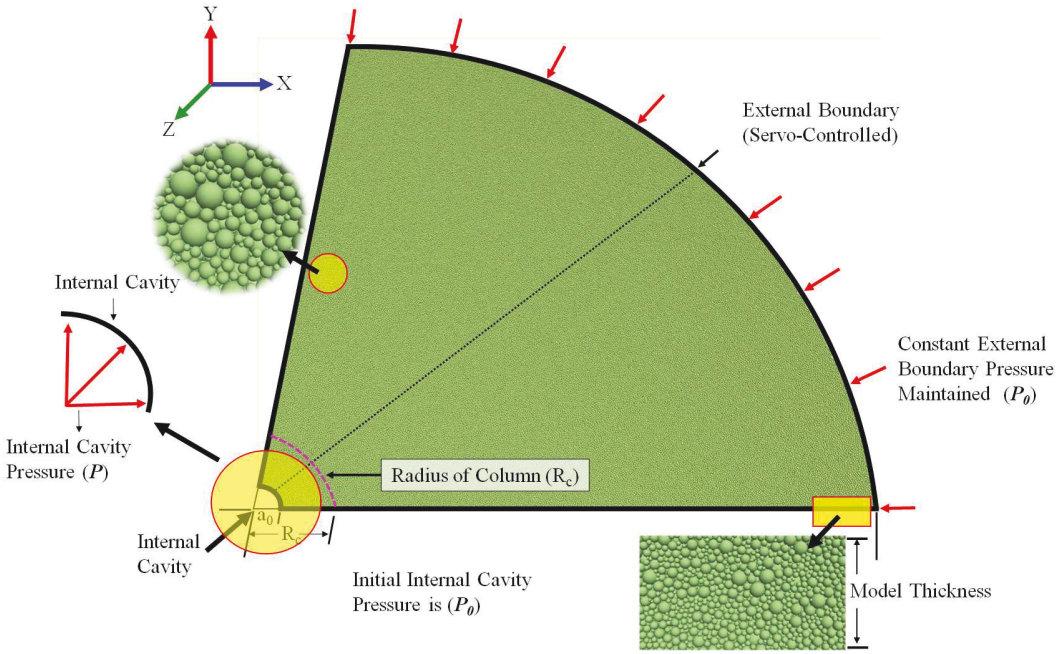


Figure 1.1 A cylindrical cavity expansion model proposed to study the installation effects subjected to driven pile installation

The selection of the cavity expansion was attributed to its widespread applications in analysing many real-life geotechnical problems, including simulation of installation of driven pile, controlled modulus column and vertical drains, and in-situ soil tests such as pressuremeter and cone penetration test (CPT) and so forth. Indeed, the response of the surrounding soil during the pile installation and the cone penetration process is analogous to the creation and expansion of cylindrical cavities (Carter et al. 1979b; Randolph et al. 1979; Salgado et al. 1997; Yu 2013). In this study, two installation processes are explicitly considered, including an expansion of a pre-existing cavity with a finite initial cavity radius, or a creation of a cavity with zero initial radius. The former analysis is to model the pressuremeter and driven pile installation process equivalent to the cases considered

in the classical cavity expansion theory, while the latter simulates the realistic installation process which cannot be easily implemented in continuum based numerical simulations due to convergence issues when dealing with problems involving large displacements or deformations. To achieve this goal, PFC$^{3D}$ software, a three-dimensional explicit discrete element modelling framework, is employed to carry out the numerical simulation. To reproduce the realistic soil behaviour and their interactions at the contacting interfaces, the microscopic contact constitutive models are calibrated against existing experimental results for both clean granular materials and lightly cemented soils. The outcomes of this study provide design and construction engineers with guidelines and suggestions to eliminate the adverse effects induced by the installation of displacement-based inclusions and raise awareness of cementation degradation effects when designing and applying such ground improvement techniques in lightly cemented soils.

In particular, there are five specific objectives formulated in this study as below:

1. Identifying research gap through works carried out previously and literature review to develop specific, measurable, novel and achievable goals and establish a suitable research methodology.
2. Selecting appropriate contact constitutive models and conducting investigations proving the feasibility, capability and effectiveness of adopted discrete element method in studying the cavity expansion problems.

3. Investigating the soil response in three-dimensional cylindrical cavity expansion starting from zero initial cavity radius and assessing the impacts of the choice of arbitrary initial cavity radius.
4. Studying the cavity expansion effects in lightly cemented soils and the impacts of the level of cementation on the soil response while considering the cementation degradation.
5. Investigating the influence of particle upscaling factor and the initial stress field on the soil response during cylindrical cavity expansions.

## 1.5 Organisation of the Thesis

This thesis is organised and structured into seven chapters, with the introduction, statement of problem, research significance, and research scope and objectives presented in the current chapter. The preview of the other six chapters is introduced below:

- Chapter 2 presents a comprehensive yet concise review of literature on common techniques adopted in studying the installation effects, surveying the existing research studies carried out on the cavity expansion theory, laboratory and field tests, as well as the numerical methods.
- Chapter 3 assesses the effectiveness of microscopic contact models commonly adopted in discrete element method and their impacts on the soil response during the expansion of a pre-existing cylindrical cavity in sandy soil, in which three contact models namely linear contact model, rolling resistance contact model and Hertz contact model are compared, and advices in selecting these models are presented and discussed.

- Chapter 4 investigates the influence of choice of initial cavity radius on the soil response during cavity expansion in sandy soil adopting three-dimensional discrete element simulations and obtaining the size of the influence zone when the expansion starts from zero initial radius. The obtained results are compared with analytical solutions and recommendations to practicing engineers are highlighted in this chapter.
- Chapter 5 studies the influence of cementation levels on the stress-strain and strength characteristics of soil during cavity expansion in lightly cemented sand deposits, with the cementation effects between adjacent sand particles being attained adopting the calibrated linear parallel bond model that mimics the cementation at the contacting interfaces. The results characterise the cementation degradation occurring during the installation process and the potential causes and consequences are also discussed and elaborated.
- Chapter 6 evaluates the particle upscaling technique which is widely adopted in discrete element simulation to reduce the computational effort, and also reports the impacts of the initial stress field on cavity pressure and local stress - strain variations in the vicinity of internal cavity. The outcomes may provide suggestions to future research on selecting appropriate modelling parameters.
- Chapter 7 presents the key conclusions of this study and makes recommendations for researcher to further expand this research field.

# Chapter 2 - Literature Review

## 2.1 General

The installation of rigid inclusions (e.g. driven piles, Controlled modulus columns) as a ground improvement approach can displaces soil radially and vertically, leading to excessive soil movement and heave, that may pose risks to piles installed previously in the vicinity and also the foundations of the existing structures (Hagerty et al. 1971; Poulos et al. 1980; Chow et al. 1990). In addition, the pile installation process can cause soil compaction, dilation and stress and strain redistribution within the influence zone, which may reduce the skin friction and hence leads a over prediction of the pile axial and lateral capacities (Cooke et al. 1979; Yi et al. 2013). Moreover, the pile penetration in cemented soils can jeopardize the structure of the soil, which reduces the shear strength and adversely affect the safety and reliability of the design.

Assessing the installation effects of rigid inclusions on the surrounding soils and nearby structures remains a challenging task in geotechnical engineering. This is partially attributed to the fact that the analysis of pile installation in soil is a large displacement and deformation problem, involving geometric complexity and nonlinearities. However, there were research works carried out in the past successfully capturing the essential characteristics of the installation effects.

In this chapter, common techniques adopted in studying the installation effects are presented, concentrating on the cavity expansion theory, laboratory and field tests, as well

as the numerical methods, surveying the existing works carried out in investigating the installation effects of rigid inclusions and in-situ tests, including the driven piles, Controlled modulus Columns (CMCs) or drilled displacement columns, pressuremeter tests, cone penetration tests and so forth.

Section 2.2 provides a brief introduction on the cavity expansion analytical solutions and strain path method. Section 2.3 and 2.4 present a selective practical applications of cavity expansion theory and strain path method, and well recognised laboratory model tests and field investigations carried out in the past. Section 2.5 lists the numerical simulations based on the continuum method in modelling the installations of driven piles or cone penetrations. Section 2.6 introduces the basics of discrete element method, the contact models developed mimicking the behaviour of granular materials, the numerical simulations investigating the installation effects, and the techniques developed simulating the cemented sand. Section 2.7 summaries the gap and limitations in the existing literatures.

## 2.2 Cavity Expansion Theory and Strain Path Method

Cavity expansion theory is the study of the changes in stresses, pore water pressures and displacement fields around spherical or cylindrical cavities in linear or nonlinear soil media. Due to its analogy to many real-life geotechnical engineering applications, for each theoretical solution derived, there is a corresponding geotechnical problem in practice that can be analysed adopting the cavity expansion theory. Like many other

theories in geotechnical engineering, the mathematical modelling in the cavity expansion theory contains simplification in geometry, idealisation of soil properties, describing only the essential features of a problem and neglecting those which are of minor importance. However, it is widely acknowledged that the cavity expansion theory provides a versatile and simple tool for modelling and reflecting many complex field behaviours of many geotechnical problems, such as interpreting the pressuremeter and cone penetration tests, as well as estimating the pile installation effects (Palmer 1971; Carter et al. 1979c; Baligh 1985; Yu 2013).

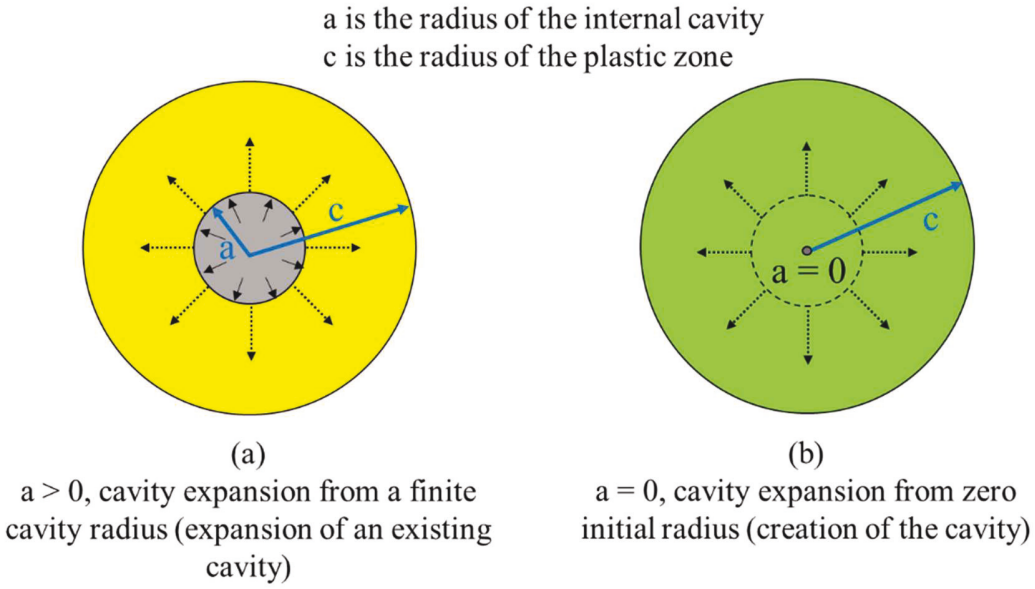


Figure 2.1 Cavity expansion from (a) a non-zero initial radius and (b) a zero-initial radius

In general, in cavity expansion problems, there are two cases, as illustrated in Figure 2.1, to be considered (1) cavity expansion from an initial finite cavity radius (i.e. expansion of a pre-existing cavity) and (2) cavity expansion from zero initial cavity radius (i.e.

creation of an cavity with zero initial radius). The former is often used to model the installation of driven piles or the cone penetration into soils (Randolph et al. 1979; Salgado et al. 1997), while the latter is to analyse the expansion of a cylindrical pressuremeter (Gibson 1961; Wroth et al. 1975; Ladanyi et al. 1998). The solution of the problem is based on the conditions of equilibrium, stress boundary conditions, compatibility and the continuum mechanics. Beside this, a constitutive model describing the soil stress and strain behaviour is also required in solving the boundary value problem associated with an expanding cavity. Therefore, a tremendous amount of effort has been put in developing advanced, realistic constitutive models in the past decades, and the developed models, based on the property, can be generally divided into elastic models and elastic-plastic models (Yu 1990).

The simplest cavity expansion problem was studied with the elastic soil medium obeying Hooke's law, which can usually yield to closed form solutions. The solution includes the radial stress, circumferential stress and radial displacement of a soil element in an infinite or finite medium as the results of the cylindrical and spherical cavity expansion, as shown in Figure 2.2.

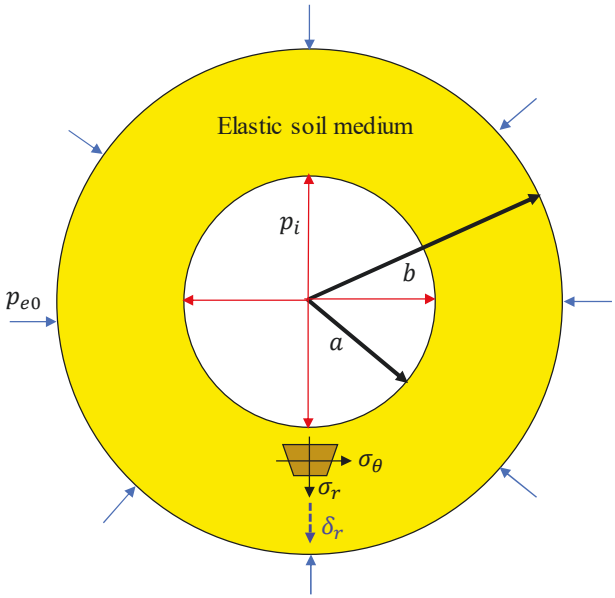


Note:
$p_i$ is the internal radial stress /cavity pressure
$p_{e0}$ is the external radial stress/initial stress field
$a$ is the internal radius of the cavity
$b$ is the external radius of the cavity
$\sigma_r$ is the radial stress and $\sigma_\theta$ is the hoop/circumferential stress
$\delta_r$ is the radial displacement induced by the expansion

Figure 2.2 Schematic diagram showing the cylindrical cavity expansion in an elastic soil medium

The solution of cavity expansion in an elastic medium is achieved based on the equilibrium of the radial and circumferential stresses acting on a soil element, with the external boundary pressure being constant. In addition to the stresses, the strains in the radial and tangential directions can be also expressed as in terms of the radial displacement. Hence, based on the theory of elasticity, the radial and tangential stress variations can be readily derived, as follows:

$$\sigma_r = -p_{e0}b^2(r^2 - a^2)/r^2\,(a^2 - b^2) - p_i a^2(b^2 - r^2)/r^2\,(a^2 - b^2) \tag{2-1}$$

$$\sigma_\theta = -p_{e0}b^2(r^2 + a^2)/r^2\,(a^2 - b^2) + p_i a^2(b^2 + r^2)/r^2\,(a^2 - b^2) \tag{2-2}$$

$$\delta_r = \frac{[(p_i - p_{e0})}{2G\left(\frac{1}{a^2} - \frac{1}{b^2}\right)}\left[\frac{r - 2\vartheta r}{b^2} + \frac{1}{r}\right] \tag{2-3}$$

where, $r$ is current radius of the cavity, $G$ is the shear modulus of the soil medium which can be calculated based on the Poisson's ratio ($\vartheta$) and the Young's modulus ($E$) of the material adopting $G = \frac{E}{2(1+\vartheta)}$.

Detailed derivation procedures of the above can be found in Timoshenko et al. (1970).

### 2.2.1 Cavity Expansion Solutions in Sand

#### 2.2.1.1 Analytical Solutions in Sand

Following the initial attempts mentioned above, the cavity expansion problem was solved for more complex soil constitutive models considering plasticity theories. A simple model of this type is the elastic-perfectly plastic solution. Most of the cavity expansion solutions assumed undrained and drained conditions for simplicity. For sand, the drained behaviour can be analysed using effective stress analysis adopting Mohr Coulomb yield criteria, which assumes that soil behaves elastically until the onset of yielding, determined by the Mohr-Coulomb yield criterion, follow by perfectly plastic behaviour. The material properties that define the stress behaviour include the shear modulus ($G$), cohesion ($C$), Poisson's ratio ($\vartheta$), friction angle ($\emptyset$) and the dilation angle ($\psi$). There were extensive studies of the cavity expansions carried out in such a material, with the yielding condition and flow rule presented by Carter et al. (1986), Collins et al. (1990) and Yu (1993).

Referring to Yu (1993), as the cavity pressure increases, the response is initially elastic with small strains. Before the initial yielding occurs at the internal wall of the cylindrical

cavity, the behaviour of the soil medium is considered to be elastic. However, with the further increase in the cavity pressure resulting the initial yielding occurring at the cavity wall, a plastic zone, shown in Figure 2.3, is formed around the internal cavity. Therefore, determining the occurrence of the yielding becomes the first procedure in any elastic - plastic stress analysis. According to Yu (1992), the cavity pressure leading to the yielding of the surrounding soil in an expanding cylindrical cavity in an finite medium can be represented adopting the following equation:

$$\begin{cases} p_{yeilding} = p_{e0} + \frac{(b^2-a^2)[Y+(\alpha-1)p_{e0}]}{(1+\alpha)b^2+(\alpha-1)a^2} \\ Y = 2c_c * cos\emptyset(1-sin\emptyset) \\ \alpha = (1+sin\emptyset)/(1-sin\emptyset) \end{cases} \quad (2\text{-}4)$$

Where, $p_{yeilding}$ is the limiting pressure; $c_c$ and $\emptyset$ are the cohesion and the friction angle of the material.

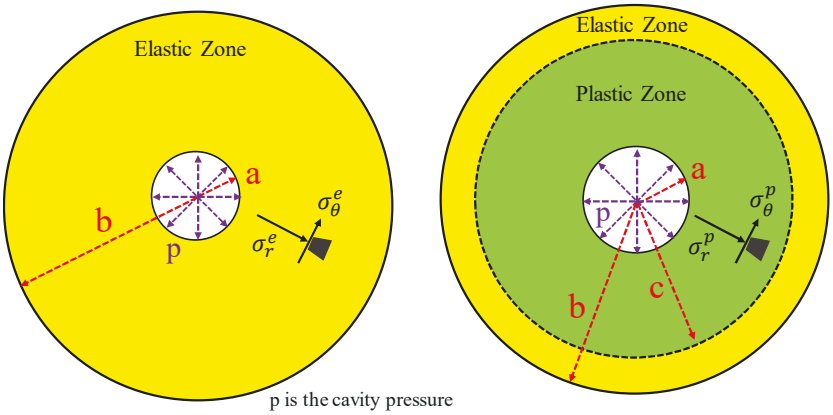


Figure 2.3 A transition from an elastic region to plastic region formed around the cavity when the cavity pressure reaches the yielding stress

Once the yielding stress (i.e. $p_{yeilding}$) has been calculated, the stress-strain and displacement variations can be readily computed based on the elastic solution, as mentioned in the previous section, given that the cavity pressure is less than the determined yielding stress. Hence, it is of paramount importance to determine the radius of the plastic and elastic interface (i.e. $c$ illustrated in Figure 2.3). Based on the equilibrium and the yield condition, the radius of the elastic - plastic boundary can be obtained based on the following equation:

$$c = a\left\{\frac{[(c/b)^2+1+\frac{2}{\alpha-1}][(Y+(\alpha-1)p]}{2+2/(\alpha-1)[(Y+(\alpha-1)p_{e0}]}\right\}^{\frac{\alpha}{\alpha-1}} \tag{2-5}$$

With the determined interface between the elastic and plastic regions induced by the cavity expansion (i.e. $c$), the variations of radial and hoop stresses in these two regions can be expressed adopting the elastic stress and strain relationship as well as the yield condition adopting the formulations below, where, the subscripts $e$ and $p$ represent stresses and strains in elastic and plastic regions, respectively.

$$\sigma_r^e = -p_{e0} + \left(\frac{1}{b^2} - \frac{1}{r^2}\right) \frac{Y + (\alpha-1)p_{e0}}{\frac{(\alpha-1)}{b^2} + \frac{(\alpha+1)}{c^2}} \tag{2-6}$$

$$\sigma_\theta^e = -p_{e0} + \left(\frac{1}{b^2} + \frac{1}{r^2}\right) \frac{Y + (\alpha-1)p_{e0}}{\frac{(\alpha-1)}{b^2} + \frac{(\alpha+1)}{c^2}} \tag{2-7}$$

$$\sigma_r^p = \frac{Y}{(\alpha-1)} - [Y + (\alpha-1)p_{e0}] \left\{ \left[ \frac{1}{(\alpha-1)} - \frac{\left(\frac{c}{b}\right)^2 - 1}{\alpha + 1 + \left(\frac{c}{b}\right)^2 (\alpha-1)} \right] \right\} c^{[(\alpha-1)/\alpha]} \left\{ r^{-[(\alpha-1)/\alpha]} \right\} \tag{2-8}$$

$$\sigma_r^p = \frac{Y}{(\alpha-1)} - \frac{\left\{ [Y + (\alpha-1)p_{e0}] \left\{ \left[ \frac{1}{(\alpha-1)} - \frac{\left(\frac{c}{b}\right)^2 - 1}{\alpha + 1 + \left(\frac{c}{b}\right)^2 (\alpha-1)} \right] \right\} c^{[(\alpha-1)/\alpha]} \right\}}{\alpha} \left\{ r^{-[(\alpha-1)/\alpha]} \right\} \tag{2-9}$$

Detailed formulations and derivation procedures regarding the elastic - perfectly plastic solutions for Mohr coulomb criterion can refer to Yu (2013).

In addition to the large strain analysis of the cylindrical cavity expansion, Yu (1992) developed a rigorous small strain solution concerning the cavity expansion of dilatant materials. Unlike the large strain approach, small strain analysis neglects the changes in geometry during the analysis and hence is only applicable when the deformation is relatively small. In addition, according to Yu (1992), the small strain displacement (i.e.

$\delta_r$) can be expressed in terms of the initial cavity radius (i.e. $a_0$) adopting the following formulations:

$$\frac{\delta_r}{a_0} = \frac{\beta \ln \eta}{\beta+1}\left[1-\left(\frac{c}{a_0}\right)^{1+\frac{1}{\beta}}\right] + \frac{(1+\vartheta)[1+(1-2\vartheta)\left(\frac{c}{b}\right)^2]\left(\frac{c}{a_0}\right)^{1+\frac{1}{\beta}}}{M[(\alpha-1)\left(\frac{c}{b}\right)^2+1+\alpha} + \frac{\alpha\beta\omega}{\alpha+\beta}\left[\left(\frac{c}{a_0}\right)^{1+\frac{1}{\beta}} - \left(\frac{c}{a_0}\right)^{\frac{\alpha-1}{\alpha}}\right] \quad (2\text{-}10)$$

where,

$$\begin{cases} \eta = exp\left\{\frac{(\beta+1)(1-2\vartheta)(1+\vartheta)}{M(\alpha-1)\beta}\right\} \\ M = \frac{E}{2c_c * cos\emptyset/(1-sin\emptyset)+(\alpha-1)p_{e0}} \\ \beta = \frac{1+\mathrm{si}}{1-\mathrm{sin}} \\ \omega = \frac{(1+\vartheta)}{M\beta}\left(\beta-\vartheta-\beta\vartheta+\frac{1-\vartheta-\beta}{\alpha}\right)\left[\frac{1}{\alpha-1}-\frac{\left(\frac{c}{b}\right)^2-1}{(\alpha-1)\left(\frac{c}{b}\right)^2+1+\alpha}\right] \end{cases} \quad (2\text{-}11)$$

$c$ is the radius of the plastic region, $b$ is the initial radius of the outer boundary, $\emptyset$ and $\psi$ are the friction and dilation angles, respectively, and $\vartheta$ is the Poisson's ratio.

Given the initial cavity radius $a_0$ as the denominator, the equation presented by Yu (1992) above clearly implicates that a cavity expansion problem must commence from an arbitrary finite initial cavity radius for the solution, and this explains that a non-zero radius is a prerequisite in the numerical modelling of a cavity expansion problem.

#### 2.2.1.2 Semi Analytical and Numerical Solutions in Sand

The solutions derived previously are based on the elastic - perfectly plastic model considering the strength of the material remains constant after the yielding, which is not true considering the fact that the strength of the materials can vary significantly depending on the deformation history. Hence, to account for this dependency, strain hardening or softening must be considered. Collins et al. (1992) presented a semi-analytical solution adopting the critical state model for both cylindrical and spherical cavity expansions in sands under drained loading condition. The primary difference of the model adopted in Collins et al. (1992) from the elastic - perfectly plastic model with constant material parameters, is that the internal friction and dilation angles depend on the current specific volume and mean stress. One of the basic assumptions made in the model is that the material is in its critical state, deforming with no plastic volume variations, and therefore the dilation angle is considered to be zero. Moreover, the material behaviour and properties before reaching the critical state is determined by a composite state parameter ($\xi$) defined as a function of the specific volume and the mean effective stress, as follows:

$$\xi = \vartheta_s + \lambda \ln {p'}/{p_{ref}} - \Gamma_1 \tag{2-12}$$

where, $\vartheta_s$ denotes the specific volume, $p'$ is the mean effective stress and $p_{ref}$ is the reference mean stress, $\lambda$ is the slope if the critical state line, and $\Gamma_1$ is the intercept on the specific volume axis when the ${p'}/{p_{ref}} = 1$, as illustrated in Figure 2.4.

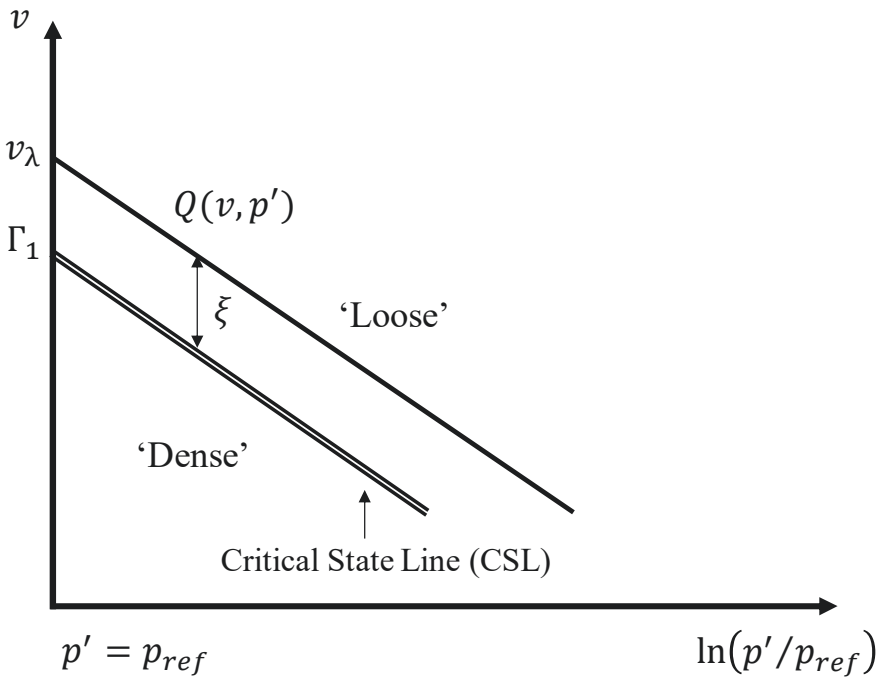


Figure 2.4 Critical state line and state parameter in $\vartheta$-$ln\,p'$ plane, after Collins et al. (1992)

In Collins et al. (1992), the yield criterion based on Mohr-coulomb was deployed describing the behaviour of sand specimen, and the relationship between the major and minor principal stresses (i.e. radial $\sigma_r$ and hoop stresses $\sigma_\theta$) at the yielding is defined as:

$$\sigma_r = \frac{1+sin\emptyset}{1-sin\emptyset}\sigma_\theta \tag{2-13}$$

Additionally, Collins et al. (1992) adopted the correlation established by Been et al. (1985) between the internal friction angle at a given state and the critical state friction angle plotted against the state parameter, which can be expressed as:

$$\emptyset_m - \emptyset'_{cv} = A_{cf}[\exp(-\xi) - 1] \quad (2\text{-}14)$$

where, $\emptyset_m$ is the mobilised friction angle and $\emptyset'_{cv}$ is the internal friction angle at critical state; $A_{cf}$ is a curve fitting parameter in the range of 0.6 - 0.95 depending on the material type.

In addition, the stress dilatancy relationship calculating the dilation and friction angles developed by Rowe (1962) and simplified by Bolton (1986) was also considered by Collins et al. (1992) in linking the plastic potential and the state parameters, as follows:

$$\psi_m = 1.25A_{cf}[\exp(-\xi) - 1] \quad (2\text{-}15)$$

where, $\psi_m$ is the mobilised dilation angle.

Given the aforementioned yield condition and flow rate, and combining the formulations presented by Carter et al. (1986) and Collins et al. (1990), the solutions of the cylindrical cavity expansion in the elastic region, as shown in Figure 2.3, were derived for both stresses and displacements:

$$\sigma_r = p_{e0} + 2G\frac{(a-1)p_{e0}}{2(1+a)G}\left(\frac{c}{r}\right)^2 \quad (2\text{-}16)$$

$$\sigma_\theta = p_{e0} - 2G\frac{(a-1)p_{e0}}{2(1+a)G}\left(\frac{c}{r}\right)^2 \quad (2\text{-}17)$$

$$\delta_r = \frac{(a-1)p_{e0}}{2(1+a)G}\left(\frac{c^2}{r}\right) \quad (2\text{-}18)$$

The derivation of the solutions in the plastic region contains material time derivative and hence detailed formulations regarding the solutions can be found in Collins et al. (1990) and Yu (2013).

In addition to the analytical solutions and semi analytical solution presented in earlier, there are also numerical techniques developed to considered more realistic and sophisticated soil constitutive models in cohesive and cohesionless soils under fully drained or undrained conditions, such as those presented by (Yu 1990).

### 2.2.2 Cavity Expansion Solutions in Clay

#### 2.2.2.1 Analytical Solutions in Clay

Beside the analytical cavity expansion solutions developed for sand, there were extensive studies carried out in clay (Hill 1950; Gibson 1961; Palmer 1971; Vesic 1972; Carter et al. 1986). For the undrained condition (typically occurring in clay), the cohesive soil is usually modelled using the Tresca yield criteria (Hill 1950). The Tresca yield criterion can be expressed by major and minor principle stresses as $\sigma_1 - \sigma_3 = 2s_u$, where $s_u$ is the undrained shear strength of a cohesive soil. Similar to the cavity expansion problem presented in Figure 2.3, as the cavity pressure increases, the response of the surrounding soil of an expansion cavity is initially elastic with small strains. Once the yield value is reached, a plastic zone is formed around the cavity extending to a radius $c = a(\frac{G}{s_u})^{1/2}$, referring to Hill (1950), where $G$ is the elastic shear modulus. Combining the equation of

equilibrium and the yield condition in the plastic region, Hill (1950) presented the radial and hoop stresses in the plastic zone in a finite medium to be:

$$\sigma_r = -p_{e0} - s_u - 2s_u \ln\frac{c}{r} + \left({}^{2s_u c^2}/_{2b^2}\right) \tag{2-19}$$

$$\sigma_\theta = -p_{e0} + s_u - 2s_u \ln\frac{c}{r} + \left({}^{2s_u c^2}/_{2b^2}\right) \tag{2-20}$$

It is important to note that when the cavity is expanded from zero radius, the pressure in the cavity is constant and can be recognised as the asymptotical limit pressure reached as a cavity with non-zero initial radius is expanded to infinity. Hill (1950) has shown that the limit pressure is reached immediately before any occurrence of the displacement. Solutions for undrained cylindrical cavity expansion in an infinite medium from zero initial radius revealed that the constant internal pressure can be calculated from:

$$p_{lim} = s_u\left(1 + \ln\left(\frac{G}{s_u}\right)\right) + p_{e0} \tag{2-21}$$

where, $p_0$ is the initial internal pressure at the cavity wall. The limiting pressure $p_{lim}$ is the pressure required to cause cavity expansion and remains constant.

In addition, a special case extending the solution presented by Hill (1950) to cylindrical cavity expanded from a non-zero initial radius in an infinite large soil medium, was established as below considering the Poisson's ratio for undrained clays being 0.5.

$$\frac{p-p_{e0}}{2s_u} = \frac{1}{2} + \frac{1}{2}\ln\left[\frac{G}{s_u}\left[1 - \left(\frac{a_0}{a}\right)^2\right] + \left(\frac{a_0}{a}\right)^2\right] \tag{2-22}$$

where, $a_0$ is the initial cavity radius and $a$ is the instant cavity radius during the cavity expansion. The cavity expansion relationship presented above is identical to the solution derived by Gibson (1961).

Beside the closed form solutions proposed by Hill (1950) and Gibson (1961), Carter et al. (1986) presented an analytical solution for the expansions in an idealistic, cohesive frictional material, which is considered to be isotropic, elastic - perfectly plastic obeying Hooke's law until yielding, in which the yielding is determined based on the Mohr-Coulomb criterion. Referring to Carter et al. (1986), yield criterion of an ideal cohesive - friction material can be expressed as:

$$\sigma_1 + c_c \cot \emptyset = \frac{1+\sin \emptyset}{1-\sin \emptyset}(\sigma_3 + c_c \cot \emptyset) \tag{2-23}$$

where, $\sigma_1$ and $\sigma_3$ are the major and minor principle stresses, respectively; $c_c$ is the soil cohesion.

According to Carter et al. (1986), a steady state cavity pressure would be approached when the ratio between the radius of the plastic region and the current cavity radius reaches a certain value (i.e. when the cavity is expanded infinitely large), based on which, the limit pressure in a cohesive friction material can be expressed as follows:

$$\frac{2G}{p_0+c_c \cot \emptyset} = \frac{\alpha-1}{\alpha+1}\left[T\left(\frac{p_{lim}+c_c \cot \emptyset}{\sigma_r+c_c \cot \emptyset}\right)^{\gamma} - Z\left(\frac{p_{lim}+c_c \cot \emptyset}{\sigma_r+c_c \cot \emptyset}\right)\right] \tag{2-24}$$

$$\begin{cases} \alpha = \frac{1+\sin \emptyset}{1-\mathrm{s} \quad \emptyset} \\ T = 2\left(1 + \frac{\chi}{\frac{1}{\beta}+\frac{1}{\alpha}}\right) \\ \chi = \frac{(1-\vartheta)-\vartheta(\beta+N)+(1-\vartheta)\beta\alpha}{\beta N} \\ \beta = \frac{1+\sin}{1-\sin} \\ \gamma = \frac{(\beta+1)\alpha}{\beta(\alpha-1)} \\ Z = \frac{2\chi}{\frac{1}{\beta}+\frac{1}{\alpha}} \end{cases} \tag{2-25}$$

where, $p_{lim}$ is the limiting pressure, $\psi$ is the dilation angle, and $\vartheta$ is the Poisson's ratio.

As discussed in Carter et al. (1986), the aforementioned equation can be also adopted to express the limit cavity pressure for a purely cohesive soil considering the friction angle $\emptyset$ being zero.

Adopting the same Poisson's ratio (i.e. 0.5) as in Gibson (1961), the limit pressure for the undrained cylindrical cavity expansion in an infinite medium can be obtained as below:

$$p_{lim} = c_c\left(1 + \ln\left(\frac{G}{c_c}\right)\right) + p_{e0} \tag{2-26}$$

The above is identical to the limiting pressure reported by Hill (1950) and Gibson (1961).

#### 2.2.2.2 Semi Analytical and Numerical Solutions in Clay

A realistic constitutive law capturing the soil behaviour should consider the soil strength changes owing to the deformation history, which must be described by a strain-hardening

or softening rule. The most well-known hardening/softening model is based on the critical state theory. The most important and relevant contributions related to pile penetration is the large strain cavity expansion problem in undrained clays modelled using Modified Cam-clay model (MCC) analysed by Collins et al. (1996b). In this model, the strength of the soil is a function of effective stress rather than total stress that is usually adopted for undrained analysis. and the soil stress history has a considerable effect on the cavity expansion solutions. The problem is illustrated in Figure 2.5, where $a_0$ and $a$ are the initial and current cavity radius, and $r$ is the current radius of a soil element which was initially at $r_0$.

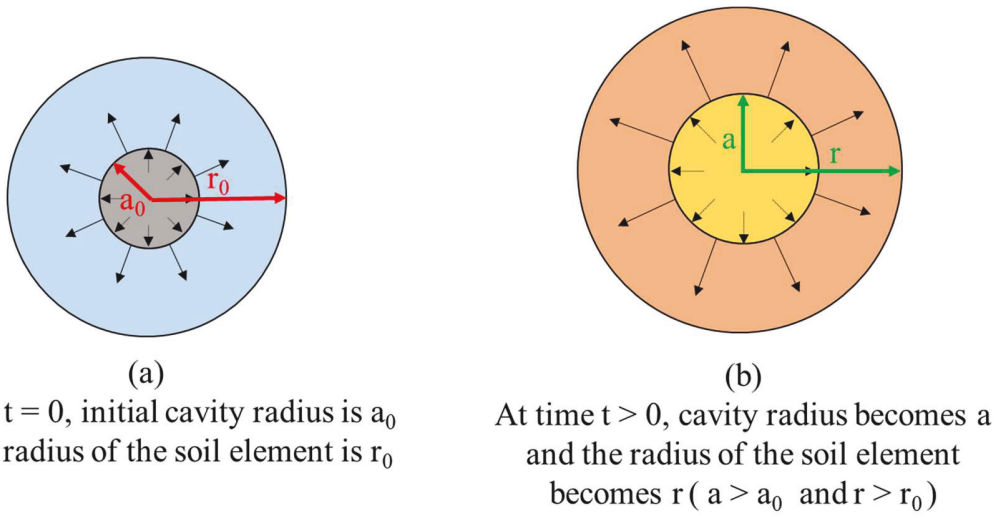


(a)
At time t = 0, initial cavity radius is $a_0$ and the radius of the soil element is $r_0$

(b)
At time t > 0, cavity radius becomes a and the radius of the soil element becomes r ( $a > a_0$ and $r > r_0$ )

Figure 2.5 (a) Prior to cavity expansion (t = 0) and (b) when cavity radius is expanded (t > 0)

Referring to Collins et al. (1996b), during both elastic and elastic - plastic phases of a cylindrical cavity expansion, the shear strain at the cavity wall ($\gamma_c$) is estimated from the equation below:

$$\gamma_c = 2\ln\left(\frac{a}{a_0}\right) \tag{2-27}$$

This implies that the shear strain at the cavity wall is infinite when the initial cavity radius is zero, which justifies why the cavity expansion from a finite radius is adopted for the numerical simulations.

Moreover, as more complicated and realistic soil constitutive models are developed representing the soil medium in a cavity expansion, especially when a saturated two-phase soil is considered, derivation of closed form solutions becomes impossible. Thus, the numerical technique may be the only approach to obtained a solution (Carter et al. 1979b; Carter et al. 1985). Carter et al. (1979b) considered a volumetric hardening, elastoplastic material based on critical state concepts (Schofield et al. 1968) to study the stress and pore pressure changes during the cylindrical cavity expansion. As mentioned in Carter et al. (1979b), the numerical calculations must begin with a finite cavity radius ($a_0 \neq 0$) to avoid the circumferential strain being infinite. Hence, Carter et al. (1979b) presented an equivalent approximation modelling the creation of the cavity (i.e. from 0 to $R_c = \sqrt{3}a_0$) to an expansion of an existing cavity (i.e. from $a_0 > 0$ to $2a_0$), by assuming the constant volume of the expansion (i.e. $V_{(0-\sqrt{3}a_0)} = V_{(a_0-2a_0)}$; $V$ being the volume of the expansion), as illustrated in Figure 2.6. This implies that an arbitrary non-

zero value may be chosen as the initial cavity radius to model the creation of the cavity (i.e. the installation of a driven pile) as long as the constant volume is satisfied.

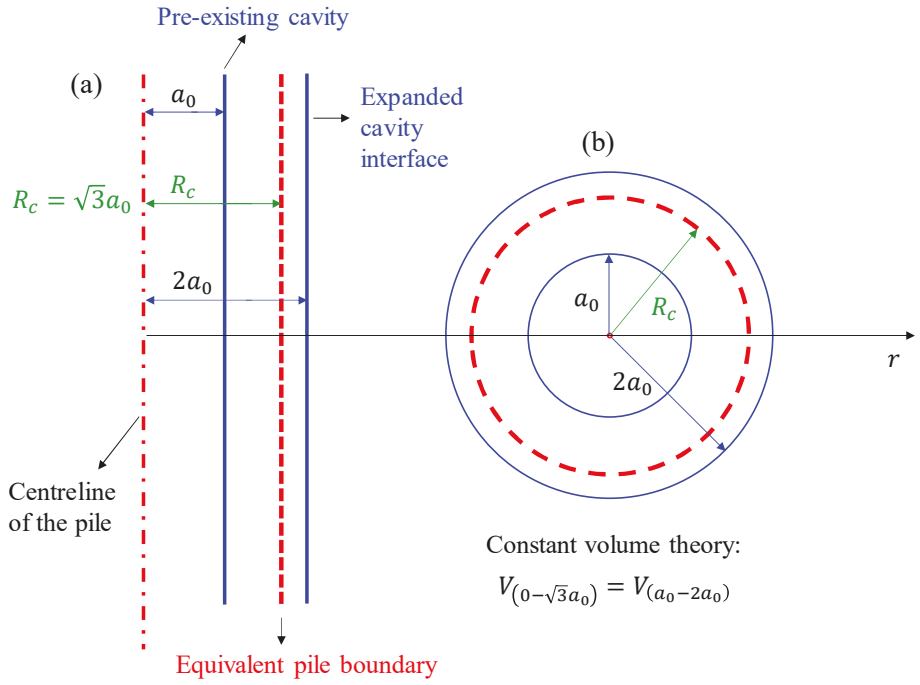


Figure 2.6 Finite cavity expansion for modelling pile installation, after Carter et al. (1979b)

### 2.2.3 Strain Path Method

In addition to the cavity expansion theories adopted to study the stress and strain variations in the soil, Baligh (1985) proposed an approximate analytical solution to predict soil disturbance induced by the installation of various rigid objects installed in the ground, called Strain Path Method (SPM). This method can be effectively used to analyse the cone penetration and is considered as a more realistic solution for the installation problem, especially at the tip of the cone and for deep penetration problems. However, it

does not offer a way to estimate the horizontal stress changes or the estimated stresses acting on the shaft, as offered by the cavity expansion theory.

Similar to the cavity expansion method, the strain path methods are only applicable to homogenous soils and do not consider the presence of the stress-free ground surface. In other words, this method is only applicable to points in the soil where the cylindrical/spherical cavity expansion model is relevant. SPM cannot predict the vertical soil movements (Poulos 1994) and more importantly, there are serious concerns about disregarding the equilibrium conditions (Randolph 2003).

Sagaseta et al. (1997) and Sagaseta et al. (2001a) modified the strain path method to consider the impact exerted from the stress free ground surface, and therefore the shallow strain path method (SSPM) was developed in predicting soil movement when the tip of the pile is located at a closer distance below the ground. The SSPM solution combines the merits of SPM for deep penetrations, and the method used to compute soil deformations due to near-surface ground loss (Sagaseta 1987). The closed-form small-strain solutions for soil movement around an axisymmetric closed-ended pile with a rounded tip are shown in Equations (2-28). These equations can be used to reliably predict the ground movements due to column installation (Sagaseta et al. 2001b)

$$\begin{cases} \delta_{rSS}(r,0) = \frac{{R_c}^2}{2} \cdot \frac{L_p}{r\sqrt{r^2+{L_p}^2}} = \frac{\Omega}{2\pi} \cdot \frac{L_p}{r\sqrt{r^2+{L_p}^2}} \\ \delta_{zSS}(r,0) = -\frac{{R_c}^2}{2} \cdot \left(\frac{1}{r} - \frac{L_p}{r\sqrt{r^2+{L_p}^2}}\right) = -\frac{\Omega}{2\pi} \cdot \left(\frac{1}{r} - \frac{L_p}{r\sqrt{r^2+{L_p}^2}}\right) \end{cases} \quad (2\text{-}28)$$

Where $R_c$ is the radius of the pile, $L_p$ is the embedded length of the pile, $\Omega$ is the cross sectional area, $SS$ refers to 'small strain', and $r$ and $z$ are the two cylindrical coordinates ($z$ at the surface is 0).

Later Ni et al. (2009) compared the results obtained from the physical modelling of pile penetration in transparent soils with the predictions using SSPM method. Good agreements were noticed although there are some disparities in terms of magnitudes of downward movements of the soil.

## 2.3 Applications of Cavity Expansion and Strain Path Methods Assessing Installation Effects

The previous section presented the theoretical aspects of the cavity expansion and strain path methods, while the major applications of these two methods in assessing the installation effects are presented in this section.

Carter et al. (1980) adopted the cavity expansion theory to model the displacement pile installation numerically under plane - strain condition based on the constant volume theory proposed by Carter et al. (1979b). Due to the fact that the soil close to the pile will be disturbed by the pile installation, a remould state may be reached immediately after the installation, which, according to Carter et al. (1980), may be well represented based on critical state concepts. Hence, an effective analysis based on the Modified Cam Clay model considering the changes of undrained shear strength with the mean effective stress as consolidation proceeds was carried out by Carter et al. (1980). The results confirmed

that the stress changes induced by the pile driving and subsequent consolidation process are not related to the initial over consolidation ratio but solely determined by the initial undrained shear strength. Furthermore, it is also observed that the size of the disturbed region in soil increases with the increase in the cross-sectional area of the pile, and due to an increase in the size of disturbed region, the magnitude of the excess porewater generated increases accordingly. However, there is no information regarding the soil displacement in Carter et al. (1980).

Chow et al. (1990) investigated the displacements in the vertical and radial directions induced by the driven pile installations in a thick deposit of saturated clay. This analysis was developed based on the closed-form solutions derived by Sagaseta (1987) to obtain the vertical soil movement within an incompressible homogeneous, isotropic linear elastic half space adopting the cavity expansion theory. As mentioned in Chow et al. (1990), the penetration of a driven pile into the ground can lead to vertical soil movement (i.e. soil heave of the pile being installed), and, in the meantime, induces the heave (i.e. uplift) of piles that have already been installed in the vicinity. Referring to Chow et al. (1990), the heave at the ground surface show an increase with the pile diameter and the penetration depth; given a radial distance of $2D$ ($D$ being the diameter of the pile), the maximum ground heave predicted can reach 6% of the pile diameter (i.e. $D$). However, as the depth of penetration increases to a certain level (i.e. critical depth), the rate of increase in the ground heave reduces continuously, and the downward and lateral soil movements at the pile toe become dominant beyond this critical depth (Chow et al. 1990).

However, the radial displacement induced by the pile installation was not comprehensively studied.

Poulos (1994) studied the installation effects of driven piles based on a modified strain path method, particularly focusing on the lateral and axial displacements generated in adjacent already installed piles. As discussed by Poulos (1994), the strain path method (SPM) developed by Baligh (1985) was for a deep homogenous clay soil with no presence of the ground surface taken into account, which was not appropriate considering the pile driving through soft clay to a stiffer stratum in common practice. Hence, a modification was applied to Baligh (1985) solution to compute the approximate vertical displacement around a pile. The results confirmed that the soil movement induced by the driven pile installation can lead to significant lateral and axial forces and movements in adjacent already installed piles. Referring to Poulos (1994), downward soil movement occurred at the early stage of the pile installation process, whereas the soil deformation became mainly lateral when the final penetration was approached. In addition, it was reported that the yield bending moment in an already installed pile may be reached or even exceeded due to the soil lateral movement induced by the pile installation, especially when the piles are closely spaced. It is therefore suggested by Poulos (1994) that the installation of driven piles with a spacing less than three times of the diameter should be avoided in the practice and pre-boring may be considered to effectively reduce the soil movements caused by the pile driving.

## 2.4 Laboratory Model Tests and Fields Investigations

Owning to the simplifications and assumptions made in assessing the installation effects analytically and numerically, including obtaining the stresses, pore water pressures and displacements, discrepancies to the site investigation data are often observed (Coop et al. 1989). Therefore, there were studies carried out by means of small-scale laboratory tests (e.g. model and centrifuge tests) and large-scale field investigations in either cohesive or cohesionless soils.

Robinsky et al. (1964) adopted radiography techniques to assess the displacement and compaction of sand around a model pile that was instrumented internally adopting strain gauges for the determination of load distribution to the surrounding soil. It was found that the compaction and the displacements induced by the pile installation showed a tendency to decrease the sand density in the vicinity of the pile wall, which, to some extent, nullified the benefits gained from the primary compaction. Moreover, as mentioned in Robinsky et al. (1964), the influence zone of the soil lateral movement detected by the radiography technique in loose and medium dense sands were approximately 3 - 5.5 times of the pile diameter.

Additionally, Hagerty et al. (1971) studied the soil heave and lateral displacements due to pile driving based on thirteen case histories. As concluded by Hagerty et al. (1971), it is more likely to induce significant soil displacements during driven pile installation in fine grained soils while the behaviour of the saturated insensitive clay was incompressible

during driving (i.e. the volume of displaced soil induced by pile installation was the same as the volume of the pile). Furthermore, it was reported that the observed soil heave in cohesionless materials may be considerably less than that occurring in insensitive clays.

Coop et al. (1989) conducted field studies on an instrumented cylindrical model pile driven into two clayey soils with different overconsolidation ratios. The site measurements were compared to the cavity expansion theoretical predictions, and it was found that the stress relief was captured immediately behind the pile tip during the pile installation process, which caused both the total radial stress and pore pressure measurements being lower than the predications based on cavity expansion theories. However, in terms of the radial effective stress, the cavity expansion theory may provide a reasonable prediction if the installations are sufficiently rapid avoiding consolidation effects. In addition, according to Coop et al. (1989), the critical state , as one of the main assumptions in many available theories assessing the installation effect, was not reached in the soil adjacent to the pile during the undrained loading.

Suleiman et al. (2015) studied the installation effect of Concrete Injected Column (CIC) on the surrounding soils in a field investigation. The field study consists of the installation of a 320 mm diameter CIC and a load test. For load testing purposes, four reinforced CICs with diameter of 395 mm were installed around the central CIC test unit, as reaction piles. The ground consisted of 1.2m thick sand over soft sandy organic soils extending to a depth of approximately 7.6 m, which overlay bedrock. The water table was found at 1.6 m below ground surface. The instrumentation included four push-in pressure sensors to

capture the change in the soil stress and the excess pore water pressure sensor, installed at 2 m depth, and four shape acceleration arrays (SAA) to monitor lateral soil displacements throughout the column installation process and load testing. It was observed that the soil horizontal stress increased when the mandrel passed the depth (location) of the pressure sensors during the downward mandrel advancement and during retrieval. At the end of CIC installation, the readings from the pressure sensors indicates an increase in the horizontal soil stress by 85.2 kPa recorded within 1D (diameter being the diameter of the CIC) distance from the CIC, by 26.1 kPa within a distance of twice of the pile diameter, and then with descending trend with the increase in distance from the CIC.

## 2.5 Continuum Based Numerical Simulations

As described in the previous sections, there are three main streams in assessing the installation effects: the use of the cavity expansion theory, the strain path methods and the experimental or field tests. However, field tests require extensive instrumentation such as pore water pressure transducers, strain gauges, and pressure cells. Hence, experimental and field tests are not always the most attractive due to the high cost.

With the rapid advancement in computational facilities, and with the development of more advanced and realistic constitutive models, the computer modelling using continuum-based method (e.g. finite element method (FEM) or the finite difference method (FDM)) is often adopted. As mentioned by Carter et al. (1979b), numerical

calculation concerning the pile installation problem must start with an finite initial radius to avoid infinite circumferential strain. Indeed, the simulation of pile installation can be assumed as a quasi-static large deformation problem, therefore, algorithms considering large strain formulations must be incorporated. Common techniques adopted in continuum-based simulation include Arbitrary Lagrangian Eulerian (ALE) technique, the Couple Eulerian Lagrangian (CEL) method and material point method (MPM). All of these aforementioned techniques were successfully adopted to model the installation process (e.g. driven pile installation, cone penetration, and stand penetration).

Susila et al. (2003) presented a large displacement FEM model simulating the cone penetration test in sand adopting an auto-adaptive remeshing technique to cope with large deformation and distortion at the vicinity of the cone tip during penetrating process. The approach adopted Lagrangian formulation to re-discretise the deformed boundary and generate a new refined mesh with all field variables defining the mechanical state inherited. The soil was model using Drucker-Prager constitutive model with a Coulomb friction and non-associative flow rule in ABAQUS. The results confirmed that the auto-adaptive remeshing technique is able to handle the large distortion induced in the surrounding proximity of the cone tip. In addition, as reported in Susila et al. (2003), the tip resistance in dense sand was affected by the soil within the distance of 16 - 22 cone diameter above and below the cone tip, whereas an influence zone within 5 - 7 cone diameter distance was observed in loose sand, which served as a guideline for future numerical modellings in selecting the size of model boundaries.

Sheng et al. (2005) proposed a finite element simulation with the capability of simulating the true installation procedure of a pile adopting large-slip friction contact in adopting Modified Cam clay material model. The updated Lagrangian formulated was used to account for the large displacements during the pile penetration. As discussed in Sheng et al. (2005), the soil situated in the vicinity of the pile shaft underwent radial and downward movements during the axial pile push-in process, leading to the compaction of the soil, and it is reported that this compressed soil zone is approximately extended $1D$ ($D$ being the diameter of the pile). In the vertical direction, however, evident compression was only observed beneath the pile tip, while the soil located near the ground surface exhibited a volumetric expansion (i.e. heave). In addition, the computed total resistance and shaft resistance based on numerical simulations were compared to the testing results obtained from centrifuge tests. It was concluded by Sheng et al. (2005) that the total resistance predicted agreed well with the experimental measurements whereas the shaft resistance depicted an evident discrepancy. This was attributed to the cone effects since the pile modelled in the simulation must contain a conic tip instead of a flat end to avoid numerical convergence and mesh distortion issue.

Henke (2010) investigated the effects of pile installation on adjacent structures adopting a three-dimensional continuum model. In the axis of the pile penetration, a rigid thin cylindrical frictionless tube was modelled first in contact with the surrounding soil. The actual pile installation process was simulated by sliding the pile over the pre-installed tube and hence the contact between the pile and the soil could be set up. As discussed in

Henke (2010), the proposed modelling approach was not able to simulate the drifting or twisting behaviour of the soil profile adjacent to the pile. However, the limitation exerted no impact on the installation effects on adjacent structures. The results confirmed that the induced installation effects contain a combination effects of rotational, translational and bending deformations. Given a pile diameter of 30 cm and a length of 5 m, the induced horizontal displacement to an already installed pile was approximately 12 mm, while the spacing between two piles was 1 m. In addition, it was reported by Henke (2010) that the horizontal stresses due to the installation of the piles could increase up to 16 times, and the increase in horizontal stress showed a direct correlation with the pile cross sectional area and the soil density. However, this increase in horizontal stress reduced significantly with the radial distance.

Pucker et al. (2012) presented a numerical study on the installation process of full displacement piles adopting a coupled Eulerian-Lagrangian approach in cohesionless sand. The material behaviour was described by the hypoplastic model based on the combination of constitution laws proposed in Niemunis et al. (1997) and Von Wolffersdorff (1996) to reproduce the realistic behaviour of granular materials. The approach combined the merits of both the Eulerian and Lagrangian formulations to overcome mesh distortion problems induced by the pile installation. To precisely capture the installation effects, the drilling tool (i.e. auger) was considered and modelled as a volumetric rigid body considering the realistic size and dimensions. The model adopted by Pucker et al. (2012) is illustrated in Figure 2.7.

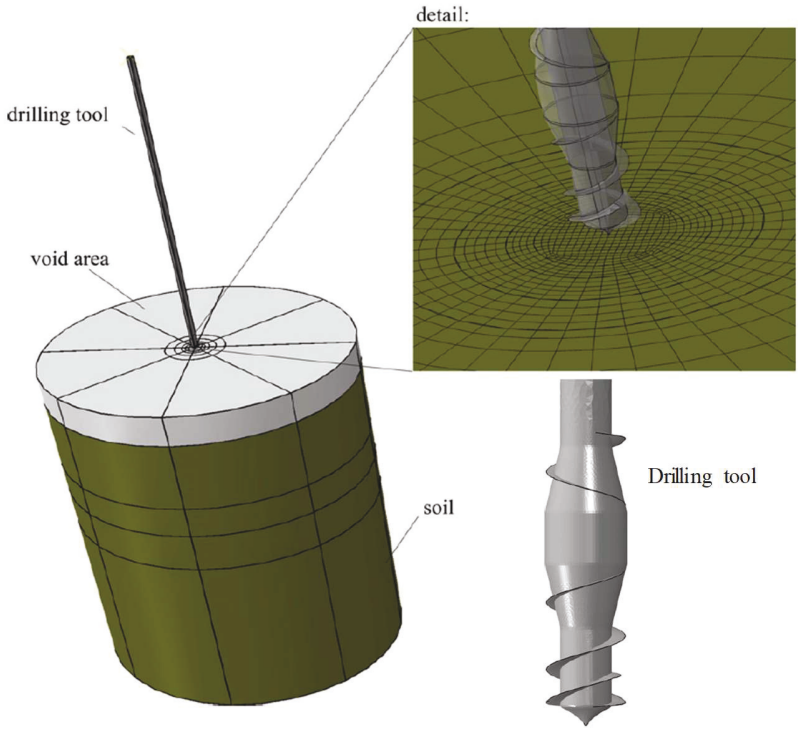


Figure 2.7 FEM model simulating the auguring process and the installation of full displacement piles, after Pucker et al. (2012)

The results focused on the horizontal displacements and void ratio variations during the installation of displacement piles. Referring to Pucker et al. (2012), the horizontal soil displacements induced by the installation generally increased with depth, whereas an inverse trend was noticed with respect to the relative density of the soil medium, given the same radial distance. In addition, it was reported in Pucker et al. (2012) that during the installation of the displacement piles, soils situated in the proximity of the pile (i.e. 1D, D being the pile diameter) was loosened up, whereas the soil located between 1D and 7D was strongly densified (i.e. reduced in void ratio). However, in a great radial distance away from the pile (i.e. 7D to 10D), the soil was slightly densified.

The technique introduced in the previous sections were mainly based on the ALE and CEL methods that can overcome the mesh distortion during the analysis. However, as pointed out by Sulsky et al. (1994) and Bardenhagen et al. (2000), direct mapping the state variables allocated to the material in these remeshing techniques can introduce uncertainties into the calculation, leading to the inaccuracy of the results. This facilitates the development of the particle methods, particularly the material point method (MPM). The primary advantage of MPM is that the state variables will be assigned to the material points and will be independent to the computational mesh. Phuong et al. (2016) studied the pile installation effects in sand adopting material point method. In order to compare the results measured in centrifuge tests, the proposed model was 0.6 m in diameter and 0.79 m in height. Considering the axisymmetric condition, a pie slice model corresponding to a central angle of $\alpha = 20°$ was considered, and the installation process was modelled as pile penetration in a constant rate. The results confirmed that the soil, during the pile installation, was pushed away downwards and radially from the pile, leading to a significant densification of the soil around the pile, and a considerably enhanced lateral stress at the tip of the pile. As mentioned in Phuong et al. (2016), the influence zone in terms of the soil densification in the radial direction extended to a radial distance of 8D (D being the pile diameter), while a 7D influence zone was noted for the soil densification occurring below the pile tip. According to Phuong et al. (2016), the bearing capacity predicted in a static load test, was significantly higher when taking the installation effects into consideration, which highlighted the importance of understanding the installation effects of piles in the real life practices.

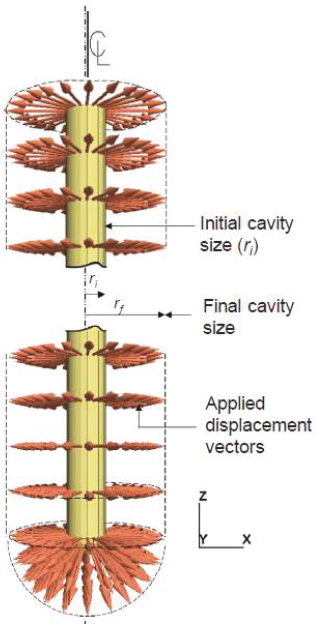


Figure 2.8 Schematic diagram showing the cavity expansion, with the tip modelled as spherical cavity expansion and the shaft simulated adopting cylindrical cavity expansion

Nguyen et al. (2019) presented a numerical investigation studying the installation sequence of plain concrete rigid inclusions, in which the effects on the installation of controlled modulus columns (CMC) were comprehensively discussed. The simulation of the CMC installation was performed in FLAC$^{3D}$ based on the finite difference method. The column was modelled based on Hoek-Brown material model while the Modified Cam Clay model was adopted to describe the behaviour of soft clay. Considering the fact that remeshing techniques such as ALE or CEL techniques generally required more computational time and were sophisticated to be implemented, the explicit simulation of the actual installation process was not considered in Nguyen et al. (2019). However, modelling of CMC installation utilising the cavity expansion method in the numerical

simulation was adopted, in which the installation of the column tip was considered as a spherical problem whereas the shaft was modelled as cylindrical cavity expansion, as it can be seen in Figure 2.8. It was found that the installation process induced both the lateral deformation and soil heave. Referring to Nguyen et al. (2019), the zone of influence in terms of lateral displacement, after the installation of a single CMC with a diameter of 0.45 m, extended approximately 24 times of the its radius (i.e. $r$). With the installation of a second column located 1.8 m away from the previously installed column, this zone of influence was furtherly enlarged to $28r$. In addition, as mentioned in Nguyen et al. (2019), the induced ground movement from the newly installed CMCs can lead to the uplift of already installed columns, and the uplifts observed at the column head and tip were 2% and 1% of the column diameter, respectively. However, the ground surface heave due to the column installation can reach three times more than the column head uplift. Hence, it was suggested that the structural integrity of the closely spaced columns should be inspected after the installation.

## 2.6 Discrete Element Method Simulations

### 2.6.1 Overview

The simulations investigating the installation effects reported in previous section, including the driven piles, cone penetration, and CMC/CIC installations, are based on continuum methods. However, most of software packages based on continuum based methods may encounter convergence issues when simulating the actual pile installation

process (i.e. when there is a cavity creation process involved). This is attributed to that the numerical calculations based on continuum method must commence from an finite initial radius to avoid infinite circumferential strains (Carter et al. 1979b). Despite the fact that the expansion of a pre-existing cavity may provide an adequate approximation to the cavity creation based on the constant volume theory, the state of stress of the soil contained in the annular region remains inaccessible (Carter et al. 1979b). As mentioned in the previous sections, there were techniques developed such as ALE, CEL and MPM overcoming the large distortion involving in the pile installation process, these mesh free or adaptive remeshing techniques are complex to be implemented and generally require more computation time (Nagashima et al. 2003; Susila et al. 2003).

In addition, the installation effects of driven piles in cemented sand has not been adequately examined or understood in macroscopic and microscopic scales. In the past decades, there were extensive experimental studies carried out on artificially cemented sands, which are mainly focusing on extending the fundamental understanding of the static and dynamic behaviour based on small scale laboratory testings, including the strength and dilatancy behaviours, yielding, pre-failure and post failure characteristics, the influence of curing environment and conditions, influence of cementation on the liquefaction resistance, and so forth (Sitar et al. 1980; Clough et al. 1981; Acar et al. 1986; Saxena et al. 1988a; Saxena et al. 1988b; Lade et al. 1989; Reddy et al. 1993; Consoli et al. 1998; Huang et al. 1998; Consoli et al. 2000; Ismail et al. 2000; Schnaid et al. 2001; Ismail et al. 2002; Haeri et al. 2005; Consoli et al. 2006; Consoli et al. 2009; Consoli et

al. 2010; Consoli et al. 2011; Al-Thawadi et al. 2012; Consoli et al. 2012; Cheng et al. 2013). However, these aforementioned studies only provide the macroscopic responses of the cemented sand, and the fundamental and inherent mechanism (e.g. cementation degradation) determining the behaviour remain hypnotised. In continuum-based simulations, the cemented granular materials are often modelled adopting simple constitutive models (e.g. Mohr Coulomb model) with an enhanced cohesion and elastic modulus (Ismail 2005; Nasr 2014), which prevents these analyses from adequately describing the post failure behaviour controlled mainly by the cementation degradation .

Considering all of these inherent issues, the simulation of the actual pile installation and cone penetration process may be more effectively treated adopting numerical studies based on the discrete element method (Cundall et al. 1979; Potyondy et al. 2004; Jiang et al. 2006; Wang et al. 2008c; Butlanska et al. 2013; de Bono et al. 2015; Ciantia et al. 2016).

### 2.6.2 Discrete Element Method (DEM)

Discrete Element Method (DEM) is an approach developed by Cundall et al. (1979) that describes the behaviour of assemblies of granular spheres. With the advancement in computational technology, DEM has been gaining an increasing popularity in addressing engineering problems, particularly problems involving large displacements, deformations, distortions (e.g. driven pile, CMC and vertical drain installations; cone penetration etc.) in granular materials such as gravel and sand.

In discrete element simulation, the behaviour of granular materials is fundamentally determined by the adopted contact properties at the contacting interfaces following the Newton's second law of motion and force-displacement law. Despite the fact that the particles in discrete element simulation may be rigid bodies with finite masses that move independently of one another, the behaviour of the contacts is characterised using a soft contact approach allowing particles to overlap in the vicinity of the contact points. The contact between particles is detected prior to the force-displacement computation based on the contact overlap ($g_s$) (Cundall et al. 1979; Itasca 2016). There are numerous contact models, utilising linear or nonlinear formulations, developed mimicking the behaviour between contacting particles for different soils. A brief introduction of two most commonly adopted contact models describing the granular material behaviour are given in the following sections.

#### 2.6.2.1 Linear Contact Model

The linear contact model corresponds to the model developed by Cundall & Strack (1979), which utilises two linear springs in normal and tangential directions to mimic the linear elastic and frictional behaviours between contacting particles. The rheological model and the operating mechanism are illustrated in Figure 2.9.

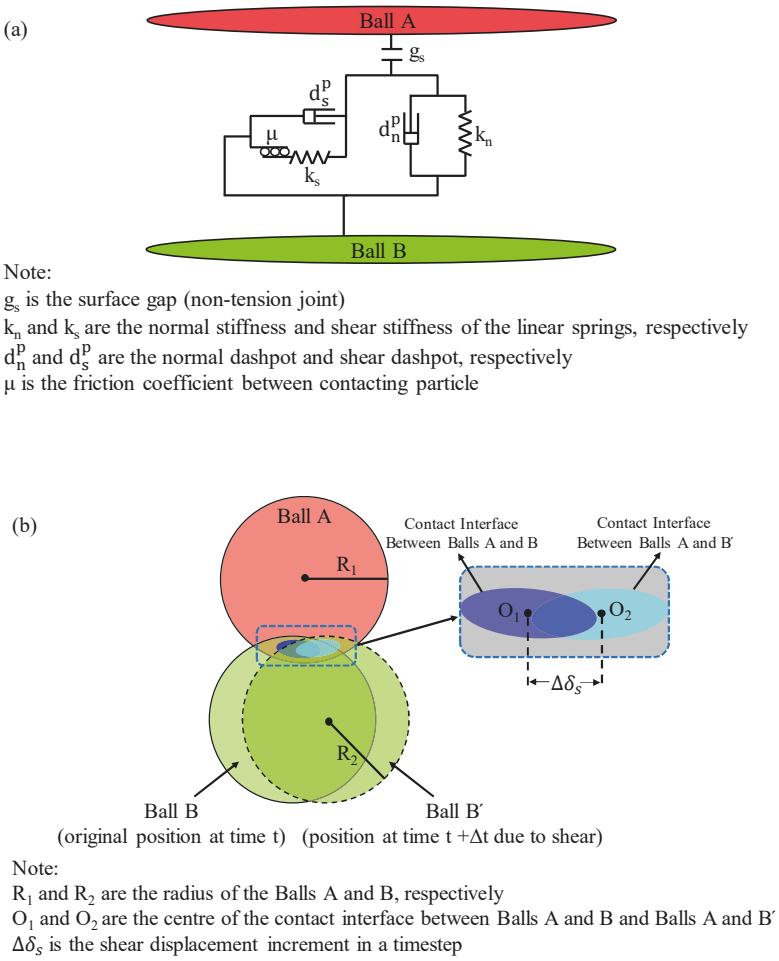


Figure 2.9 Linear contact model (a) rheological model and (b) schematic diagram

The magnitudes of the normal force ($F_n$) and the shear force ($F_s$) are determined by the normal stiffness $k_n$ and shear stiffness $k_s$, respectively based on the following equations:

$$\begin{cases} F_n = k_n g_s \\ g_s = d - (R_1 + R_2) \\ F_s = F_s^0 + k_s \Delta\delta_s \end{cases} \tag{2-29}$$

where, $F_n$ and $F_s$ are the normal force and shear force, respectively, $k_n$ and $k_s$ are the normal stiffness and shear stiffness of the linear springs, respectively, $g_s$ is the surface gap, measuring the overlap between particles (i.e. $g_s$= 0 when particles contact yet not overlap, $g_s$ < 0 when particles overlap), $R_1$ and $R_2$ are the radius of two contacting particles, $d$ is the distance between two contacting particles, $\Delta\delta_s$ is the relative shear displacement increment, and $F_s^0$ is the initial shear force.

#### 2.6.2.2 Rolling Resistance Contact Model

Rolling Resistance contact model, developed based on the Linear contact model, is used to mimic the rolling effect between particles with angular shapes (Iwashita & Oda 1998; Oda & Kazama 1998; Jiang et al. 2005; O'Sullivan 2011). Hence, it is considered as a more realistic contact constitutive model for granular materials where the rolling of particles is dominant in determining the strength. The formulations of the rolling resistance contact model are similar to the linear contact model except the incorporation of the rolling resistance moment ($M_{RR}$) acting at the contacting points of particles to counteract the relative motion and therefore can simulate the interlocking behaviour between contacting particles as explained by Ai et al. (2011). The rheological model and the schematic diagram of the particle interaction for this model are illustrated in Figure 2.10. The magnitude of the rolling resistance moment ($M_{RR}$) is computed based on the following equations (Jiang et al. 2005; Iwashita & Oda 1998):

$$\begin{cases} M_{RR} = k_r \Delta\varphi_r \\ k_r = k_s [R_1 R_2/(R_1 + R_2)]^2 \end{cases} \tag{2-30}$$

where, $M_{RR}$ is the rolling resistance moment, $\Delta\varphi_r$ is the relative rotation increment between contacting particles, $k_r$ and $k_s$ are the rolling stiffness and shear stiffness of the linear springs, respectively, $R_1$ and $R_2$ are the radius of two contacting particles.

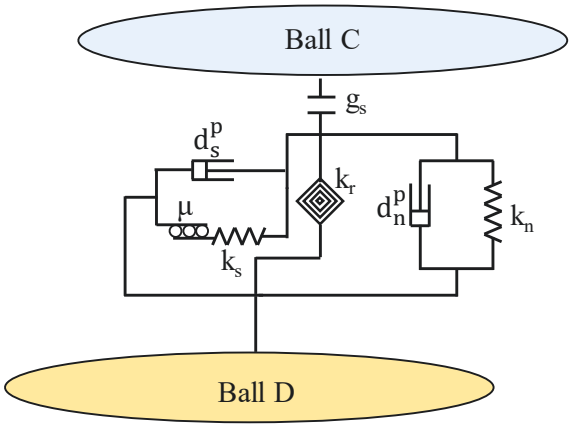


Note:
$g_s$ is the surface gap (non-tension joint)
$k_r$ is the rolling stiffness of the linear spring
$k_n$ and $k_s$ are the normal stiffness and shear stiffness of the linear springs, respectively
$d_n^p$ and $d_s^p$ are the normal dashpot and shear dashpot, respectively
μ is the friction coefficient between contacting particle

(a)

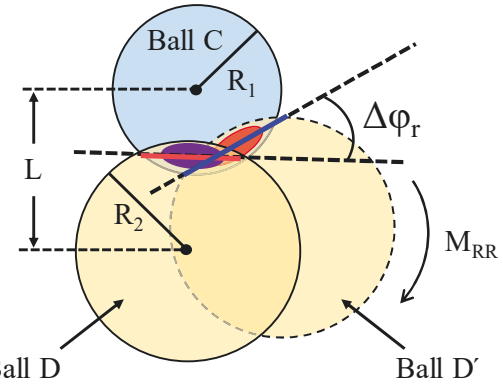


(original position at time t) (position at time t +Δt due to loading)

Note:
$R_1$ and $R_2$ are the radius of the Balls C and D, respectively
L is the distance between the centres of Balls C and D
$\Delta\varphi_r$ is the rotation increment in a timestep
$M_{RR}$ is the rolling resistance moment

(b)

Figure 2.10 Rolling Resistance contact model (a) rheological model and (b) schematic diagram

### 2.6.3 DEM Simulations Studying the Installation Effects

With the introduction of contact models mimicking the behaviour of granular materials, discrete element studies were readily conducted to investigate the installation effects. Lobo-Guerrero et al. (2005) carried out an investigation on the pile installation in carbonate sand adopting DEM. Referring to Lobo-Guerrero et al. (2005), a 2D numerical analysis adopting the linear contact model was carried out. The pile installation process was simulated as a model pile penetration into a virtual calibration chamber with a constant penetration rate. The model contained 26,000 particles, with the friction coefficient between the particles and pile selected to be 0.7 to simulate a rough pile surface. One of the innovations in Lobo-Guerrero et al. (2005) was the consideration of

particle crushing that many occur during the penetration process. The scheme was to replace the particles with equivalent smaller particles once the predefined failure criterion of a single particle was reached. The results confirmed that the particle crushing in the carbonate sand was mainly concentrated at the pile tip, and the crushed particles were then pushed away to the sides and moved along the pile shaft. In addition, downward and radial movements of the particles were observed mainly at the pile tip whereas the particles along the shaft were heavily rotated and followed an arbitrary path moving upward, causing the surface heave. However, the contact parameters adopted in Lobo-Guerrero et al. (2005) were not calibrated against experimental data and hence the results could be questionable.

Jiang et al. (2006) modelled the deep penetration in granular materials adopting 2D discrete element simulations to study the CPTs in centrifuge test. The penetrometer was modelled as rigid walls with a 60º conic pile tip. To reduce the boundary effects, a servo-control mechanism was adopted to maintain the stress level on the external walls Jiang et al. (2006) observed that the soil in the vicinity of the penetrometer displaced in a complex path. It was indicated that the soil along the shaft initially moved downward, and then shifted upwards and simultaneously sideway. As mentioned in Jiang et al. (2006), the displacement of the soil near the penetrometer may not be well captured with the conventional meshing available in continuum based analysis.

Zhou et al. (2012) proposed a coupled 3D discrete and continuum numerical model, studying the penetration effects of a flat ended pile in sand. The pile penetration was

simulated adopting discrete element method, while the soil located further away was model as continuum obeying linear elastic behaviour. The contact forces and displacements were obtained based on the discrete zones and transferred as nodal forces to the continuum boundaries, whereas the interface velocities in the continuum zone were transferred to the discrete boundaries. The information exchange between the discrete and continuum phases was achieved for a coupled analysis. To ensure the contact model adopted could describe the realistic behaviour of the granular material, the microscopic contact parameters were calibrated against the experimental triaxial test results. A typical arrangement of the triaxial test simulation in discrete element modelling is depicted in Figure 2.11.

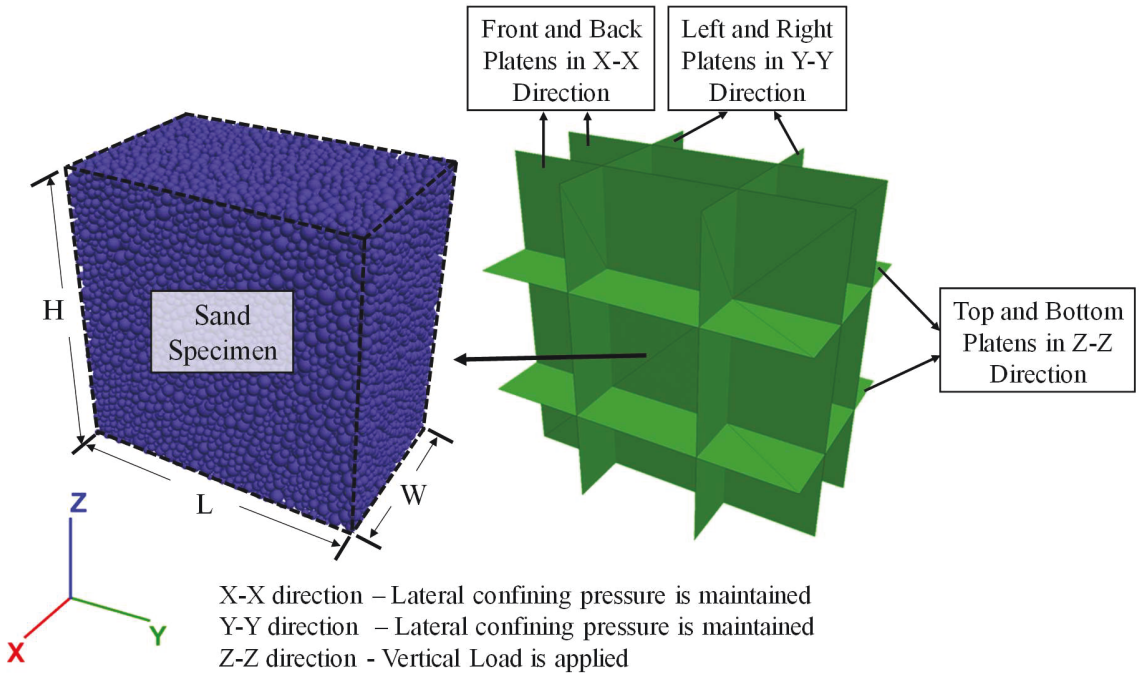


Figure 2.11 Typical triaxial test setup in the discrete element simulations

The results showed that the pile tip resistance approached a steady state with the penetration depth reaching 0.7 D (D being the diameter of the pile). It was also found that the porosity of the soil near the pile tip was decreased due to the compactions induced during the installation except the soils slightly above the pile tip. Due to the friction stemming from the contacting interfaces between sand and pile, a shear zone was formed, leading to the dilation of the soil and hence an increased porosity. This finding was contradicting the observations in the experimental test and numerical simulations conducted adopting continuum method, especially when the tip of the pile was considered to be conic.

Geng et al. (2013) presented a three-dimensional discrete element simulation of cavity expansion subjected to pressuremeter test. The pressuremeter test was modelled as a cylindrical cavity expansion from a finite initial radius following the identical boundary conditions presented in the cavity expansion theory, as illustrated in Figure 2.12. The initial cavity radius considered in Geng et al. (2013) was 1 m and the external boundary had a radius of 13 m, with the external pressure servo-controlled to maintain a same magnitude as the initial internal cavity pressure. The simulations were carried out in sandy soils with arbitrary initial porosity representing various relative densities. The cavity pressure variations obtained on dense sands showed an evident strain softening behaviour, with a peak explicitly captured. The results showed that the pressure required to expand an existing cavity in granular material may not be well predicted by many existing analytical solutions assuming an elastic - perfectly plastic material behaviour,

especially in dense granular materials, in which the effect of dilatancy is significant. However, there were no calibrations conducted against the realistic experimental data and no displacements were reported in Geng et al. (2013).

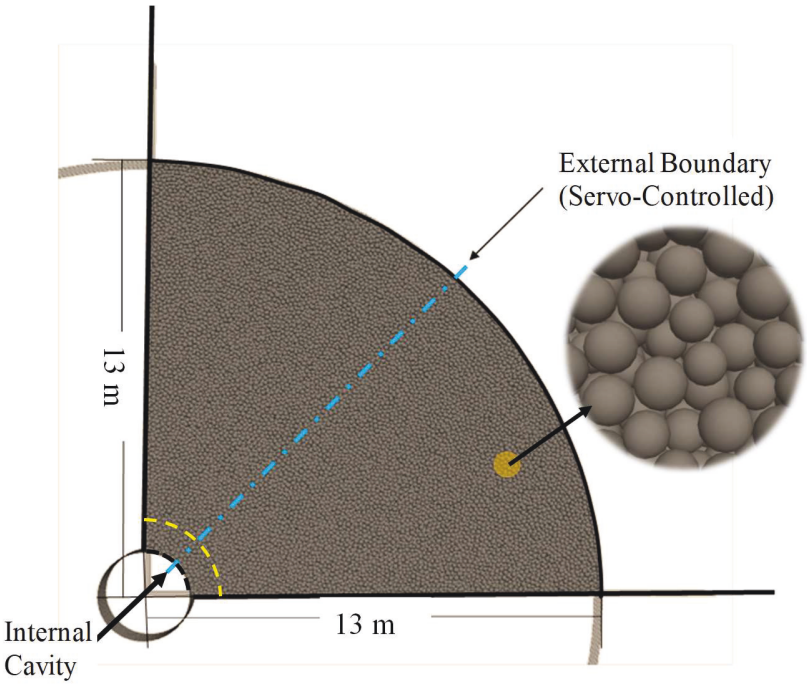


Figure 2.12 Typical cavity expansion arrangement in 3D discrete element simulations

Duan et al. (2018) conduced a numerical analysis studying the driven pile installation effect in sand adopting a two-dimensional model. As pointed out by Duan et al. (2018), the installation of the driven pile resulted in a rearrangement and repacking of the surrounding particles, with the particles situating at a shallower depth loosened due to the disturbance induced by the installation, whereas the deep layers experienced a densification process due to the extrusion. In addition, it was reported that the lateral

stresses were also significantly altered due to the installation of the driven pile, and the increase in lateral pressure depended not only on the distance in radial direction measured from the pile but also the overburden pressure (i.e. the vertical distance from the ground). After the installation of the driven pile, an uplift was expected due to the rebound of soil below the pile tip.

In addition to these aforementioned studies, there were also discrete element investigations carried out in analysing the mechanism of in-situ soils tests, such as cone penetration and stand penetration tests in calibration chambers (Arroyo et al. 2011; Butlanska et al. 2013; Zhang et al. 2019). However, the outcomes were mainly focusing on demonstrating the capability of DEM in simulating in-situ tests, and the tip resistance predictions and comparing with empirical correlations.

### 2.6.4 DEM Simulations of Cemented Granular Materials

Beside the discrete element studies in granular materials, there were also research studies investigating the behaviour of cemented sand. To reproduce the behaviour of cemented granular materials, the contact model adopted must be capable of capturing both the cementation and frictional effects between sand particles, before and after the breakage of a cemented bond. The contact model, extensively adopted mimicking the cementation at the contacts of adjacent particles, is the Linear Parallel Bond (LPB) model, which consists of two components, including a frictional contacting interface with zero tensile strength and a cementation bond component which acts in parallel with the first component (Wang et al. 2008a; de Bono et al. 2015; Feng et al. 2017). The behaviour of

the former component is linear elastic in normal direction with zero tension cut-off, while in the tangential direction, a linear elastic - perfectly plastic behaviour is utilised, with the maximum shear force at the contact being the Coulomb limit, determined by the $\mu^l F_n$, where $\mu^l$ is the friction coefficient, and $F_n^l$ is the normal component of force acting on the contacting interface (Cundall et al. 1979; Itasca 2016). The latter component obeys a brittle linear elastic constitution law that allows both the tension and moment to develop and transmit between contacting particles until either of these stresses exceed the bond strength. Once the bond strength is exceeded, the second component of the LPB model will be nullified, with its associated forces and moments eliminated (Potyondy et al. 2004; Potyondy 2015). The rheological model showing the concept of the LPB model is depicted in Figure 2.13.

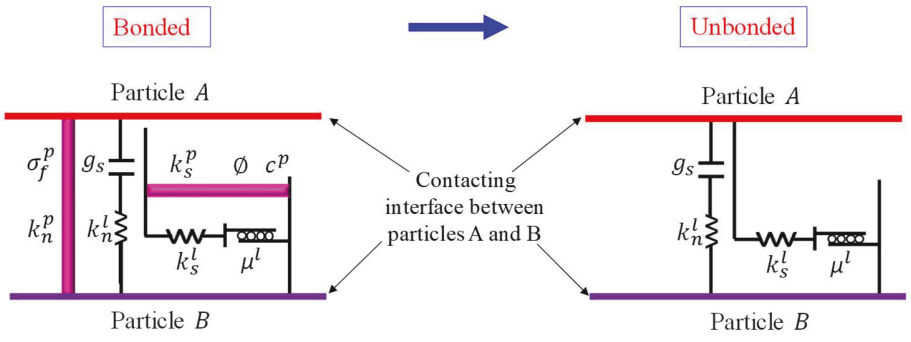


Note:
$g_s$ is the surface gap
$\mu^l$ is the friction coefficient between contacting particle
$\sigma_f^p$ is the tensile strength of the bond element
$\emptyset$ and $c^p$ are the friction angle and the cohesion of the bond element, computing the shear strength of the bond element
$k_n^l$ and $k_s^l$ are the normal stiffness and shear stiffness of the linear springs, respectively
$k_n^p$ and $k_s^p$ are the normal stiffness and shear stiffness of the bond element, respectively

Figure 2.13 rheological model of the linear parallel bond (LPB) model

As illustrated in Figure 2.13, the cementation bond component of the model is activated once the contact gap (i.e. $g_s$ ) between adjacent particles are less than or equal to the installation gap defined by the user. However, with the breakage of a cementation bond once the tensile strength (i.e. $\sigma_f^p$) or shear strength (i.e. $\tau_f^p$, define through the friction angle $\emptyset$ and cohesion of the bond element $c^p$, as shown in Figure 2.13) is exceeded, the grain behaviour approaches that of granular materials with frictional sliding at the contacting interface, referring to Figure 2.13. In addition, the force-displacement law for the forces and moments is schematically demonstrated in Figure 2.14.

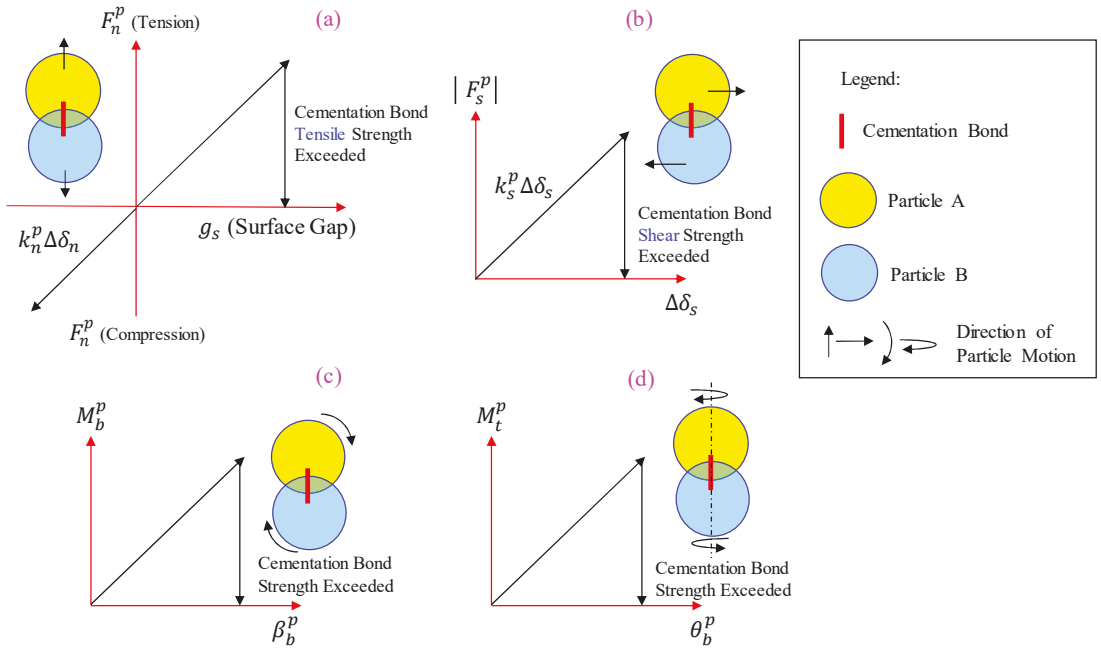


Figure 2.14 force-displacement law for the forces and moments in a LPB bond model (modified after Itasca (2016))

In DEM simulation of cemented sand in literature, the cementation effects were usually modelled as discrete sand particles bonded together adopting a contact model (e.g. linear parallel bond model). Hence, the cemented sand modelled utilising this technique is considered as a single-phase material consisting of only one type of particle (i.e. sand particles). The different level of cementation was modelled by adjusting one or a few of particular microscopic parameters, such as the reference gap and cementation radius, cementation bond tensile strength (Jiang et al. 2013; de Bono et al. 2014a; de Bono et al. 2015; Feng et al. 2017). In addition, there were also techniques that considered the cemented sand as a material with two phases, consisting of both cemented and uncemented particles, and the cementation level was controlled based on the percentage of cemented particles involved in a specimen (Wang et al. 2008a; Wang et al. 2008c; Obermayr et al. 2013). These common techniques to simulate the cemented sand are briefly introduced in this section.

Wang et al. (2008a) and Wang et al. (2008c) adopted 2D DEM simulations to investigate the behaviour of artificially cemented sand in drained triaxial tests. The cemented sand was modelled as a two-phase material containing both sand and cement particles, as illustrated in Figure 2.15.

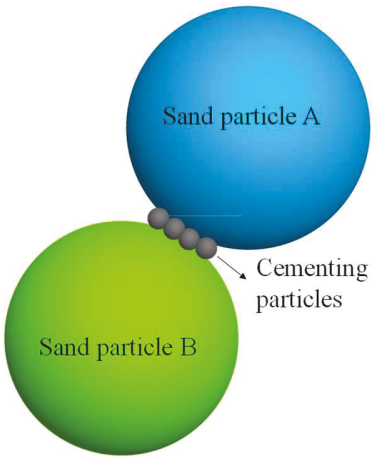


Figure 2.15 Schematic diagram illustrating the simulation of the cemented sand (after Wang et al. (2008a)

In the generation stage, the sand particles were initially generated following the given particle size distribution, while the cemented particles were created and randomly attached to sand particles. The linear parallel bond model was adopted to bind the cement and sand particles, while the interaction between two discrete sand particles were described adopting the linear model. As mentioned in Wang et al. (2008a), introducing the cementing particles directly at the contacts between discrete sand grains mimicked the realistic features of cementation in the experimental test, and the different cementation levels could be directly reproduced based on the number of cementing particles generated in the specimen.

de Bono et al. (2014a) modelled the one-dimensional compression in cemented sand adopting a 2D discrete element simulation. Based on analysing the SEM photos of cemented sands, de Bono et al. (2014a) claimed that an increase in cement content leads to an reduced voids due to cementation, helping to bind the particles that would otherwise

not be in contact. Hence, it was argued that cemented specimens with different levels of cementation can be achieved by controlling the reference gap (i.e.$g_s$ in Figure 2.13). By default, the reference gap detecting the establishment of the contact between adjacent particles is zero, which means that a cementation bond will be activated if the distance between the edges of two spherical particles is less than zero. Increasing the reference gap inevitably increases the bonding proximity, resulting in more contacts, and hence an increased cohesion and tensile strength (de Bono et al. 2014a). The technique simulating the cemented sand by controlling the reference gap is illustrated in Figure 2.16.

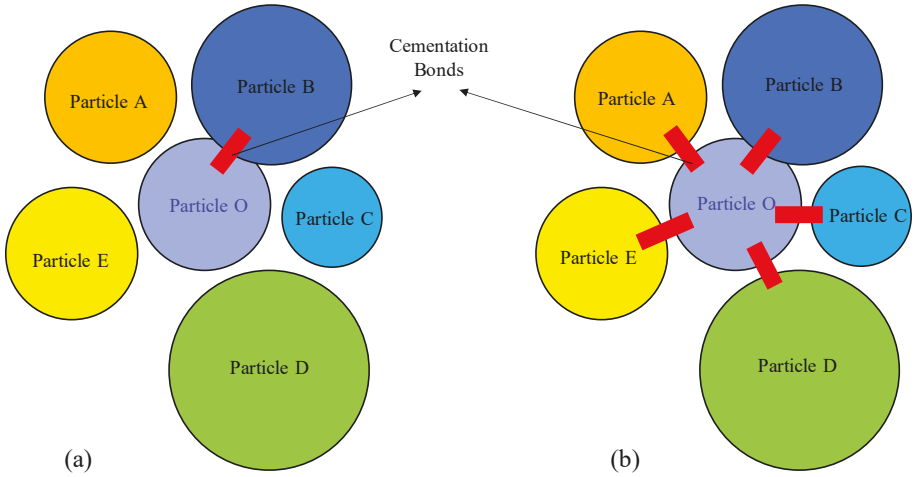


Figure 2.16 Schematic diagram illustrating the simulation of the cemented sand based on the reference gap technique (a) when $g_s$ is less than 0 and (b) when $g_s$ is larger than 0 (modified after de Bono et al. (2014))

Feng et al. (2017) explored the triaxial behaviour of bio-cemented sand adopting 3D discrete element simulations. The cementation between contacting particles were simulated adopting linear parallel bond model, as illustrated in Figure 2.17.

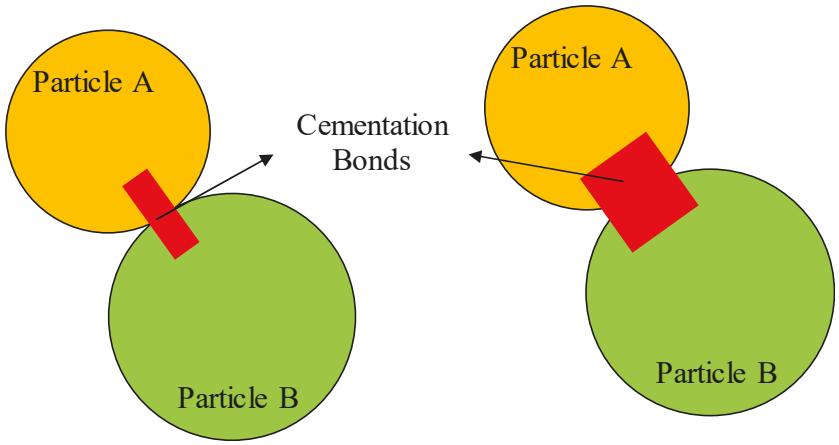


Figure 2.17 Schematic diagram illustrating the cemented sand simulation based on the cementation bond radius, after Feng et al. (2017)

Feng et al. (2017) asserted that specimens with higher cement content, observed in the realistic bio-cemented sand formation, generally have a larger volume of cementation at the contacting interface. Hence, referring to Feng et al. (2017), the different levels of cementation may be adequately represented adopting the cross-section area of the cementation bond (i.e. a higher bond radius corresponds to a larger cementation interface and therefore a higher cement content).

Obermayr et al. (2013) proposed a boned-particles model for cemented sand simulation based on the Timoshenko's beam theory and the extension of the linear parallel bond contact model. The cemented sand was modelled as a two-phase material, consisting of

both the cohesive particles (i.e. cemented particles) and non-cohesive particles, as illustrated in Figure 2.18.

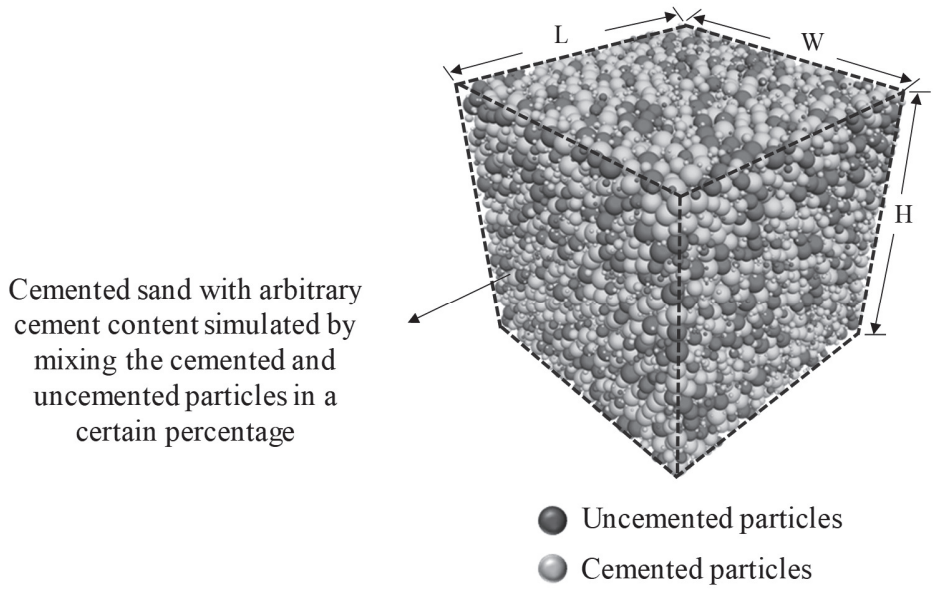


Figure 2.18 Simulating the cemented sand with arbitrary cement content by mixing the cemented and uncemented particles in a certain percentage

The proposed bonded model resisting tension, shear and moments (e.g. bending and twisting moments) was assigned at the contacting interfaces between adjacent cohesive particles. However, the contact model developed in Obermayr et al. (2011) based on non-linear Hertzian law (i.e. no-tension allow at the contact) was utilised to mimic the interaction between contacting non-cohesive particles, and the different levels of cementation was achieved by controlling the percentage of cohesive particles in the specimen. Referring to Obermayr et al. (2013), the triaxial tests simulation results

confirmed that the method proposed is adequate to simulate the behaviour of cemented sand with varying cement content.

## 2.7 Summary

The review of existing literature shows that the cavity expansion theory, as one of the most common adopted approaches, provides a simple and fast solution in assessing the installation effects, particularly in obtaining limiting pressures, assessing radial displacement, and stress and strain variations in the proximity of the cavity. However, analytical solutions can be only derived for the special cases considering simplified geometries, isotropic and homogenous materials, and simple constitutive models. Despite the fact that numerical techniques may be adopted for solving the cavity expansion problems with more realistic soil models, the expansion must commence from a finite cavity radius to avoid infinite circumferential strains. Although the constant volume theory may offer an approximate solution, the state of stresses and strains of the soil within the annular region remain inaccessible.

Field tests are generally considered as the most accurate ways to investigate the installation effects. However, large scale field testings are not always cost effective, since the required field instrumentations are expensive, especially when the point of interest is in a deep ground, and the equipment may be prone to damage during its usage. In addition, results obtained may not be easily applied to other projects where the ground conditions are not the same.

Continuum based numerical simulations with a realistic soil constitutive model may be adopted to assess the installation effects. However, the simulation of the actual installation process may encounter convergence issues due to the excessively large distortion induced. Despite the fact that there are mesh free or adaptive remeshing techniques (e.g. ALE, CEL, and MPM) developed to overcome the large distortion, these methods are sophisticated to be implemented in commercially available software packages for the use by practicing engineers and generally require significant computational effort. In addition, the continuum simulation is not capable of providing insight into the fundamentals of granular material behaviours, such as the dilatancy, particle crushing and cementation degradation in microscopic scale.

Discrete element simulations are gaining increasing popularities in recent years in studying the granular materials due to its discontinuous nature and the superior performance and have been proven capable in analysing problems involving large deformation and displacement. However, no systematic studies were carried out in assessing the influence of particle contact models and selecting the most appropriate contact model mimicking the behaviour of granular materials. In addition, an arbitrary finite cavity radius is required in many existing cavity expansion solutions to obtain the pressure expansion curve. However, there are no studies available assessing the influence on the choice of arbitrary initial cavity radius (including zero initial radius) in the cavity expansion related problems. Furthermore, there are no research studies available in the literature simulating cavity expansion in cemented soils helping to assess installation

effects of displacement based rigid inclusions on surrounding ground. Therefore, this research study attempts to address these issues, which can help with better understanding of cavity expansion from zero initial radius in granular and structured soils.

# Chapter 3 - Influence of Particle Contact Models on Soil Response of Poorly Graded Sand during Cavity Expansion in Discrete Element Simulation

## 3.1 General

In discrete element simulations, the behaviour of geomaterials in a macro level is utterly determined by microscopic properties, highlighting the importance of contact models. Despite the fact that there are numerous contact models proposed to mimic the realistic behaviour of granular materials, there are lack of studies on the effects of these contact models on the soil response. Hence, in this chapter, a series of three-dimensional numerical simulations with different contact constitutive models were conducted to simulate the response of sandy soils during cylindrical cavity expansion. In this numerical investigation, three contact models namely linear contact model, rolling resistance contact model, and the Hertz contact model are considered. It should be noted that the former two models are linear based models, providing linear elastic and frictional plasticity behaviours, whereas the latter one consists of nonlinear formulation based on an approximation of the theory of Mindlin and Deresiewicz. To examine the effects of these contact models, several cylindrical cavities were created and expanded gradually from an initial radius of 0.055 m to a final radius of 0.1 m. The numerical predictions confirm that the calibrated contact models produced similar results regarding the variations of cavity pressure, radial stress, deviatoric stress, volumetric strain, as well as

the soil radial displacement. However, the linear contact model may result in inaccurate predictions when highly angular soil particles are involved. In addition, considering the excessive soil displacement induced by the pile installation (i.e. cavity expansion), a minimum distance of 11 $a$ ($a$ being the cavity radius) is recommend for practicing engineers to avoid the potential damages to the existing piles and adjacent structures.

## 3.2 Introduction

The rapid advancement in computational technology has facilitated the application of discrete numerical analysis for many complex geotechnical problems, especially investigations involving large deformations or displacements. For instance, analysing the installation mechanism of driven piles and vertical drains adopted for ground improvement requires cavity expansion theory to better interpret smear zone characteristics. (Huang et al. 1994; Jiang et al. 2006) have employed discrete element simulation to study the mechanism of the deep penetration in granular materials. (Arroyo et al. 2011; Ciantia et al. 2016) successfully modelled the cone penetration tests in a calibration chamber while taking the particle crushing behaviour into consideration. (Geng et al. 2013) simulated the cylindrical cavity expansion and pressuremeter test using discrete element analysis. All of these studies have indicated that the discrete element method (DEM) is capable and reliable for simulating the behaviour of the granular materials, while comprehending the microscopic contact properties employed by the discrete numerical studies is of paramount importance. In DEM simulations, particles interact at pair-wise contacts by means of internal forces and moments. In addition,

contact mechanics are embodied in particle-interaction laws that are responsible for recognising particle interfaces, updating the internal forces and moments, computing the induced displacements and rotations of all particles involved in the system (Cundall et al. 1979; Potyondy et al. 2004). Hence, it can be explicitly concluded that only by adopting the most appropriate contact model, the simulation can attain the most accurate outcome. There are mainly three types of contact models widely used by researchers that are capable of simulating granular materials such as sand, namely (i) Linear, (ii) Rolling Resistance and (iii) Hertz contact models. Linear contact model, developed by Cundall & Strack (1979), describes the constitutive behaviour in normal and tangential directions between particles at their contact interface adopting linear springs with normal and shear stiffnesses. This model has been extensively employed to investigate granular materials in many disciplines ranging from chemical to geotechnical engineering. Its capabilities in mimicking the behaviour of sandy soils under various loading conditions have been successfully verified by many researchers (Jenck et al. 2009; Zhao et al. 2009; Chen et al. 2011; Zhou et al. 2012; Lai et al. 2014; Falagush et al. 2015; Tran et al. 2016). Despite the fact that classical theories believe that it is mainly the sliding between adjacent particles that plays the dominant role in controlling the strength and dilatancy, Oda & Kazama (1998) observed that the effect of rolling between contacting particles, is very significant. Therefore, the Rolling Resistance Contact Model has been developed based on the linear contact model by introducing a rolling resistance mechanism that incorporates a torque acting on the contacting pieces to counteract the rolling motion (Iwashita et al. 1998; Oda et al. 1998; Irazábal et al. 2017). It is indispensable that the

rolling resistance model is suitable to simulate granular materials particularly when most grains are angular, intensifying the interlocking of particles (Tordesillas et al. 2002; Jiang et al. 2005; Ai et al. 2011; O'Sullivan 2011). In addition to these two linear based models, Hertz contact model also demonstrates its competency in capturing the behaviour of granular materials in discrete numerical modelling. The most distinct feature differentiating Hertz contact model from others is that it has nonlinear formulations and utilises the simplified theory of Mindlin and Deresiewicz as force-displacement laws to compute contact forces (Mindlin 1953; Tsuji et al. 1992). As the Hertz contact model requires more accessible and macroscopic parameters that can be directly correlated to the macroscopic parameters measured in the laboratory, such as Poisson's ratio and shear modulus, it is also considered as a simple yet efficient constitutive contact model by many researchers (Gu et al. 2013; Ng et al. 2015; Ning et al. 2015; Zeghal et al. 2015; Ciantia et al. 2016). Although those three contact models have already well demonstrated their own competency in simulating the behaviour of sandy soils, there is very limited research to investigate the effects of these contact models on soil response. Furthermore, the cavity expansion theory, an effective technique to interpret the mechanism of pile installation and in-situ tests, has been extensively employed by many researchers. However, obtaining closed-form solutions may become difficult to be obtained when more realistic constitutive models are incorporated, and therefore numerical approaches can offer a better solution (Carter et al. 1979b). Hence, there are numerous analyses available adopting numerical techniques and simulations based on continuum method for cavity expansion (Carter et al. 1979a; Carter et al. 1985; Mo et al. 2014; Li et al. 2017). However,

the discrete element studies may provide researchers with a microscopic level of insight to study the complex cavity expansion related problems. Therefore, the purpose of this study is to compare the results obtained from the cavity expansion simulation adopting different contact models and evaluate the effectiveness of each contact model in discrete element simulations.

## 3.3 Material Contact Models

### 3.3.1 General Characteristics of Adopted Contact Constitutive Models

In this study, three contact models have been employed to mimic the interaction between particles at their contacting points, namely linear contact model, rolling resistance and Hertz contact models. It is noteworthy to state that all adopted contact models are elastic – perfectly plastic, in which the former two contact models are linear elastic – perfectly plastic whereas the latter is elastic – perfectly plastic model with non-linear formulations. Therefore, all three-contact models can capture both elastic and plastic behaviours. In the linear contact model, the behaviour is linear elastic in normal direction with zero tension cut-off, while in the tangential direction, a frictional behaviour using linear springs and plastic sliders are utilised, as illustrated in Figure 3.1.

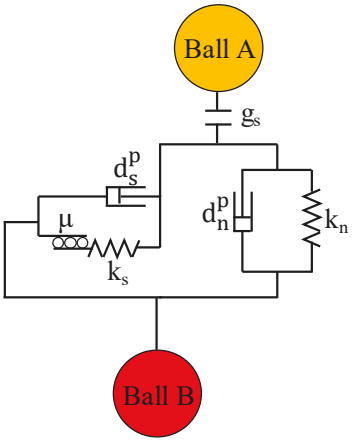


Note:
$g_s$ is the surface gap (non-tension joint)
$k_n$ and $k_s$ are the normal stiffness and shear stiffness of the linear springs, respectively
$d_n^p$ and $d_s^p$ are the normal dashpot and shear dashpot, respectively
μ is the friction coefficient between contacting particle

(a)

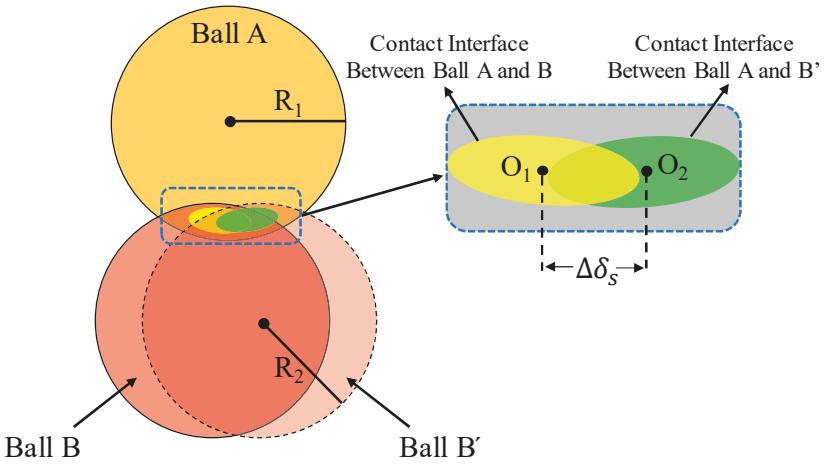


Note:
$R_1$ and $R_2$ are the radius of the Ball A and Ball B, respectively
O1 and O2 are the centre of the contact interface between Ball A and B and Ball A and B'
$\Delta\delta_s$ is the shear displacement increment in a timestep

(b)

Figure 3.1 Linear contact model (a) rheological model and (b) schematic diagram

In this contact model, slip is accommodated by imposing a Coulomb limit on the shear force using the friction coefficient $\mu$ (i.e. slider). Both normal and shear forces are computed linearly using the linear force displacement law based on the linear springs, and the maximum shear force at the contact is the frictional force ($\mu F_n$), where $F_n$ is the normal force acting at the contacting interface.

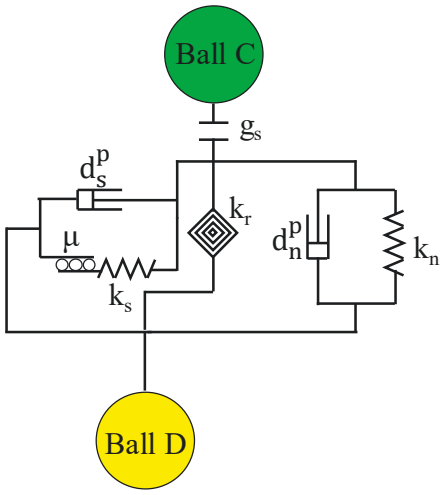


Note:
$g_s$ is the surface gap (non-tension joint)
$k_r$ is the rolling stiffness of the linear spring
$k_n$ and $k_s$ are the normal stiffness and shear stiffness of the linear springs, respectively
$d_n^p$ and $d_s^p$ are the normal dashpot and shear dashpot, respectively
μ is the friction coefficient between contacting particle

(a)

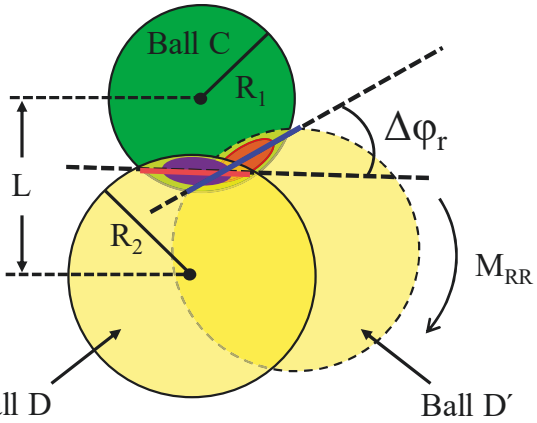


(original position at time t) (position at time t +Δt due to loading)

Note:
$R_1$ and $R_2$ are the radius of the Balls C and D, respectively
L is the distance between the centres of Balls C and D
$\Delta\varphi_r$ is the rotation increment in a timestep
$M_{RR}$ is the rolling resistance moment

(b)

Figure 3.2 Rolling Resistance contact model (a) rheological model and (b) schematic diagram

Rolling resistance contact model, as depicted in Figure 3.2, developed from linear contact model, has a similar behaviour, except that the internal moment is incremented linearly with the accumulated relative rotation of the contacting pieces at the contact points. The limiting toque at the contact is proportional to the normal contact force and acts in opposite to the rolling direction.

Hertz contact model, utilising a nonlinear formulation based on an approximation of the theory of Mindlin (1953), incorporates both normal and shear forces based on the theoretical analysis of the deformation of elastic spheres. Figure 3.3 describes the rheological model for Hertz contact mode. The main difference between Hertz and Linear

model is that the Hertz contact model employs nonlinear formulations to compute the normal and shear forces at the contact. The maximum shear force at the contact is also determined based on the frictional force ($\mu F_n^H$), where $F_n^H$ is the Hertz normal force.

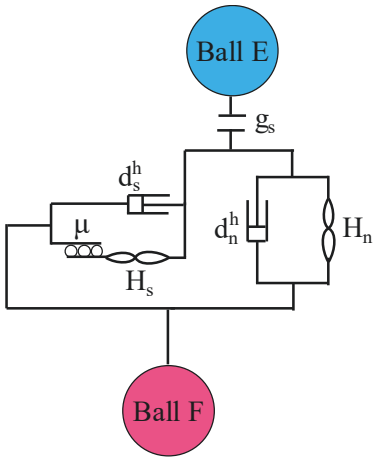


Note:
$g_s$ is the surface gap
$H_n$ and $H_s$ are the Hertz normal coefficient and tangent shear stiffness of the springs, respectively
$d_n^h$ and $d_s^h$ are the normal dashpot and shear dashpot, respectively
μ is the friction coefficient between contacting particle

Figure 3.3 Rheological model for Hertz contact model

### 3.3.2 Formulations of Adopted Contact Constitutive Models

In discrete element simulations, the behaviour of granular materials is fundamentally determined by the adopted contact properties at the contacting interfaces following the Newton's second law of motion and force-displacement law. Despite the fact that the particles in discrete element simulation may be rigid bodies with finite mass that move independently of one another, the behaviour of the contacts is characterised using a soft contact approach allowing particles to overlap in the vicinity of the contact point. The

contact between particles is detected prior to the force-displacement computation based on the contact overlap ($g_s$) detected (Cundall et al. 1979; Cundall et al. 1992; Itasca 2016). The linear contact model adopted in this study corresponds to the model developed by Cundall & Strack (1979), which utilises two linear springs in normal and tangential directions to mimic the linear elastic and frictional behaviours between contacting particles. The rheological model and the operating mechanism is illustrated in Figure 3.1. The magnitudes of the normal force ($F_n$) and the shear force ($F_s$) are determined by the normal stiffness $k_n$ and shear stiffness $k_s$, respectively based on the following equations:

$$\begin{cases} F_n = k_n g_s \\ g_s = d - (R_1 + R_2) \\ F_s = F_s^0 + k_s \Delta\delta_s \end{cases} \tag{3-1}$$

where, $F_n$ and $F_s$ are the normal force and shear force, respectively; $k_n$ and $k_s$ are the normal stiffness and shear stiffness of the linear springs, respectively, $g_s$ is the surface gap, measuring the overlap between particles (i.e. $g_s$= 0 when particles contact yet not overlap, $g_s$ < 0 when particles overlap), $R_1$ and $R_2$ are the radius of two contacting particles, d is the distance between two contacting particles, $\Delta\delta_s$ is the relative shear displacement increment, and $F_s^0$ is the initial shear force.

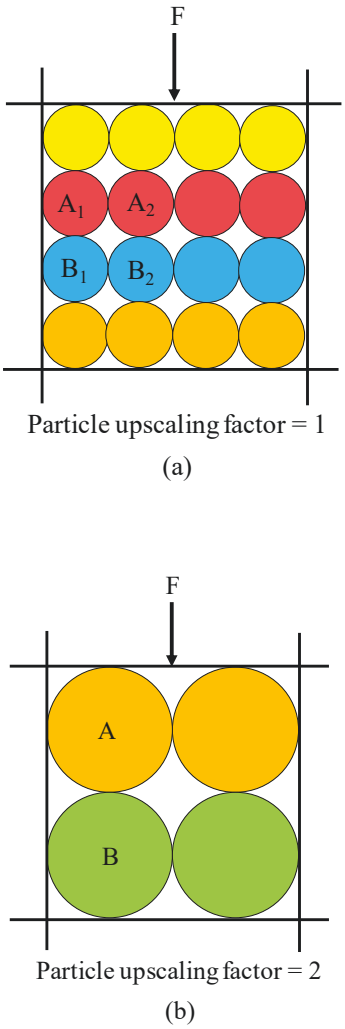


Figure 3.4 Illustration of particle assembly in DEM (a) particle upscaling factor = 1 (b) particle upscaling factor = 2

In DEM simulations, the magnitudes of the normal stiffness $k_n$ and shear stiffness $k_s$ can be specified by the users directly. In this circumstance, referring to Figure 3.4 (a) and (b), applying the same compressive force (F), the normal contact forces between two particles (e.g. A1 & B1 or A & B) will be doubled if the particles are enlarged twice.

Therefore, it is obvious that the magnitude of the normal contact force increases with the increase in the particle size. Therefore, it is evident that the normal stiffness $k_n$ should be upscaled, according to respond to the increase in normal contact forces. However, besides the direct approach, the linear model deformability method can be alternatively employed to control the normal and shear stiffness in real time by introducing the effective Young's modulus $E^*$ and the stiffness ratio $k^*$ of the normal and shear stiffness of the linear springs based on the following equations (Itasca 2016):

$$\begin{cases} k_n = \pi[\min(R_1, R_2)]^2 E^*_{mod}(R_1 + R_2) \\ k_s = k_n / k^* \end{cases} \tag{3-2}$$

The effective Young's modulus $E^*_{mod}$ and the stiffness ratio $k^*$ have direct correlations to the material macroscopic properties, such as the Young's modulus ($E$) and the Poisson's ratio ($\vartheta$). In Equation (3-2), particle upscaling leads to the increase in the normal stiffness ($k_n$) which, at the same time, increases the shear stiffness ($k_s$) due to the constant ratio adopted (i.e. $k^*$). This implicates that the upscaling adopting the linear model deformability method automatically takes the effect of particle upscaling into account. Similar techniques were also used by other researchers (Ding et al. 2014). This is especially advantageous when the particles are upscaled to reduce the computational effort so that large-scale simulation can be conducted.

Rolling Resistance contact model, developed based on the linear contact model, is used to mimic the rolling effect between particles with angular shapes (Iwashita & Oda 1998;

Oda & Kazama 1998; Jiang et al. 2005; O'Sullivan 2011). Hence, it is considered as a more realistic contact constitutive model for granular materials where the rolling of particles is dominant in determining the strength. The formulations of the rolling resistance contact model are similar to the linear contact model except the incorporation of the rolling resistance moment ($M_{RR}$) acting at the contacting points of particles to counteract the relative motion and therefore simulate the interlocking behaviour between contacting particles (Ai et al. 2011; Wensrich et al. 2012). The rheological model and the schematic diagram of the particle interaction are illustrated in Figure 3.2. The magnitude of the rolling resistance moment ($M_{RR}$) is computed based on the following equations (Jiang et al. 2005; Iwashita & Oda 1998):

$$\begin{cases} M_{RR} = k_r \Delta\varphi_r \\ k_r = k_s [R_1 R_2/(R_1 + R_2)]^2 \end{cases} \tag{3-3}$$

where, $M_{RR}$ is the rolling resistance moment, $\Delta\varphi_r$ is the relative rotation increment between contacting particles, $k_r$ and $k_s$ are the rolling stiffness and shear stiffness of the linear springs, respectively, $R_1$ and $R_2$ are the radius of two contacting particles.

In addition to these two linear based contact constitutive models, Hertz contact model, as illustrated in Figure 3.3 is employed to simulate the behaviour of granular materials (Ciantia et al. 2016; Gu & Yang 2013; Ng & Meyers 2015; Zeghal & Tsigginos 2015). The Hertz contact model adopts the simplified Mindlin and Deresiewicz theory (Itasca 2016; Mindlin 1953) to reproduce the non-linear force-displacement formulation to

calculate the normal and shear forces during analysis using the following equations (Holt et al. 2005; Agnolin et al. 2007):

$$\begin{cases} F_n^H = [2G\sqrt{2R_e^H}/3(1-\vartheta)]{g_s}^{\alpha_H} \\ F_s^H = F_{s_0}^H + [\frac{2(1-\vartheta)}{2-\vartheta}\alpha^H [2G\sqrt{2R_e^H}/3(1-\vartheta)]F_n^{H(\alpha^H - 1/\alpha^H)}]\Delta\delta_s \\ R_e^H = 2R_1R_2/(R_1+R_2) \end{cases} \quad (3\text{-}4)$$

where, $F_n^H$ and $F_s^H$ are the Hertz normal force and Hertz shear force, respectively, $G$ is the effective shear modulus, $\vartheta$ is the Poisson's ratio, $\alpha_H$ is the Hertz exponent, $R_e^H$ is the effective radius, $R_1$ and $R_2$ are the radius of contacting particles, respectively, $g_s$ is the surface gap ($g_s \leq 0$ when particles are in contact / overlapped), $\Delta\delta_s$ is the relative shear displacement increment and $F_{s_0}^H$ is the initial Hertz shear force.

It can be clearly noted that the Hertz contact model utilises the material properties such as Poisson's ratio and effective shear modulus to define the contact behaviour. The size of the particles ($R_e^H$) is taken into account during the force-displacement computation, confirming that the Hertz contact model, similar to the Linear model deformability method, can be applicable when particles are upscaled.

Furthermore, it is worthy to mention that the allowed overlapping at the contacts between particles in the normal direction is directly related to the normal stiffness of the spring and the normal forces acting on the contact plane for the linear and rolling resistance contact models. This study employs the linear model deformability method, and therefore the allowed overlapping is determined by the effective modulus, $E_{mod}^*$ specified.

Referring to Equation (3-1), the detected overlap ($g_s$) and the normal stiffness of the linear spring between two particles are used to determine the normal force ($F_n$). Also, according to Equation (3-2), the allowed overlapping ($g_s$) can be expressed in terms of the normal force ($F_n$) and effective modulus ($E^*_{mod}$) as follows:

$$g_s = \frac{F_n}{\pi[min(R_1,R_2)]^2 E^*_{mod}(R_1+R_2)} \tag{3-5}$$

Hence, it can be explicitly concluded that the overlap is determined by the magnitude of the normal force acting on the contact plane, and the effective modulus of particles. Given a constant normal force, the overlap between contacting particles decreases as the effective modulus increases. For the Hertz contact model, referring to the Equation (3-4), in a similar way, the allowed overlap can be determined as below:

$$g_s = \sqrt[\alpha_H]{\frac{F_n^H}{[2G\sqrt{4R_1R_2/(R_1+R_2)}/3(1-\vartheta)}} \tag{3-6}$$

Hence, it can be concluded that the allowed overlapping at the contacts is determined by the effective shear modulus ($G$), Poisson's ratio ($\upsilon$) as well as the Hertz normal force ($F_n^H$).

In this study, PFC$^{3D}$ 5.0 software (Itasca 2016) has been adopted to evaluate the performance of these three contact models for cavity expansion simulation. Moreover, it is noteworthy to state that the constitutive behaviours of linear contact model, Rolling Resistance contact model as well as Hertz contact model discussed above contain only

the essential characteristics and readers can refer to existing literature for further detailed explanations (e.g. Itasca 2016; Cundall & Strack 1979; Mindlin 1953; Iwashita & Oda 1998).

It is acknowledged that disparities may exist between the microscopic parameters of these adopted contact models and the actual behaviour that can be investigated when laboratory tests are done in microscopic scale. For instance, according to micromechanical experiments conducted by Sandeep et al. (2018) and Sandeep et al. (2017) , with the increase in the normal loads, repeated shearing causes increase in friction. However, the frictional forces between particles for a given normal force in many existing contact constitutive models are constant (e.g. linear, rolling resistance, Hertz contact models). The advance micromechanical inter-particle loading apparatus can directly measure the contact properties such as $k_n$ and $k_s$ between particles, which indisputably lead to the new direction in the micromechanical studies. It also offers the possibility to study the behaviour of the contacting particles in a microscopic level, which is advantageous for the development of more comprehensive and realistic contact constitutive models adopted in the DEM analysis (O'Sullivan 2011; Senetakis et al. 2013; Senetakis et al. 2014).

## 3.4 Numerical Modelling

### 3.4.1 Calibration of Contact Parameters Adopting Triaxial Test

Investigating the effects of contact models on the macroscopic soil response can never be attained if the variables are not controlled since each contact model contains multiple parameters that fundamentally determine the contact behaviour between particles. Hence, three adopted contact models were calibrated to represent realistic sandy soil by matching the results obtained from the numerical simulations of triaxial compression tests against existing laboratory results. Typically, the stress-strain relationships obtained from the experiments are used for calibration of the contact models, which is a common practice adopted by many researchers (Chareyre et al. 2002; Arroyo et al. 2011; Wang et al. 2014; Ciantia et al. 2016). In this study, the contact properties were calibrated by matching the overall (macroscopic) stress - strain and volume change – axial strain curves obtained for the soil sample.

#### 3.4.1.1 Selection of Existing Experimental Triaxial Test Results for Calibration Exercise

Experiments adopted for calibration exercise was conducted by Cornforth (1964) to compare the drained strengths of medium to fine grained sand under the plane strain condition as well as the conventional triaxial condition (Cornforth 1964). Detailed experimental procedure and specimen information can be found in Cornforth (1964). It is preferred to use comprehensive test results (e.g. triaxial test with various confining

pressures) for calibration of the micro-mechanical properties of the soil for general simulation of soil under different confining pressures. However, it should be noted that the calibration exercise conducted in this study compared predictions and measurements for both axial stress and the volumetric strain variations with shear strains. In addition, since the test results reported by Cornforth (1964) include the required information for calibration of micro-mechanical properties namely particle size distribution, void ratio, variation of volume change with shear strain, and stress-strain results, as well as the experimental procedure and the loading rate, these results have been used in this study. Similar calibration techniques were also adopted by many other researchers (Arroyo et al. 2011; Ciantia et al. 2015)

#### 3.4.1.2 Numerical Simulation of Triaxial Test

Considering the current computational power, it is not realistic to simulate the triaxial test using the true particle sizes. For instance, a laboratory scale triaxial test on a sand specimen with 30 mm diameter and 60 mm height would comprise approximately 4 million particles. Directly mapping such a huge number of particles into the simulation is unrealistic and computationally infeasible. Hence, only by reducing the number of particles, the analyses can become efficient and possible (O'Sullivan 2011). Therefore, before the initial condition has been assigned to the particles, an upscaling factor should be applied to reduce the number of particles immensely so that the simulation becomes computationally feasible. An appropriate upscaling factor is of paramount importance to ensure that the soil properties will not be altered. In this case, a very small upscaling

factor has been initially adopted and has been gradually increased to 16.5 so that the porosity can steadily reach the desired value. The particle size distribution adopted by Cornforth (1964) and the uniformly upscaled particle size distribution employed in the calibration exercise are presented in Figure 3.5.

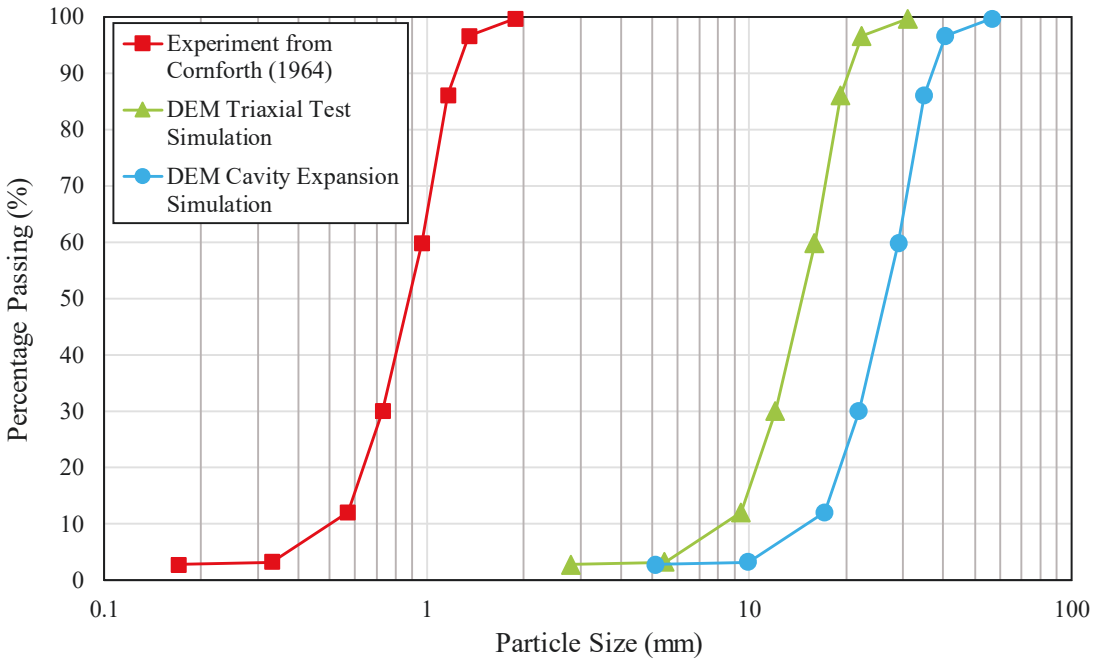


Figure 3.5 Particle size distribution adopted in experimental test, calibration exercise and cavity expansion simulation

Hence, the triaxial simulations comprised of 20,000 spherical particles after upscaling, with the maximum diameter of the particle after upscaling being 12.35 mm while the minimum particle has a diameter of 1.245 mm, and the setup of the triaxial test is shown in Figure 3.6.

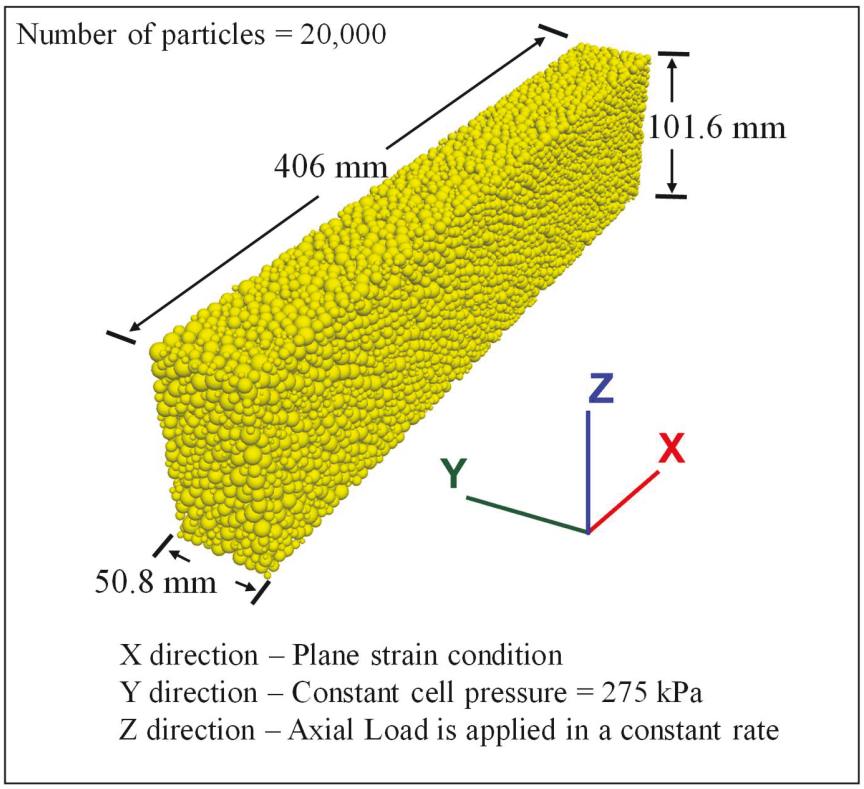


Figure 3.6 Triaxial compressive test in plane strain condition in discrete element simulation

As illustrated in Figure 3.6, the generated model for calibration exercise has a length of 406 mm, while the height and width are 101.6 mm and 50.8 mm, respectively, which are identical to sample size adopted in the experimental test conducted by Cornforth (1964). The initial porosity of the generated DEM model for calibration exercise is 0.392, similar to the porosity measured in the laboratory, corresponding to a medium dense specimen. The common approaches adopted to generate a relatively dense specimen is to apply a small friction at grain contacts during the sample generation stage so that inter-particle sliding can occur in a relatively effortless manner. The boundary walls are controlled using a servomechanism until the target void ratio and stress state are achieved at

equilibrium. Once the initial conditions are satisfied, the friction can be adjusted back to the value determined from the calibration exercise (Thornton 2000; Chareyre et al. 2002; Jiang et al. 2003; O'Sullivan 2011; Tong et al. 2012). This technique is also adopted in this study to prepare a medium dense specimen. The lateral confining stress (Y direction) of 275 kPa were maintained while the facets in the intermediate direction (X direction) were fixed to simulate the plane strain condition, and then axial load was applied on the top of the specimen (Z direction) in a constant rate. During the simulation, stress and strain variations as well as volume changes were continuously recorded. To investigate the effects of different contact models on soil response, Rolling Resistance, Linear and Hertz contact models have been calibrated.

#### 3.4.1.3 Calibration Methodology

The linear and the rolling resistance contact models are based on the linear deformability model, which is a method controlling the normal and shear stiffness of the linear springs based on the effective modulus ($E^*_{mod}$) and the normal to shear stiffness ratio ($k^*$), as denoted in Equation (3-2). The effective modulus ($E^*_{mod}$) is related to the Young's modulus ($E$) of the material, and $E$ increases as $E^*_{mod}$ increases, confirming a direct correlation. In addition, the Poisson's ratio ($\vartheta$) is related to the normal to shear stiffness ratio ($k^*$); with $\vartheta$ increasing up to a limiting positive value as $k^*$ increases (Itasca, 2016). Therefore, it can generally be concluded that the effective modulus ($E^*_{mod}$) controls the elastic part of the stress-strain curve, while the normal to shear stiffness ratio ($k^*$) influences the volumetric behaviour. The selection of the values of $E^*_{mod}$ and $k^*$ adopted

for the initial trial is based on the recommendations made by Plassiard et al. (2009), considering a comprehensive parametric study for the triaxial test simulation. Since the macroscopic Young's modulus ( $E$ ) of the sand in the calibration exercise is approximately 70 MPa, as reported in Cornforth (1964), the corresponding magnitude of the effective modulus ($E^*_{mod}$) can be estimated to be approximately 1000 MPa referring to Plassiard et al. (2009). In addition, an interparticle friction coefficient of 0.5 is selected as the initial trial value. Considering the initial value of the effective modulus, a series of sensitivity analyses are conducted to investigate the effects of the interparticle friction coefficient and the normal to shear stiffness ratio ($k^*$) using control variable method, as illustrated in Figure 3.7and Figure 3.8.

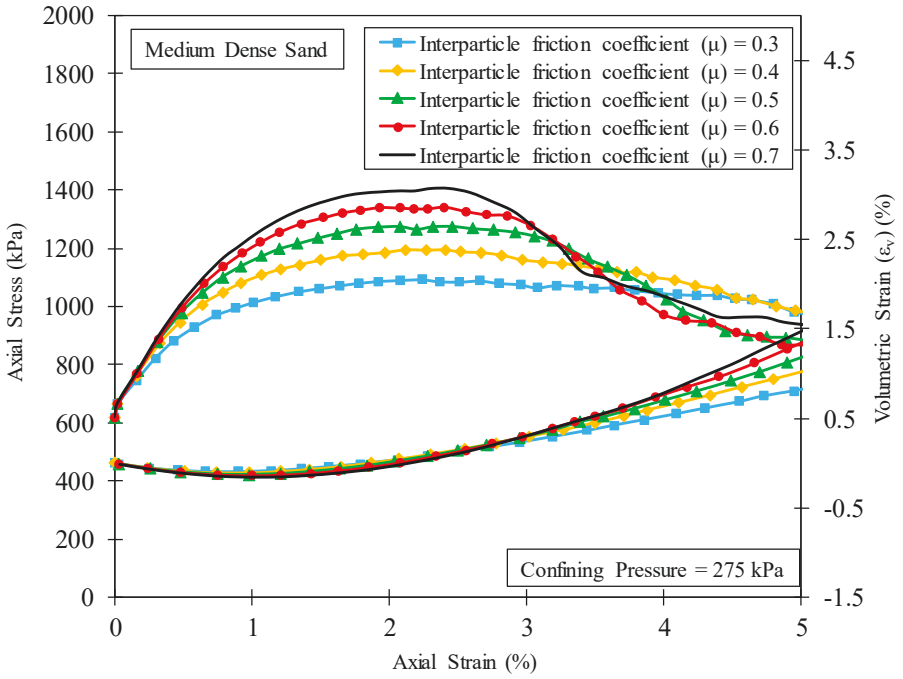


Figure 3.7 Influence of interparticle friction coefficient on the axial stress-strain relationship

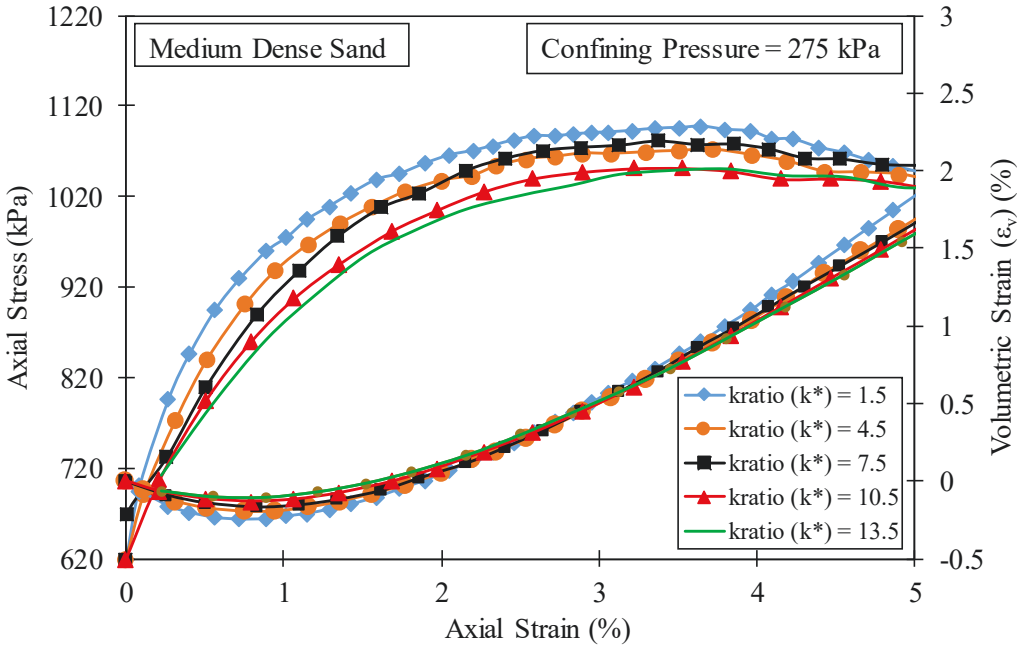


Figure 3.8 Influence of normal to shear stiffness ratio (k ratio) on the axial stress-strain relationship

According to the preliminary studies on the influence of the interparticle friction coefficient reported in Figure 3.7, increasing the friction coefficient can, by and large, enhance the material shear strength, especially when the friction coefficient is less than 0.5. However, when the inter-particle friction is larger than 0.5, the increase of shear strength becomes rather unpronounced. Huang et al. (2014) conducted a comprehensive DEM investigation exploring the influence of interparticle friction on critical state behaviour of granular materials. The study indicated that the interparticle friction can affect the critical state parameter M as well as the position of the CSL in *e-log p'* space, particularly when the friction coefficient is less than 0.5, whereas such effects are insignificant when the friction coefficient increases beyond 0.5. In addition, more rolling

was observed in comparison to the sliding occurring at the contact points when a high interparticle friction coefficient was adopted. In addition, Yan et al. (2009) conducted a series of numerical studies investigating the influence of micro-properties on the macroscopic stress-strain behaviour of granular material. The results confirm that the inter-particle friction affects both strength and the overall volumetric dilation. The peak of the stress-strain curve increases with the increases in the friction coefficient, and the volumetric dilation becomes more significant with the increase of the inter-particle friction. Similar findings are also presented by Yang et al. (2012) and Hosn et al. (2017) in studying the influence of inter-particle friction and dilatancy of granular materials. All of these studies carried out confirm that the interparticle friction indeed influence the soil behaviour significantly.

However, referring to Figure 3.8, it is observed that in this study the normal to shear stiffness ratio ($k^*$) has insignificant effect on the stress-strain relationship compared with the effect induced by the interparticle friction coefficient. Hence, the normal to shear stiffness ratio could be fixed provisionally.

The interparticle friction coefficient is then adjusted to match the rest of the stress – strain curve to obtain the best match, then the interparticle friction coefficient is fixed and then the effective modulus ($E^*_{mod}$) and the normal to shear stiffness ratio ($k^*$) are further adjusted to achieve the optimum match with the experimental results. The method discussed above is the technique adopted for the linear model calibration. The technique

adopted to calibrate the rolling resistance and the Hertz contact models is similar to the one reported above. In summary, the following procedure can be used for the calibration:

(1) Estimating the initial trial values of micro-mechanical properties based on the tests and parametric studies carried out by other researchers,

(2) Conducting a sensitivity analysis and then fixing the parameters influencing the predictions to less extent in the range of stresses applied,

(3) Adjusting the parameters influencing the stress-strain predictions notably until a reasonable match is achieved, and

(4) Optimising further by fine-tuning all parameters to achieve the best possible predictions.

It should be noted that for further information regarding the calibration procedure adopting the Hertz contact model, Cheng et al. (2017) can be referred to. Despite the fact that each parameter exerts complex influence on the overall soil response (Chen 2017; Yang et al. 2018), there are existing studies which indicated that the calibrated parameters have unique values even in a predictive way when different confining pressures were imposed to the same sample (Plassiard et al. 2009). In fact, the sensitivity analyses carried out in this study during the calibration exercises also confirmed that a unique set of parameters matches the overall macroscopic stress and strain relationship.

#### 3.4.1.4 Calibration Results

Calibrated results for stress-strain relationship as well as volumetric behaviour are plotted in Figure 3.9 and Figure 3.10 respectively.

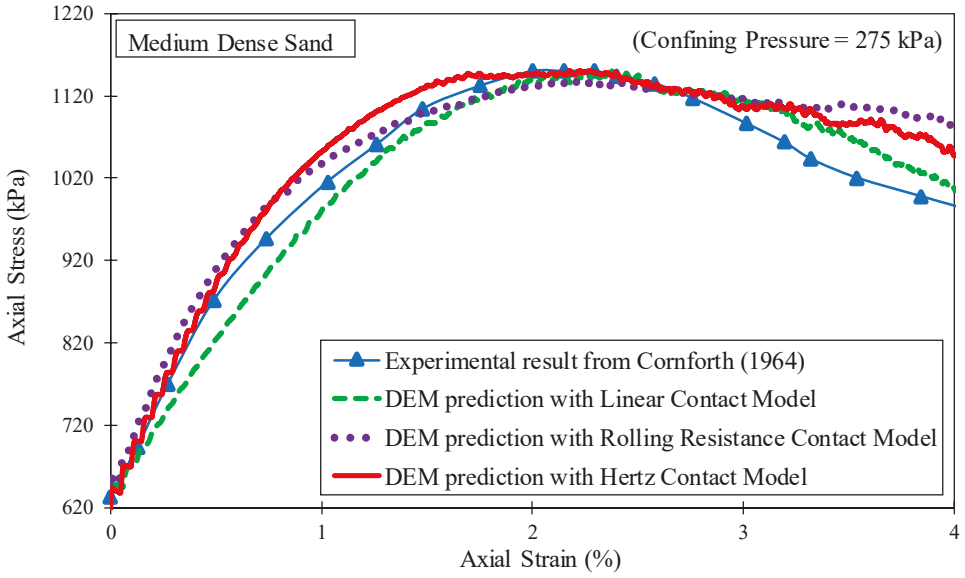


Figure 3.9 Comparisons of axial stress and strain relationship obtained from calibration numerical simulation and experimental results.

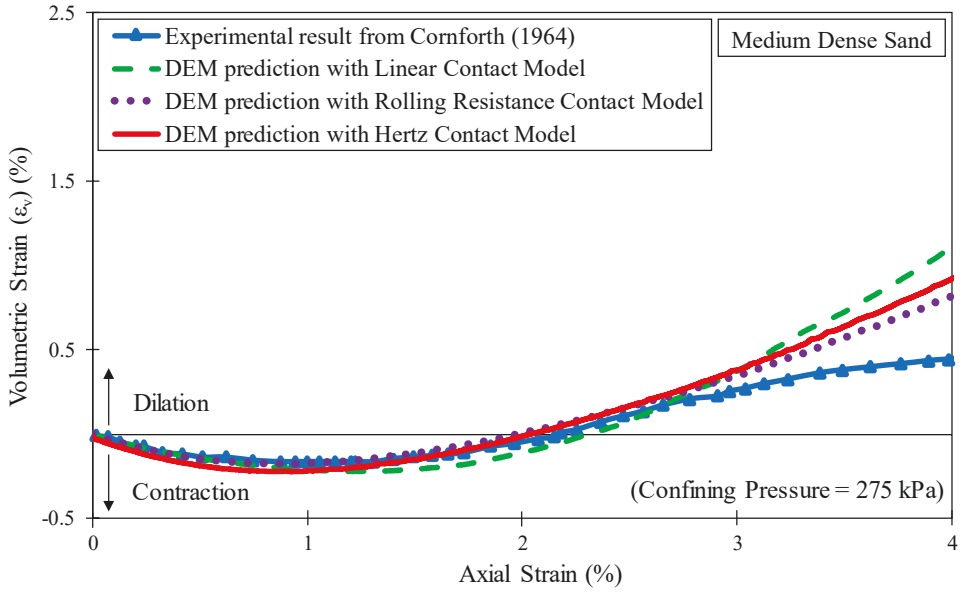


Figure 3.10 Comparisons of variations of volumetric strain with axial strain obtained from calibration numerical simulation and experimental results

As observed, the axial stress shows a continuous rise with the increase in axial strain until the peak stress of 1150 kPa has been reached, while strain softening has been observed when the axial strain is greater than 2.2%. Additionally, the volumetric strain demonstrates a contraction at the initial stage (i.e. axial strain < 1%) and dilation when the simulation continues, confirming the medium dense state of the specimen simulated in DEM.

Referring to Figure 3.7and Figure 3.8, it can be concluded that the numerical predictions have a good agreement with experimental data, indicating reliability of calibrated parameters reported in Table 3.1.

Table 3.1 Summary of calibrated contact parameters for poorly graded sand

| Linear Contact Model | | |
|---|---|---|
| Parameters | Descriptions | Value |
| $E^*_{mod}$ | Effective Modulus | 145 MPa |
| $k^*$ | Stiffness Ratio (Normal Stiffness/ Shear Stiffness) | 1.75 |
| $\mu$ | Interparticle friction coefficient | 0.85 |
| Rolling Resistance Contact Model | | |
| $E^*_{mod}$ | Effective Modulus | 150 MPa |
| $k^*$ | Stiffness Ratio (Normal Stiffness/ Shear Stiffness) | 4.0 |
| $\mu$ | Interparticle friction coefficient | 0.50 |
| $\mu_r$ | Rolling Friction | 0.10 |
| Hertz Contact Model | | |
| $G$ | Effective Shear Modulus | 1.5 GPa |
| $\vartheta$ | Poisson's Ratio | 0.15 |
| $\mu$ | Interparticle friction coefficient | 0.55 |
| $\alpha^H$ | Hertz Exponent | 1.50 |

### 3.4.2 Cavity Expansion Simulation

The ultimate objective of this study is to investigate the effects of different contact models on soil response during the cavity expansion process. To achieve this goal, a large-scale numerical model simulating the cylindrical cavity expansion has been proposed adopting PFC$^{3D}$ software and calibrated parameters. Considering the fact that many cavity expansion related problems, such as pressuremeter test and driven pile installation, are in plane-strain condition (Alshibli et al. 2000), and taking the advantage of the axisymmetric geometry, only a quarter of the geometry with plane-strain condition has been simulated, as shown in Figure 3.11.

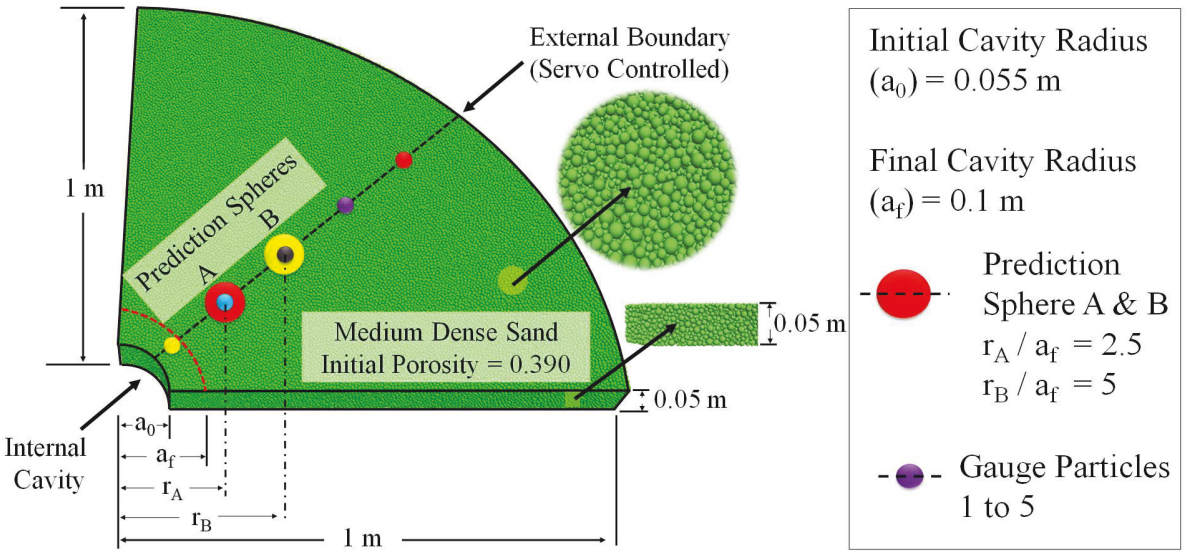


Figure 3.11 Cavity expansion model setup

The discrete element model established for three different contact models contains 75,010 spherical particles, generated using the radius expansion method, with its external boundary located 1 m away from the centre of the initial cavity, as shown in Figure 3.11. The measured soil initial porosity is approximately 0.390, similar to the porosity reported in the experiment used for calibration for medium dense sand. The initial friction assigned to particles is 0.20 at the generation stage and the internal and external boundaries as well as the top and bottom walls are servo-controlled (as illustrated in Figure 3.11) to satisfy the stress state and the void ratio. Once the target void ratio and stress state are reached at the equilibrium, the friction is set to the friction determined in the calibration exercise. The initial stress field adopted was 500 kPa ($\sigma_{r_0} = \sigma_x = \sigma_y =$ 500 kPa), and wall servo mechanism was enabled to ensure that the external pressure remains equal to the initial

stress field at all time at the outer boundary during the cavity expansion process. After the initial condition has been satisfied, all three groups of analyses adopting different contact models have the same properties, including the same initial stress field and the porosity equaling 500 kPa and 0.390, respectively. In addition, the average number of active contacts per particle (i.e. coordination number) was 5.7 for all contact models, confirming the specimen is in medium dense state according to the empirical equation to relate coordination number and porosity proposed by Mitchell et al. (2005).

Three groups of simulations were conducted using different yet calibrated contact models (see Table 3.1), and the above conditions were consistently applied to all analyses. After the initial conditions were satisfied, the cylindrical cavities were expanded gradually from an initial cavity radius $a_0$ = 0.055 m to a final cavity radius $a_f$ = 0.1 m in a constant strain rate of 0.001 m/s to ensure quasi-static loading condition. Internal cavity pressure ($P_a$) is measured using appropriate subroutines that can obtain the contact forces acting on the internal cavity wall and then divided by the corresponding contact area. On the other hand, there were five equally spaced gauge particles selected along angular bisector, as shown in Figure 3.11, and the displacements and positions of these gauge particles are continuously monitored during the cavity expansion. Additionally, the radial stress ($P_r$) distribution at various stages of the cavity expansion are also recorded using numerous prediction spheres created in the radial direction. Furthermore, referring to Figure 3.11, the variations of the deviatoric stresses and volumetric strains with the shear strain during the cavity expansion are continuously recorded adopting two particular predication

spheres, A and B (see Figure 3.9), which are situated at $r_A/a_f$ = 2.5 and $r_B/a_f$ = 5, respectively.

In a DEM model, averaging procedure is necessary to compute the microscale stresses. The calculation of the average stress in a prediction sphere of volume $V$ is based on Christoffersen et al. (1981) using the following formulation:

$$\bar{\sigma} = -\frac{1}{V}\sum F^{(c)} \otimes L^{(c)}{}_{N_c} \tag{3-7}$$

Where, $N_c$ is the number of contacts within the prediction sphere, $F^{(c)}$ is the contact force vector, $L^{(c)}$ is the branch vector joining the centroids of the two bodies in the contact, $\otimes$ denotes outer product, and compressive stress is negative by convention.

## 3.5 Results and Discussion

### 3.5.1 Cavity Pressure Variations during Cavity Expansion

Variations of cavity pressure during the cavity expansion process is plotted against the cavity radius ratio ($a/a_0$) in Figure 3.12.

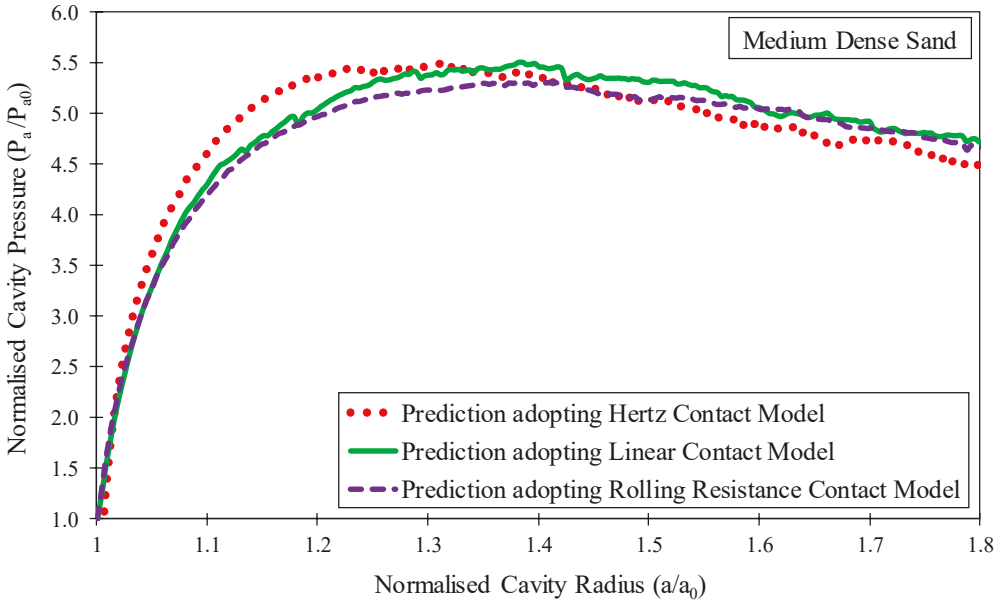


Figure 3.12 Cavity pressure variations during cavity expansion

Pressure variations are represented by the ratio of the measured cavity pressure ($P_a$) over the initial cavity pressure ($P_{a_0}$). It is observed that the cavity pressure variations follow the same pattern irrespective of the adopted contact model. The peak cavity pressure acquired for all three contact models is approximately 5.5 times of the initial cavity pressure (i.e. $P_{max}$ = 2.75 MPa). However, it is noticed that the cavity pressure obtained from the simulation with Hertz contact model tends to reach the peak at slightly less expansion radius. This finding complies with the soil stress-strain behaviour obtained in the triaxial test Figure 3.9), in which, Hertz contact model resulted in the peak axial stress at a lower axial strain. It can be readily concluded that the soil response during the cavity expansion is largely dependent on the soil behaviour during the triaxial compressive test. Additionally, the simulation process takes approximately 40 hours for the simulations

adopting Linear contact model and Rolling Resistance contact model on a computer with an Intel i7 processor @3.4GHz and 16GB RAM, while about 50 hours are required for the analysis adopting Hertz contact model. This may be attributed to the fact that the Hertz contact model employs non-linear formulations and hence complicated and time-consuming computational algorithms are required. It should be noted that for all adopted contact models, strain softening behaviour is captured, which is likely due to the dilatancy of granular material since the specimen generated in the simulation is defined as medium dense sand.

#### 3.5.1.1 Dilatancy of Granular Material in Microscopic View

The dilatancy in macroscopic view is explained as the volume expansion when the specimen is subjected to the shear deformation. However, in discrete element modelling, the dilation can be fundamentally interpreted by the interactions between contacting particles adopting the equilibrating force system. As inspired by (Budhu 2008), the dense assembly of sand particles in microscopic view can be simplified to the packing shown in Figure 3.13.

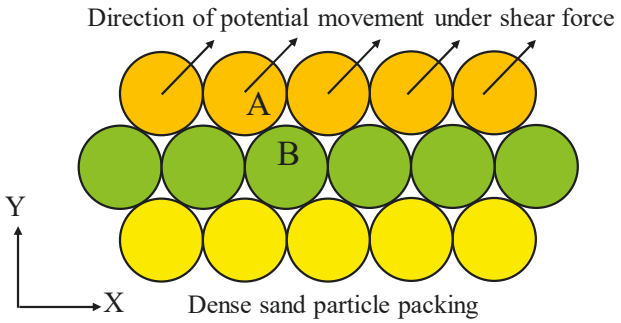


Figure 3.13 Illustration of the dense sand assembly in DEM

With continuous shearing, particles on the top layer (e.g. Particle A) tend to override the particles underneath (e.g. Particle B). Hence, the potential slipping plane between two particles can, at any stage, be idealised to an inclined surface with an angle of $\alpha_d$ to the horizontal plane as shown in Figure 3.14.

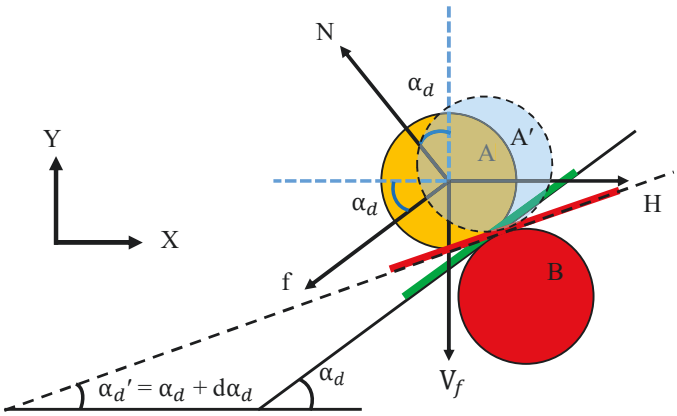


Note:
N is the normal force acting perpendicular to the slipping plane
f is the friction force acting parallel to the slipping plane (f = μN)
H and $V_f$ are horizontal and vertical forces applied due to external loading, respectively
$\alpha_d$ is the dip of slipping plane

Figure 3.14 Free-body diagram of the particles on the slipping plane

Referring to Figure 3.14, the angle α reduces to $\alpha_d'$ ($\alpha_d' = \alpha_d + d\alpha_d$; $d\alpha_d < 0$) when the Particle A moves to location A′ while a new slipping plane with Particle B would be formed.

If the horizontal force (H) is applied in a slow manner and considering a constant vertical force ($V_f$) during the shearing process, quasi-static condition can be satisfied. In this case, equilibrium of forces in both horizontal and vertical directions can be expressed as:

$$\sum F_x = 0 \longrightarrow \mu N\cos(\alpha_d + d\alpha_d) + N\sin(\alpha_d + d\alpha_d) = (H + dh) \tag{3-8}$$

$$\sum F_y = 0 \longrightarrow N\cos(\alpha_d + d\alpha_d) - \mu N\sin(\alpha_d + d\alpha_d) = V_f \tag{3-9}$$

Combining Equations (3-8) and (3-9) leads to:

$$\frac{H + dH}{V_f} = \frac{\mu\cos(\alpha_d + d\alpha_d) + \sin(\alpha_d + d\alpha_d)}{\cos(\alpha_d + d\alpha_d) - \mu\sin(\alpha_d + d\alpha_d)} \tag{3-10}$$

where, $\mu = \tan\phi'$, and $\phi'$ is the friction angle.

Assuming that the surface area of the specimen remains constant during the shearing process, Equation (3-10) can be expressed directly in terms of the relationship between the shear and normal stresses:

$$\frac{\tau + d\tau}{\sigma} = \frac{\tan\phi'\cos(\alpha_d + d\alpha_d) + \sin(\alpha_d + d\alpha_d)}{\cos(\alpha_d + d\alpha_d) - \tan\phi'\sin(\alpha_d + d\alpha_d)} =$$

$$\frac{\tan\phi' + \tan(\alpha_d + d\alpha_d)}{1 - \tan\phi'\tan(\alpha_d + d\alpha_d)} \tag{3-11}$$

Hence,

$$(\tau + d\tau) = \sigma \cdot \tan[\phi' + \alpha_d + d\alpha_d)] \quad (3\text{-}12)$$

Referring to Equation (3-12), when the friction angle ($\phi'$) is assumed to be constant, the predicted deviatoric stress increases ($d\tau > 0$) as the dilation angle increases ($d\alpha_d > 0$). On the contrary, a decrease in dilation angle ($d\alpha_d < 0$) would contribute to a reduction in the deviatoric stress ($d\tau < 0$), which is known as the strain softening behaviour, which is observed after the peak deviatoric stress in macroscopic point of view.

### 3.5.2 Radial Stress Distributions during Cavity Expansion

A comparison for the distribution of the radial stresses measured at various distances ($r/a_0$) during the cavity expansion is presented in Figure 3.15.

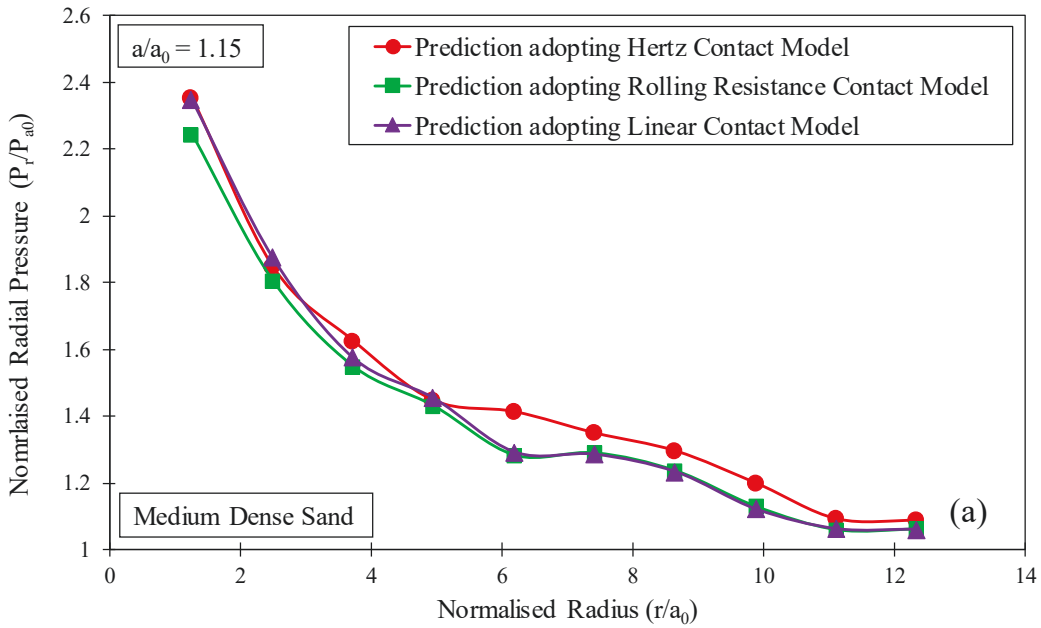

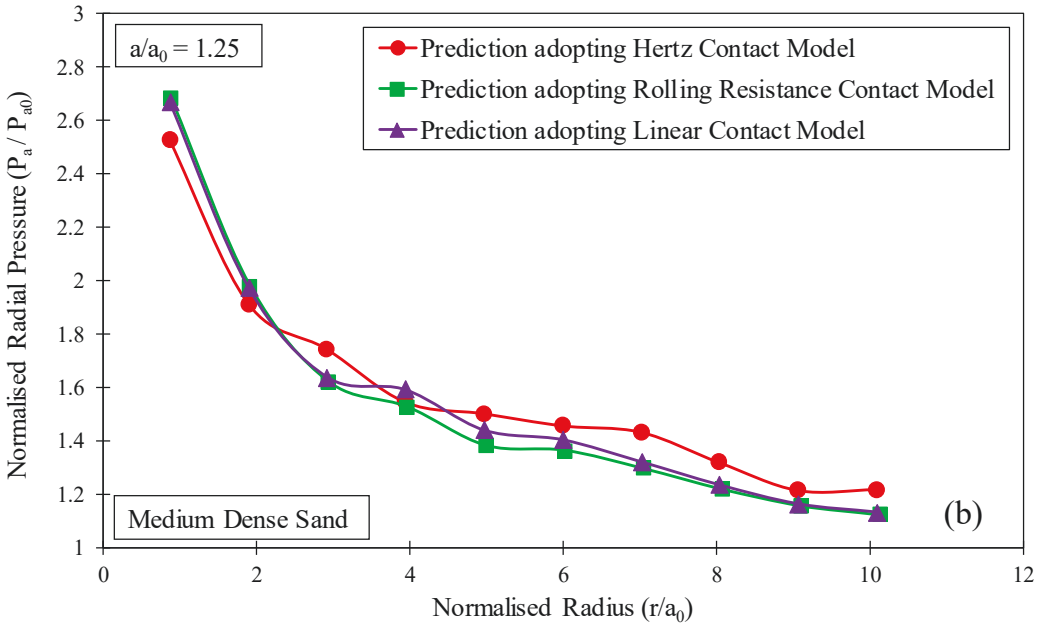


Figure 3.15 Radial stress distributions at various stages (a) $a/a_0$ = 1.15 and (b) $a/a_0$ = 1.25 during cavity expansion

Results have been plotted for a selection of cavity sizes. Figure 3.15 (a) and (b) present the results for $a/a_0$ = 1.15 and $a/a_0$ =1.25, respectively. It can be generally concluded that the magnitude of the radial pressure changes significantly with the distance from the internal cavity. As $r$ increases, the radial stresses ($P_r$) reduce more significantly, while further away from the cavity, this reduction rate becomes less pronounced. For example, the normalised radial pressure decreases immensely when the normalised cavity radius ($r/a_0$) is less than 5, while insignificant radial pressure variations are observed when $r/a_0 > 11$. It is projected that the measured radial stresses eventually reach the initial in-situ stress (i.e. $P_a / P_{a_0} = 1$) at a large radial distance (i.e. $r \to \infty$) . Furthermore, comparisons were made for radial pressure variations with the radial distance, and it is

clearly noticed that there are no pronounced differences between predictions obtained from simulations with three different contact models (see Figure 3.15).

### 3.5.3 Soil Radial Displacement during Cavity Expansion

Figure 3.16 shows the soil movement obtained in radial direction due to the cavity expansion.

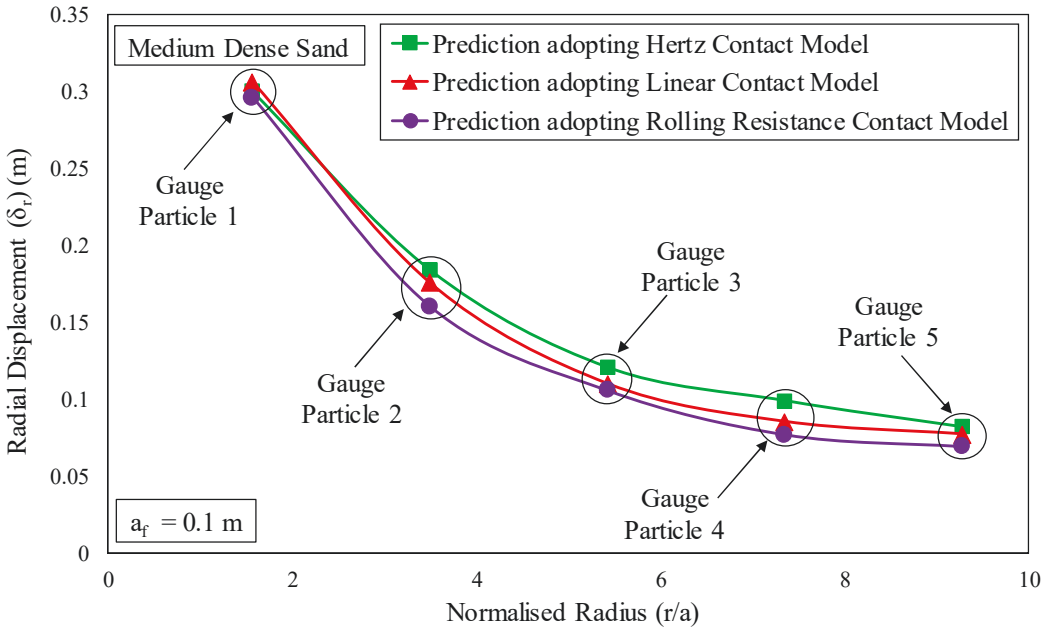


Figure 3.16 Radial displacement of five equally spaced gauge particles during the cavity expansion

The results are plotted based on the total displacement of five gauge particles from the beginning of the cavity expansion (i.e. $a = a_0 = 0.055$ m) till the end ($a = a_f = 0.1$ m). These five gauge particles are equally spaced, and the locations of these particles are represented using the normalised distance of $r/a$ (refer to Figure 3.11). As expected,

particles located closer to the centre of the cavity experience a larger radial displacement. For instance, the Gauge Particle 1 positioned 0.1 m away from the internal cavity moved 0.03 m in the radial direction when the cavity expanded from 0.055 m to 0.1 m. However, the Gauge Particle 5 located 0.4 m from the internal cavity experienced a total radial displacement of 0.0075 m during the entire cavity expansion process. Referring to Figure 3.16, it can be observed that the total radial displacement shows a dramatic decrease with radius when the normalised radius ($r/a$) is less than 6, while the changes become almost insignificant when the normalised cavity radius is larger than 8. Furthermore, it can be concluded that the calibrated contact models express very similar results in terms of the distribution of the radial soil movement.

### 3.5.4 Deviatoric Stress and Volumetric Variations during Cavity Expansion

A comparison of the deviatoric stress and the volumetric strain variations with the shear strain during the cavity expansion is presented in Figure 3.17 and Figure 3.18

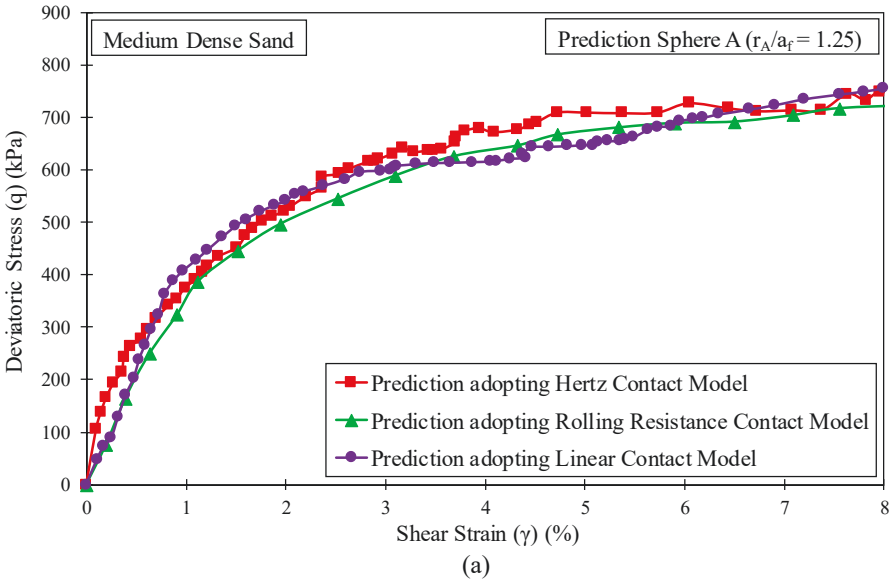


Figure 3.17 (a) Deviatoric stress – shear strain relationship and (b) volumetric strain-shear strain relationship at predication sphere A

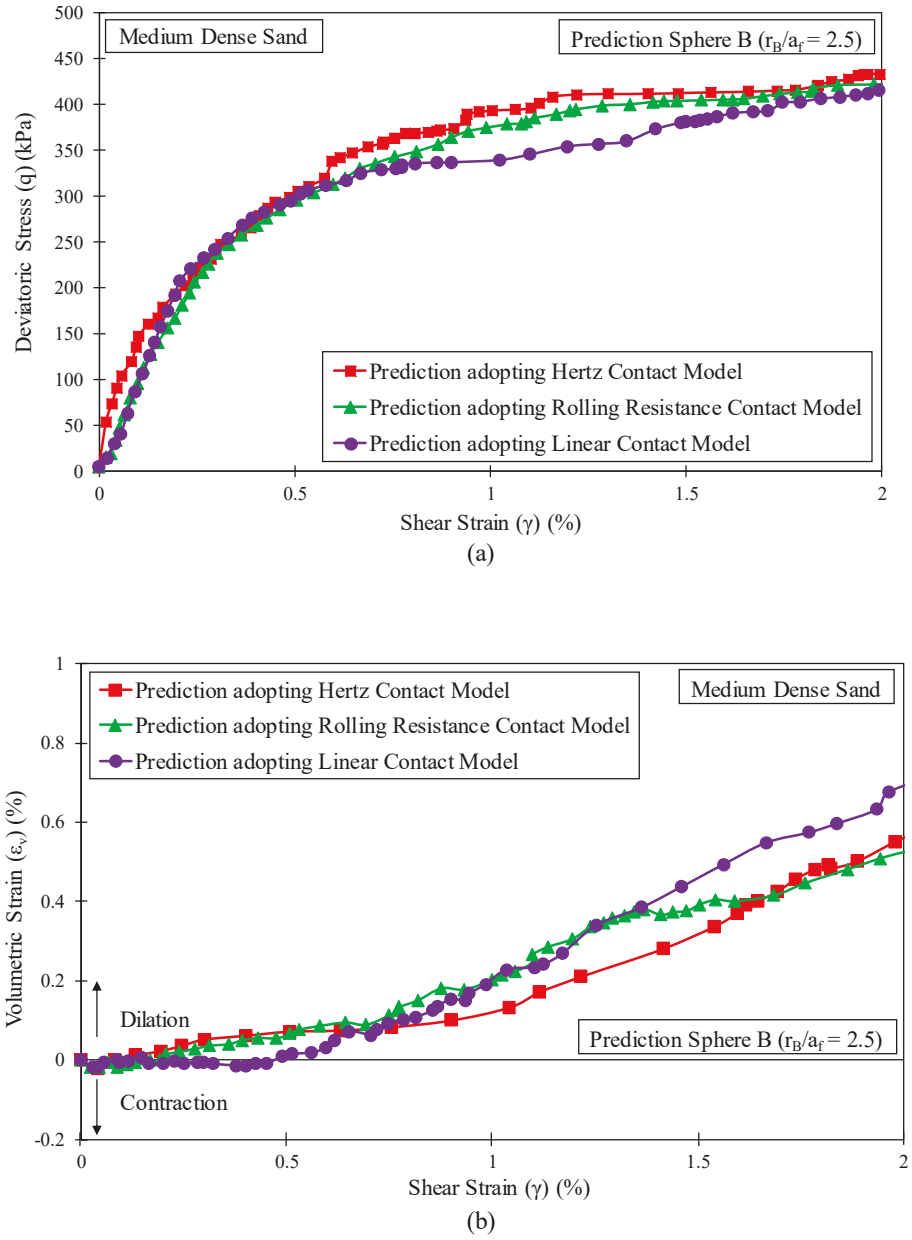


Figure 3.18 (a) Deviatoric stress – shear strain relationship and (b) volumetric strain-shear strain relationship at predication sphere B

Results obtained are reported based on two prediction spheres situated at a radial distance of $r_A$ and $r_B$ , as illustrated in Figure 3.11. As it can be clearly observed in Figure 3.17(a)

and Figure 3.18(a), the deviatoric stresses reveal a continuous increase with the increase of the shear strain, and the soil particles close to the internal cavity experience larger deviatoric stresses compared with those situated further away. Similar findings are also reported by (Manassero 1989) and (Silvestri 2001) when attempting to interpret the self-boring pressuremeter test in the calibration chamber. Additionally, as depicted in Figure 3.17(b) and Figure 3.18(b), the volumetric strain variations show a contraction during the initial stage of the cavity expansion and then dilation when the cavity is expanded further, confirming the medium dense state of the sandy soil simulated. As expected, the soil close to the centre of the cavity (e.g. $r_A/a_f$ = 1.25) experience more evident volume changes while the variations of the volumetric strain predicted becomes less pronounced with the increase in the radial distance (e.g. $r_B/a_f$ = 2.5). It is projected that the predicted volumetric strains would eventually approach zero when the radial distance is extremely large (i.e. $r \rightarrow \infty$). Furthermore, it can be explicitly concluded that the numerical results obtained for three different, yet calibrated contact models are in a good agreement.

### 3.5.5 Dilatancy Variations during the Cavity Expansion

Dilation angle is the measure of the change in the volumetric strain with respect to the change of the shear strain (Budhu 2008). Hence, it is possible to use the current model and results to further investigate the dilatancy variations.

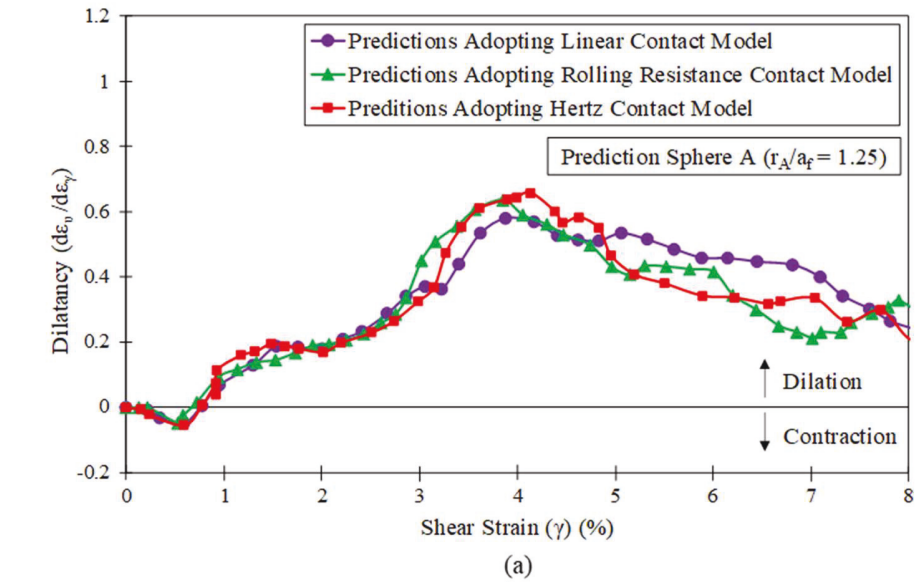


Figure 3.19 Variations of dilatancy during cavity expansion at (a) prediction sphere A and (b) prediction sphere B

Figure 3.19 depicts the variations of dilatancy with shear strain based on the prediction spheres A and B (as shown in Figure 3.11).It is observed that dilatancy is negative at the

initial stage of the cavity expansion and then positive when the cavity expands further, confirming a transient contraction and subsequent continuous expansion at both predictions spheres. In addition, referring to Figure 3.19 (a), the dilatancy shows a persistent reduction after the peak, and it is projected that the dilatancy will eventually approach zero when the specimen reaches the critical state.

### 3.5.6 Contact Forces and Displacement Contour

Figure 3.20 shows an example of contact forces between particles and total displacement contours adopting rolling resistance contact model.

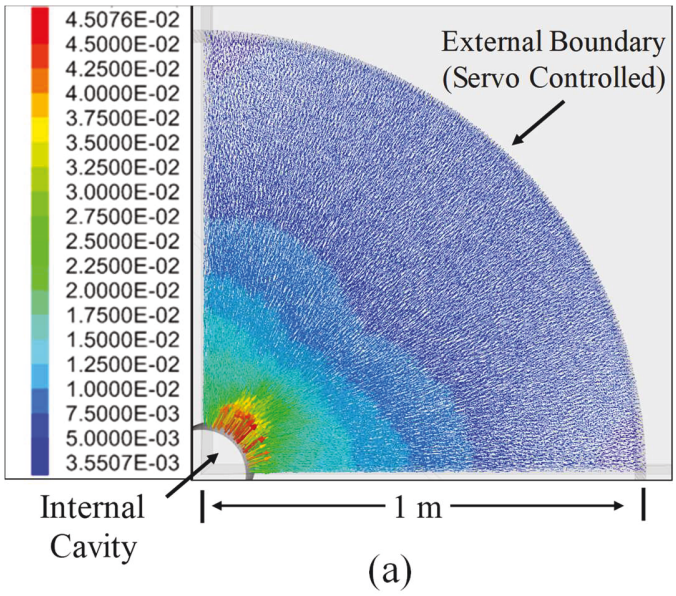


(a)

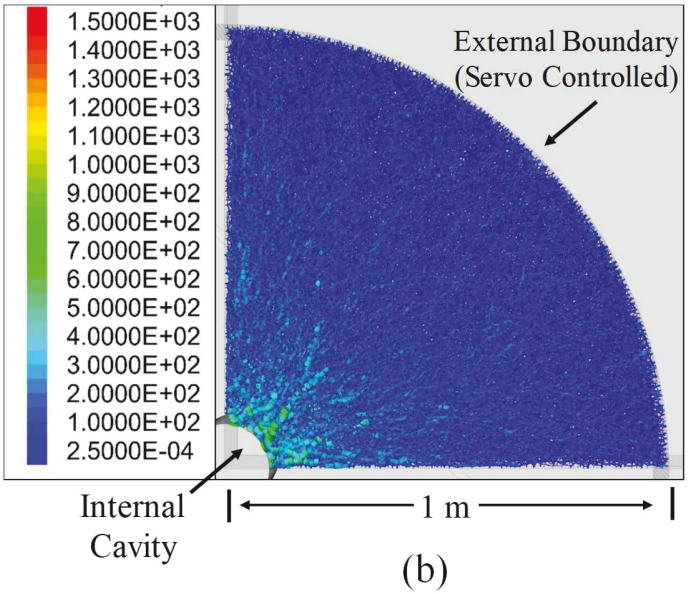


Figure 3.20 (a) Particle displacement contour and (b) particle contact force contour for Rolling Resistance Contact Model

As the contours obtained from three different contact models are very similar, only one case is presented. As expected, the contact forces close to the internal cavity are larger and change more dramatically with radius. Additionally, referring to Figure 3.20(a), the maximum soil displacement of approximately 0.045 m is observed at the internal cavity, while the displacement reduces gradually with the increasing distance from the centre of the cavity. It should be highlighted that Linear contact models may not be able to simulate the behaviour of particles that are highly angular. Instead, these angular particles may be more accurately simulated using Rolling Resistance contact model. Consequently, it is always strongly suggested that the choice of the most appropriate contact model should be deliberated based on the properties and characteristics of the materials to be studied.

## 3.6 Further Discussion and Limitations

This study has presented an investigation on the influence of particle contact models on soil response of sandy soil during cavity expansion. According to the USCS, the specimen used in this study was categorised as poorly graded sand. The calibration exercise was conducted using the same PSD reported by Cornforth (1964) as reported in Figure 3.5. Hence, the calibrated contact parameters could mimic the shear behaviour and obviously correspond to the poorly graded sand adopted in the experiment. Obviously, the micro-mechanical characteristics including the particle contact properties very much depend on the texture of the surface of particles, particle roundness and sphericity, mineralogy of the parent material, and geological processes involved (Horn et al. 1962; Herle et al. 1999; Bareither et al. 2008). For instance, Bareither et al. (2008) indicates that sand with lower shear strength is usually derived from weathering of underlying sandstones, and tends to have medium to fine and well-rounded yet poor graded particles. However, higher shear strength is expected from the sand particles formed as a result of recent glacial activities leading to coarser, more angular and well graded particles. Obviously, if the calibration exercise is conducted for another type of soil that is well graded, then the micro-mechanical properties would be different, which in turn will influence the soil response during the cavity expansion process. For instance, the shear strength of the well graded sand is generally larger due to its relatively stable particle structure resisting the sliding and the collapse of the interlocking (Enomoto et al. 2015). In addition, Kirkpatrick (1965)

and Leslie (1969) pointed out that the increase in the coefficient of uniformity ($C_u$) can enhance the peak shear strength of granular material significantly.

As mentioned earlier, this study has employed the discrete element simulations to investigate the influence of the particle contact models on response of poorly graded sand during cavity expansion. The contact models utilised contain simplifications and assumptions that inevitably induce disparities between the numerical predictions and the realistic soil responses. Hence, it is noteworthy to highlight the limitations of this study as summarised below:

1. Soil particle crushing and cracking have not been captured in this study. Therefore, the ploughing behaviour causing permanent plastic deformation at the contact at high normal loads has not been captured (Senetakis et al. 2013). According to Sandeep et al. (2018), the ploughing behaviour, is responsible for the decrease in interparticle friction during shearing, and this ploughing might also trigger the increase in particle friction during unloading process. Hence, particle crushing can contribute to strength and stiffness degradation. Similar findings were also report by (Miura et al. 1984). Hence, it is recommended for future studies to capture particle crushing during cavity expansion process to assess the extent to which the particle crushing can influence stress and strain predictions. Indeed, the particle crushing can be considered by means of the user defined contact models through a pre-defined particle crushing criteria. When the contact forces (or stresses) between particles exceed the threshold, the particles will be crushed and replaced by a certain number of smaller particles.

Granular soils, at elevated pressures when particle crushing occurs, tend to experience reductions in the void ratio and the peak state strength but increase the volumetric strain due to the reduction in the maximum angles of dilation and shearing. Hence, at elevated pressures, contractive behaviour may be more pronounced compared to the case with no particle crushing (Bolton 1986; Lade et al. 1996; Yu 2017; Wu et al. 2020). Therefore, the penetration resistance of driven piles may be overestimated based on cavity expansion theory if the particle crushing is not properly characterised. In addition, stress relaxation and rearrangement induced by particle crushing may also lead to a lower bearing capacity of the foundation. However, due to the increase in volumetric strain, the induced horizontal displacement during the pile installation may also increase accordingly.

2. The viscous behaviours of particles and interfaces have not been included. Indeed, the material behaviour can be influenced by both compression and shear creep causing stress relaxation or further deformation (Pham Van Bang et al. 2007; Wang et al. 2008b). For instance, Kuwano et al. (2002) indicated that the shear creep deformation observed within two hours of the end of anisotropic consolidation contributed to 30%-80% of the "primary" deformation observed during the fully drained loading stages.
3. In this study, ideal spherical particles have been used in both the calibration exercise and the cavity expansion simulation, while angularity of particles and sharp corners may influence the results (Zhao et al. 2015; Fu et al. 2017; Sandeep et al. 2018). Zhao et al. (2015) reported that the interlocking of the particles is more dramatic in a high

angular assembly, resulting in high shear strength and dilatancy. In addition, the non-uniform distribution of normal contact forces near the shear plane is more significant in high angular assembly during shearing, confirming that less particles share the majority of the shear force.

## 3.7 Summary

The numerical predictions indicated that commonly adopted contact models in simulating granular materials in DEM studies (i.e. linear model, rolling resistance, and Hertz nonlinear contact model) produced similar results when adopted assessing the installation effects of rigid inclusion in sandy soils. This confirmed that the soil response during the cavity expansion is highly correlated to its behaviour during the triaxial test used for the model calibration. However, it should be highlighted that if the soil particles are highly angular (e.g. ballast particles), modelling adopting simplified Linear contact model may result in inaccurate predictions, particularly the peak stress and the volumetric dilation may not be well reproduced. Hence, selecting an appropriate contact model and performing the parameter calibration is of significant importance in DEM studies. In term of the particle upscaling technique often adopted to reduce the computational effort, the results from this study confirmed that given a constant model size, the cavity pressure measured on the internal cavity adopting different particle upscaling factors is highly correlated to the size effects between the internal cavity and the median particle size (i.e. $R_c/d_{50}$; $R_c$ is the radius of column to be installed). It can be concluded $R_c/d_{50} > 8$ is a prerequisite to obtain reliable results using discrete element cavity expansion simulations.

# Chapter 4 – Three-Dimensional Discrete Element Simulation of Cylindrical Cavity Expansion from Zero Initial Radius in Sand

## 4.1 General

This chapter presents the study seeking to assess the influence of choice of initial cavity radius on the soil response during cavity expansion in sandy soil adopting three-dimensional discrete element simulations and obtaining the size of the influence zone when the expansion starts from zero initial radius. Sandy soil is modelled adopting rolling resistance contact model to capture the effects of particle interlocking, and the microscopic parameters are calibrated utilising linear model deformability method for both loose and dense sands against experimental results. Four cylindrical cavity expansions that commenced from different initial radii are simulated in dense and loose sand specimens. The large-scale three-dimensional model is proposed with more than 500,000 particles, enabling precise volumetric dilation and contraction predictions using strain rate tensors. During the cavity expansion process, cavity pressure is constantly recorded by appropriate subroutines, while the stress-strain and void ratio variations are continuously monitored using an array of prediction spheres situated close to the internal cavities.

The results confirm that the initial cavity radius chosen has conspicuous effects on the cavity pressure, the stress path, the volumetric strain and the deviatoric stress, especially

at the initial stage of expansion; however, these effects become less pronounced and are ultimately minor as the cavity reaches full expansion. The results confirmed that given the same expansion volume, the pressure required to create a cavity is significantly larger than expanding an existing cavity in the same soil medium, whereas the pressure needed to maintain an already expanded cavity is not sensitive to the choice of initial cavity radius. The results obtained were further validated adopting the variations of stress path, deviatoric stress and volumetric strain in the vicinity of the cavity wall. The findings from this study may provide practicing engineers with confidence in determining the appropriate size of the pilot hole in driven pile installation and horizontal directional drilling for trenchless piping in sandy soil. In addition, the lateral soil displacement induced by cavity expansion is also examined in this study. It is concluded that the radial displacement due to cavity expansion in loose sand can reach 25 $a_f$ ($a_f$ representing the final cavity radius), while a larger influence zone must be considered by practicing engineers when dealing with dense sand.

## 4.2 Introduction

Cavity expansion theories study the changes in stresses, pore water pressures and displacements induced by the expansion or contraction of cylindrical and spherical cavities. The cavity expansion was initially noticed by Bishop et al. (1945) in connection with indentations in ductile materials by cylindrical punches with conical heads. Earlier studies were carried out subsequently on deformable solids, particularly on metals with associated flow rules (Chadwick 1959; Durban et al. 1976), and then analytical solutions

were presented in infinite, homogeneous, and isotropic soil media (Palmer 1971; Vesic 1972; Carter et al. 1986). However, as more complex and realistic soil models were developed, analytical solutions could be considered as overly simplified, and numerical techniques may be the most effective way to obtain accurate solutions (Carter et al. 1979b; Yu 1990). Hence, numerical solutions were developed to consider more realistic and sophisticated soil constitutive models in cohesive and cohesionless soils under fully drained or undrained conditions (Carter et al. 1979b; Carter et al. 1985; Collins et al. 1994; Ladanyi et al. 1998; Salgado et al. 2001). Along with progress made in the development of fundamental solutions for cavity expansion in geomaterials, the cavity expansion theories have been widely adopted to analyse real-life geotechnical problems such as the installation of driven piles, interpreting pressuremeter and cone penetration tests and so forth. Indeed, the response of soil due to the pile installation, pressuremeter and cone penetration is analogous to the creation and expansion of cylindrical cavities. For instance, Randolph et al. (1979) developed a closed form analytical solution based on the cavity expansion theories for the radial consolidation around a driven pile. Salgado et al. (1997) and Salgado et al. (2007) proposed two solutions computing the cone penetration resistance in sand from cavity limit pressure. Zhuang et al. (2018) presented an analytical method based on cavity expansion theory to predict the peak uplift resistance of shallow horizontal strip anchors buried in sand. Marshall (2012) proposed an analytical method estimating the effect of tunnel construction on the response of end-bearing piles installed above. Beside these successful applications of cavity expansion theories in studying real-life geotechnical problems, numerical simulations are often performed to study the

complex mechanism of such problems adopting advanced constitutive models considering more realistic boundary conditions. In conventional Finite Element Method (FEM) modelling, the simulation involving large displacement and deformation (e.g. cone penetration test or cavity expansion with an initial cavity radius of zero) may not be achievable easily since numerical calculations must begin with an initial finite cavity radius to avoid an infinite circumferential strain (Carter et al. 1979b). Despite the fact that the expansion of a pre-existing cavity may provide an adequate approximation to the creation of a cavity based on constant volume theory, the state of stress of the soil contained in the annular region remains inaccessible (Carter et al. 1979b). Hence, arbitrary Lagrangian-Eulerian (ALE) technique is developed to prevent excessive mesh distortion. Susila et al. (2003) and Tolooiyan et al. (2011) successfully adopted Finite Element Method (FEM) to model the cone penetration test in sand using ALE method to minimise significant mesh distortion that often lead to premature numerical termination in conventional continuum method (Nguyen et al. 2019). In addition to ALE method, the Material Point Method (MPM) and coupled Eulerian-Lagrangian method are also adopted as effective tools to tackle the issue related to excessive mesh deformation during the simulation (Dutta et al. 2014; Ceccato et al. 2016). However, those aforementioned methods adopting mesh free or adaptive remeshing techniques are complex to be implemented, and generally require more computational time (Nagashima et al. 2003; Susila et al. 2003). On the contrary, the Discrete Element Method (DEM) may treat problems like large deformation and discontinuity more effectively due to its capability incorporating the discontinuous nature of granular materials (Liu et al. 2015). Jiang et al.

(2006) simulated deep penetration in granular soils by adopting a two-dimensional DEM model, while Zhou et al. (2012) carried out a coupled 3D discrete - continuum numerical simulation to study soil - pile interactions during pile penetration in sand. Arroyo et al. (2011) and Butlanska et al. (2013) investigated the mechanism of cone penetration tests in a virtual calibration chamber, while a similar numerical model was proposed by Ciantia et al. (2016) to study the effects of grain crushing on the CPT tip resistance during the penetration process. Geng et al. (2013) modelled the actual cylindrical cavity expansion process to interpret the thick cylindrical test conducted by Fahey (1986) to study the pressuremeter testing process. However, since these studies mainly focused on the penetration mechanism, there is very limited information reported on the effect of choice of initial cavity radius on the soil response during cavity expansion. Since the DEM can be easily implemented to model the cavity expansion/creation from a zero initial cavity radius (i.e. no initial cavity present), the impact of an arbitrary initial cavity radius (simply assumed for the sake of numerical convergence) on the predictions can readily be assessed using this technique.

This study presents a comprehensive numerical investigation using the Discrete Element Method to study the influence of the choice of initial cavity radius on the soil response in dense and loose sandy soils during cylindrical cavity expansion. The contact model that mimics the behaviour of sandy soil is calibrated beforehand against existing experimental results and is then used to analyse several large-scale three-dimensional numerical models, simulating cavity expansions with different initial radii. The results are used to assess the

variations of cavity pressure, the stress path, the volumetric strain, the deviatoric stress, the void ratio and so forth during cavity expansion, considering the choice of initial cavity radius. These results aim to provide some practical guidelines and suggestions for practising engineers on estimating the influence zone. In addition, they would be useful for predicting the maximum driving force required by pile drivers induced by the installation of displacement-based inclusions (such as driven piles and concrete injected columns).

## 4.3 Adopted Contact Constitutive Model for Particle Interaction

In discrete element simulation, the contact constitutive model is employed to define the behaviour of soil particles at their points of contact. To investigate the effects of initial cavity radius on sandy soil response during cavity expansion using the discrete element method, a contact model that is capable of mimicking the behaviour of granular material must be adopted. Iwashita et al. (1998) pointed out that the rolling of neighbouring particles is the dominant micro-deformation mechanism that controls the strength and dilatancy of granular materials. On this basis, the conventional DEM proposed by Cundall et al. (1979) has been modified by introducing an additional element at each contact through which the rolling mechanism is incorporated. By considering the rolling resistance, the development of shear bands can be captured in the same way as natural granular soils (Iwashita et al. 1998).

In this study, Rolling Resistance contact model has been adopted, which is the contact model initially proposed by Iwashita et al. (1998) and modified by Ai et al. (2011) and Wensrich et al. (2012) to introduce an additional torque that is applied at each contact between neighbouring particles to resist the rolling motion. This model is suitable for simulating granular materials, particularly angular shaped particles, because modelling the precise shape of each particle is computationally impossible (Tordesillas et al. 2002; Jiang et al. 2005; O'Sullivan 2011; Wensrich et al. 2012; Zhu et al. 2017; Jing et al. 2018).

The schematic diagram of the rolling resistance contact model, adopted in this study, is depicted in Figure 4.1.

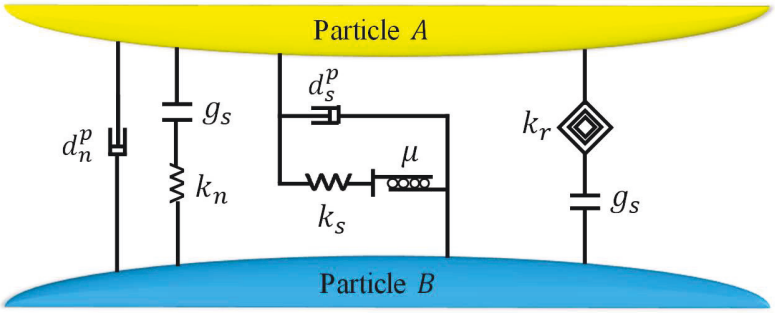


Note:
$g_s$ is the surface gap (non-tension joint)
$k_r$ is the rolling stiffness of the linear spring
$k_n$ and $k_s$ are the normal stiffness and shear stiffness of the linear springs, respectively
$d_n^p$ and $d_s^p$ are the normal dashpot and shear dashpot, respectively
$\mu$ is the friction coefficient between contacting particle

Figure 4.1 Schematic diagram of rolling resistance contact model

It is noteworthy to state that the adopted contact model is elastic – perfectly plastic, and therefore the model can capture both elastic and plastic behaviour. As illustrated in

Figure 4.1 the behaviour is linear elastic in normal direction with zero tension cut-off, whereas in the tangential direction, frictional behaviour using linear springs and plastic sliders is utilised. Slip in this contact model is accommodated by imposing a Coulomb limit on the shear force using the friction coefficient $\mu$ (i.e. slider). With the normal stiffness ($k_n^l$) and shear stiffness ($k_s^l$) of the linear springs, the normal force ($F_n$) and the shear force ($F_s$) at the contact interface are computed based on the normal and shear displacement increments (i.e. $\Delta\delta_n$ and $\Delta\delta_s$), as illustrated in Figure 4.2, by adopting the following formulations:

$$\left.\begin{aligned} F_n &= F_n^0 + k_n^l \Delta\delta_n \\ F_s &= F_s^0 + k_s^l \Delta\delta_s \\ F_s^{max} &= \mu F_n \end{aligned}\right\} \tag{4-1}$$

where, $F_n^0$ and $F_s^0$ are the initial normal and shear forces between two contacting particles, and $F_s^{max}$ is the shear strength at the contact interface.

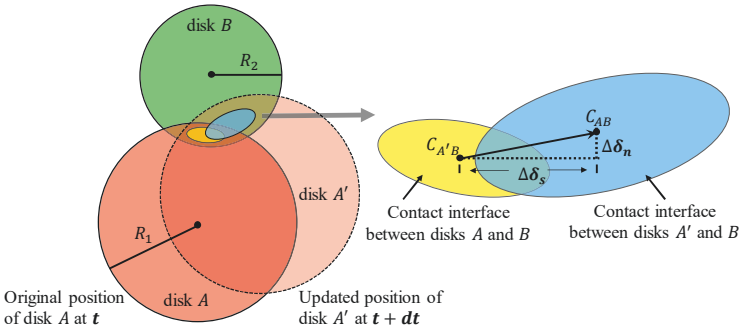


Note:
$R_1$ and $R_2$ are the radius of the disks $A$ and $B$, respectively
$C_{AB}$ and $C_{A'B}$ are the centres of the contact interfaces between disks $A$ and $B$ and disks $A'$and $B$, respectively
$\Delta\delta_n$ and $\Delta\delta_s$ are the normal and shear displacement increments in a timestep, respectively

Figure 4.2 Rheological model of rolling resistance contact model computing the normal and shear forces

As well as computing the normal and shear forces at the contact, the internal moment is incremented linearly with accumulated relative rotations of the contacting pieces at the contact points. The limiting torque in the contact is proportional to the normal contact force and acts in the opposite direction to the rolling direction.

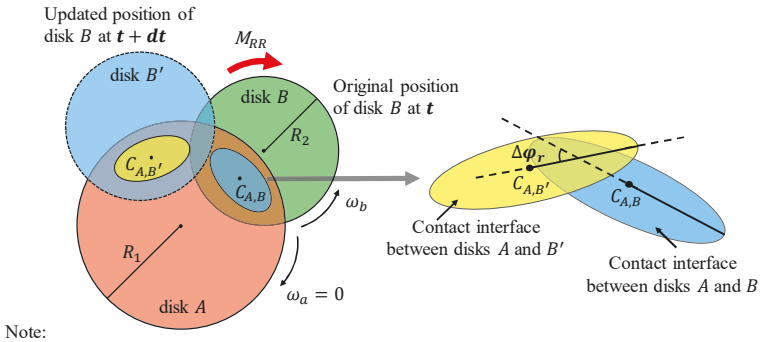


Note:
$R_1$ and $R_2$ are the radius of the disks $A$ and $B$, respectively
$C_{AB}$ and $C_{A,B'}$ are the centres of the contact interfaces between disks $A$ and $B$ and disks $A$ and $B'$, respectively
$\omega_a$ and $\omega_b$ are the rotational velocities of disks $A$ and $B$, respectively
$\Delta\varphi_r$ is the rotation increment in a timestep
$M_{RR}$ is the rolling resistance torque

Figure 4.3 Rheological model of rolling resistance contact model computing the rolling resistance moment

Referring to Figure 4.3, the rolling resistance torque ($M_{RR}$) is introduced to resist the rolling motion induced by the relative rotation increment ($\Delta\varphi_r$) that occurs between Disks $A$ and $B$; the magnitude of this rolling resistance torque is calculated based on the following equations:

$$\left.\begin{aligned} M_{RR} &= k_r^l \Delta\varphi_r \\ \Delta\varphi_r &= (\omega_b - \omega_a)dt \\ M_{RR}^{max} &= \mu_r F_n \left[R_1 R_2/(R_1 + R_2)\right] \end{aligned}\right\} \quad (4\text{-}2)$$

where, $k_r^l$ is the rolling stiffness of the linear spring, $M_{RR}^{ma}$ is the limiting toque, and $\mu_r$ is the coefficient of rolling resistance.

Detailed formulations regarding the rolling resistance contact model can be found in Iwashita et al. (1998), Ai et al. (2011) and Itasca (2016). It must be highlighted that in this study the formulations adopted to compute the normal stiffness and the shear stiffness were based on the linear model deformability method. This method utilises the effective Young's modulus ($E_{mod}^*$) of the particles to determine the normal stiffness of the linear spring, while the shear stiffness and the rolling stiffness of the springs were controlled by adopting the stiffness ratio ($k^*$) between the linear springs acting in the normal and tangential directions, based on the following equations:

$$\left.\begin{aligned} k_n^l &= \pi \left[\min(R_1, R_2)\right]^2 E_{mod}^*/(R_1{+}R_2) \\ k_s^l &= k_n^l/k^* \\ k_r^l &= k_s^l \left[R_1 R_2/(R_1 + R_2)\right]^2 \end{aligned}\right\} \quad (4\text{-}3)$$

Referring to Equation (4-3), the linear model deformability method can automatically consider the effect of particle size when determining the stiffness parameters of the linear springs in normal, tangential, and rolling directions. Hence, this method is beneficial when the particles are upscaled during the numerical simulation to reduce the computational effort.

## 4.4 Calibration of Contact Model

### 4.4.1 Numerical Simulation of Triaxial Test

To investigate the effects of initial cavity radius on the soil response, the contact model must be calibrated to mimic the realistic behaviour of sandy soil. The calibration exercises were carried out by matching the numerical simulation predictions with the existing experimental measurements. The experimental test adopted in this study was conducted by Green et al. (1975) as part of a comprehensive study on the boundary conditions and sample shape effects on the stress-strain behaviour of medium to fine uniform sand during triaxial compression tests. Detailed information and the experimental procedures can be found in Green et al. (1975). However, some essential details regarding the material information is presented here. According to Green et al. (1975), the sand adopted for the experimental test and the calibration exercises in this study is the Ham River sand, which consists of mainly rounded quartz particles with a specific gravity of 2.66. The particle size distribution indicates that the sand is fine to medium uniform sand with the particle size ranging from 0.1 mm to 0.25 mm, and the maximum porosity of dry sand by rapid

tilt test (Kolbuszewski 1948) was 48%. Typically, the stress-strain relationships from the experiments are used for calibration of contact models, which is a common practice adopted by many researchers (Chareyre et al. 2002; Arroyo et al. 2011; Wang et al. 2014; Ciantia et al. 2016). In this study, the unique characteristic contact properties have been calibrated by matching the overall (macroscopic) stress - strain and volume change - axial strain curves from the dense and loose sand specimens.

It is not realistic, given the current computational power, to simulate a triaxial test using the true particle size. For instance, a laboratory scale triaxial test on a 50 mm diameter by 100 mm height specimen of sand would consist of approximately 16 million particles, and therefore, directly mapping such a large number of particles into a simulation is unrealistic and computationally infeasible. It is only by reducing the number of particles that such analyses can become efficient and possible (O'Sullivan 2011). Therefore, before assigning the initial condition to the particles, an upscaling factor was applied to dramatically reduce the number of particles so that the simulation process could be accelerated. In this study, a rather small upscaling factor was used initially, and then gradually increased to 20, hence, the porosity could steadily reach the desired value. The triaxial test simulations have been used for the calibration exercises after upscaling consist of 27,500 spherical particles. The setup of the triaxial test is shown in Figure 4.4.

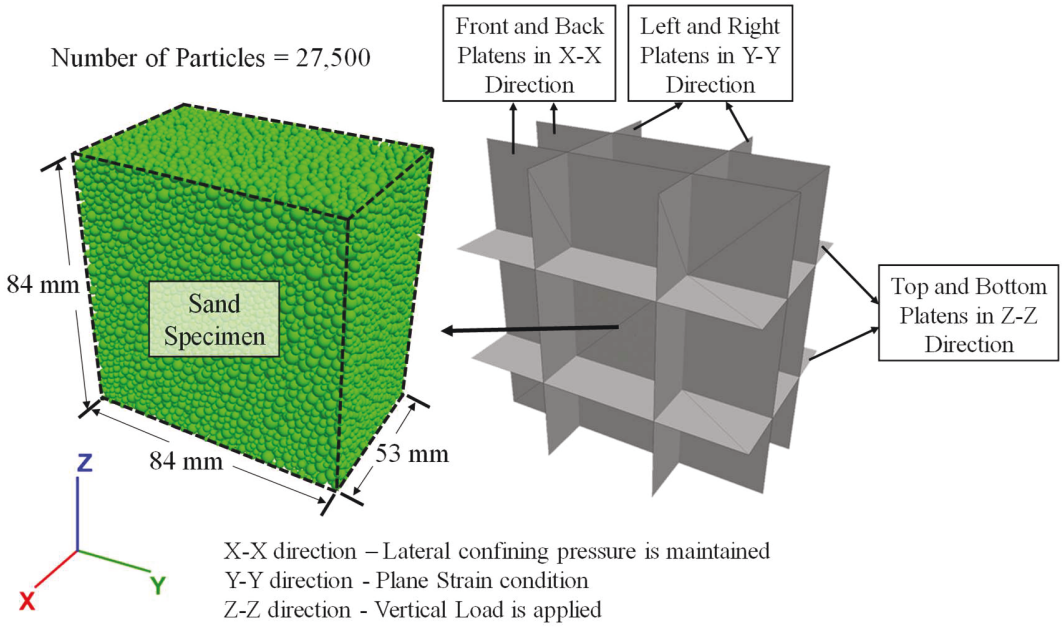


Figure 4.4 Triaxial test in plane strain condition in discrete element simulation

As illustrated in Figure 4.4, the model generated has a length of 84 mm, while the height and width are 84 mm and 53 mm, respectively, which are identical to sample dimensions adopted in the experimental test conducted by Green et al. (1975). The initial porosities of the generated DEM model were 0.388 and 0.458 for the dense and loose sand specimens, respectively, similar to the porosities measured in the laboratory.

Referring to the previous studies (Thornton 2000; Chareyre et al. 2002; Jiang et al. 2003; O'Sullivan 2011; Tong et al. 2012), a relatively dense specimen is generated using a small friction at the grain contacts during the generation stage, so that the inter-particle sliding could occur in a relatively effortless manner. After assigning this inter-particle friction to all particles, the boundary walls were controlled with a servomechanism until the target

void ratio and stress state reached the equilibrium. Once the initial conditions were satisfied, the friction was then adjusted back to the value determined from the calibration exercise. In plane strain triaxial tests reported by Green et al. (1975), the true triaxial apparatus was adopted and the platens in the intermediate direction maintained a fixed distance apart during shearing (i.e. $\varepsilon = 0$). To calibrate the contact parameters of the DEM model, identical conditions were adopted in this study to mimic the experimental condition. To simulate the triaxial test in the plane strain condition, the lateral confining pressure (X direction) of 207 kPa was maintained, while the faceted walls (i.e. platens in the experimental test) in the intermediate direction (Y direction) were fixed to simulate the plane strain condition, and then axial load was applied on the top of the specimen (Z direction) in a constant rate, as illustrated in Figure 4.4. During this simulation, variations of stress, strain, and changes in volume were continuously recorded adopting pre-defined subroutines, so that the variations of axial stress and volumetric strain with the axial strain could be obtained directly and then compared with the experimental measurements until a good agreement was observed.

### 4.4.2 Calibration Techniques and Results

The calibration of the contact model was based on the linear model deformability method, which is described by the effective modulus ($E^*_{mod}$) and the normal to shear stiffness ratio ($k^*$), as denoted in Equation (4-3). These two microscopic parameters are fundamentally related to the macroscopic material constants, namely Young's modulus ($E$) and Poisson's ratio ($\vartheta$) (Plassiard et al. 2009; Itasca 2016). It can therefore be

concluded that the effective modulus ($E^*_{mod}$) controls the elastic part of the stress-strain curve, while the normal to shear stiffness ratio ($k^*$) influences the volumetric behaviour.

The values of $E^*_{mod}$ and $k^*$ adopted for the initial calibration trial were based on recommendations made by Plassiard et al. (2009). Since the macroscopic Young's modulus ($E$) and Poisson's ratio ($\vartheta$) of the medium dense sand used in the calibration exercise were approximately 140 MPa and 0.20, as reported in Green et al. (1975), the corresponding effective modulus ($E^*_{mod}$) and the normal to shear stiffness ratio ($k^*$) were estimated to be approximately 350 MPa and 5, by referring to Plassiard et al. (2009). Along with the elastic parameters, the influence of the inter-particle friction coefficient ($\mu$) and the rolling friction coefficient ($\mu_r$) were investigated. Previous studies confirmed that the rolling friction coefficient controls the state of stress at the peak and residual states, whereas the inter-particle friction coefficient affects the peak stress level and the dilatancy angle (Plassiard et al. 2009; Yang et al. 2012; Hosn et al. 2017).

Hence, calibration was conducted adopting the predetermined effective modulus ($E^*_{mo}$ ) and the normal to shear stiffness ratio ($k^*$) to initially match the elastic part of the stress-strain curve. The rolling friction coefficient was then adjusted to match the residual stress state, and the inter-particle friction coefficient was subsequently calibrated by trial and error until an optimum match with the experimental results observed. It is noteworthy to mention that the calibration process adopted for both loose and dense specimens was the same. However, given the same volume, the number of soil particles in a loose state is less than those in the dense sand in the triaxial apparatus. Therefore, the number of

particles simulating the triaxial test on loose sand were calculated based on the target porosity and the corresponding number of particles used in the dense state.

The calibrated contact parameters are summarised in Table 4.1.

Table 4.1 Summary of calibrated contact parameters for dense and loose Ham River sand specimens

| **Calibrated Rolling Resistance Contact Model Adopting Linear Model Deformability Method** | | |
|---|---|---|
| **Parameters** | **Descriptions** | **Value** |
| $E^*_{mod}$ | Effective Modulus | 350 MPa |
| $k^*$ | Stiffness Ratio (Normal Stiffness/ Shear Stiffness) | 4.50 |
| $\mu$ | Inter-particle Friction Coefficient | 0.40 |
| $\mu_r$ | Rolling Friction | 0.35 |
| $\mu_{wall}$ | Wall Friction Coefficient | 0.0 |
| $d_c$ | Damping Constant at the Contact | 0.02 |
| $\Delta t$ | Increment of time step | $1\times10^{-5}$ s |

The calibration results for variations of axial stress and volumetric strain with axial strain for dense and loose sandy soils are plotted in Figure 4.5 and Figure 4.6.

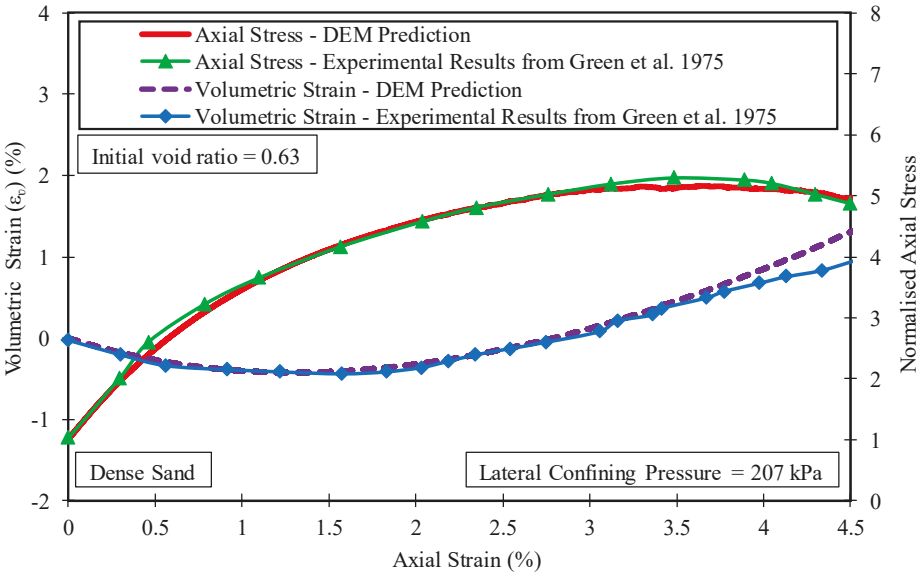


Figure 4.5 Variations of normalised axial stress with axial strain and variations of volumetric strain with axial strain – dense sand (DEM predictions versus experimental measurements)

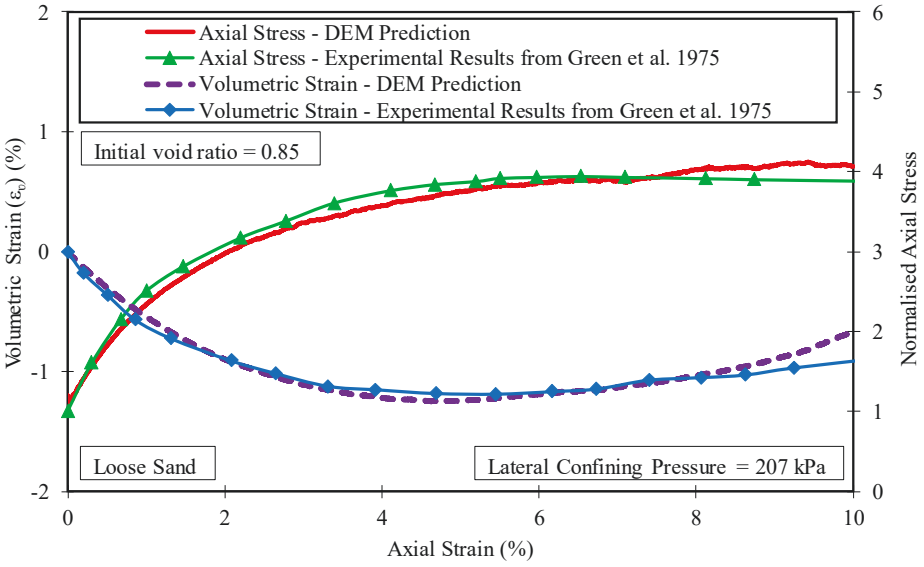


Figure 4.6 Variations of normalised axial stress with axial strain and variations of volumetric strain with axial strain – loose sand (DEM predictions versus experimental measurements)

It is observed that the predictions obtained from the numerical simulation that used calibrated contact parameters, agrees well with the experimental results, confirming the reliability of the calibrated contact parameters mimicking the behaviour of loose and dense sandy soils in the experiments.

## 4.5 Cavity Expansion Simulation

This study aims to investigate the influence of initial cavity radius on soil response during cavity expansion using DEM. To achieve this goal, a series of large-scale three dimensional cavity expansion models were proposed in PFC$^{3D}$ (Itasca 2016). Considering that many problems related to cavity expansion such as pressuremeter tests and installing driven piles occur in the plane-strain condition (Alshibli et al. 2000; Silvestri 2001), and to take the advantage of the axisymmetric geometry to accelerate the simulation process, a quarter of the cylindrical geometry was simulated, as shown in Figure 4.7 (a).

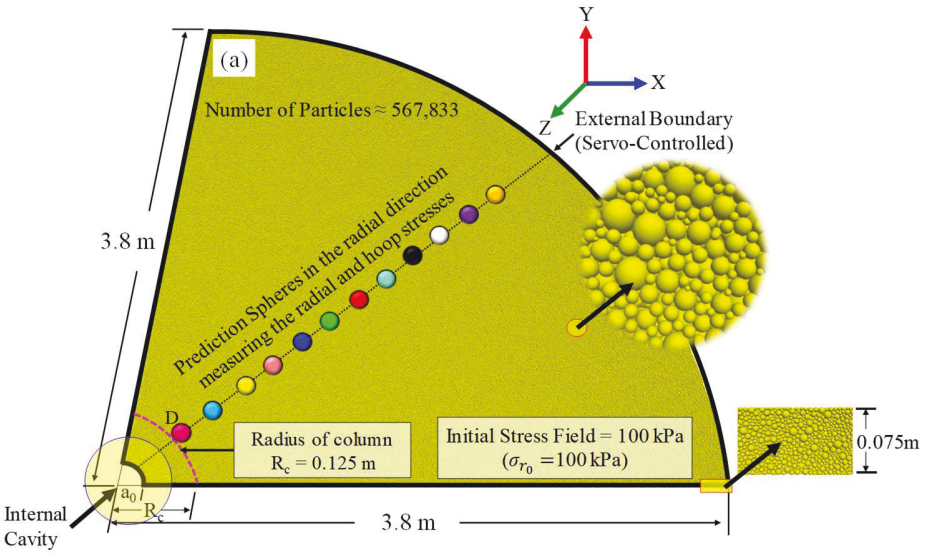

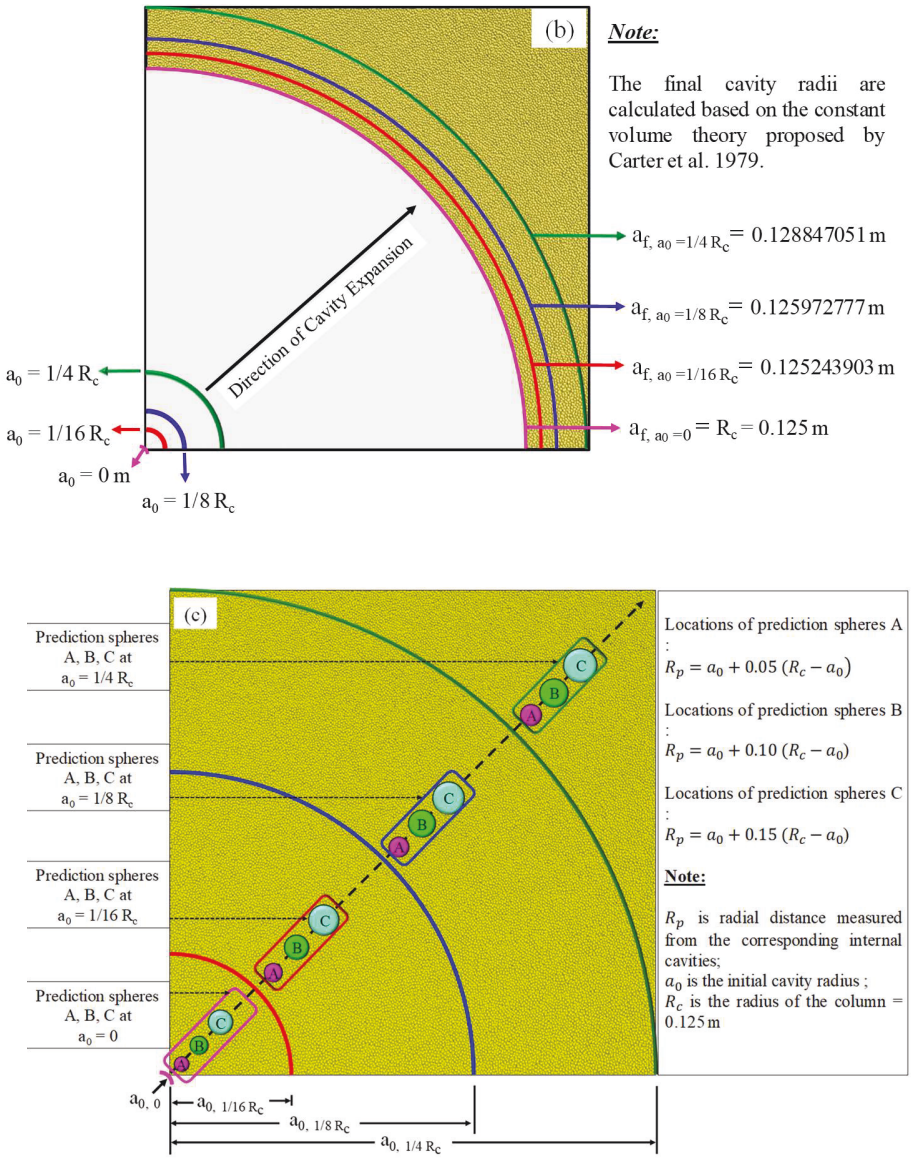


Figure 4.7 (a) Large-scale 3D numerical model simulating cavity expansion, (b) illustration of different final cavity radii calculated based on constant volume and (c) the arrangement of prediction spheres at internal cavities with different initial radii

To eliminate the boundary effect that may influence predictions near the internal cavity, the size of the model must be sufficiently large. Bolton et al. (1999) carried out

comprehensive centrifuge experiments on cone penetration tests in sand and recommended that a minimum container-to-cone diameter ratio of 20 must be satisfied to reduce the boundary effect to an insignificant level. According to the calculated final cavity radii presented Figure 4.7(b), the largest final cavity was chosen (i.e. $a_{f,a_0=1/4\,R_c} =$ 0.1288 m) to estimate the radius of the numerical model that would eliminate the boundary effect. Hence, an outer radius of 3.8 m was adopted for the model so that the ratio between the size of the model and the final cavity radius is 29.5, which is larger than the minimum ratio recommended by Bolton et al. (1999).

Having an increase in the radius of the model, the thickness was reduced accordingly to control the number of particles involved to a reasonable value without compromising the simulation efficiency. However, the thickness of the model must be carefully determined to eliminate the boundary effect. According to Lackenby et al. (2007) and Marschi et al. (1972), as the ratio of specimen to maximum particle size approaches 6 in triaxial test, equipment size effects can be ignored. In addition, Geng (2010) has adopted a three dimensional discrete element model to investigate the effect of the model thickness on the cavity pressure variations during cavity expansion in plane strain condition. There were three numerical simulations carried out, with the ratio between the model thickness and maximum particle size ranging from 5 to 20. It was pointed out that the thickness of the sample has no effects if there is sufficient number of particles in the model. It was suggested that the suitable thickness of the sample can be determined based on the sample geometry and the number of particles that can be simulated base on the current

computational power. Adopting the technique suggested by Geng (2010), the thickness of the model in this study was determined to be 0.075 m, ensuring a minimum ratio of 6 between the model thickness and the maximum particle size. Besides the determination of an appropriate model thickness, the number of particles in contact with the cavity wall at the initial stage must be deliberately evaluated, since the simulations proposed in this study contain the creation of the cavity. This size effect has been studied by many researchers using 3D models. For instance, Phillips et al. (1987) and Bolton et al. (1999) suggested that the minimum ratio between the penetrometer radius and the median particle size is 10. Jiang et al. (2006) adopted this ratio in modelling of deep penetration in granular soils and observed that there are about 13 particles always in contact with the cone tip. Arroyo et al. (2011) conducted a numerical simulation of cone penetration test in a virtual calibration chamber adopting PFC$^{3D}$, and the ratio between the cone diameter and the median particle size was approximately 2.7. Zhang et al. (2019) studied the standard penetration test in a virtual calibration chamber adopting a rod to particle (i.e. $d_{50}$) ratio of 3.06. Beside those studies carried out by others, the authors had previously conducted a sensitivity analysis investigating the size effect on the soil response during cylindrical cavity expansion. According to Dong et al. (2018), the minimum ratio of 8 between the final cavity radius and the median particle size is a prerequisite to obtain reliable results for cavity pressure measurement. Given a ratio of 8, it was observed that there are at least 20 particles in contact with the internal cavity wall. Therefore, the thickness of the model adopted in this study (i.e. 0.075 m) allows more than 25 particles in contact with the internal cavity wall as the cavity is being created (i.e. cavity expansion

with a zero initial radius). It must be clarified that this minimum number (i.e. 25 particle) is only at the cavity creation stage for the case with a zero initial radius. The number of particles contacting with the internal cavity for other cases are significantly larger than 25, and this number continuously increases as the cavity is expanded further. In addition, an initial radial stress of 100 kPa (i.e. $\sigma_{r_0}$ = 100 kPa) was adopted, and the wall servo mechanism was enabled to ensure that the stress acting on the external boundary remains equal to the initial radial stress at all time during the cavity expansion process.

To study the effects of initial cavity radius on the soil response, four discrete element models with different choice of initial radii were proposed for both dense and loose specimens. Referring to Figure 4.7 (b), the initial radii adopted include $a_0 = 0$ (simulating the installation of a column / the creation of a cylindrical cavity from a zero initial radius), $a_0 = 1/16\, R_c$, $a_0 = 1/8\, R_c$, and $a_0 = 1/4\, R_c$ (representing expansions from existing initial cavities), where $R_c$ represents the radius of the column to be installed, is also the final cavity radius ($a_f$) of the case with $a_0 = 0$ (i.e. $a_{f,a_0=0} = R_c = 0.125\, m$, as illustrated in Figure 4.7 (b). With the different choice of initial radii, the corresponding final cavity radii were calculated based on the constant volume proposed by Carter et al. (1979b). In the constant volume theory, Carter et al. (1979b) gave an adequate approximation of modelling the pile installation (i.e. from 0 to $R_c = \sqrt{3}a_0$ ) to an expansion of an existing cavity (i.e. from $a_0 > 0$ to $2a_0$) by assuming the deformation occurring at constant volume (i.e. $V_{(0-\sqrt{3}a_0)} = V_{(a_0-2a_0)}$; $V$ being the volume of the expansion). The schematic illustration of cavity expansion scenarios with different choice

of initial cavity radii and their corresponding final radii calculated based on constant volume theory are shown in Figure 4.7 (b).

To reduce the computational effort of the simulations, the particle-upscaling technique was applied to reduce the number of particles involved. Dong et al. (2018) investigated the effects of particle scaling when simulating cavity expansion and found it was important to determine the most appropriate particle-upscaling factor to avoid impulsive oscillation and inaccurate numerical prediction. The studies suggested that the ratio between the final cavity radius ($a_f$) and the median particle size ($d_{50}$) must be larger than 8, and a minimum ratio between the size of the prediction sphere ($D_m$) and the median particle size ($d_{50}$) of 6 is a prerequisite to obtain reliable results. Considering these criteria, the particle-upscaling factor adopted in this study was selected to be 50, which resulted in approximately 570,000 and 510,000 particles for the dense and loose specimens, respectively.

Samples were generated using the radius expansion method, in which the size of the particles were gradually increased until the desired porosity was reached. Dense specimens were prepared by assigning an initial particle friction coefficient of 0.10, whereas the loose samples adopted an initial particle friction coefficient of 0.30, which was the same as the procedure adopted in the calibration exercises. After generating the specimens, the soil close to the internal cavities were then deleted and replaced by cylindrical walls with various radii to represent the initial cavities with non-zero radii, as revealed in Figure 4.7 (b). Prediction spheres were also created to continuously monitor

the porosity of the soil specimen and to ensure a uniform distribution of initial porosity when the initial condition has been established.

After the initial conditions were established, all the dense specimens had a porosity of 0.384 and a coordination number of 5, whereas the porosity and coordination number of loose sandy soils were 0.455 and 4, respectively. It should be noted that the coordination number, measuring the average number of active contacts, can be used as a guideline to determine the density of the soil (Itasca 2016; Shen et al. 2017). Once the initial condition was satisfied, the cylindrical cavities were expanded from their initial cavity radii to the predetermined final cavity radii based on constant volume theory, as shown Figure 4.7 (b).

To ensure an accurate measurement of the stress and strain during the cavity expansion, the cavities must be expanded in a strain-controlled condition at an appropriate constant strain rate to ensure quasi-static loading condition until the final cavity radius was reached. Quasi static condition refers to a sufficiently slow loading rate so that the specimen remains in quasi static equilibrium during the loading and therefore the inertial effects can be avoided. In discrete element modelling, it is the combination of the loading rate and the time step controlling the loading type (Zhang et al. 2014). For instance, in a triaxial test, an axial loading rate of 1 mm/s and a time step of $10^{-6}$ s for each calculation cycle is equivalent to $1 \times 10^{-6}$ mm/step. This implies that $10^{6}$ calculation steps are required for each millimetre movement of the loading platen. In discrete element modelling, an automatically calculated time step is often adopted by many researchers, and therefore

the loading rate becomes the only parameter to control to ensure the quasi static loading condition. For instance, Potyondy et al. (2004) adopted a loading rate of 0.05 m/s for uniaxial and biaxial test simulations. Arroyo et al. (2011) modelled a cone penetration test with a 0.1 m/s penetration rate, and 0.4 m/s penetration rate was adopted by Zhang et al. (2019) to simulate the standard penetration test. Based on these studies carried out, a constant strain rate of 0.001 m/s with an automatic time step determination mode was adopted for this study. Moreover, referring to Itasca (2016), a constant load reading after stopping the platens in a simulation could be an evident sign of quasi static equilibrium. Hence, a preliminary simulation was carried out prior to the actual simulation to ensure that the 0.001 m/s is sufficiently slow for a quasi-static analysis.

The cavity pressure was then measured using predefined subroutines that can constantly measure the contact forces acting on the internal cavity, divided by the corresponding contact area. In addition, prediction spheres were added into the model to measure the stress and strain variations in the vicinity of the internal cavities, as shown in Figure 4.7 (c). Hence, the prediction spheres were categorised into three groups, namely A, B and C, at various distances measured from their corresponding internal cavities. For instance, the locations of prediction spheres A was expressed as $R_p = a_0 + 0.05(R_c - a_0)$, with $R_p$ being the radial distances measured from the corresponding initial cavities. Since the initial cavity radii (i.e. $a_0$) adopted in this study were different, the radial distances (i.e. $R_p$) measured from the corresponding internal cavities were indisputably different for each prediction sphere A. However, the progress of the cavity expansion ($P\ \% = \frac{R_p - a_0}{R_c - a_0}$)

for those initial cavities to reach the corresponding prediction spheres were the same (e.g. 5% for prediction spheres A). It is noteworthy to mention that the motivation of adopting the same cavity expansion progress (i.e. the same $P\%$) rather than the same radial distance (i.e. the same $R_p$) as the controlled variable is to reduce the errors induced by the size effect between the internal cavities and their corresponding prediction spheres. Prediction spheres B and C followed the same principle while being located farther away from the internal cavities, (e.g. $P\%$ equal to 10% for prediction spheres B and 15% for prediction spheres C), as illustrated in Figure 4.7 (c).

Moreover, since there were four different initial cavity radii, the size of the prediction spheres were altered so that the ratio between the initial cavity radius and the radius of the prediction sphere remains constant, as suggested by Dong et al. (2018). As well as having these prediction spheres situated in the vicinity of the internal cavities, there were also prediction spheres created in radial direction along the angular bisector to investigate the distribution of radial stresses and hoop stresses with the radial distance, as illustrated in Figure 4.7 (a). These variations in stress and strain and changes in the void ratio and coordination number were continuously recorded using those prediction spheres. Furthermore, 20 gauge particles were selected along the angular bisector, as shown in Figure 4.7. The displacement and positions of these gauge particles were continuously monitored during cavity expansion to investigate the influence zone induced by the expansion of each cylindrical cavity.

## 4.6 Results and Discussion

### 4.6.1 Cavity Pressure Variations and Validation Exercise

Variations of cavity pressure for cavity expansions starting from different initial radii for loose and dense specimens during cavity expansion process were plotted against the cavity radius, as shown in Figure 4.8.

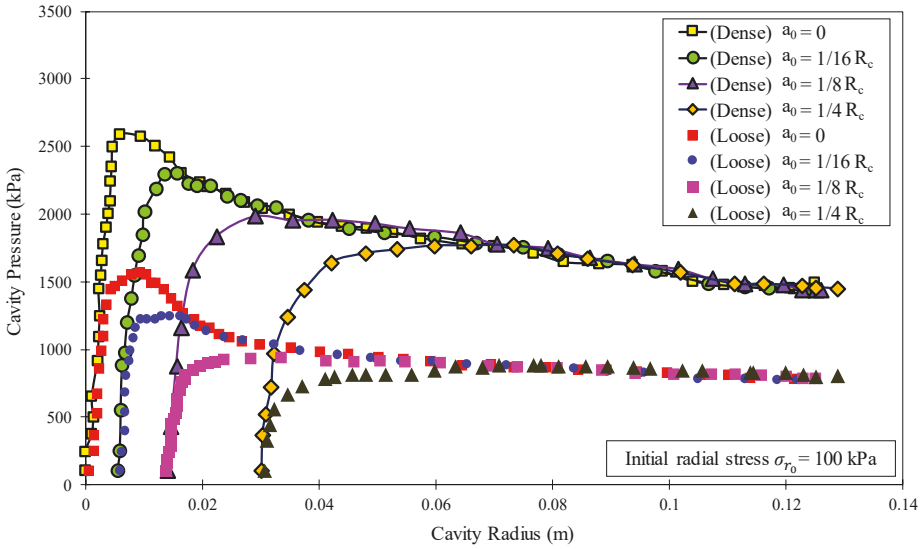


Figure 4.8 Cavity pressure variations during cavity expansion process

It is observed that the cavity pressure variations, predicted for dense sandy soils, as expected, are significantly large compared to that in loose specimens for all four different choices of the initial radii. It should be noted that for all dense specimens, the strain-softening behaviour was captured, and such phenomena became more pronounced as the initial cavity radius decreased. For instance, the cavity pressure measured during cavity

expansion at a zero initial radius reached its peak (i.e. 2600 kPa) rapidly followed by a continuous descending when the cavity expanded further, reaching a limiting pressure of 1500 kPa at the end of the expansion process (a reduction of 1100 kPa due to softening). However, referring to Figure 4.8 ,a reduction of 250 kPa was observed in the corresponding internal cavity pressure, when an initial cavity radius, equal to a quarter of the column to be installed (i.e. $a_0$ = 1/4 $R_c$), was adopted.

Figure 4.8 also shows that in loose specimens, and particularly for cavity expansions with relatively large initial radii (i.e. $a_0$ = 1/4 $R_c$ and $a_0$ = 1/8 $R_C$), the cavity pressures gradually increase to the limiting pressure with continuous strain hardening. However, strain softening behaviour is captured when the cavity is created (i.e. $a_0$ = 0) or expanded from an infinitesimal size (i.e. $a_0$ = 1/16 $R_c$). This may be attributed to the plane strain condition applied in the vertical direction, which restrained the soil from moving, and due to this confinement, an expanding cavity could easily densify the surrounding soil and lead to an increase in the cavity pressure. In cases with a larger initial radius (i.e. $a_0$ = 1/4 $R_c$ and $a_0$ = 1/8 $R_c$), the increase in cavity pressure could dissipate over a larger contacting area, and therefore, the strain softening response was not pronounced. Moreover, Cudmani et al. (2001) asserted that the size of the calibration chamber (i.e. outer boundary ) can exert certain effects on the pressure-expansion curve in the studies evaluating the state of cohesionless soil, particularly in cone penetration and pressuremeter tests. Referring to results reported in their study, the cavity pressure showed a descending branch after reaching the maximum in loose sand, and Cudmani et

al. (2001) ascribed the decrease in cavity pressure to the finite outer radius. Therefore, similar to the above study, the strain softening behaviour captured in the current study, to some extent, may be attributed to the size effect.

Referring to the results depicted in Figure 4.8, it can be concluded that the cavity pressure needed to create a cavity or expand an existing cavity with an infinitesimal radius would be larger compared to expanding an existing cavity with a larger initial radius, regardless of the relative density of the soil medium. However, the ultimate pressure required to maintain the continuous expansion of cavities already expanded would be independent of the initial cavity radius.

To evaluate the reliability of the predicted cavity pressure from the numerical simulation, the method proposed by Carter (1978) was adopted, in which it was assumed that soil behaves elastically until the onset of yielding, determined by the Mohr-Coulomb yield criterion, followed by perfectly plastic behaviour (isotropic elastic –perfectly plastic material model).

The material properties that define the pressure expansion curve and stress distributions include the shear modulus ($G$), Poisson's ratio ($\vartheta$), cohesion ($c$), the friction angle ($\emptyset$), and the dilation angle ($\psi$). For this comparison, the upper and lower bound analytical predictions were presented. The upper bound was determined utilising the peak friction and dilation angles while the lower bound was determined adopting the critical friction angle, with the corresponding values obtained from Green et al. (1975). However, in the cavity expansion, the mean effective stress, as illustrated in Figures 10 and 11,

continuously increase, which inevitably induced an increase in the shear modulus ($G$) of the soil (Janbu 1963; Duncan et al. 1980; Puebla et al. 1997). Hence, the effect of the increase in the shear modulus was considered in the derivation of the pressure-expansion curve. According to Puebla et al. (1997), the variation of $G$ with the mean effective stress $p'$ can be represented by the following equation:

$$G = K_G^e p_a (\frac{p'}{p_{ref}})^{ne} \quad (4\text{-}4)$$

where, $K_G^e$ and $ne$ are the elastic shear modulus number and modulus exponent, respectively. In fact $ne$ can be taken as 0.5 for clean sand (Hardin et al. 1972; Yu et al. 1984; Byrne et al. 1987), and $p_{ref}$ is the atmospheric pressure equal to 100 kPa.

Hardin (1978) pointed out that the elastic shear modulus exponent $K_G^e$ is a function of the void ratio ($e$), and it can be estimated from the following equation:

$$K_G^e = A_p \cdot F(e) \quad (4\text{-}5)$$

where, $A_p$ is a particle size and shape variable and $F(e)$ is a void ratio function.

Yu et al. (1984) suggested that $A_p$ could be taken as 700 for clean rounded sand, and $F(e)$ can be estimated using the equation below:

$$F(e) = (2.17 - e)^2/(1 + e) \quad (4\text{-}6)$$

It must be highlighted that the Ham River sand adopted in Bishop et al. (1965) and Green et al. (1975) was categorised as clean rounded sand, and therefore $A$ could reasonably be

taken as 700. In addition, knowing the void ratio of both the dense and loose sand specimens adopted in this study (reported in Figures 5 and 6), the elastic shear modulus exponent $K_G^e$ was calculated to be 1018 and 659 for dense and loose sands, respectively. It is noteworthy to state that these material parameters agree well with the elastic shear modulus suggested by Duncan et al. (1980) for Ham River sand, and are within the range of the elastic shear modulus recommended by Byrne et al. (1987).

To estimate the change in shear modulus during cavity expansion, the range of the mean effective stress $p'$ during the entire cavity expansion process was determined adopting the prediction sphere D, as indicated in Figure 4.7 (a), which is positioned at a radial distance $(r)$ where $r = R_c = 0.125$ m. The mean effective stress obtained for the loose and dense sand specimens at the end of cavity expansion process was 650 kPa and 1.2 MPa, respectively. Therefore, the effective shear modulus was calculated based on the previously mentioned equation (i.e. Equation 4-4) to be 168 MPa and 353 MPa, respectively. Hence, the lower bound and upper bound of the cavity pressure using the method proposed by Carter (1978) were determined, as shown in Figure 4.9 where the DEM predictions lie in between the lower and upper bounds determined by Carter (1978), thus confirming the validity of the DEM predictions.

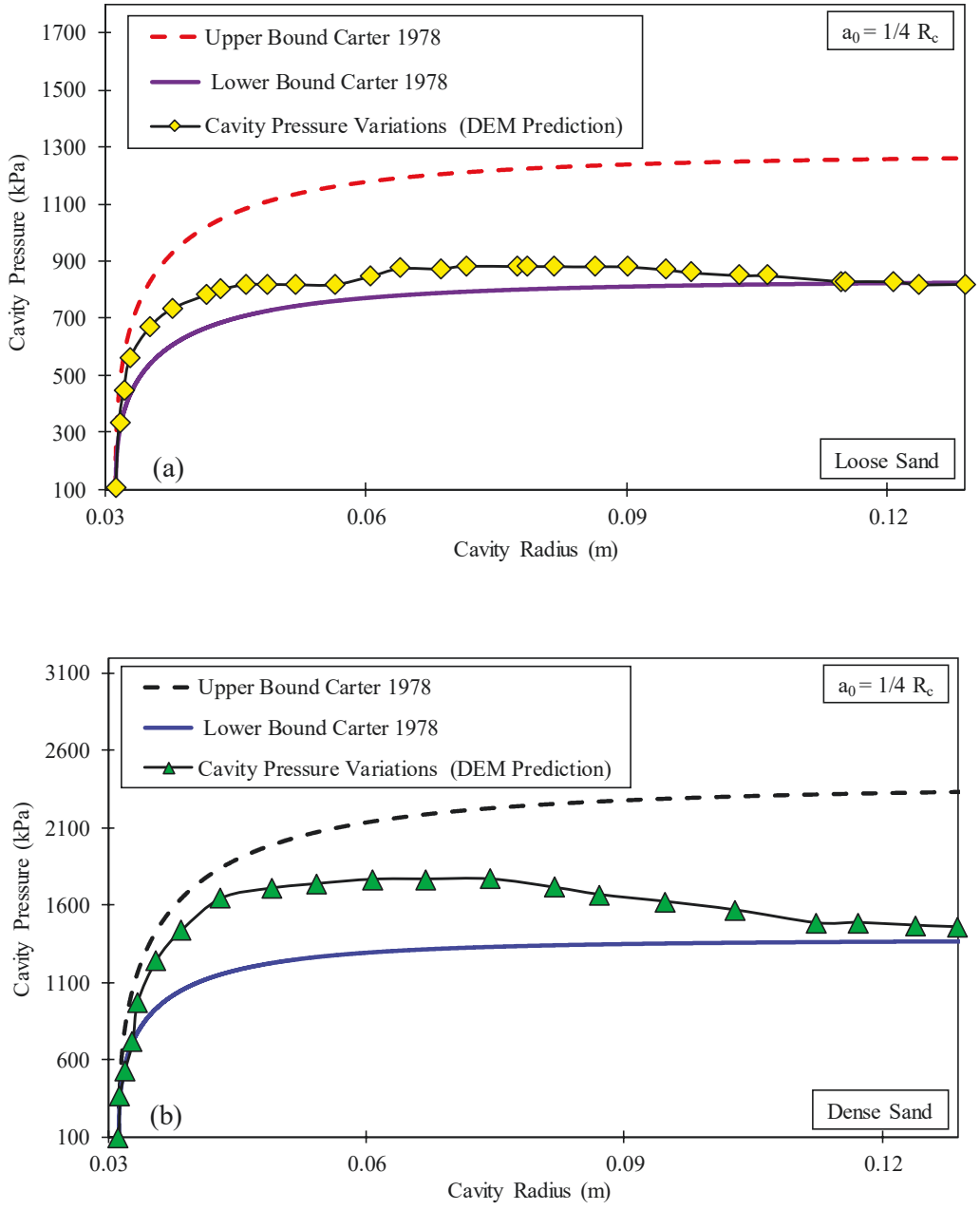


Figure 4.9 Comparisons between the DEM predictions and Carter's method for cavity expansions with initial radii $a_0$ =1/4 $R_c$ in (a) loose sand and (b) dense sand

### 4.6.2 Stress Path at the Proximity of the Internal Cavity Wall

To further assess the validity of the cavity pressure variations reported in the previous section, the stress path was plotted adopting the prediction spheres A, B, and C situated in the vicinity of the internal cavity walls, as illustrated in Figure 4.7 (c).

There were more than 100 prediction spheres introduced into the model to have a comprehensive measurement on the stress variations, and therefore the mean and the deviatoric stresses of prediction spheres were computed by programming FISH subroutines. Due to the large number of data points and conditions, a selection of results is elaborated, as depicted in Figures 10 and 11, for specimens of dense and loose sand, respectively. The stress path was plotted in the $p' - q$ plane and all the stresses were normalised against the initial mean effective stress. The critical state line in the $p - q$ plane can be determined adopting the following equations (Atkinson et al. 1977; Budhu 2008).

$$q = Mp' \tag{4-7}$$

where,

$$M = \frac{6\,sin\emptyset'_{cv}}{3-sin\emptyset'_{cv}} \tag{4-8}$$

where, $\emptyset'_{cv}$ is the critical state friction angle.

The constant volume friction angle is a material constant and according to Negussey et al. (1988) and Bolton (1986), the postulate that the constant volume friction angle of a granular material is unique and a function of mineral composition was verified experimentally. Hence, considering the stress-dilatancy relationship for the static equilibrium of an assembly of particles in contact, as presented by Rowe (1962) and referring to Schanz et al. (1996), the following equation was adopted to calculate the critical state friction angle (i.e. $\emptyset'_{cv}$).

$$sin\emptyset'_{cv} = \frac{sin\emptyset_f - sin\psi_f}{1 - sin\emptyset_f sin\psi_f} \tag{4-9}$$

where, $\emptyset_f$ and $\psi_f$ are the ultimate values of the friction and dilation angles.

Therefore, an approach proposed by Bolton (1986) has been used for calculating the maximum dilation angle for the plane strain condition applicable in this study adopting the following equation.

$$\sin\psi_f = \left(-\frac{d\varepsilon_v}{d\gamma_{13}}\right)_P = -\frac{(d\varepsilon_1/d\varepsilon_3)_{max}+1}{(d\varepsilon_1/d\varepsilon_3)_{max}-1} = \frac{-(d\varepsilon_v/d\varepsilon_1)_f}{2-(d\varepsilon_v/d\varepsilon_1)_f} \tag{4-10}$$

The ultimate friction angle of the dense sand used in Green et al. (1975) was 43.6 degrees, and by referring to Bolton (1986), the corresponding ultimate dilation angle was determined to be 14.4 degrees. Hence, from Equation (4-9), the critical state friction angle $\emptyset'_{cv}$ was estimated to be 32 degrees, and therefore the $M$ (i.e. the slope of the critical state line in Equation (4-8)) was calculated to be approximately 1.28.

In addition to the above calculation method adopting the ultimate friction and dilation angles in Equation (4-9), the mobilised friction angle at constant volume (i.e. $\emptyset'_{cv}$) may be computed directly using the predicted principle stresses (i.e. axial stress and lateral confining pressure) at critical state (i.e. in a large strain). Hence, the prediction of the stress - strain curves from the numerical simulation for both loose and dense specimens for axial strains up to 35% are plotted in Figure 4.12.

As illustrated in Figure 4.12, the axial stresses of both loose and dense sands approached the same value after 32% axial strain, confirming the critical state is reached. Hence, Equation (4-11), from the well-known stress dilatancy theory by Rowe (1962), as explained by Schanz et al. (1996) was adopted to calculate the critical state friction angle $\emptyset'_{cv}$.

$$\frac{(\sigma'_3)_{\mathrm{cv}}}{(\sigma'_1)_{\mathrm{cv}}} = \frac{1-\sin\emptyset'_{\mathrm{cv}}}{1+\sin\emptyset'_{\mathrm{cv}}} \tag{4-11}$$

The calculated $\emptyset'_{cv}$ is approximately 32 degrees, which is in good agreement with the critical state friction angle calculated using Bolton's theory (Bolton 1986). This verification carried out further validates the reliability of the calibrated parameters from the laboratory tests.

Referring to Figure 4.10 and Figure 4.11, it is noted that all the stress paths initially moved in an approximate vertical direction and then moved continuously towards the critical state line.

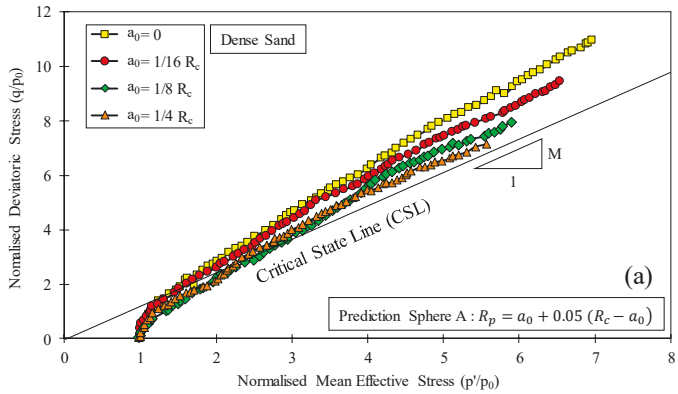


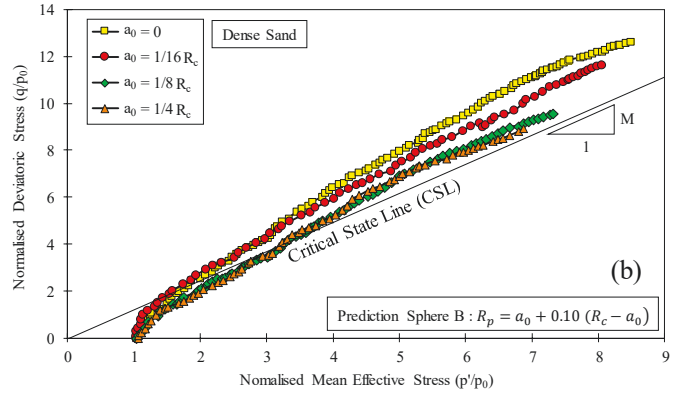


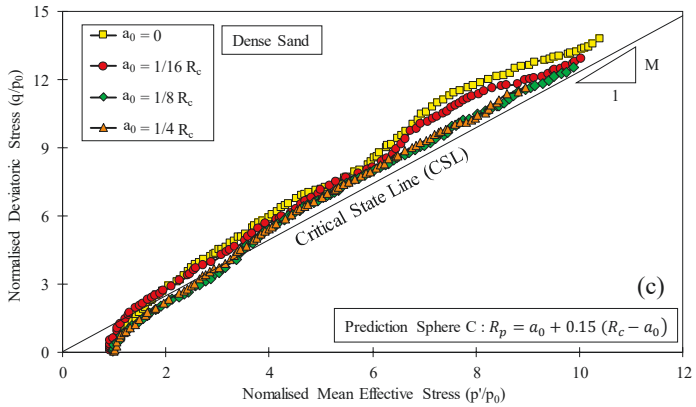


Figure 4.10 Stress path plotted adopting different prediction spheres for cavity expansions with different initial cavity radii in dense sand

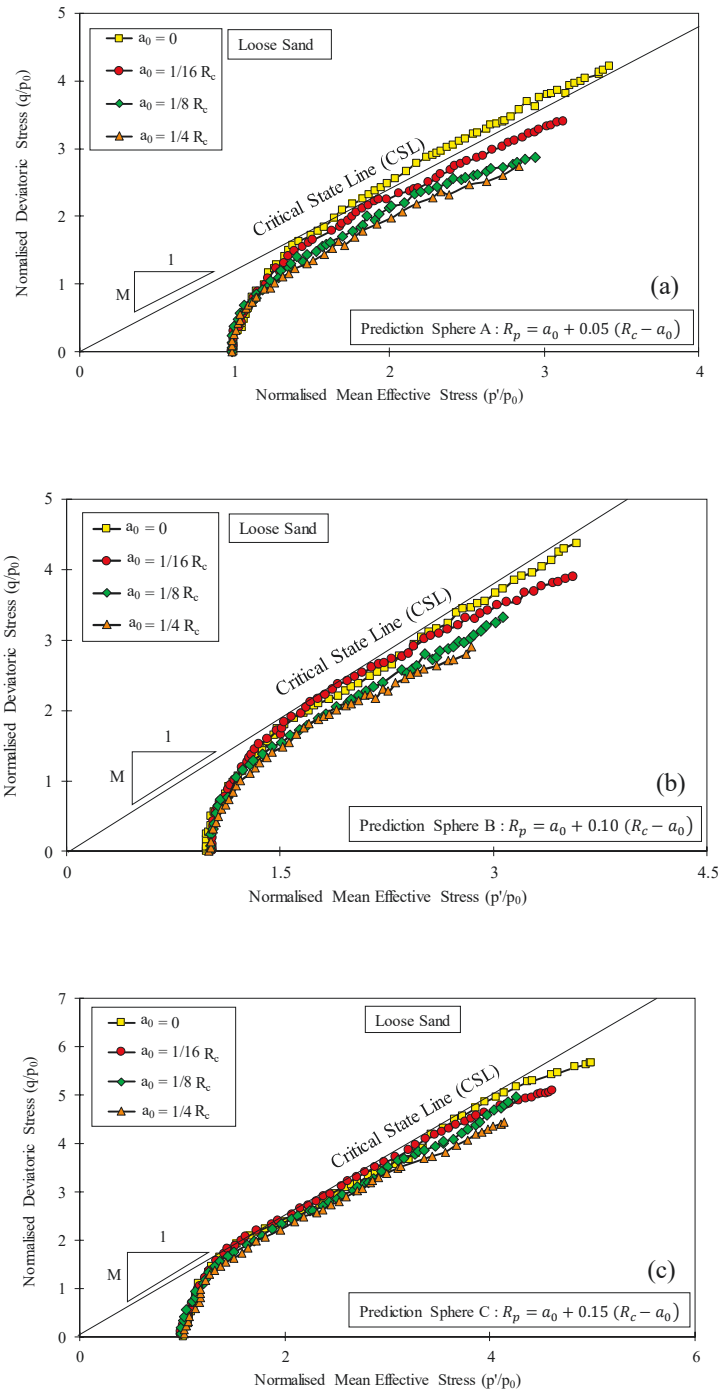


Figure 4.11 Stress path plotted adopting different prediction spheres for cavity expansions with different initial cavity radii in loose sand

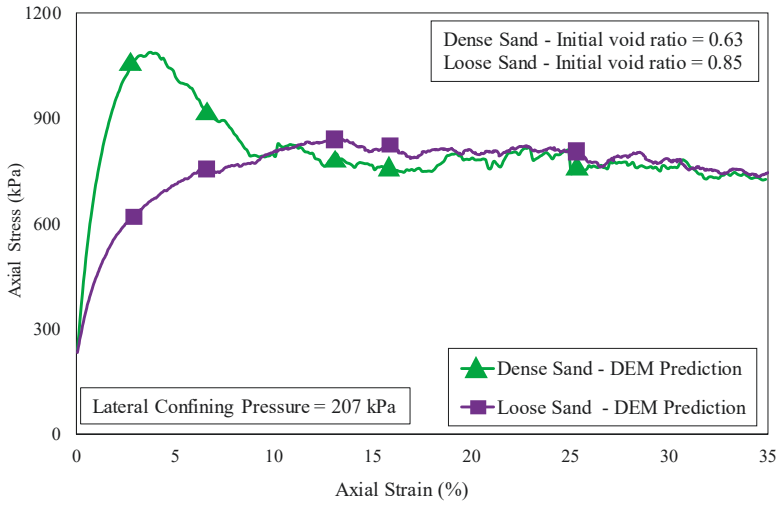


Figure 4.12 Variations of axial stresses for both loose and dense specimens up to 35% axial strains

In the dense specimens (see Figure 4.10), the stress paths, measured adopting prediction spheres A, passed the critical state line, thus confirming the strain softening behaviour which occurred during cavity expansion. With the increase of the radial distance (i.e. moving from prediction spheres A to B to C), the stress paths showed a tendency of approaching the critical state line. Therefore, it can be projected that the critical state can be reached if the cavities are expanded further. In addition, stress paths, plotted for loose sand in Figure 4.11, were positioned below the critical state line, except the cavity expansion with zero initial cavity radius measured by prediction sphere A. This may be explained by the volumetric strain measured by the same prediction sphere during the cavity expansion from zero initial radius, as depicted in Figure 4.14 (a). As can be seen in this Figure, the volumetric strains during the cavity expansion from zero initial radius showed a decrease at the initial stage of the cavity expansion, whereas dilation was

observed when the cavity expanded further contributing to a volume expansion. Similar observations were reported by Silvestri (2001) and Manassero (1989) when interpreting the pressuremeter tests in sand. Li et al. (2017) also presented similar findings when studying the drained cavity expansion in sand.

Furthermore, it is worthwhile to mention that the stress paths, especially measured by prediction spheres A (see Figure 4.10(a) and Figure 4.11(a)) were significantly impacted by the choice of initial cavity radius. Given the same percentage of expansion in both dense and loose sands, the initial cavity radius of zero (i.e. $a_0 = 0$) results in the largest mean effective and deviatoric stresses, whereas cavity expansion starting from a quarter of the column radius (i.e. $a_0 = 1/4\,R_c$) leads to the lowest stresses. The above observations regarding the stress inside the soil comply well with the cavity pressure variations predicted directly via measured forces applied onto the internal cavity wall, as shown in Figure 4.8. This confirms that using prediction spheres to obtain the internal soil stresses in the numerical model adopted in this study is reliable.

### 4.6.3 Volumetric Response of Soil during Cavity Expansion

The variations of volumetric strain with respect to the shear strain during cavity expansion were plotted for simulations adopting different initial cavity radii for dense sand. The average volumetric strain was calculated based on the strain variations of three prediction spheres (i.e. prediction spheres A, B, and C, as shown in Figure 4.7. It is observed that all the volumetric strains reveal an overall dilative behaviour for dense sand.

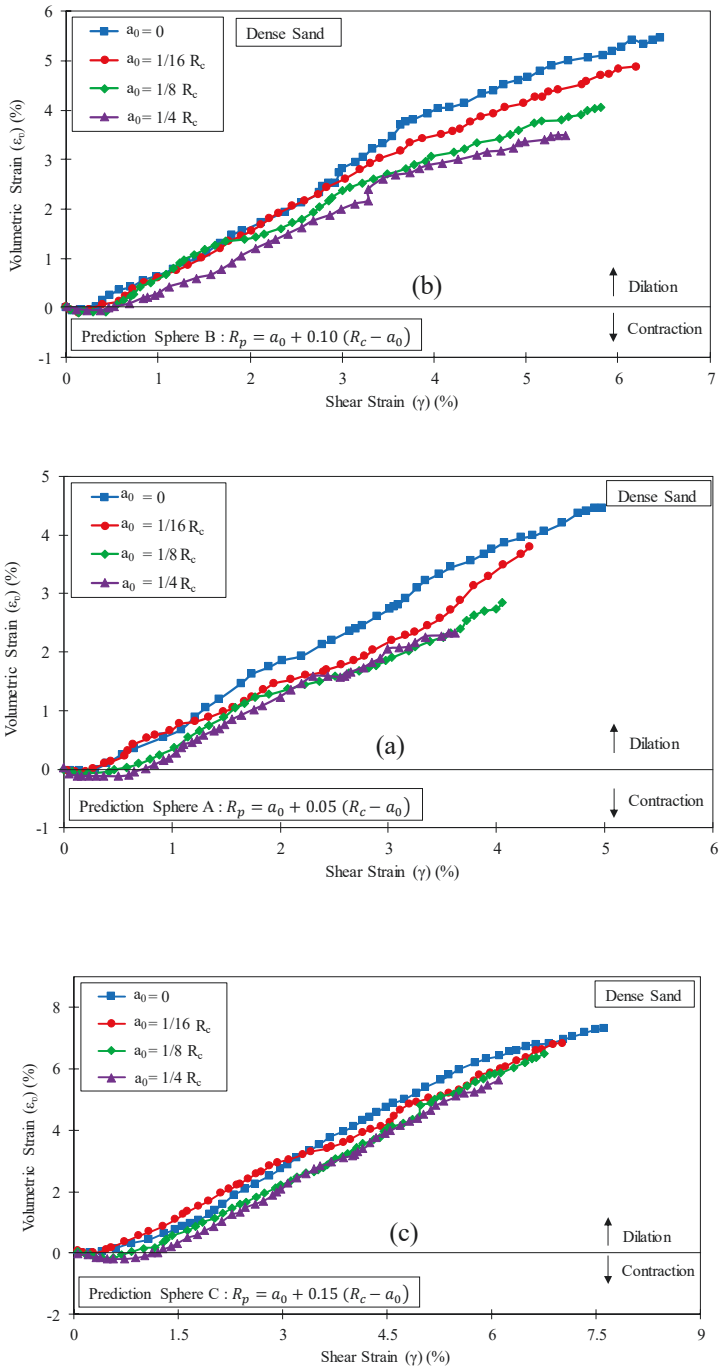


Figure 4.13 Variations of volumetric strain with shear strain during cavity expansions with different initial cavity radii in dense sand

As can be seen in Figure 4.13, the volumetric strain variations reported for the cavity expansions with relatively small initial radii (i.e. $a_0$ = 0 and $a_0$ = 1/16 $R_c$) depicted a continuous and prompt dilation as soon as the expansion initiated. However, for those cavities starting from larger initial sizes (i.e. $a_0$ = 1/8 $R_c$ and $a_0$ = 1/4 $R_c$), a slight contraction at the beginning of expansion was observed followed by dilation when the cavities expanded further. Hence, the magnitude of the soil dilatancy (i.e. the change in volume of the soil when the soil is distorted by shearing) when the cavity expansion started from relatively smaller initial radius (i.e. $a_0 = 0$ and $a_0 = 1/16\,R_c$), in general, was larger than corresponding values observed in the cases with larger initial radius (i.e. $a_0 = 1/8\,R_c$ and $a_0 = 1/4\,R_c$). This finding here confirms that the choice of initial cavity radius can impact the soil volumetric strains particularly close to the cavity wall. In addition, as observed in Figure 4.13, given the same progress (i.e. $P$ %) during the cavity expansion, the case with the initial cavity radius of zero resulted in both the largest shear strains and volumetric strains among all four expansion scenarios. For instance, when the cavity expansion progressed only 5%, the case with the initial cavity radius of zero experienced a shear strain of 5% and a volumetric strain of 4.5% were experienced at the prediction spheres A, while the corresponding strain values for the case with an initial radius of a quarter of the column, were 3.8% and 2.3%, respectively. Furthermore, referring to Figure 4.13, it can be concluded that the differences between the predicted volumetric strains in the soil during cavity expansion for various initial cavity radius scenarios gradually reduced as the observation points were positioned further away from the cavity wall.

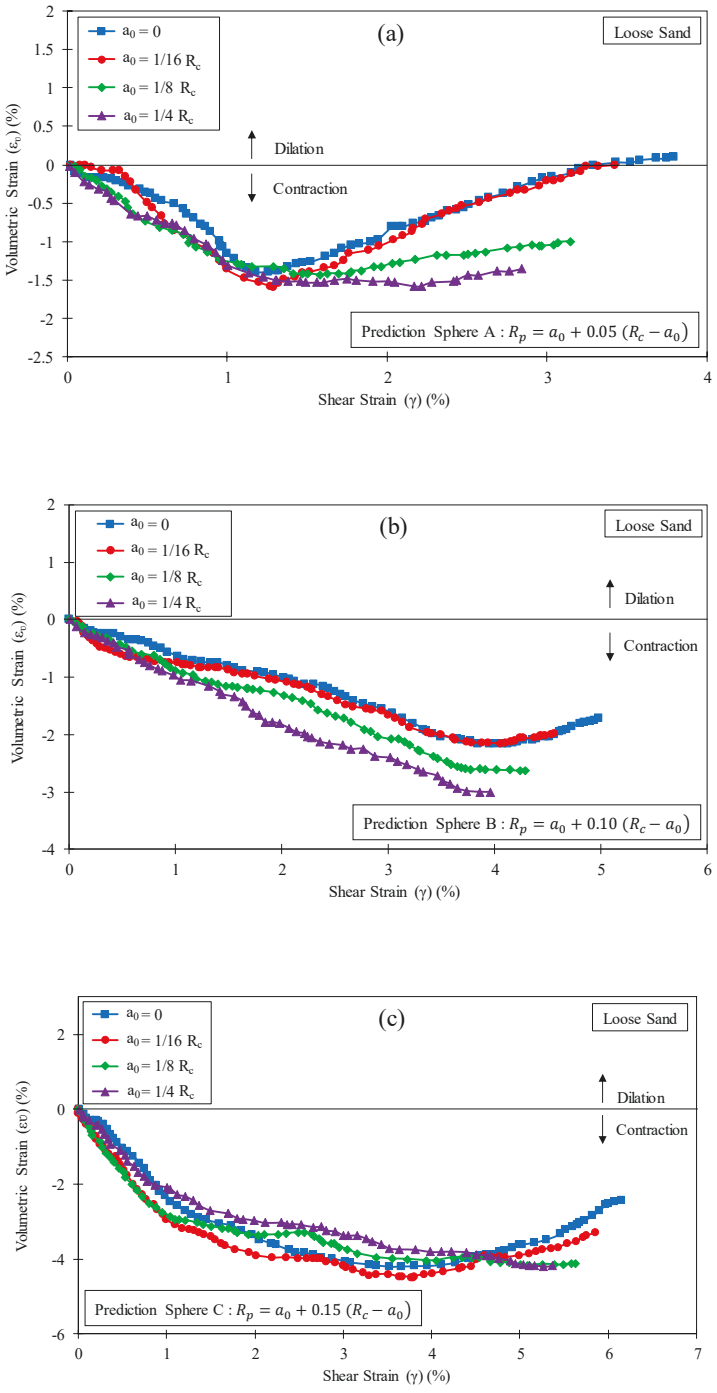


Figure 4.14 Variations of volumetric strain with shear strain during cavity expansions with different initial cavity radii in loose sand

Similar to the dense specimen, the variations of the volumetric strain for loose sand are plotted in Figure 4.14 for the cavity expansions with different choices of the initial cavity radii. Figure 4.14 (b) and (c) show that the volumetric strains measured by prediction spheres B and C reveal an overall contractive response. However, it is of interest to note that the volumetric strains plotted based on the prediction spheres A, depicted varying degrees of dilative response after the initial contraction in the earlier stages of the cavity expansion process, as illustrated in Figure 4.14 (a). As demonstrated in Figure 4.14 (a), the predicted volumetric strains for the zero initial radius case showed a continuous dilation for shear strains beyond 1.2%, while such dilative behaviour became less pronounced in other cases with their initial cavity radii larger than zero, as shown in Figure 4.13 (a). In addition, the strain-softening phenomenon, noticed in the cavity pressure variations in loose sand and plotted in Figure 4.8, is well correlated to the volumetric strain variations i.e. Figure 4.14 (a) during the cavity expansion process. Indeed, it can be noticed that the loose specimen could exhibit some level of dilation near the internal cavity when the plane strain condition is applied.

### 4.6.4 Deviatoric Stress Variations during Cavity Expansion

Figure 4.15 and Figure 4.16describe the variations of deviatoric stress with shear strain during cavity expansion in dense and loose specimens, respectively.

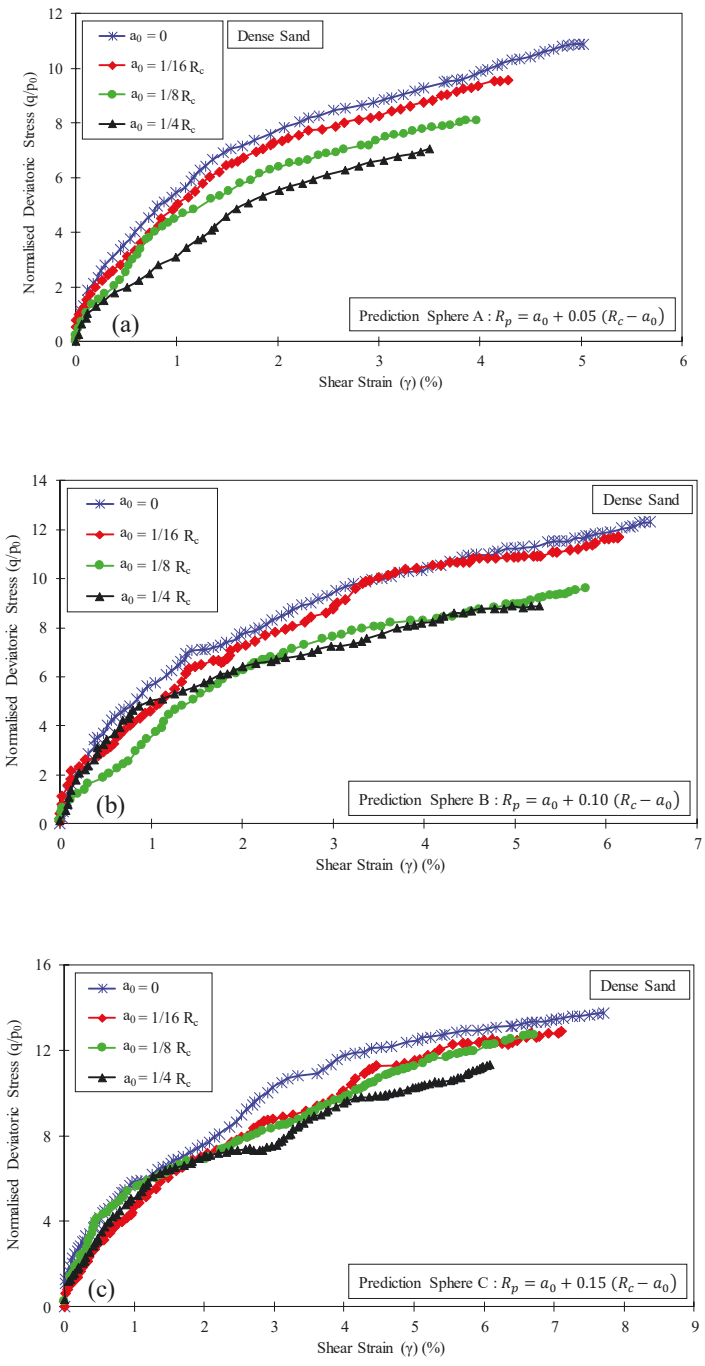


Figure 4.15 Variations of normalised deviatoric stress with shear strain during cavity expansions with different initial cavity radii in dense sand

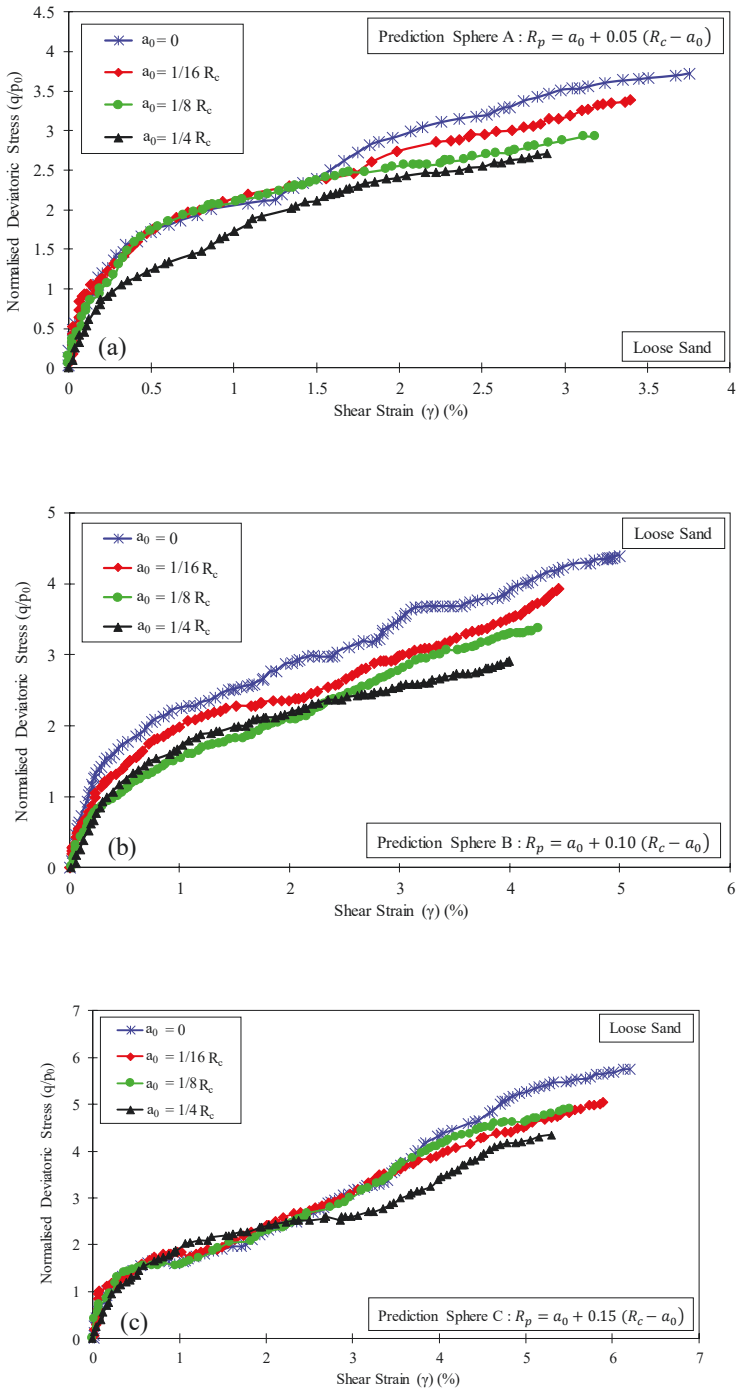


Figure 4.16 Variations of normalised deviatoric stress with shear strain during cavity expansions with different initial cavity radii in loose sand

As expected, during the cavity expansion, the induced deviatoric stresses for a given shear strain in loose sands were significantly less than that in dense specimens, and it could be noticed that the deviatoric stresses increased continuously yet in a reducing rate. Comparing Figure 4.15 and Figure 4.16, it is observed that in both dense and loose soils, cavities expanded from smaller initial radii experienced larger deviatoric stresses and shear strains, given the same progress of expansion.

In addition, it is of interest to note that no obvious peak in the deviatoric stress versus shear strain was observed despite the fact that the maximum dilation rate was clearly captured in the volumetric strain variations, as shown in Figure 4.13 and Figure 4.14, and similar findings have been reported by other researchers. Manassero (1989) has developed a numerical method to obtain complete stress and strain paths during a drained self-boring pressuremeter test in sand in plane strain condition. The proposed method was verified adopting a large number of self-boring pressuremeter tests in a calibration chamber. The results reported include the variations of both volumetric strain and deviatoric stress against the shear strain. It was clearly captured that the deviatoric stress shows a continuous increase in a reducing rate without reaching the peak even if the maximum dilation is captured for the volumetric strain. Silvestri (2001) has also reported similar findings when interpreting the pressuremeter tests in sand, and results obtained were verified using the calibration chamber studies as well as the field tests. In addition, it is of interest to note that the volumetric strain variations of loose sand, reported in both studies, show a certain degree of dilation, which bears a strong resemblance as the

volumetric strain behaviour measured adopting the predication sphere A presented in this study as shown in Figure 4.14.

As indicated by Silvestri (2001), in a pressuremeter test, the shear resistance of the soil around the pressuremeter probe, develops along the vertical failure planes rather than across a succession of horizontal planes. Due to the confinement as a result of plane strain condition, the mean stress continuously increases, and therefore the shear strength (i.e. measured deviatoric stress) also shows a continuous increase during the cavity expansion. In fact, there are well established studies confirming that the peak shear stress has a tendency to disappear when the normal effective stress continuously increases (Budhu 2008). This phenomenon may also be explained by the pull-out test of the geosynthetic reinforcement placed at a certain level within a densely compacted granular fill. According to Alfaro et al. (2005), the application of the pull-out force will lead to the mobilisation of shear at the vicinity of the interface between the geosynthetic reinforcement and the granular material and generates soil dilatancy. However, due to an increase in the confinement/restraining by the surrounding non-dilating soil, the tendency of the dilation at the interface may be suppressed. This in turn induces an increase in normal stress and hence enhance the shear resistance (i.e. continuous increase in deviatoric stress before reaching the peak).

Indeed, the soil tests on dense sand is believed to exhibit strain softening behaviour which fundamentally lead to a stress reduction due to dilation. On the other hand, the increase in the mean stress in the soil during cavity expansion can give rise to the shear strength.

Therefore, it may be reasonable to deduce the fact that the rate of the mean stress increase outweighs the rate of the dilation in this study leading to the absence of the peak or limiting pressure in the deviatoric stress curves, reported in Figure 4.15 and Figure 4.16. However, further numerical and experimental research on various sand types and cavity expansion sizes are recommended to further verify the observation of this study for plane strain cavity expansion.

Furthermore, Figure 4.15 and Figure 4.16 compare the predictions adopting different initial cavity radii. It can be concluded that smaller initial radii lead to higher deviatoric stresses for a given shear strain level. Moreover, predicted stresses became less sensitive to the initial cavity radius as the radial distance of observation point (i.e. $R_p$) increased.

### 4.6.5 Void Ratio Variations during Cavity Expansion

The results reported in the previous section (i.e Figure 4.10 to Figure 4.16) clearly indicate that the initial cavity radius can impact the soil response during cavity expansion, particularly those points near the internal cavity wall (e.g. prediction spheres A). Hence, further investigation into the variations of void ratio with shear strain during cavity expansion was carried out for prediction spheres A, as shown in Figure 4.17.

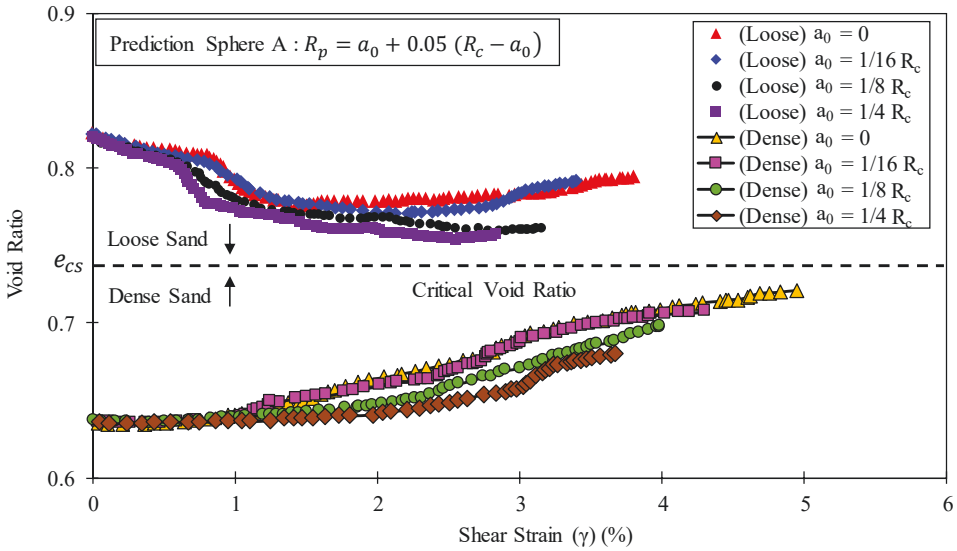


Figure 4.17 Variations of void ratio with shear strain measured at prediction spheres A during cavity expansions in (a) dense sand, and (b) loose sand

Referring to Figure 4.17, the void ratio of the dense sand specimen continuously increased during the cavity expansion process, while the final void ratio when all cavity expansions reached the prediction spheres A was strongly correlated with the initial cavity radius. As observed in Figure 4.17, for a given shear strain in the soil, the cavity expansion with zero initial radius led to the largest increase in void ratio near the cavity wall, whereas the expansion with the largest initial cavity radius (i.e. $a_0 = 1/4\,R_c$) corresponded to the least change in the void ratio. For the loose sand however, the void ratio decreases gradually in the process of cavity expansions when rather large initial radii was adopted (i.e. $a_0$ = 1/8 $R_c$ and $a_0$ = 1/4 $R_c$), whereas slight increases were observed in the cases with smaller initial radii (i.e. $a_0$ = 0 and $a_0$ = 1/16 $R_c$). This complies with the observations regarding the volumetric strain variations reported in Figure 4.14 (a). The

cases with initial larger radii experienced contractive volumetric strains, resulting in an overall void ratio reduction, whilst the scenarios with smaller initial radii sustained slight initial contraction followed by a consecutive dilation, leading to the increase in void ratio.

Furthermore, as observed in Figure 4.17, the void ratios of both loose and dense specimens tend to approach a critical void ratio. The critical state would eventually be reached after significant cavity expansion and soil straining. It should be noted that the critical void ratio in Figure 4.17 was estimated based on the critical state line (CSL) in $\vartheta - \log\ p'$ space reported in Coop (2005) adopting extensive triaxial test results conducted on Ham River sand and for $p' = 1000$ kPa.

### 4.6.6 Soil Radial Displacement and Distribution of Contact Forces

Figure 4.18 shows the radial displacement of soil during cavity expansion in both dense and loose specimens.

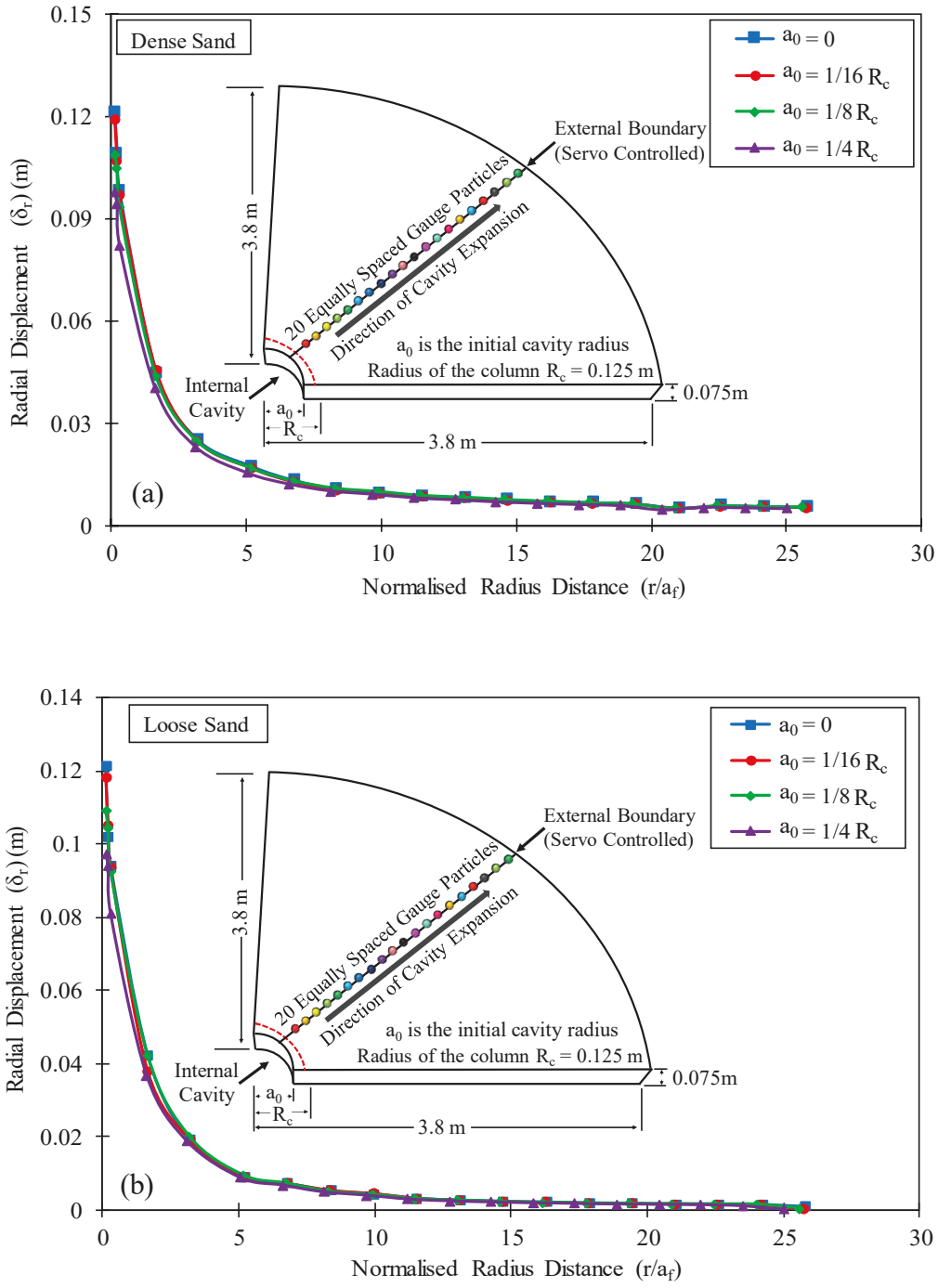


Figure 4.18 Radial displacement of 20 equally spaced gauge particles during the cavity expansion in (a) dense sand, and (b) loose sand

The results were plotted based on the total radial displacement of 20 gauge particles during the entire cavity expansion process (i.e. $a_0$ to $a_f$). These gauge particles were equally spaced, and their locations can be identified using the normalised radial distance of $r/a_f$ ($r$ being the radial distance measured from the internal cavity wall). It can be noted that the radial displacement variations during cavity expansion in both loose and dense soils showed a very similar trend. As expected, particles located closer to the centre of the cavity experienced larger radial displacements and the radial displacement continuously dissipated with the radial distance. Referring to Figure 4.18, it can be observed that the total radial displacement shows a dramatic decrease with radius when the normalised radius ($r/a_f$) was less than 10, while the changes become almost insignificant when the normalised cavity radius was larger than 15. It is projected that the radial displacement would approach zero if the measurement could be taken at a considerably large radial distances away from the internal cavity. Furthermore, it is noteworthy to state that the radial displacement predicted in loose sand was infinitesimal ($\delta_r \approx 0$) when the normalised radial distance was larger than 25. It can be explicitly concluded that the influence zone induced by the cavity expansion in loose sand and its analogues activities (i.e. pile installation, pressuremeter test) is 25 $a_f$. However, in dense sand, a larger value must be considered to eliminate the boundary effect.

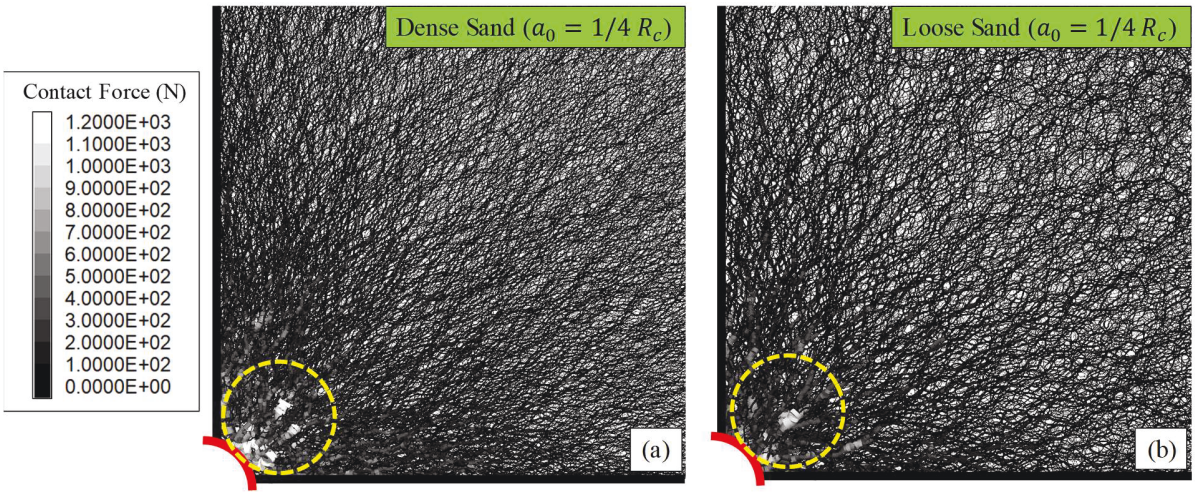


Figure 4.19 Distribution of contact forces at a= $a_f$ for cavity expansions with initial radii $a_0$ =1/4 $R_c$ in (a) dense sand, and (b) loose sand

Figure 4.19 shows the distribution of the contact force chain at the end of the cavity expansion process when $a_0 = 1/4\ R_c$ was adopted in both dense and loose sands. Contact forces between particles were plotted as branches (cylinders) whose diameters are proportional to their magnitude. For the purpose of comparison, the contact forces obtained on both samples were normalised adopting the same scale, as illustrated in Figure 4.19. It is noticed that the distribution of the contact force chain, in both loose and dense specimens, propagates radially with the maximum contact force appearing in the internal cavities whereas the magnitude of the contact force reduces dramatically with the radial distance, as seen in the circles in Figure 4.19. It can be observed that the magnitude of contact forces acting on the internal cavity wall in dense sand is, as expected, remarkably larger than the corresponding values in the loose sand, similar to the cavity pressure variations presented in Figure 8. In addition, the distribution of the contact force

chain is found to be more intensive in dense sand, confirming that the influence zone induced by the cavity expansion in dense soil is larger, similar to the radial soil displacement illustrated in Figure 4.18.

### 4.6.7 Variations of Radial and Hoop Stresses during Cavity Expansion

The distribution of the radial and hoop stresses measured at various radial distances ($r/a_f, r$ being the radial distance measured from the internal cavity wall) during cavity expansion is presented in Figure 4.20 and Figure 4.21 for dense and loose soils, respectively.

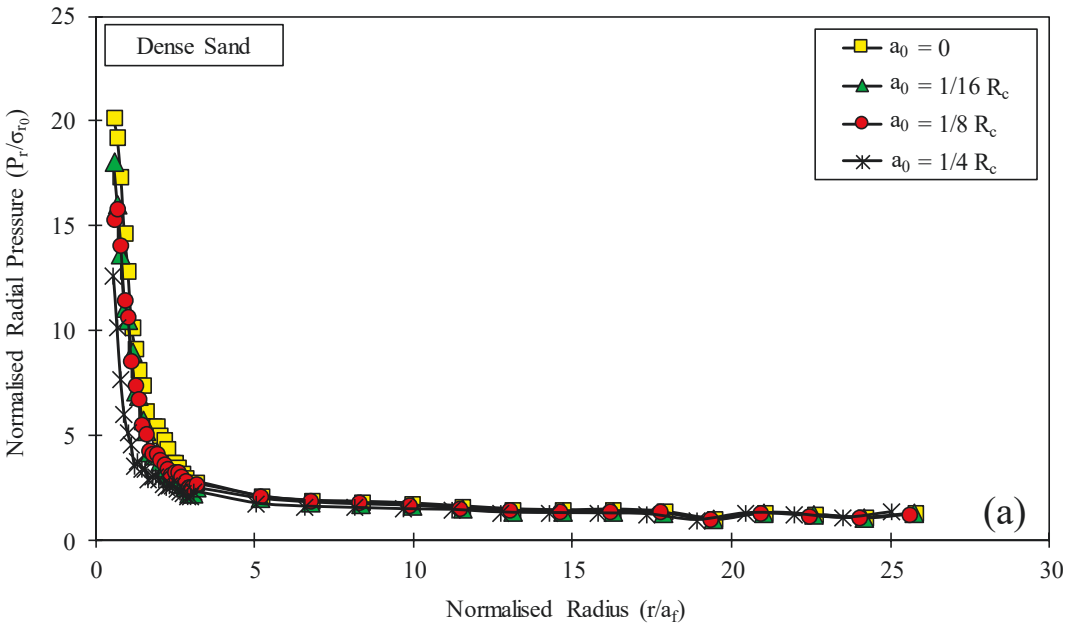

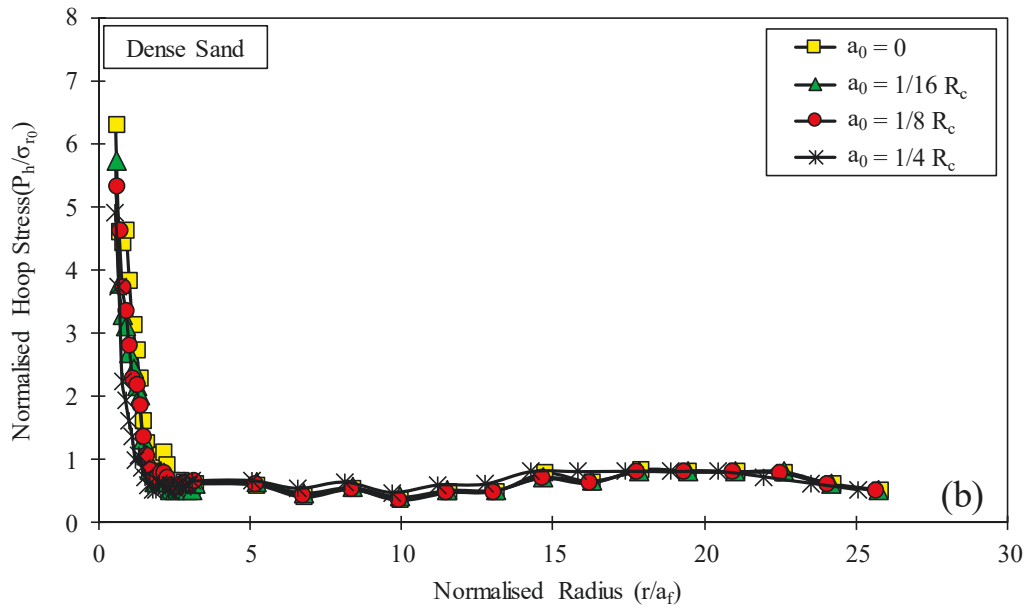


Figure 4.20 (a) Radial stress, and (b) hoop stress distributions at 20% of cavity expansion in dense sand

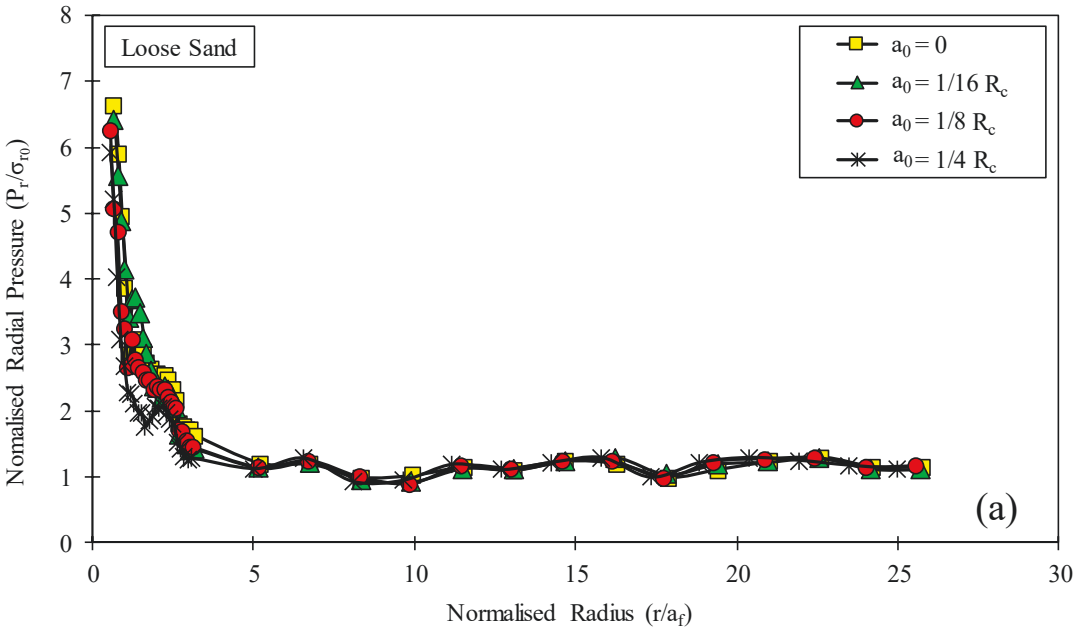

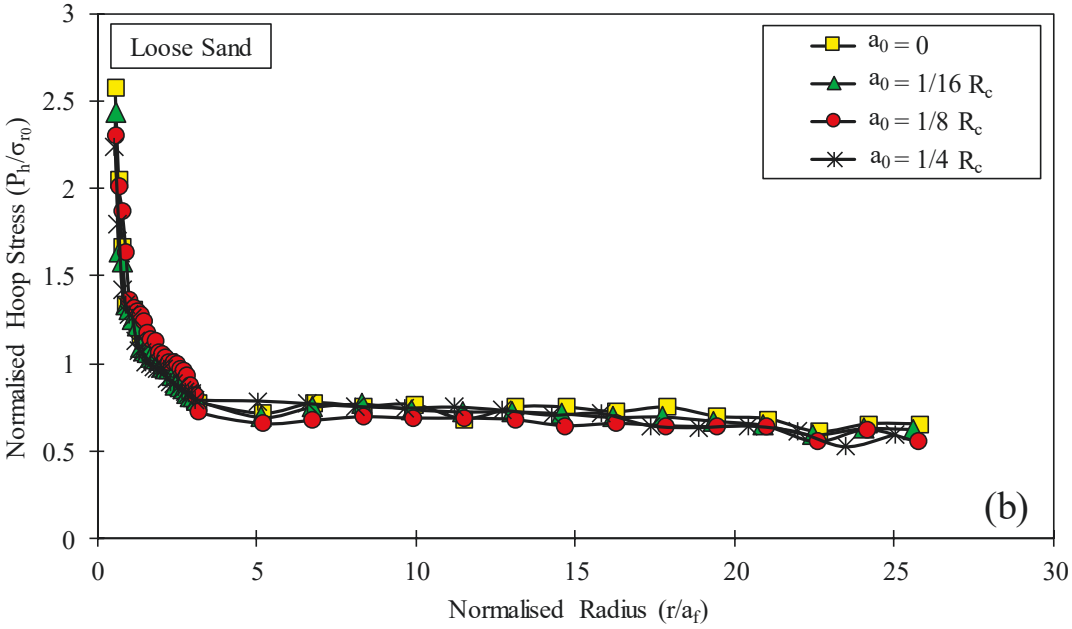


Figure 4.21 (a) Radial stress, and (b) hoop stress distributions at 20% of cavity expansion in loose sand

Results have been plotted for a particular stage of the cavity expansion when $\frac{a-a_0}{R_c-a_0} = 20\%$ (where $a$ is the radius of the cavity at 20% progress during the expansion). It should be noted that the radial and hoop stresses are the major and minor principle stresses during the cavity expansion process (Carter et al. 1979b; Carter et al. 1985) and therefore presented here. Referring to Figure 4.20 and Figure 4.21, it can be generally concluded that for both loose and dense specimens, the magnitude of the radial pressure and hoop stress changed significantly with the distance from the internal cavity. As $r$ increased, both radial pressure ($P_r$) and hoop stress ($P_h$) reduced significantly, while further away from the cavity, this reduction becomes less pronounced. For example, in both dense and loose specimens, the normalised radial pressure decreased immensely when the

normalised cavity radius ($r/a_f$) was less than 5, while insignificant radial pressure variations were observed when $r/a_f > 5$. However, Figure 4.20 (a) illustrates that the measured radial stress in dense sand would eventually reach the initial radial stress (i.e. $P_r = \sigma_{r_0}$) at a radial distance (i.e. $r/a_f$) larger than 20, while a smaller value could be noticed in loose sand (i.e. $r/a_f > 10$), as shown in Figure 4.21 (a). In addition, the hoop stress variations, as illustrated in Figure 4.20 and Figure 4.21, show a very similar trend but with considerably diminished values, compared with the radial stress variations reported.

The results obtained in this study clearly indicate that the choice of an initial cavity radius impacts the soil response during the cavity expansion, particularly the cavity pressure. Results of this study provide insight into the practical applications such as driven pile installation process. In the design of a pile foundation, a detailed analysis is required to predict the impact stresses in the piles during driving and to estimate the static soil resistance, from which the type and size of hammer, the required driving force could be determined (Smith 1962; Hirsch et al. 1970). Assessing the maximum driving force is essential to use a suitable hammer since an underestimation of the driving force may prevent the driving the pile to the required depth, whereas the excessive driving stress can lead to the extravagance of the diesel fuel and enhance the risk of damaging the pile (Rajapakse 2016). The results of this study can help practicing engineers to estimate the shaft friction that is the function of internal cavity pressure induced by the pile driving.

In addition, referring to the cavity pressure variations depicted in Figure 4.8, it is worth mentioning that the pressure required for creating a cylindrical cavity (i.e. the zero initial radius) is considerably larger than the pressure required to expand an existing cavity for a given expansion volume. This may explain why pilot hole is adopted in the pile driving practice to facilitate the driving process. Indeed, predrilled pilot hole is adopted aiding the driving of the pile when soil strata close to the ground surface is extremely firm, and with the use of the pilot hole, the thrust force can be significantly reduced (Tsao et al. 2003; Tomlinson et al. 2014). The pilot hole is considered as an initial cylindrical cavity which is enlarged and therefore helps to reduce the disturbance to the surrounding soil. Thus, based on the findings reported in this study, it may be reasonably deduced that the appropriate size of the pilot hole should be considered by practicing engineers so as to ease the subsequent pile driving process. This will in turn reduce the assumptions of the diesel fuel and facilitate the project progress.

Furthermore, the study presented here may draw some inspiration for studying the smear zone characteristics induced by vertical drain installation. Prefabricated vertical drains (PVDs) are often used to accelerate the consolidation process and to increase shear strength under embankments on soft soil (Parsa-Pajouh et al. 2015). However, it is well recognised that the installation of the prefabricated vertical drains adopting a mandrel, disturbs the surrounding soil significantly, resulting in a smear zone with reduced permeability and over consolidation ratio that adversely affects the consolidation process (Sharma et al. 2001; Azari et al. 2014). The numerical simulation of the cavity expansion

shows the potential of utilising the DEM to study the characteristics of the smear zone. For instance, the variations of the void ratio at the proximity of the cavity wall may be used to determine the reduction in permeability, while the radial stress and soil displacement may be adopted to correlate to the extent of the smear zone.

## 4.7 Summary

In modelling the cavity expansion subjected to driven pile installation, the initial cavity radius chosen had conspicuous effects on the cavity pressure, the stress path, the volumetric strain and the deviatoric stress, especially at the initial stage of expansion; however, these effects become less pronounced and are ultimately minor as the cavity reaches full expansion. Given a same expansion percentage, the pressure required to create a cavity (i.e. $a_0 = 0$, $a_0$ is the initial cavity radius) is significantly larger than expanding an existing cavity (i.e. $0 < a_0 < R_c$) in the same soil medium, whereas the pressure needed to maintain an already expanded cavity is not sensitive to the choice of initial cavity radius. In addition, the radial soil displacement showed a significant decrease with the radial distance, with the influence zone induced by the cavity expansion in loose sand was approximately 25 $R_c$, while a larger influence zone (approximately 30 $R_c$) must be considered in the dense sand to eliminate the boundary effects. The findings may provide practicing engineers with criteria to eliminate the adverse effects of lateral soil movement to adjacent structures when installing the displacement-based inclusions in granular materials and determining the appropriate size of the pilot hole in driven pile installation and horizontal directional drilling for trenchless piping in sandy soil.

# Chapter 5 - Discrete Element Simulation of Cavity Expansion in Lightly Cemented Sands Considering Cementation Degradation

## 5.1 General

This chapter aims to investigate the influence of cementation on the stress-strain and strength characteristics of soil during cavity expansion in lightly cemented sand deposit using three-dimensional discrete element simulations. Contact models, simulating the cementation effects of bonded clumps and capturing the interlocking effects between discrete sand particles, are incorporated to mimic the cemented sands with various cement contents. The microscopic parameters are calibrated and validated against existing experimental results. Real scale cylindrical cavity expansion models starting from zero initial cavity radius with different levels of cementation are developed, and each proposed model consists of 150,000 particles with boundary conditions carefully selected to reproduce the realistic scenario. The embedded scripting is utilised to precisely measure both the local and global stress-strain variations, and record and analyse the cementation bond breakage during the cavity expansion process.

The results confirm that the cementation enhances the material strength through the increase in cohesion and tensile strength at the contacting interfaces, whereas the friction angle is not altered notably. Hence, the failure envelope of the cemented sand gradually merges with the critical state line due to the cementation degradation, particularly at a

high confining pressure. It was found that the failure mode of the lightly cemented sand adopted in this study, was mainly controlled by the shear rather than tensile strength at the contacting interfaces. Referring to the numerical predictions it is evident that the zone with significant cementation degradation due to the cavity expansion extends as far as $4a_f$ for all cemented specimens ($a_f$ being the final cavity radius). In addition, specimens with higher cement content experience a more pronounced dilation at the internal cavity wall, while an inverse trend is captured at a greater radial distance. Furthermore, the radial displacement induced by the cavity expansion reveals a larger influence zone in specimens with higher cement content. Therefore, the effects of excessive lateral displacement transferred to neighbouring structures during installation of the displacement-based inclusions in lightly cemented sand should be carefully assessed by practicing engineers.

## 5.2 Introduction

Cemented sand, in geotechnical engineering, is defined as a sand specimen with its particles held together by a binding agent which may be naturally present such as calcium carbonate, or artificially introduced such as Portland cement or microbially induced calcite precipitation (Clough et al. 1981; DeJong et al. 2006; Budhu 2008). Nearly all soils found in nature have a certain degree of cementation, and due to the wide distribution and the decisive effect of the cementation in controlling the mechanical behaviour of the cemented soils, extensive research has been carried out to study the stress-strain and strength characteristics of the soil over the last few decades (Shen et al. 2016). Clough et

al. (1981) adopted triaxial compression tests to investigate the behaviour of natural cemented sands found along the California coast , which is considered as one of the pioneering works that comprehensively studied the drained behaviour of the cemented sand. Airey (1993) also studied the naturally cemented carbonate soil adopting both the conventional and stress-path controlled triaxial tests and noticed that the presence of the cementation can enhance the shear modulus, while exerting less impact on the volumetric response. Besides, Leroueil et al. (2009) proposed the concept of "structured soils" to describe the cementation in natural soils, and highlighted that the effects of the structure on the soil behaviour are independent of the origins. In Leroueil et al. (2009), the post yield transition from "structured" to "unstructured" states, due to the gradual loss of structure with further strain, was also captured, and this transition was termed as "degradation" in subsequent studies (Coop et al. 1993; Lagioia et al. 1995; Cuccovillo et al. 1997, 1999). However, naturally cemented specimens, in general, have inherent variabilities in the void ratio and degree of cementation, and most importantly the extraction and trimming process in obtaining undisturbed samples are extremely difficult (Clough et al. 1981; de Bono et al. 2015). Therefore, considering the difficulties with in-situ undisturbed sampling of lightly cemented soils, artificially cemented sand specimens, whose properties can be well controlled, are often adopted in characterising the behaviour of cemented sands.

In the past decades, there were extensive experimental studies carried out on artificially cemented sand, which are mainly focusing on extending the fundamental understanding

of the static and dynamic behaviour based on small scale laboratory testings, including the studies on the stress – strain, strength and dilatancy behaviours; yielding, pre-failure and post failure characteristics; the influence of curing environment and conditions; influence of cementation on the liquefaction resistance, and so forth (Sitar et al. 1980; Clough et al. 1981; Acar et al. 1986; Saxena et al. 1988a; Saxena et al. 1988b; Lade et al. 1989; Reddy et al. 1993; Consoli et al. 1998; Huang et al. 1998; Consoli et al. 2000; Ismail et al. 2000; Schnaid et al. 2001; Ismail et al. 2002; Haeri et al. 2005; Consoli et al. 2006; Consoli et al. 2009; Consoli et al. 2010; Consoli et al. 2011; Al-Thawadi et al. 2012; Consoli et al. 2012; Cheng et al. 2013). However, these aforementioned studies only provide the macroscopic responses of the cemented sand, and the fundamental and inherent mechanisms (e.g. cementation degradation) determining the soil response require further research. Although the scanning electron microscope (SEM) photos, X ray $\mu$CT, neutron radiography and stereophotogrammetry may be adopted tracing individual particle movements, it is very challenging to quantify and characterise the cementation degradation during the testing process at the scale of grains (Wang et al. 2008a; Jiang et al. 2013; Feng et al. 2017).

In the numerical modelling front, particularly in continuum-based simulations, the cemented granular materials are often modelled adopting simple constitutive models (e.g. Mohr Coulomb model) with an enhanced cohesion and elastic modulus (Ismail 2005; Nasr 2014), which cannot adequately describe the post failure behaviour controlled mainly by cementation degradation . On the other hand, there were constitutive models

developed for cemented sand considering the cementation degradation effects (Yu et al. 2007; Gao et al. 2012; Rahimi et al. 2015) that are capable of capturing the general stress-strain responses. However, the effects of cement content, initial mean effective stress, and how the cementation degradation influences the mechanical behaviour of cemented granular materials are not well understood (Yu et al. 2007; Jiang et al. 2013), which prevent the wide implementation of these constitutive models in continuum-based numerical simulations.

Considering the discontinuous nature of granular materials, and the capabilities in investigating the problem in microscopic level (e.g. cementation degradation), discrete element method (DEM) can be adopted as an effective tool to study the behaviour of cemented sand capturing the interparticle micro-mechanics. To precisely simulate the behaviour of cemented sand, numerous modelling techniques have been proposed in DEM (Wang et al. 2008a; Wang et al. 2008c; Jiang et al. 2013; Obermayr et al. 2013; de Bono et al. 2015; Feng et al. 2017), mainly based on the bonded model developed by Potyondy et al. (2004), in which the cementation effects between two contacting pieces were mimicked using a virtual cementation bond that can sustain both tension and shear forces until either tensile or shear strength was exceeded. These techniques can be generally divided into two categories; the first category is simulating the cemented sand as a two-phase material, consisting of both cemented and uncemented particles, and the cementation level was controlled based on the percentage of cemented particles in the specimen (Wang et al. 2008a; Wang et al. 2008c; Obermayr et al. 2013);in the second

category, however, a cemented granular sample is simulated by adopting cemented particles only (i.e. cementation exists at all contacts), and the cementation level is controlled by adjusting a particular contact parameter in the bonded model, including the cementation bond strength or the radius of the cementation bond (Jiang et al. 2013; de Bono et al. 2015; Feng et al. 2017). With these techniques available, there have been a plethora of discrete element studies carried out studying the cemented sand mechanics, including the shear behaviour , strain localisation, shear band formation, dilatancy, cementation degradation and so forth (Wang et al. 2008a; Wang et al. 2008c; Jiang et al. 2011; Jiang et al. 2013; Obermayr et al. 2013; de Bono et al. 2015; Feng et al. 2017). The findings of these studies are indisputably complementary to the experimental observations, particularly in the comprehension of fundamental micro mechanics of cemented sands. However, nearly all DEM studies on cemented sands were based on the simulations of small scale laboratory testings such as triaxial test, and most were based on 2D qualitative analysis, or with no calibration of the contact parameters against experimental results (Wang et al. 2008a; Camusso et al. 2009; Jiang et al. 2013; de Bono et al. 2014a).Thus, the response of the cemented sand for realistic geotechnical applications (e.g. driven pile and vertical drain installations) may not be well reproduced if the contact properties are not calibrated against actual experimental results.

Hence, this study is proposed adopting three-dimensional DEM model to investigate the effect of light cementation on the soil response during cavity expansion. Since the DEM can be easily implemented to model the cavity expansion/creation from a zero initial

cavity radius (i.e. no initial cavity present), the impact of various cement contents on the predictions can readily be assessed using this technique. The selection of the cavity expansion problem is attributed to its application in analysing many real-life geotechnical problems, such as pile installation, and in-situ soil tests such as pressuremeter and cone penetration test (CPT). Indeed, the response of the surrounding soil during the pile installation and the cone penetration process is analogous to the creation and expansion of cylindrical cavities (Carter et al. 1979b; Randolph et al. 1979; Salgado et al. 1997; Yu 2013). Since the DEM is very effective in incorporating the discontinuous nature of granular materials and can be easily implemented to model the cavity creation and expansion, the influence of cementation on the lightly cemented sand response can be readily assessed.

## 5.3 Adopted Contact Model

To reproduce the behaviour of cemented granular materials, the contact model adopted must be capable of capturing both the cementation and frictional effects between sand particles, before and after the breakage of a cemented bond. The contact model adopted in this Chapter to mimic the cementation at the contacts of adjacent particles, is the Linear Parallel Bond (LPB) model, which consists of two components, including a frictional contacting interface with zero tensile strength and a cementation bond component which acts in parallel with the first component (Wang et al. 2008a; de Bono et al. 2015; Feng et al. 2017). The behaviour of the former component is linear elastic in normal direction with zero tension cut-off, while in the tangential direction, a linear elastic-perfectly plastic

behaviour is utilised, with the maximum shear force at the contact being the Coulomb limit, determined by the $\mu^l F_n$, where $\mu^l$ is the friction coefficient, and $F_n^l$ is the normal component of force acting on the contacting interface (Cundall et al. 1979; Itasca 2016).

The latter component obeys a brittle linear elastic constitution law that allows both the tension and moment to develop and transmit between contacting particles until either of these stresses exceed the bond strength. Once the bond strength is exceeded, the second component of the LPB model (i.e. cementation effects) will be nullified, with its associated forces and moments removed (Potyondy et al. 2004; Potyondy 2015). The rheological model showing the concept of the adopted LPB model is illustrated in Figure 5.1.

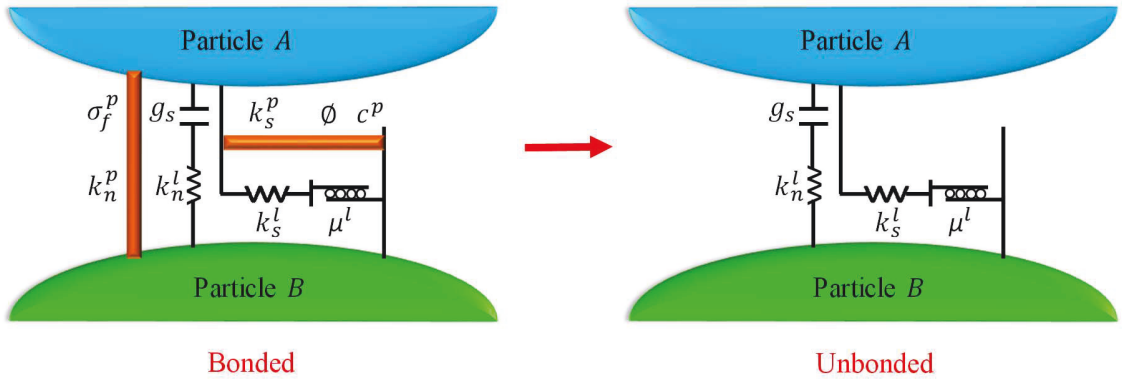


Note:
$g_s$ is the surface gap
$\mu^l$ is the friction coefficient between contacting particle
$\sigma_f^p$ is the tensile strength of the bond element
$\emptyset$ and $c^p$ are the friction angle and the cohesion of the bond element, computing the shear strength of the bond element
$k_n^l$ and $k_s^l$ are the normal stiffness and shear stiffness of the linear springs, respectively
$k_n^p$ and $k_s^p$ are the normal stiffness and shear stiffness of the bond element, respectively

Figure 5.1 Rheological model of Linear Parallel Bond (LPB) contact model computing normal and shear forces for linear component and bond element

As shown in Figure 5.1, the cementation bond component of the model is activated once the contact gap (i.e. $g_s$ ) between adjacent particles is less than or equal to the installation gap defined by the user. However, with the breakage of a cementation bond once the tensile strength (i.e. $\sigma_f^p$) or shear strength (i.e. $\tau_f^p$, define through the friction angle $\emptyset$ and cohesion of the bond element $c^p$, as shown in Figure 5.1) is exceeded, the grain behaviour approaches that of clean granular materials with frictional sliding at the contacting interfaces, as evident in Figure 5.1. The adopted formulations to compute the forces in normal and shear directions in the contacts between grains are:

$$\left.\begin{aligned} F_n &= F_n^l + F_n^p = F_{n0}^l + k_n^l \Delta\delta_n + F_{n0}^p + k_n^p \Delta\delta_n \\ F_s &= F_s^l + F_s^p = F_{s0}^l + (k_n^l/k^*)\,\Delta\delta_s + F_{s0}^p + (k_n^l/k^*)\,\Delta\delta_s \end{aligned}\right\} \quad (5\text{-}1)$$

where, $F_n$ and $F_s$ are the total normal and shear forces between two contacting particles, while the superscripts $l$ and $p$ represent the linear frictional and parallel cementation bond components, respectively; the subscript 0 stands for the forces measured at the beginning of the time step (i.e. at time t); $k_n^l$ and $k_n^p$ are the normal stiffnesses of the interface between contacting surfaces and cementation bonds, respectively; $k^*$ is the ratio between the normal and shear stiffness of the interface of contacting surfaces; and $\Delta\delta_n$ and $\Delta\delta_s$ are the relative displacement increments of contacting surfaces in the normal and shear directions, respectively.

For the adopted bonded interface between sand particles, the shear strengths of the cementation bond and linear frictional component were calculated based on the Equations (5-2a) and (5-2b), respectively. It should be highlighted that since the interface strength

composed of the cementation and the frictional resistance were not necessarily achieved at the same level of shear strains, these two components were separated and not subjected to direct additive function.

$$F_{s_{max}}^{l} = \mu^{l} F_{n}^{l} \tag{5-2a}$$

$$F_{s_{max}}^{p} = \tau_{f}^{p} \pi \left[min(R_a, R_b)\right] = \left[\left|\sigma_{n}^{p} - \sigma_{f}^{p}\right| tan\emptyset + (c^{p} - \sigma_{f}^{p} tan\emptyset)\right] \pi \left[min(R_a, R_b)\right] \tag{5-2b}$$

where, $F_{s_{max}}^{l}$ and $F_{s_{max}}^{p}$ are the maximum shear strength of the linear frictional component and the parallel cementation bond component, respectively; $R_a$ and $R_b$ are the radii of two contacting particles; $\sigma_{n}^{p}$ and $\sigma_{f}^{p}$ are the instant normal stress and the tensile strength of the cementation bond correspondingly; $\emptyset$ and $c^{p}$ are the angle of friction and the cohesion of the cementation bond, respectively.

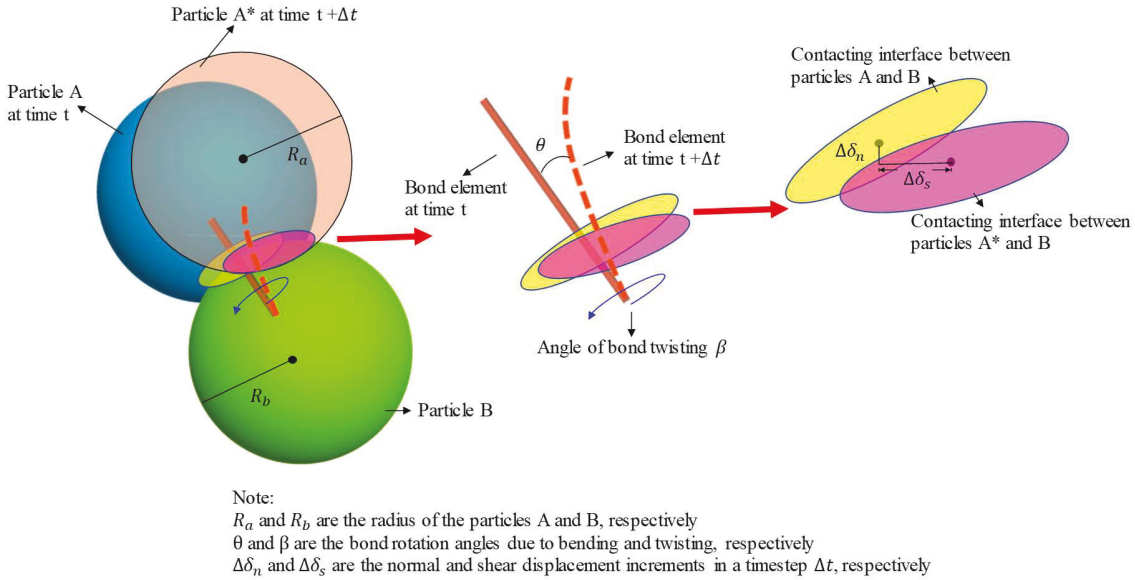


Figure 5.2 Schematic diagram of LPB contact model computing forces and moments

In addition to the tensile and shear forces, the adopted cementation bond can also sustain the bending and twisting moments, as illustrated in Figure 5.2, based on the following equations

$$\left.\begin{aligned} M^p &= M_b^p + M_t^p \\ M_t^p &= \frac{1}{2}(k_n^p/k_*^p)\,\pi\,[min(R_a,R_b)]^4\theta_{t=0}{}_t^p - \frac{1}{2}(k_n^p/k^*)\,\pi\,[min(R_a,R_b)]^4\frac{d\theta^p}{dt}_t \\ M_b^p &= \frac{1}{4}k_n^p\pi\,[min(R_a,R_b)]^4\beta_{t=0}{}_b^p - \frac{1}{4}k_s^p\pi\,[min(R_a,R_b)]^4\frac{d\beta^p}{dt}_t \end{aligned}\right\} \quad (5\text{-}3)$$

where, $M^p$ is the resultant moment sustained by the cementation bond, which can be decomposed into a twisting (i.e. $M_t^p$) and a bending moment (i.e. $M_b^p$); $\theta$ and $\beta$ are the angles of the rotations of the cementation bond due to twisting and bending, respectively.

In addition to the LPB model for interaction of cemented particles, the interaction at the contact between discrete sand particles with no cementation present at the interface, as indicated in Figure 5.7 (a), should also be captured. Considering the fact that the rolling and interlocking of neighbouring particles are the dominant micro-deformation mechanisms for the cohesionless materials (Iwashita et al. 1998; Oda et al. 1998; O'Sullivan 2011), the rolling resistance contact model (i.e. RR model) was incorporated along with the LPB model to simulate the cemented sand with arbitrary cement content. According to Jiang et al. (2005) and Tordesillas et al. (2002), RR model is suitable for simulating granular materials, particularly angular shaped particles, because modelling the precise shape of each particle is computationally impossible. The rolling resistance contact model includes a frictional contacting interface with zero tensile strength, and the behaviour is linear elastic in normal direction and linear elastic and perfectly plastic in tangential direction (similar to the first component in a LPB bond model). The rheological model of the rolling resistance contact model is illustrated in Figure 5.3.

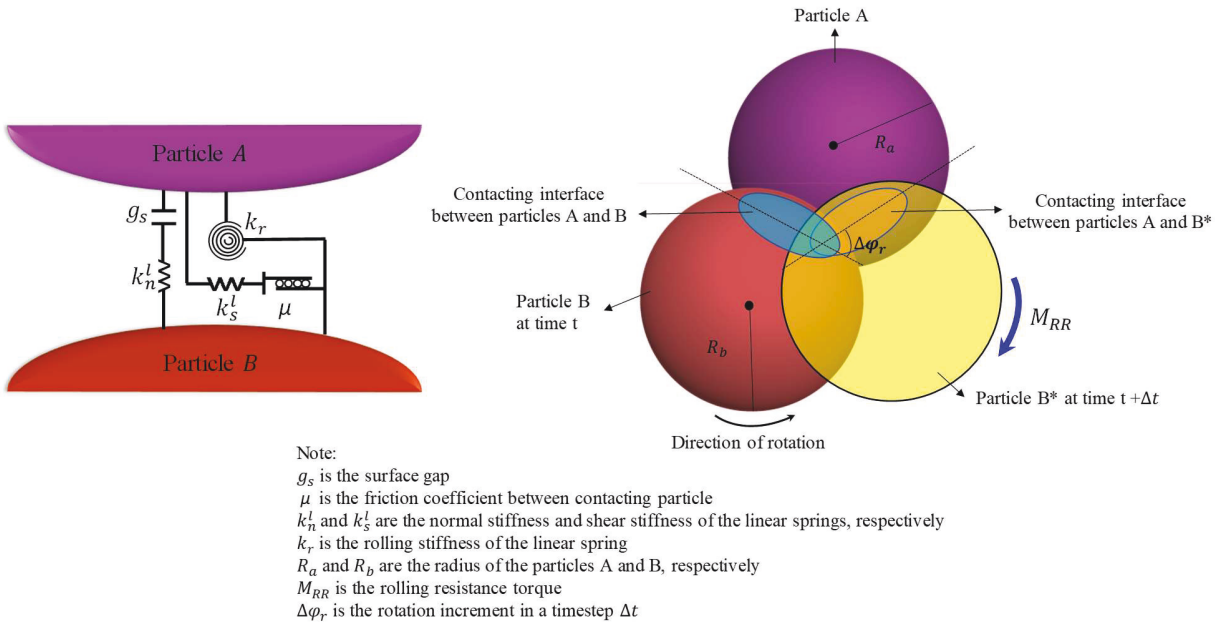


Figure 5.3 Rheological model and schematic diagram of rolling resistance contact model

To simulating the interlocking behaviour between angular particles, a limiting toque in the contact is introduced, which acts in the opposite direction to the rolling direction, as shown in Figure 5.3. Referring to Figure 5.3, the rolling resistance torque ($M_{RR}$) is imposed to resist the rolling motion induced by the relative rotation increment ($\Delta\varphi_r$) that occurs between particles $A$ and $B$; the magnitude of this rolling resistance torque is calculated based on the following equations:

$$\left.\begin{aligned} M_{RR} &= k_r \Delta\varphi_r \\ M_{RR}^{max} &= \mu_r F_n^l \ [R_a R_b/(R_a + R_b)] \end{aligned}\right\} \tag{5-4}$$

where, $k_r$ is the rolling stiffness of the linear spring, $M_{RR}^{max}$ is the limiting toque, and $\mu_r$ is the coefficient of rolling resistance. Detailed formulations regarding the rolling resistance (RR) contact model can be found in Ai et al. (2011) and Wensrich et al. (2012).

## 5.4 Calibration of Micromechanical Parameters for Various Cement Contents

### 5.4.1 Proposed Calibration Technique

To investigate the effects of the level of cementation on the soil response during the cavity expansion, the contact micromechanical models required in DEM simulations must be calibrated to mimic the realistic interaction mechanism of the cemented sand particles at their contacting interfaces. According to Abdulla et al. (1997), the cemented sand can be generally classified into two categories, including contact bonded and void bonded, which represent lightly and heavily cementation conditions, respectively. Park (2010) studied the effect of wetting on unconfined compressive strength (UCS) of cemented sand, in which the silica Baekma River sand was mixed with Portland cement to form cemented sand specimens with the cement contents ranging from 4% to 16%. The SEM images clearly captured the transition from contact bonded to void bonded once the cement content increased above a certain threshold (i.e. 6% - 8% cement content). Similar findings were also reported by Marri et al. (2012), Ismail et al. (2002) and Cui et al. (2017) in studying the cementation of the porous materials. Moreover, as evident in SEM images reported by Cui et al. (2017), not all particle contacts in a lightly cemented sand are

structurally bonded, which confirmed that a certain percentage of sand particles remained free of cementation. Therefore, it can be reasonably deduced that there must be a threshold cement content, at which the cementation exists at all contacts between contacting particles, whereas a certain portion of particles, depending on the level of cementation below this yardstick cement content, remain unbonded. Considering all of these characteristics of the lightly cemented sand, it is reasonable to assume that the mechanical behaviours of cemented sand, with any arbitrary cement contents less than the threshold value, can be simulated by controlling the percentage of bonded particles. A similar technique to simulate the cemented sand with different cement content using DEM was adopted by Obermayr et al. (2013). However, it must be clarified that the scope of this chapter is on lightly cemented sands only, where cementations only present at the contacts between adjacent particles. Indeed, this technique may not be appropriate to simulate the heavily cemented soils, where the voids can be largely occupied by the cementing agent (i.e. void bonded). This is attributed to the fact that the behaviour of heavily cemented soils is largely dependent on the increased relative density due to the reduction in the void ratio. It should be noted that an extremely high level of cementation can lead to very brittle failure, such as the mortar, which may not be accurately simulated adopting the LPB contact model (Potyondy 2012; Potyondy 2015).

Hence, to investigate the effects of different cementation levels on the soil response, the calibration exercises were carried out by matching the numerical simulation predictions with existing experimental measurements. The experimental tests adopted in this Chapter

were conducted by Abdulla et al. (1997) and Abdulla (1992) to study the effects of specimen size and slenderness on the stress-strain characteristics of cemented sand. Detailed information regarding the material properties can be found in Abdulla (1992), and therefore only the essential information is presented here. According to Abdulla (1992), the sand adopted in the experimental test is poorly graded, with the maximum and minimum void ratio being 0.93 and 0.60, respectively, and the medium grain size $D_{50}$ is 0.67 mm. Detailed information and the experimental testing procedure can be found in Abdulla et al. (1997) and Abdulla (1992). Due to the fact that a weakly cemented sand, as discussed earlier, consists of both cemented and uncemented particles, the interactions between both the bonded particles and the unbonded particles must be calibrated adopting different contact models as discussed earlier.

### 5.4.2 Details of Calibration Exercises

Four calibrations exercises were carried out in this study to obtain the micromechanical parameters required for DEM simulations. The first two calibrations were performed on the uncemented sand (i.e. cement content CC = 0%) and the fully cemented sand (i.e. the threshold case with a CC = 6%) for deriving the contact parameters for rolling resistance (RR) and LPB models, respectively. The other two calibration exercises for sands with 2% and 4% cement content were achieved by mixing the cemented and uncemented sand particles in a certain percentage, inspired by Obermayr et al. (2013), which could also serve as the verification exercise, validating the effectiveness and reliability of the proposed technique and calibrated parameters.

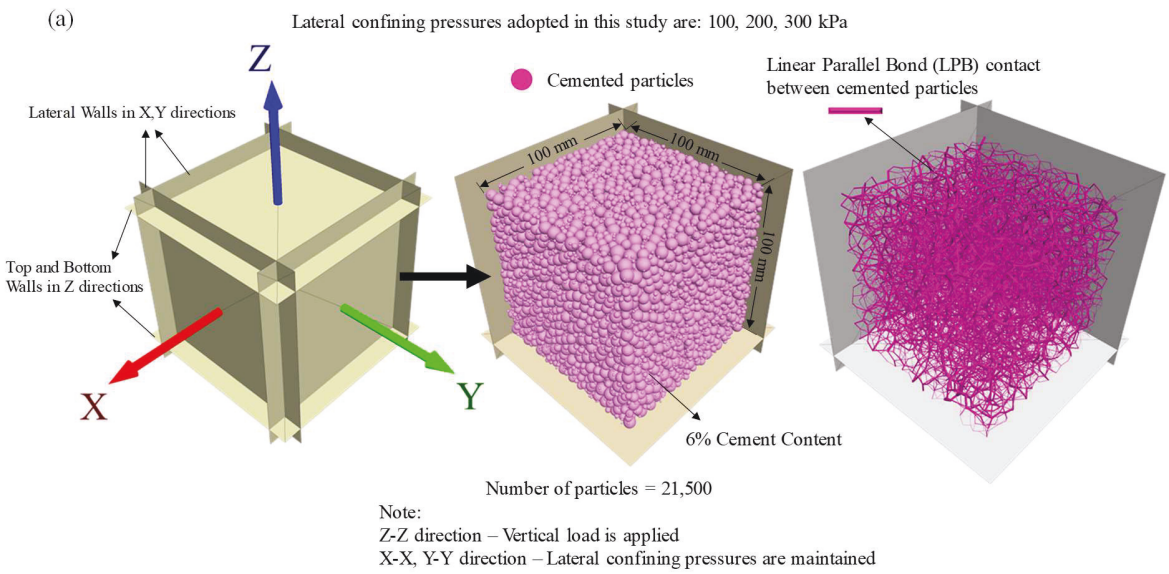


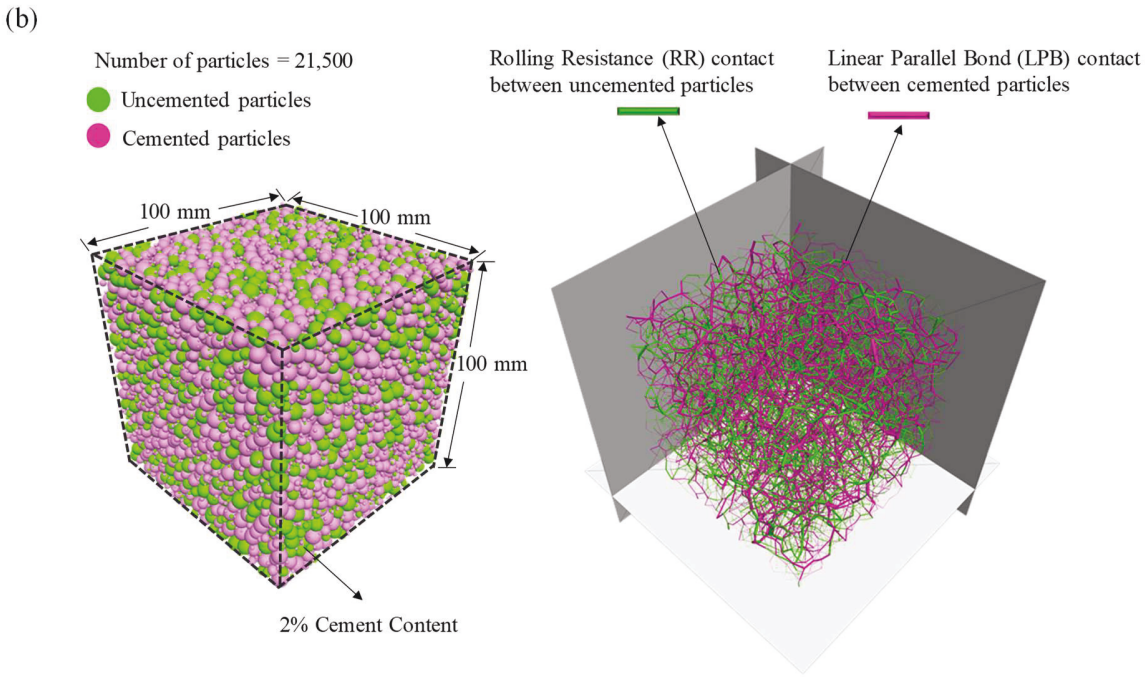


Figure 5.4 Triaxial test simulation setup and contact force chain for the calibration of (a) 6% cemented sand; (b) 2% cemented sand

The calibration setup for the 6% cemented sand is illustrated in Figure 5.4 (a). As shown in Figure 5.4 (a), the numerical model is cuboidal with a side length of 100 mm, which is equivalent to the experimental setup reported by Abdulla et al. (1997). Adopting identical sample dimensions and particle size distribution as in the laboratory experiments, the generated specimen consisted of 21,500 particles. For the cemented sand with 6% cement content, the LPB model was activated once the particles were generated, and the boundary walls were controlled with a servomechanism until the target void ratio (i.e. 0.66) and stress state reached the desired values at the equilibrium. Referring to Figure 5.4 (a), a confining pressure was maintained at the lateral walls in X and Y directions, while the axial load was applied on the top of the specimen (i.e. Z direction). During the triaxial testing, the axial stress and strain variations as well as the volumetric strain variations were continuously recorded adopting pre-defined subroutines for the comparison with the experimental measurements. A similar arrangement and procedures were adopted for the calibration of the uncemented sand (i.e. CC = 0%) except that the rolling resistance (RR) contact model was assigned mimicking the interlocking behaviour between clean sand particles. The calibrated micro-mechanical contact parameters are summarised in Table 5.1.

Table 5.1 Summary of calibration contact parameters for uncemented and cemented sand specimens

| Contact Model | Model Parameter | Descriptions | Values |
|---|---|---|---|
| Rolling Resistance (RR) model for Uncemented Sand | $E^*_{mod}$ | Linear Component Effective Modulus | 360 MPa |
| | $k^l_*$ | Linear Component Spring Stiffness Ratio (Normal Stiffness/Shear Stiffness) | 4.75 |
| | $\mu^l$ | Inter-Particle Friction Coefficient | 0.5 |
| | $\mu_{rr}$ | Rolling Friction Coefficient | 0.55 |
| | $\mu_{wall}$ | Wall Friction Coefficient | 0 |
| Linear Parallel Bond (LPB) model for Cemented Sand | $E^p_*$ | Bond Effective Modulus | 550 MPa |
| | $k^p_*$ | Bond Stiffness Ratio (Normal Stiffness/Shear Stiffness) | 12 |
| | $\sigma^p_f$ | Bond Tensile Strength | 28 MPa |
| | $c^p$ | Bond Cohesion | 5 MPa |
| | $tan\emptyset$ | Friction Coefficient | 1.25 |
| | $\lambda^p$ | Bond Radius Multiplier | 1 |

Once the micro-mechanical contact parameters for uncemented (i.e. CC = 0%) and fully cemented (i.e. CC = 6%) sand specimens were calibrated, the parameters were adopted for the verification exercises on the sand with 2% and 4% cement contents, adopting the same simulation setup, as shown in Figure 5.4 (b). Considering the characteristics of the LPB model reported in Potyondy et al. (2004) and Itasca (2016), an increase in cement content in lightly cemented soils is essentially the increase in the number of cemented bonds at the contacts, and therefore it is reasonable to logically assume that the number of cemented bonds follows an approximate linear relationship with the cement content. In fact, Obermayr et al. (2013) tabulated the percentages of bonded particles adopted for the different cement contents, which indeed exhibited an approximate linear correlation. Hence, the percentage of the cemented particles for 2% and 4% specimens were initially assumed to be linearly proportional to the fully cemented sand (i.e. CC = 6%), and

therefore the approximate number of cemented particles required were computed through interpolation. The discrete element model details in terms of proportions of bonded and unbonded particles for each adopted cement content are presented in Table 5.2.

Table 5.2 Summary of calibration information for specimens with 0%, 2%, 4% and 6% cement content

| Cement Content (CC%) | Contact Models | Number of Cemented Particles | Number of Uncemented Particles | Number of Cemented Bonds | Number of Uncemented Bonds |
|---|---|---|---|---|---|
| 6% | LPB | 21,500 | 0 | 32,924 | 0 |
| 4% | LPB and RR | 15,000 | 6,500 | 17,213 | 8,837 |
| 2% | LPB and RR | 13,500 | 8,000 | 13,599 | 11,858 |
| 0% | RR | 0 | 21,500 | 0 | 18,006 |

Note: LPB is Linear Parallel Bond Model; RR is Rolling Resistance Contact Model

With the estimated number of cemented particles, the calibrations of the 2% and 4% cemented sand were carried out subsequently. Then for fine-tuning the model, the estimated number of cemented particles were slightly adjusted by trial and error until a good agreement between experimental measurements and numerical predictions was achieved.

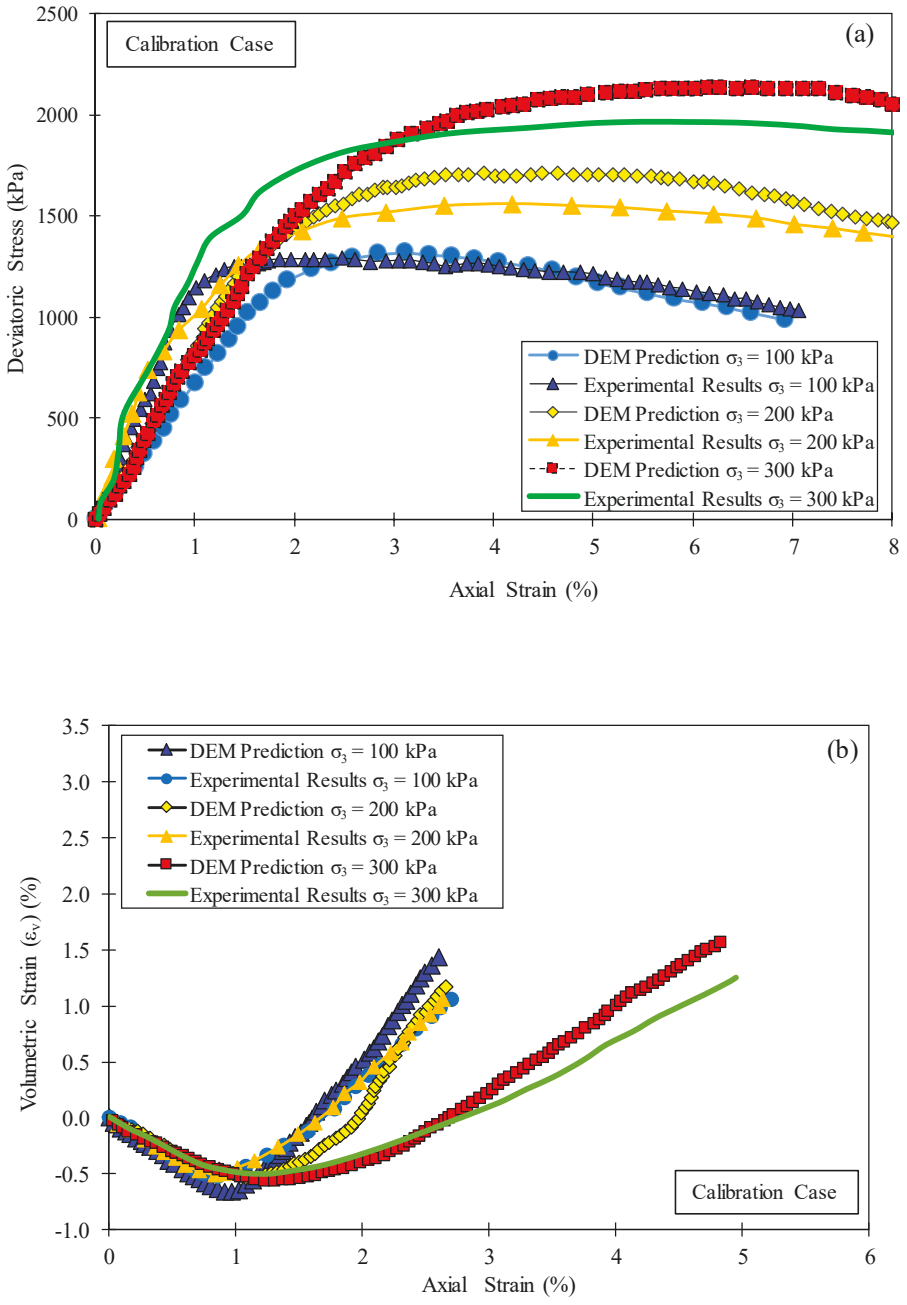


Figure 5.5 (a) Variations of axial stress with axial strain and (b) variations of volumetric strain with axial strain for sand specimen with 6% cement content and 100, 200, 300 kPa lateral confining pressures (DEM predictions versus experimental measurements)

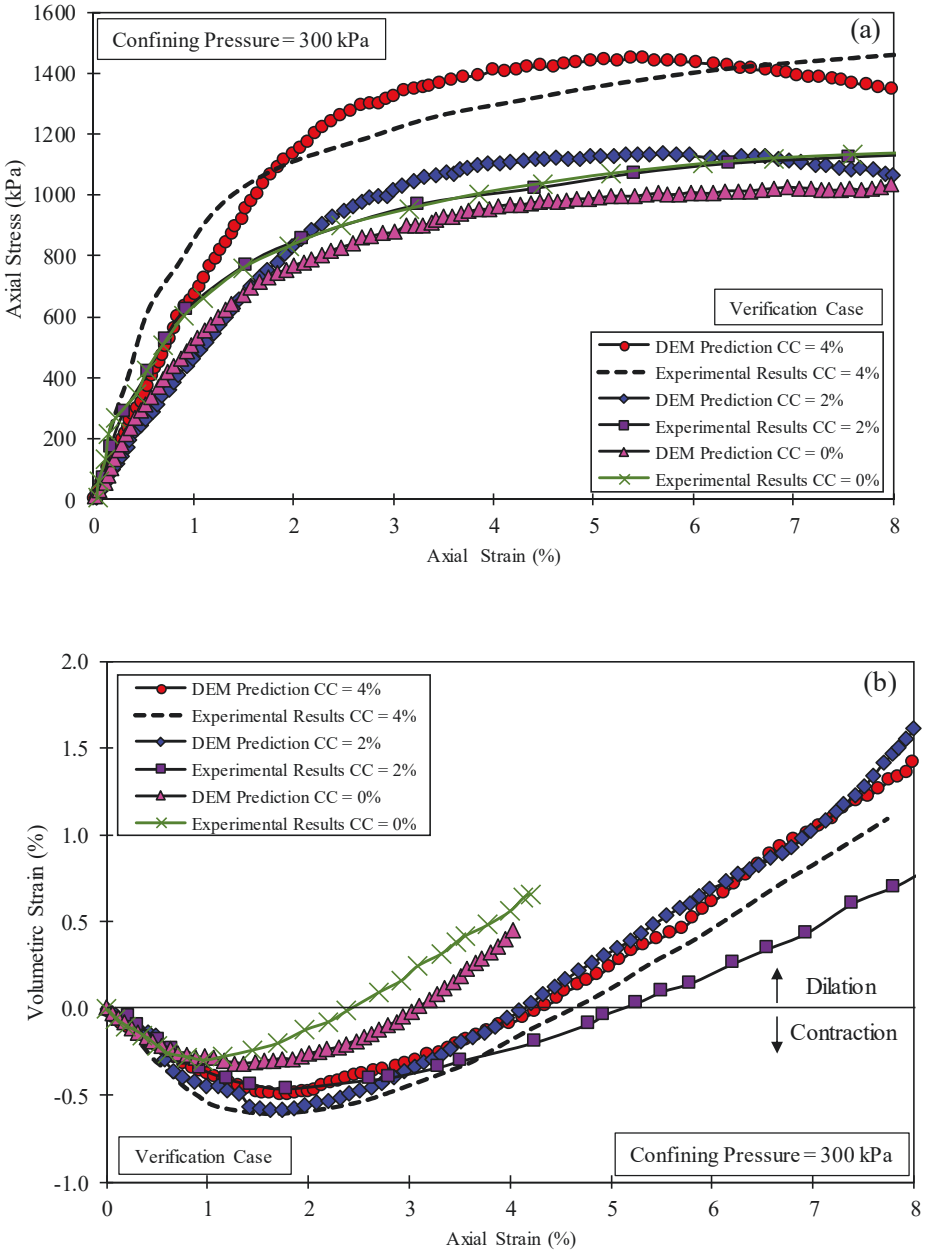


Figure 5.6 (a) Variations of axial stress with axial strain and (b) variations of volumetric strain with axial strain for sand specimens with 0%, 2% and 6 % of cement content (DEM predictions versus experimental measurements)

The numerical predictions versus experimental measurements for different cement contents are shown in Figure 5.5 and Figure 5.6. Moreover, the calibrated parameters were validated adopting different lateral confining pressures to provide further assurance on the reliability of the calibrated parameters, as it can be seen in Figure 5.5. It can be observed that the predictions obtained from the numerical simulations adopting the calibrated contact parameters, agree well with the experimental results. This confirms the reliability of the calibrated parameters mimicking both the cemented and uncemented sand responses subjected to loading, and it also verifies the rationality of the proposed technique to simulate cemented sand with arbitrary cement content using discrete element method (DEM).

## 5.5 Cavity Expansion Simulation

To investigate the effects of the cement content on the soil response during cavity expansion subjected to rigid inclusion installation (e.g. driven piles or concrete injected columns), large-scale three-dimensional cavity expansion models were proposed in PFC$^{3D}$ program (Itasca 2016). Considering that many geotechnical field problems related to cavity expansion such as pressuremeter test occur in plane strain condition (Alshibli et al. 2000; Silvestri 2001), and due to the fact that the pressuremeter test and driven pile installation can be simplified as axisymmetric problems, a pie slice model corresponding to one-third of a quadrant (i.e. central angle $\alpha_c = 30°$) was considered, as shown in Figure 5.7 (a).

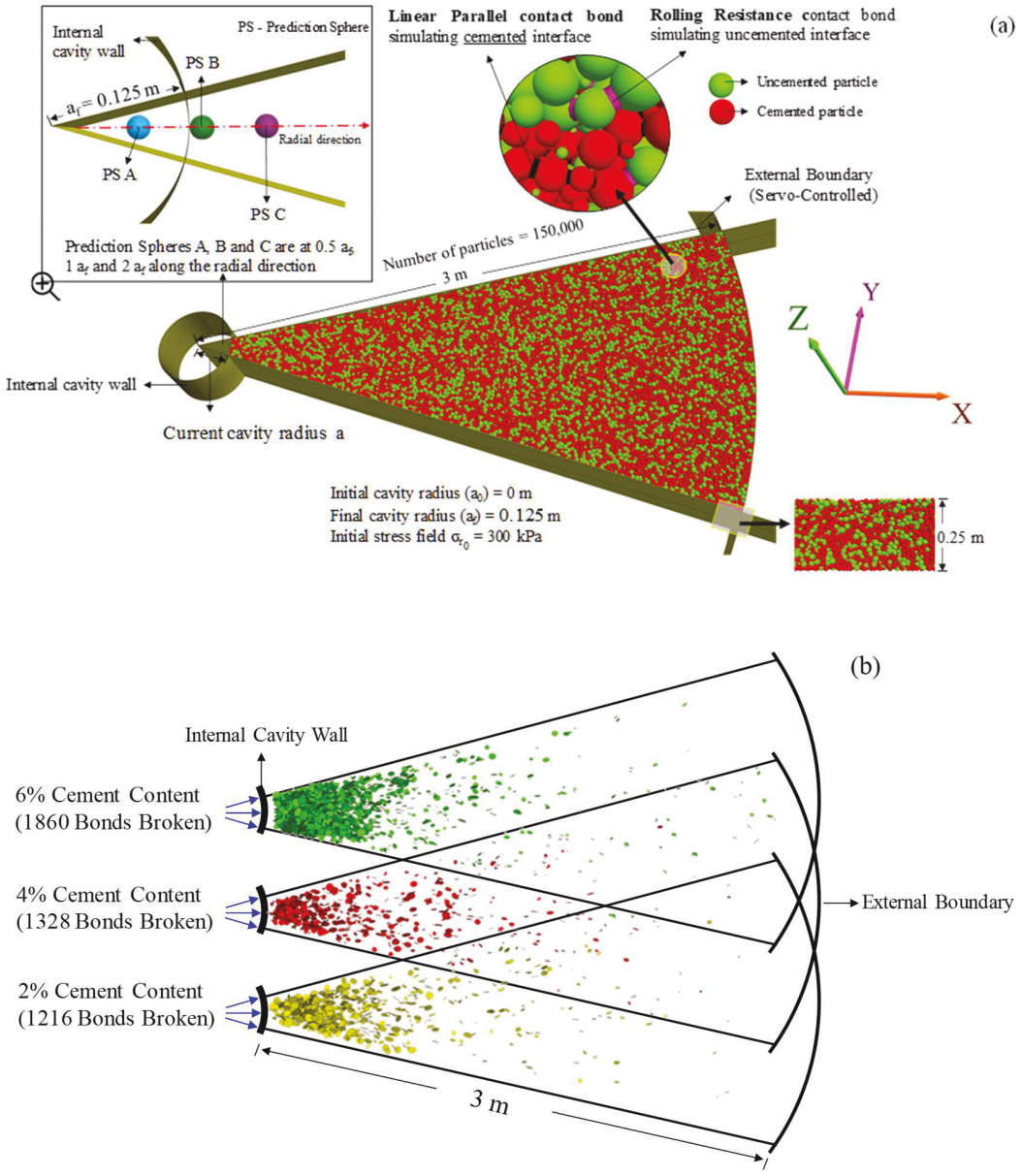


Figure 5.7 (a) Three-dimensional numerical model simulating cavity expansion; (b) position of bond breakage during the cavity expansion for cemented sand specimens with 2%, 4% and 6% cement content

This significantly reduces the number of particles and enhances the computation efficiency, while still capturing the 3D nature of aggregate arrangement. It should be noted that the selected central angle of the model should ensure that a sufficient number of particles contacting with the internal cavity wall are available to ensure the reliability of the measurements, particularly when the cavities are expanded from zero initial radius (i.e. creation of the cavities).

In this chapter, all cavities were expanded in a constant rate from zero initial radius to a final radius of 0.125 m, which is corresponding to the minimum driven pile diameter of 225 mm adopted in practice. To eliminate the boundary effects, the radius of the model must be sufficiently large to avoid the unexpected increase of the confining stress at the external boundaries. Bolton et al. (1999) carried out comprehensive centrifuge experiments on cone penetration tests in sand and suggested that a minimum chamber-to-cone diameter ratio of 20 must be satisfied to reduce the boundary effects to an acceptable level. Hence, the radius of the model was adopted to be 3 m so that the ratio between the external boundary and internal cavity is 24, larger than the minimum value recommended in Bolton et al. (1999).

With the radius of the model determined, the height of the model and the size effects between the internal cavity wall and the mean particle size ($D_{50}$) must be also deliberately considered to ensure a sufficient number of contacts are present between the internal cavity and particles during cavity expansion without compromising the simulation efficiency. Marschi et al. (1972) and Lackenby et al. (2007) claimed that the size effects

can be ignored as the ratio of specimen to maximum particle size reaches 6 in a triaxial test. Phillips et al. (1987) asserted that the minimum ratio required between the penetrometer radius and the median particle size to eliminate the size effects should be 10. In addition, Jiang et al. (2006) pointed out that a minimum number of 13 contacts between the cone tip and particles is a prerequisite to obtain a reliable tip resistance in discrete element simulation. Considering all of these conditions, the height of the model was adopted to be 0.25 m, ensuring that there are more than 25 particles contacting with the internal cavity at the initial stage of the cavity expansion, and this number continuously increases as the cavity expands further, leading to an enlarged contacting area between the particles and the internal cavity wall. With a 30 degrees central angle pie slice shape, 3 m radius and 0.25 m thickness of the model, there were 150,000 particles generated, following the particle size distribution reported in Abdulla (1992) and adopted in the calibration exercises.

The cylindrical cavity expansion was modelled by expanding the internal cavity radially from an initial radius (i.e. $a_0$) of zero to a final radius ($a_f$) of 0.125 m. The initial lateral stress field adopted (i.e. radial stress $\sigma_{r0}$) was 300 kPa, the same as the lateral confining pressure adopted in the calibration exercises, to simulate the soil stress state at a great depth below the ground level where the plane strain condition is considered to be reasonable. The geometry and arrangements of the model setups for cavity expansions in cemented sand with varying cement content were identical, and therefore only the overview of the model with 2% cement content during cavity expansion is presented in

Figure 5.7. Similar to the technique adopted in the calibration exercises, cemented sand was generated by controlling the percentage of cemented particles, while the rest of particles remained uncemented. The estimation of the number and proportion of cemented particles were based on the calibration results reported in Table 5.2. Taking the 2% cemented sand as an example, the ratio between the cemented and uncemented particles based on Table 5.2 was 1.15, and hence the number of cemented particles in the cavity expansion simulation was readily computed following the same ratio (i.e. 1.15) which was approximately 77,000, while the total number of particles in the model was 150,000 as mentioned earlier.

Referring to Figure 5.7, it can be observed that the contact model capturing the rolling and interlocking of sand particles (i.e. RR model) was assigned at the contacting interfaces between uncemented particles, while the LPB model mimicking the cementation was installed between the contacts of cemented sand particles. Samples were generated adopting the radius expansion method with a particle upscaling factor of 4.5, which is a common technique to increase the size of the particles in a controlled manner until the desired void ratio was reached. Once the particles have been generated, the initial stress field was applied through the servocontrol of the external boundary to achieve an initial radial stress of 300 kPa. After the initial conditions were established, all specimens had an average porosity of 0.40, consistent with the porosities reported in Abdulla et al. (1997) and adopted in the calibration exercises. In the next step, all cavities were expanded radially in a constant and sufficiently slow rate (i.e. 0.001m/s) to ensure a quasi-

static loading condition so that the inertial effects leading to impulsive oscillation and inaccuracy could be eliminated (Zhang et al. 2014).

The cavity pressure was measured using predefined subroutines that constantly measured the resultant contact forces acting on the internal cavity wall, and then divided by the instant corresponding contact area. To compute the stress and strain variations during the cavity expansion, there were three primary prediction spheres created, as illustrated in Figure 5.7 (a), namely PSA, PSB and PSC, situated at a radial distance of $0.5a_f$, $1a_f$, and $2a_f$($a_f$ being the final cavity radius, i.e. $a_f$ = 0.125 m), respectively. Apart from these primary prediction spheres, there were other prediction spheres generated in the model, recording the void ratio variations during the cavity expansion. Moreover, to study the effects of cementation on the radial displacement induced by the cavity expansion subjected to pile installation, there were more than twenty particles selected in the radial direction along the angular bisector, and their positions and displacements were continuously monitored. Furthermore, a function containing FISH intrinsic, recording the breakage of the cemented bond during the cavity expansion was programmed. The recorded information includes the number and the position of the bond breakage event, as well as distinguishing between the tensile and shear failures of the cemented bonds. The positions of bond breakage events in the entire cemented sand specimens were recorded during the cavity expansion as shown in Figure 5.7 (b). The relationship between the cementation bond breakage, due to shear and tension, with the cavity pressure will be depicted and discussed in the following section.

## 5.6 Results and Discussion

### 5.6.1 Variations of Cavity Pressure

The variations of the cavity pressure with respect to the cavity radius during the expansion for models with different cement content are plotted in Figure 5.8.

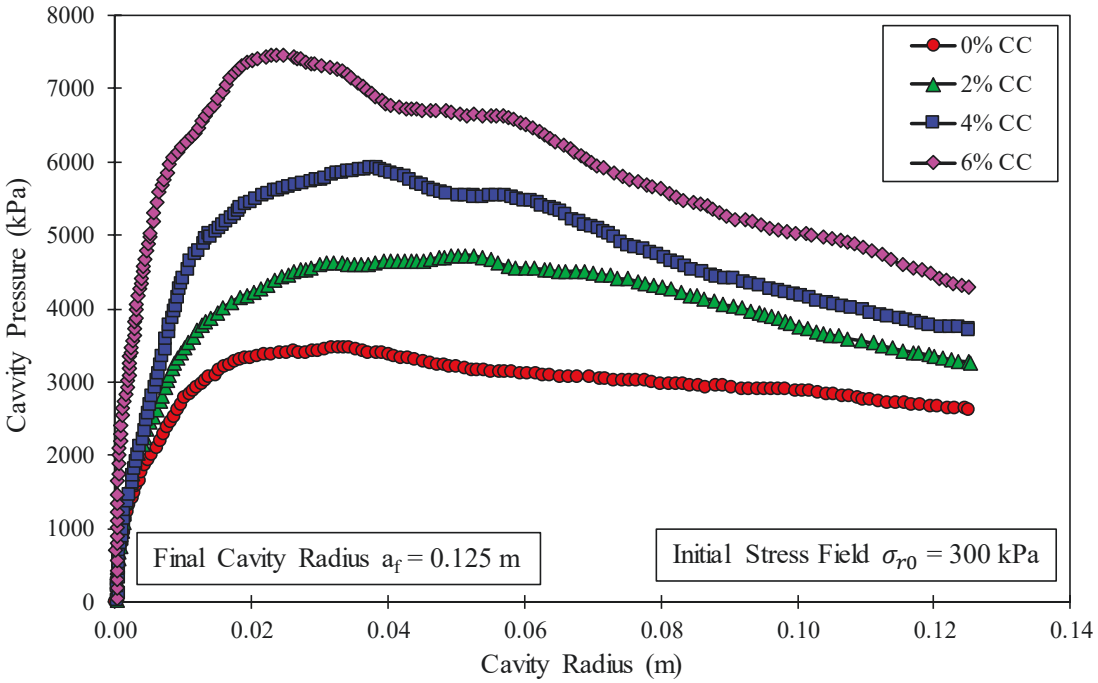


Figure 5.8 Cavity pressure variations during cavity expansion process

It is observed that the cavity pressure, as expected, increased with the cement content. This is simply due to the fact that increase in cement content introduced a cohesion intercept and a tensile strength to the sand, leading to the increase in the soil stiffness and strength (Clough et al. 1981; Lade et al. 1996; Consoli et al. 1998). Referring to Figure

5.8, the peak cavity pressure measured reveals a direct correlation with the cement content. For instance, the peak pressure measured for the sample with 6% cement content is approximately 7500 kPa, which is more than twice of that observed in the uncemented sample. However, the cavity pressure measured in all soils showed a continuous reduction after reaching the peak, and this softening behaviour was less pronounced as the cement content decreased. The strain softening behaviour in sand, in general, can be attributed to (a) the dilation or (b) the structural degradation of the cementation. However, since the calibration exercise reported in Figure 5.5 shows that dilatancy was supressed when the confining pressure reached 300 kPa (same as the adopted stress field in the cavity expansion simulation i.e. $\sigma_{r0}$ = 300 kPa), it may be reasonably deduced that the strain softening behaviour was largely dominated by the degradation of cementation bonds during the cavity expansion. Furthermore, it is noteworthy to mention that the cavity pressure, for both uncemented and cemented sands, appear to converge with the increase in the cavity radius. This is attributed to the fact that the cementation structure formed at the particle contacts underwent gradual de-structuration or degradation process (i.e. continuous bond breakage) under loading, leading to the reduction in both the shear and tensile strengths.

To assess the reliability of the numerical prediction and to validate the adopted cavity expansion modelling technique, the cavity pressures were compared with the results obtained from the computer program developed by Carter (1978), which adopts an elastoplastic constitutive model obeying Mohr-Coulomb failure law, requiring shear

modulus ($G$), Poisson's ratio ($\vartheta$), friction angle ($\emptyset'$), dilation angle ($\psi$), and cohesion ($c$). However, the numerical calculations proposed by Carter (1978) must necessarily initiate from a finite cavity radius to avoid an infinite circumferential strain, whereas all simulations presented in this chapter using DEM involved the creation of a cylindrical cavity (i.e. $a_0 = 0$). Hence, the constant volume theory proposed by Carter et al. (1979b) providing an adequate approximation to the cavity creation problems based on the analysis of expanding pre-existing cavities was considered. As discussed in Carter et al. (1979b), the creation of a cylindrical cavity from $r = 0$, to $r_f = \sqrt{3}a_0$ is equivalent to doubling the size of an existing cavity (i.e. from $a_0$ to $2a_0$), assuming a constant volume condition (i.e. $V_{0-\sqrt{3}a_0} = V_{a_0-2a_0}$). Since all cavity expansions simulated in this chapter using DEM commenced from a zero-initial radius to a final radius of 0.125 m ($r_f = 0.125$ m), the equivalent initial and final cavity radii required were determined to be to be 0.072 and 0.144 m, respectively.

Since the solution presented in Carter (1978) does not capture the cementation degradation effect, the upper and lower bounds approach was adopted. The upper bound captured the peak strength of the cemented sand without considering the cementation degradation, while the lower bound assumed no presence of the cementation, i.e. complete cementation degradation. In addition, due to the increase in confining pressure, as depicted in Figure 5.17, the shear modulus of the material considered would also increase accordingly. Hence, the effect of confining pressure on the shear modulus must be taken into account in the upper bound determination.

The variation of the shear modulus ($G$) with the mean effective stress ($p'$), proposed by

$$G = G_{ref} p_{ref} \left(p'/p_{ref}\right)^{n_e} \tag{5-5}$$

where, $p_{ref}$ is the reference pressure which is taken as atmospheric pressure of 100 kPa in this study, $G_{ref}$ and $n_e$ are modulus number and modulus exponent, respectively.

Since the laboratory experiments results adopted for calibration exercises were quite comprehensive, the shear modulus and modulus exponent could be readily computed by adopting the technique reported by Duncan et al. (1980). Indeed, Equation (5-5) can be transformed into Equation (5-6) facilitating the regression analysis to back calculate the shear modulus as a function of effective confining pressure:

$$\log\left(\frac{G}{p_{ref}}\right) = n_e \log\left(\frac{p\prime}{p_{ref}}\right) + \log G_{ref} \tag{5-6}$$

Based on triaxial test results reported by Abdulla et al. (1997) for adopted cemented sand subjected to various confining pressures, the modulus number and modulus exponents for sand with 6% cement were determined to be 501 and 0.4, respectively. In addition, considering that the maximum mean effective stress for cemented sand with 6% cement content reached 3 MPa during the cavity expansion, the corresponding shear modulus ($G$) was determined to be 195 MPa based Equation (5-5).

Hence, the upper and lower bounds of the cavity pressure - radius curves were determined based on Carter (1978) and plotted in Figure 5.9.

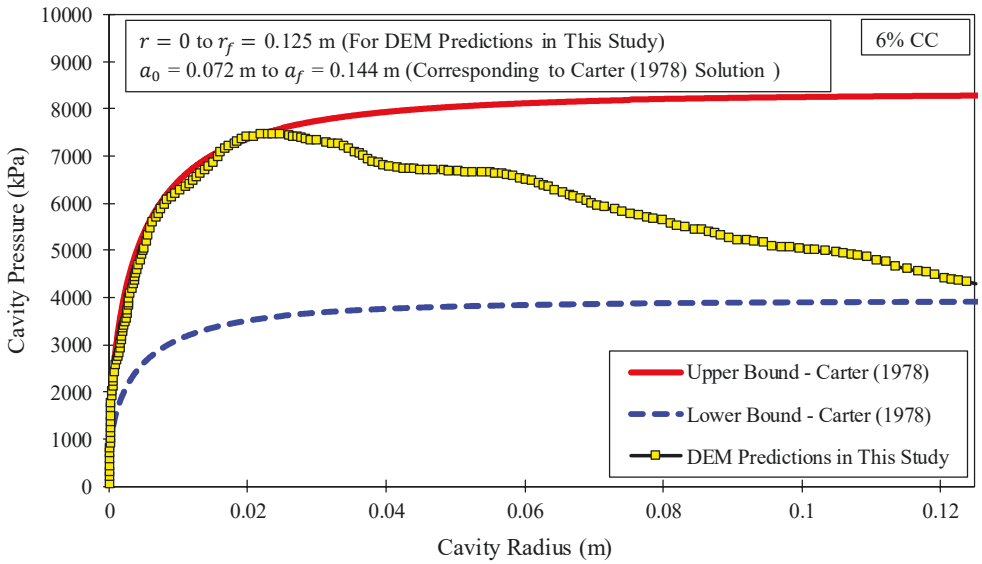


Figure 5.9 Comparisons between the DEM predictions and Carter's method for cavity expansions in 6% cemented sand

It is evident that the cavity pressure variation predicted by DEM simulation in this study lies in between the upper and lower bounds determined by Carter (1978), which confirms the validity of the pressure expansion curve predicted by DEM in this study capturing gradual cementation degradation during expansion.

### 5.6.2 Extent of Cementation Degradation

To obtain a better understanding about the extent of cementation degradation during the cavity expansion, the history of the bond breakage is plotted in Figure 5.10, with the horizontal axis being the cavity radius and the vertical axis being the normalised number of broken bonds.

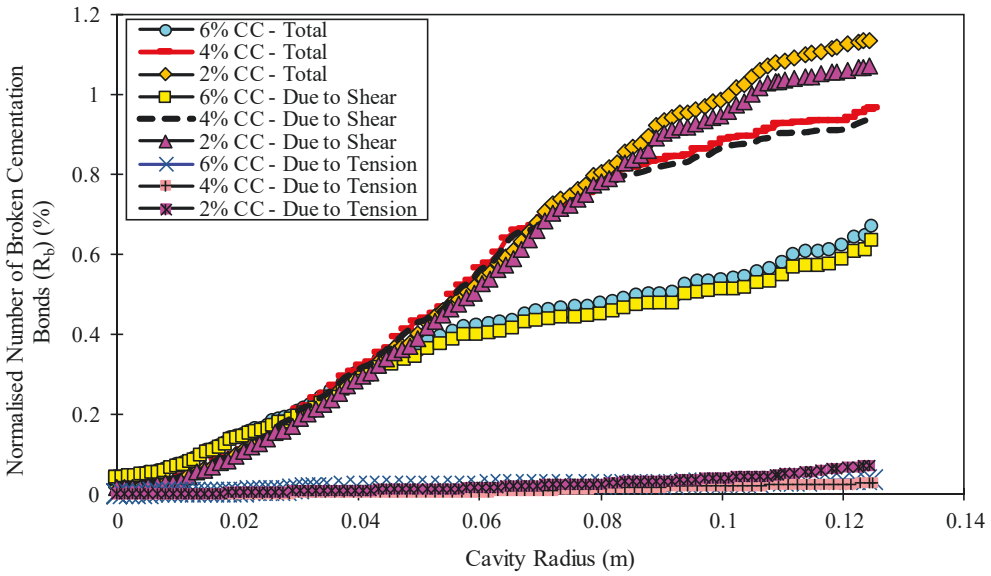


Figure 5.10 Normalised number of broken cemented bonds during cavity expansion

It should be noted that the normalised number of broken bonds (i.e. $R_b = N_b/N_c$) is defined as the ratio between the total number of cementation bonds (i.e. $N_c$) and the total number of broken cementation bonds (i.e. $N_b$), as illustrated in Figure 5.7 (b). It can be seen that for cemented sands with different cement contents, the number of bond breakage induced by shearing significantly overweighed that of due to tension. This implies that during the cavity expansion, the failure mode of the lightly cemented sand adopted in this study, was mainly controlled by the shear rather than tensile strength at the contacting interfaces. It must be highlighted that the failure mode of a cemented granular sample can be different given the same type of the test (e.g. triaxial test), which may depend on the particle size, sample anisotropy, the microscopic properties calibrated and so forth (Potyondy et al. 2004). For instance, de Bono et al. (2014b) reported that a vast majority

of bonds failed in shear rather than tension during the one-dimensional compression of cemented sand. However, Jiang et al. (2013) conducted an biaxial compression tests on loose cemented granular materials, and noticed that the occurrence of strain localization was associated with a concentration of bonds failing in tension. Hence, it is suggested that the contact parameters should be calibrated against realistic experimental tests before implementation. In addition, referring to Figure 5.10, it is noticed that the degradation of the cementation bonds was more significant during cavity expansion in samples with lower cement content (i.e. 2%), and the normalised number of broken bonds during the cavity expansion increased with the reduction in cement content.

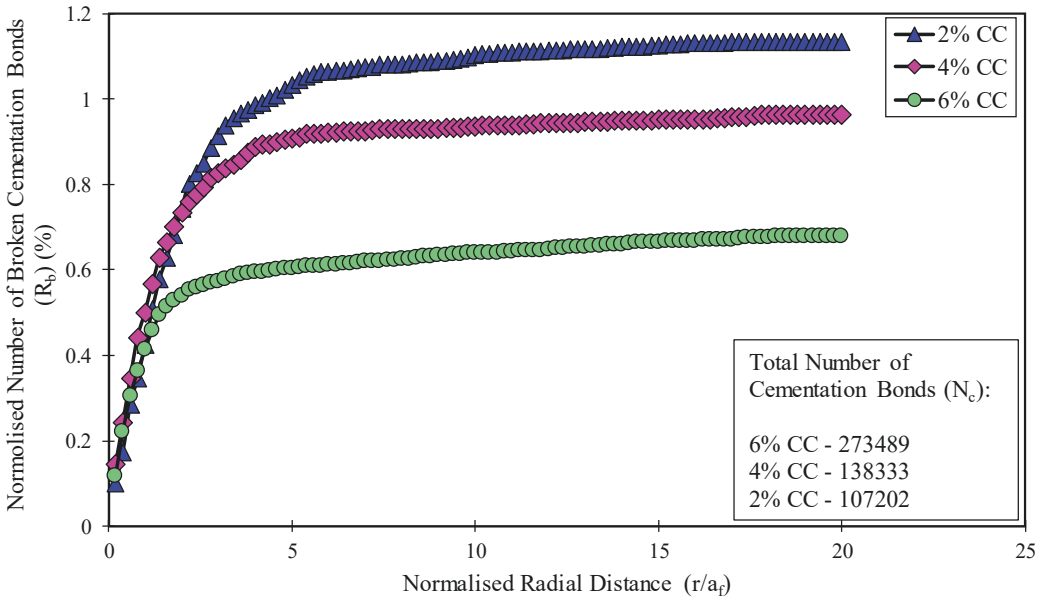


Figure 5.11 Normalised number of broken cemented bonds versus normalised radial distance at the end of cavity expansion

Figure 5.11 shows the normalised number of broken cementation bonds ($R_b$) versus the normalised radial distance ($r/a_f$) recorded at the end of cavity expansion. It can be seen that the normalised number of bond breakage increased dramatically with the radial distance up to $4a_f$ ($a_f$ being the final cavity radius = 0.125 m), less pronounced changes were observed for points further away from the cavity. It is interesting to note that the normalised number of broken cementation bonds (i.e. the portion or percentage of the broken cementation bonds) is larger in specimens with lower cement content (i.e. $R_{b-2\%\,\mathrm{CC}} > R_{b-4\%\,\mathrm{CC}} > R_{b-6\%\,\mathrm{CC}}$). Similar findings were also captured in Feng et al. (2017) when studying the triaxial behaviour of bio-cemented sands adopting DEM. This is simply attributed to the fact that the shear resistance and stiffness of specimens with lower cementation level are less than those of cemented sands with higher cement contents, and hence the cementation bonds became more fragile and easier to be broken under shearing. Additionally, the observed phenomenon may be also explained adopting the energy dissipation mechanics. Bolton et al. (2008) studied the micro- and macro-mechanical behaviour of crushable materials adopting DEM triaxial test simulations, and reported that a portion of energy stemming from the work input at the test boundaries (i.e. loading from the internal cavity in this study) would be dissipated in the form of bond breakage. Similar findings were also reported by Wang et al. (2008c) in characterising the cemented sand behaviour through experimental and numerical investigations. Hence, it is reasonable to conclude that specimens with less cement content (i.e. lower stiffness) would have a larger portion of cementation bond breakage, given the same cavity expansion progress (i.e. work input at the test boundaries). Referring to the results

reported in Figure 5.11, however, the influence zone, in which vast majority of cementation bonds (i.e. more than 85%) were broken due to the induced stress and strain fields during cavity expansion, could be reasonably considered to extend as far as $4a_f$ for all cemented specimens ($a_f$ being the final cavity radius = 0.125 m).

To further explore the characteristics of the cementation bond breakage and its influence on the soil response, the changes in volumetric strain based on the prediction sphere A (PSA) located at the radial distance of 0.5 $a_f$ from the internal cavity wall (as seen in Figure 5.7 (a)) is plotted in Figure 5.12 to compare with the variations in cavity pressure during the cavity expansion.

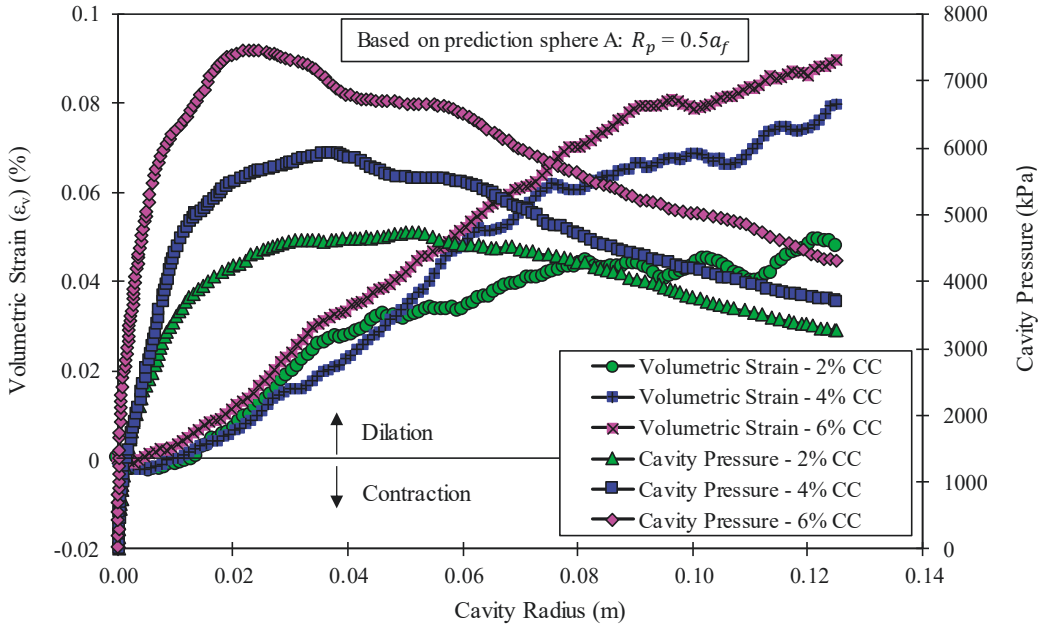


Figure 5.12 Relationship between the variations of volumetric strain and cavity pressure versus cavity radius

The softening behaviour observed in the cavity pressure in granular materials is often attributed to the dilation, and it is believed that a peak in the cavity expansion corresponds to the maximum dilatancy (i.e. the maximum gradient in the volumetric strain response) (Geng 2010; Dong et al. 2020). Similar findings were reported by Silvestri (2001) and Manassero (1989) when studying the drained self-boring pressuremeter tests in sands. However, these conclusions may not be fully applicable to the cases associated with cemented sand. According to Cuccovillo et al. (1999), de Bono et al. (2015) and Wang et al. (2008c), the presence of the cementation can hinder the dilatancy effects of the granular material, which means that the maximum dilatancy, unlike uncemented sand, does not occur at the strain level corresponding to the peak stress. This distinctive phenomenon is observed and confirmed in this study, as evident in Figure 5.12. Referring to Figure 5.12, the peak cavity pressures occurred slightly before the point corresponding to the maximum dilation gradient. Indeed, the observed offset increased with the cement content. In fact, this delayed dilation effect can be explained via fundamentals of the dilation in microscopic view. In granular material, the dilation initiates when a particle is riding over its neighbouring particles due to shearing, leading to the expansion in volume. However, such process cannot be achieved until the particles are free from the restrictions stemming from the cementation bond. Therefore, as shown in Figure 5.12, in cemented sands the maximum dilatancy takes place after the peak of the cavity pressure is reached. Considering the fact that the 4% and 2% cemented sand specimens contained more uncemented particles, the inhibition effects on the dilatancy were not as pronounced as the specimen with 6% cement content.

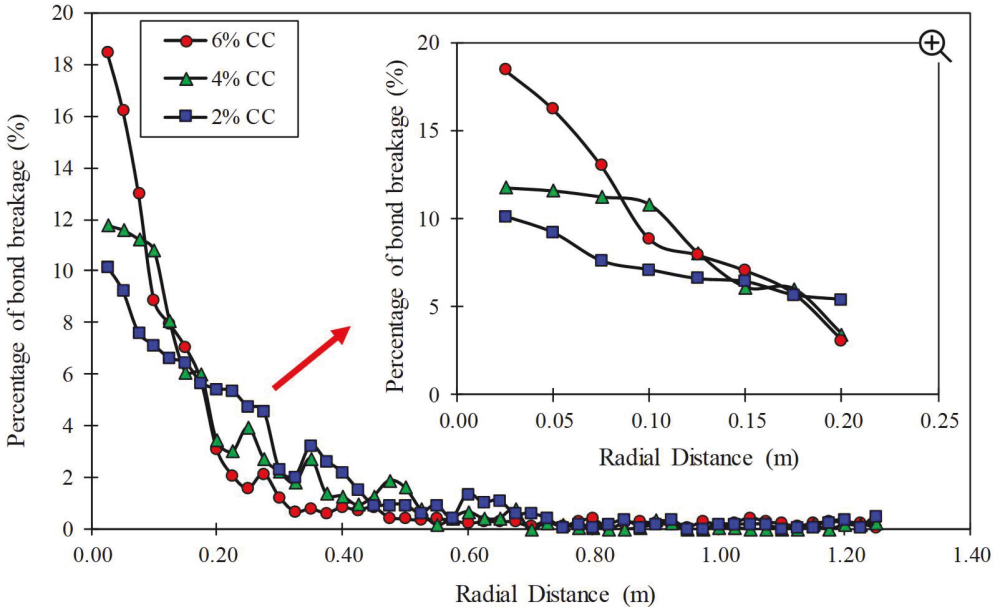


Figure 5.13 Variations of the local percentage of cementation bond breakage within radial distance at the end of cavity expansion

Figure 5.13 illustrates the variations of the local percentage of cementation bond breakage with radial distance. It is observed that the percentage of bond breakage showed a drastic and continuous decrease with the radial distance and approached zero when the radial distance exceeded 0.50 m (i.e. $4a_f$, representing the influence zone where the cementation bond breakage was notable). Additionally, it is interesting to note that for each adopted cement content, the maximum percentage of cementation bond breakage was observed at approximately 0.025 m radial distance (i.e. $4a_f$), as illustrated in Figure 5.13. Comparing it with the cavity pressure variations reported in Figure 5.8, Figure 5.13 shows that the maximum percentage of cementation bond breakages for 6% cemented sand occurred when the cavity radius reached approximately 0.025 m (i.e. $4a_f$), at which the cavity

pressure was also at its peak (refer to Figure 5.8). Similar trends were observed for cases with 2% and 4% cement contents. Hence, it can be reasonably asserted that the peak cavity pressure was reached when the breakage of the cement bonds reached its maximum. After reaching the peak, the number of cementation bond breakage gradually increased as the cavity expanded further, yet in a reducing rate. Similar observations were also captured by de Bono et al. (2015) when studying the micro mechanics of cemented sand by simulating triaxial test using DEM.

### 5.6.3 Variations of Volumetric Strains and Radial Displacement

During the installation of displacement based inclusions, including the driven piles, concrete injected columns (CIC) and vertical drains for ground improvement, the surrounding ground displacements are of the key concern for the contractors due to the potential risks of jeopardizing the existing structures and other neighbouring inclusions due to excessive lateral displacement (AS 1995).

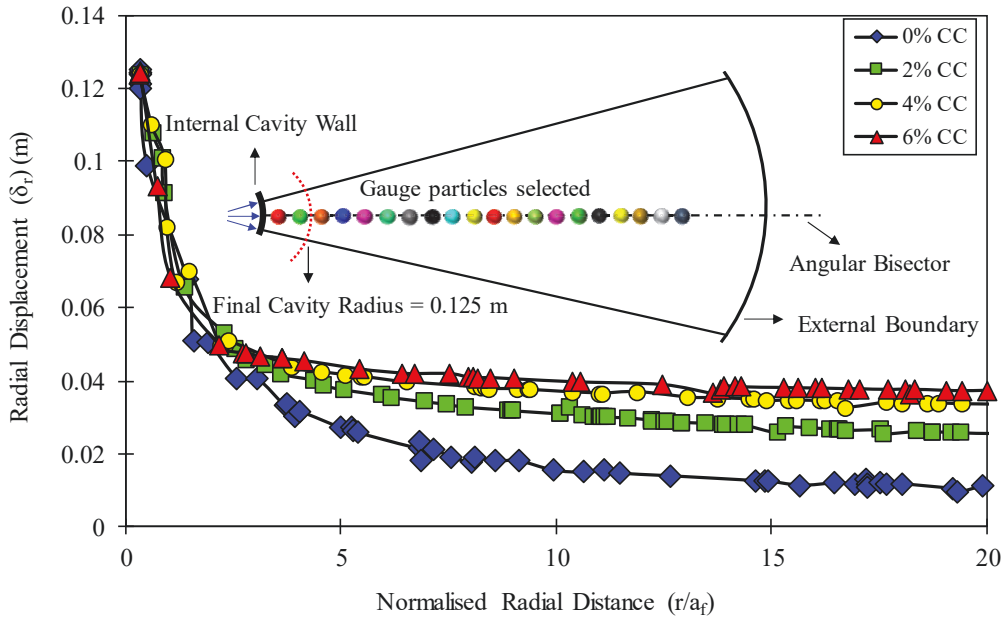


Figure 5.14 Radial displacement of selected gauge particles along the angular bisector at the end of cavity expansion

Figure 5.14 illustrates the radial displacement history of the selected gauge particles situated along the angular bisector. The displacements reported in Figure 5.14 are the radial displacements measured when the final radius of the cavity was established. It can be noted that the radial displacement variations at the end of the cavity expansion when the final cavity radius was reached show a similar trend in both the lightly cemented and uncemented sands. As expected, particles located closer to the internal cavity experienced larger radial displacements compared to those located further away, while the predicted radial displacements continuously dropped with the radial distance. It can be reasonably projected that the radial displacement would eventually approach zero when the radial distance is sufficiently larger than the internal cavity radius. As evident in Figure 5.14,

most significant radial soil displacements occurred in the vicinity of the cavity within the radial distance of $4a_f$ identified as the influence zone ($a_f$ being the final cavity radius) irrespective of the cement content. A similar influence zone size was also identified in Figure 5.13 when plotting the local percentage of cementation bond breakage with radial distance. It should be noted that soils with higher cement content experienced more notable displacement due to cavity expansion beyond the influence zone. For instance, for a given radial distance of 20 $a_f$, the uncemented soil experienced 0.01 m of radial displacement due to cavity expansion, while a 0.04 m radial displacement was observed for the sand with 6% cement. This is attributed to the fact that uncemented specimens, due to the lack of cementation, are more discrete with less structural cementation bonds, thus less cable of transferring the displacements to a greater distance, compared to cemented materials with chain of cemented particles helping to transfer the displacements further away from the internal cavity. This explanation is especially true considering that a majority of cemented bonds outside the influence zone (i.e. $r > 4a_f$; $r$ being the radial distance from the internal cavity wall) had remained intact as shown in Figure 5.13.

To further assess the rationality of the predicted radial displacements induced by cavity expansion reported in Figure 5.14, the variations of soil volumetric strains are presented in Figure 5.15.

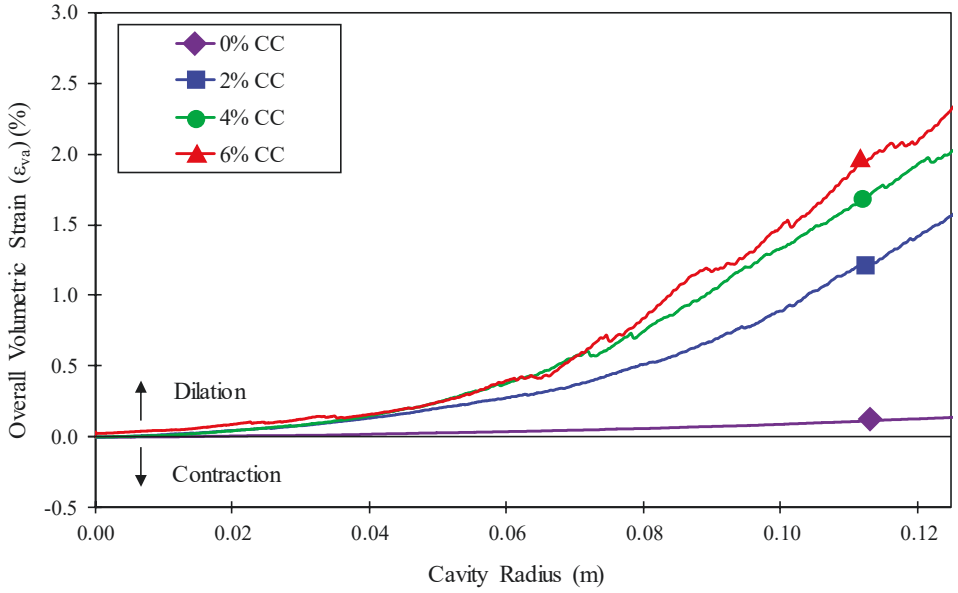


Figure 5.15 Volumetric changes of the entire model during cavity expansion

As explained earlier, the top and bottom facets of the cavity expansion model were fixed in position to simulate the plane strain condition, while the external boundaries were servo-controlled to maintain a constant radial stress as in-situ. Indeed, with an increase in the internal cavity radius, the external boundary will move radially to satisfy the stress boundary condition. Referring to Figure 5.15 it is observed that all specimens show a different level of dilation during the cavity expansion, among which the sand with 6% cement experienced the largest volumetric changes while the uncemented sand (i.e. 0% cement) corresponded to the least volumetric strains. This finding is consistent with the radial displacement variations reported in Figure 5.14, where the radial displacement induced by cavity expansion during the cavity expansion was mainly due to the volumetric changes of the soil. Furthermore, according to Figure 5.15, it can be readily

concluded that introducing the cementation could increase the dilatancy during shearing, and the changes in volumetric strains increased as degree of cementation increased. Moreover, since all specimens were generated with identical initial void ratio (i.e. $e_0$= 0.66), it can be reasonably deduced that the dilatancy during the cavity expansion simulations were mainly governed by the breakage of cementation bonds instead of relative density. Taking the sand with 6% cement content as an example, the cementation bond breakage occurring during the cavity expansion resulted in some level of cementation degradation (i.e. breakage of some of the cemented bonds), forming large particle clusters. These clusters could form a new structure with interlocking which could lead to an increase in soil dilation during shearing.

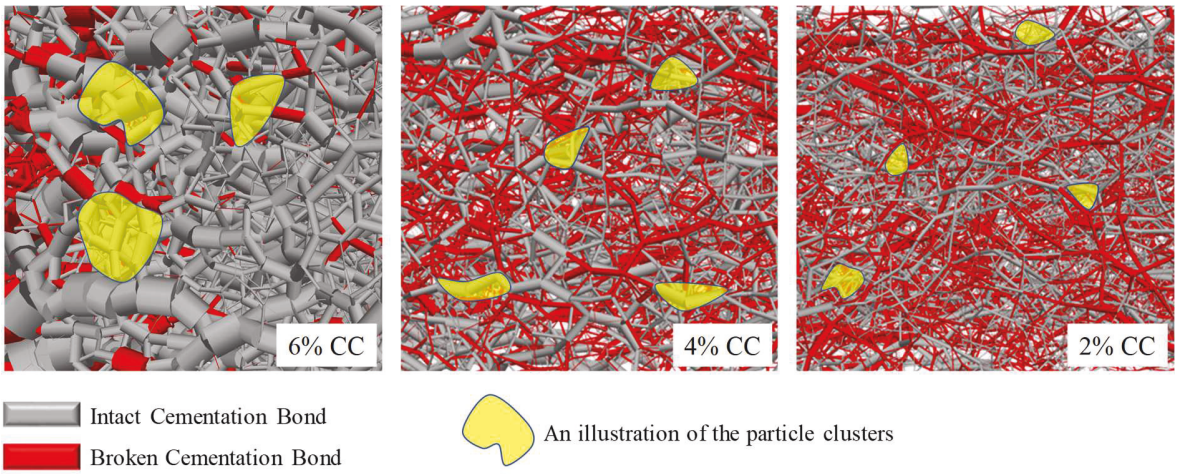


Figure 5.16 Network of intact and broken cementation bonds for cemented sand specimens with different level of cementations

Figure 5.16 shows the network of intact and broken cementation bonds for cemented sand specimens with different level of cementations, which can be adopted to relate to the formation of clusters during the cavity expansion as cementation degradation progressing. Referring to Figure 5.16, the broken cementation bonds segmented the cemented sand into pieces, and the portion with intact cementation bonds formed particle clusters, as depicted in Figure 5.16, which enhanced the dilation under shearing. Since the samples with higher cementation level (e.g. 6%) consisted of more and larger clusters during shearing, as it can be seen from Figure 5.16, the dilatancy exhibited could be inevitably more pronounced than soils with lower cement content. It should be noted that similar observations were also reported by other researchers for the response of cemented sands during loading (Clough et al. 1981; Saxena et al. 1988a; de Bono et al. 2015).

### 5.6.4 Stress Paths during Cavity Expansion

To study the effects of cementation degradation on the soil response during the cavity expansion, the stress paths were plotted in the $p' - q$ plane based on the prediction spheres A, B and C (i.e. PSA, PSB and PSC), located at 0.5 $a_f$, 1 $a_f$ and 2 $a_f$ (see Figure 5.7), respectively, as illustrated in Figure 5.17.

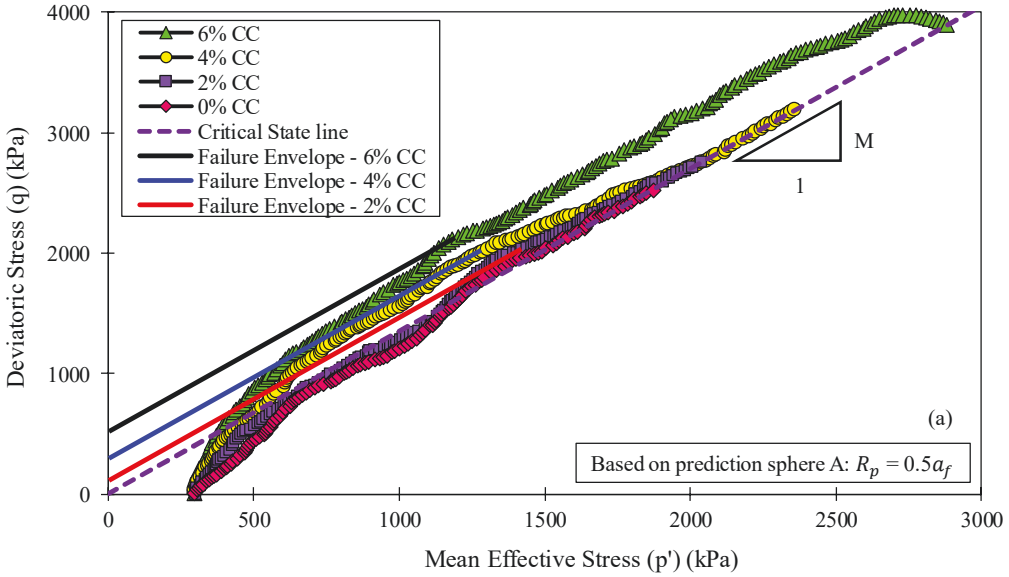
6% CC
4% CC
2% CC
0% CC
Critical State line
Failure Envelope - 6% CC
Failure Envelope - 4% CC
Failure Envelope - 2% CC
M
1
(a)
Based on prediction sphere A: $R_p = 0.5a_f$
Deviatoric Stress (q) (kPa)
Mean Effective Stress (p') (kPa)
0
1000
2000
3000
4000
0
500
1000
1500
2000
2500
3000

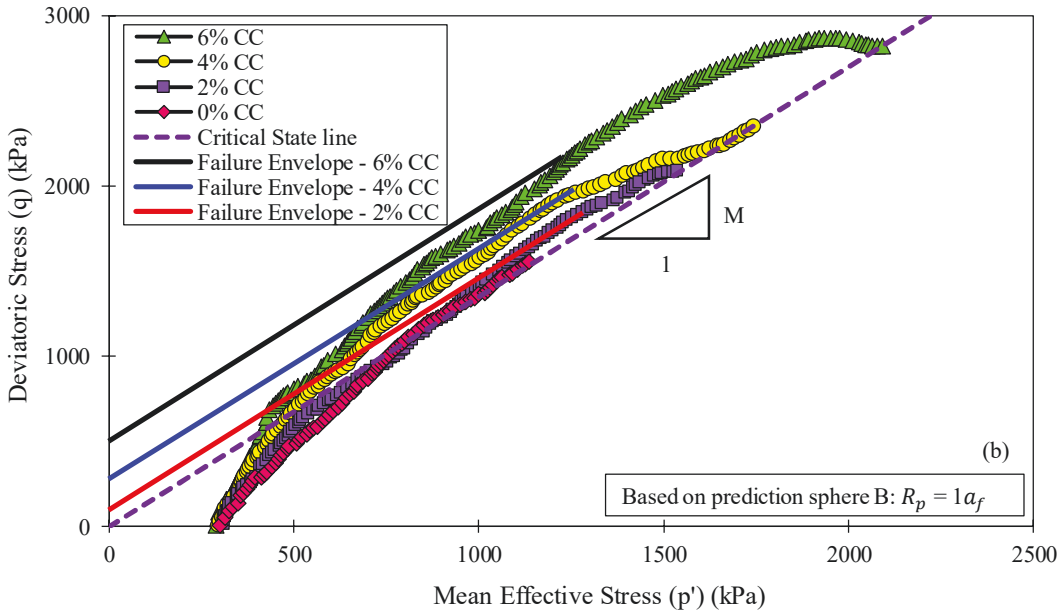
6% CC
4% CC
2% CC
0% CC
Critical State line
Failure Envelope - 6% CC
Failure Envelope - 4% CC
Failure Envelope - 2% CC
M
1
(b)
Based on prediction sphere B: $R_p = 1a_f$
Deviatoric Stress (q) (kPa)
Mean Effective Stress (p') (kPa)
0
1000
2000
3000
0
500
1000
1500
2000
2500

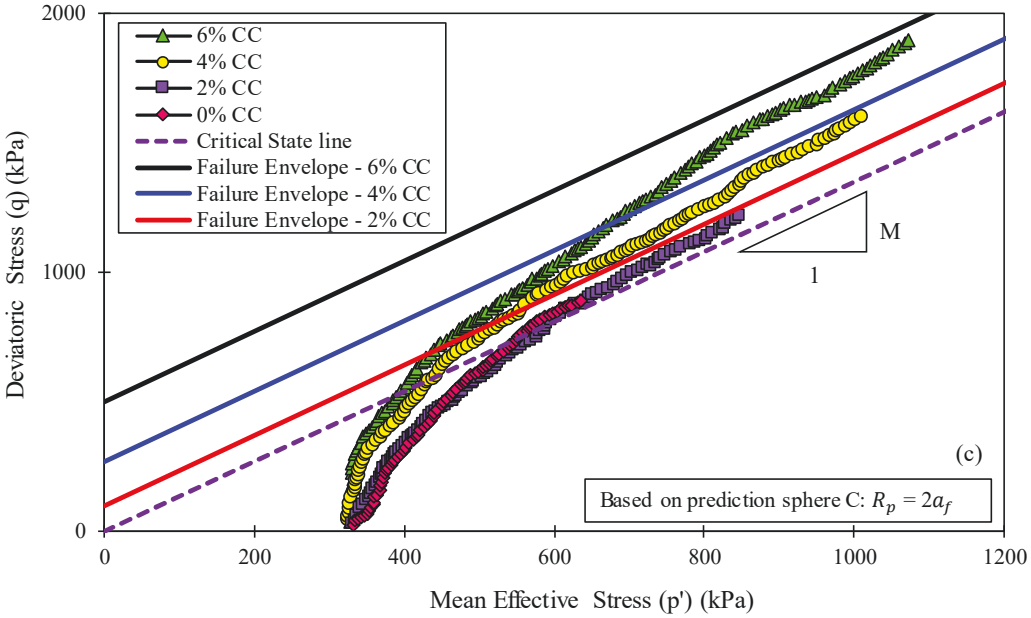


Figure 5.17 Stress path plotted based on different prediction spheres for cavity expansions in sand specimens with different level of cementations

Referring to Figure 5.17 for all stress paths measured at different locations during the cavity expansion process, the soil with higher cement content experienced larger mean effective and deviatoric stresses. For further understanding of the effects of cementation degradation on the stress path, the critical state line and the failure envelopes in $p' - q$ plane were plotted in Figure 5.17. According to Negussey et al. (1988) and Bolton (1986), the constant volume friction angle is unique, which is a material constant and depend on the mineral composition. Previous experimental studies (Clough et al. 1981; Abdulla et al. 1997) showed that the critical state friction angle does not altered by the cement content, since when the critical state is reached, the cementation bonds are broken along the failure line. Hence, the slope of the critical state line ($M$) depends on the stress-

dilatancy relationship for the static equilibrium of an assembly of particles in contact; indeed referring to Rowe (1962) and Schanz et al. (1996), the following equations were adopted in this study to determine $M$.

$$q = Mp' \tag{5-7a}$$

$$M = \frac{6\,sin\emptyset'_{cv}}{3-sin\emptyset'_{cv}} \tag{5-7b}$$

$$sin\emptyset'_{cv} = \frac{sin\emptyset_f - sin\psi_f}{1-sin\emptyset_f sin\psi_f} \tag{5-7c}$$

where, $\emptyset_f$ and $\psi_f$ are the ultimate values of the friction and dilation angles, and $\emptyset'_{cv}$ is the constant volume friction angle.

Based on the experimental tests reported by Abdulla (1992) and adopted in the calibration exercise in this study, and referring to Bolton (1986), the slope of the critical state line (i.e. $M$) was calculated to be approximately 1.35. In addition, based on the experimental tests conducted with different confining pressures, the corresponding mean effective stress and the deviatoric stress in a conventional triaxial test state could be readily calculated adopting the following equations,

$$\left.\begin{aligned} q &= \sigma_1 - \sigma_3 \\ p' &= \frac{\sigma_1 + 2\sigma_3}{3} \end{aligned}\right\} \tag{5-8}$$

where, $\sigma_1$ is the major principle stress and $\sigma_3$ is the minor principle stress (i.e. lateral confining pressure) in a Mohr's circle setting.

Based on the calculated stresses, the failure envelop of the cemented sand could be plotted in the $p' - q$ plane, as shown in Figure 5.17. There were a total number of three failure envelopes plotted for specimens with varying cement content (i.e. corresponding to 2% CC, 4% CC and 6% CC). It must be highlighted that these failure envelopes were parallel to each other with the only difference being the vertical axis intercepts that were calculated based on the cohesion reported in Abdulla et al. (1997).

It can be observed that all stress paths plotted initially move upwards passing through the critical state line, confirming the strain softening behaviour occurring during the cavity expansion. In addition, with the increase in the mean effective stress (i.e. confining pressure), the stress path became non-linear and gradually approached its failure envelope, after which the stress path remained on the failure envelope and showed a slight reduction in its slope (i.e. the concave in the stress path) and bended towards the critical state line, confirming that the failure envelope of a cemented sand is nonlinear. In fact, the failure envelopes were plotted as straight lines in Figure 5.17 based on the simplification that the strength of the cemented sand remained constant. However, as discussed earlier and also reported in Nguyen et al. (2017), the actual failure envelope of cemented soils is non-linear since the cementation degradation gradually reduces the strength of the cemented sand.

The slope of failure line at the initial stages of cavity expansion corresponds to the stresses and strains experienced by the soil which are not sufficiently large causing the cementation degradation, whereas the slope at the final stages is impacted by the mean

effective stress and shear strains experienced by the soil which would be considerably large inducing significant cementation degradation contributing to reduction in the shear strength. In between of these two stages, continuous cementation degradation occurs with the increase in mean effective stress, leading to a non-linear failure envelope eventually merging with the critical state line.

Referring to Figure 5.17, the concave stress path after failure point is evidently observed for cemented specimens, in particular for the stress paths plotted based on the prediction spheres situated at 0.5 $a_f$ and 1 $a_f$, while this phenomenon was not observed in uncemented sand as the softening due to breakage of cementation bonds was absent. This confirms that the stress path and failure envelope would merge with the critical state line (CSL), since the cementation degradation due to volumetric and shear strains experienced by the soil during cavity expansion occurs. As evident in Figure 5.17, the shifting between the critical state line and the failure envelope and subsequent merging of two as a result of cementation degradation are more pronounced in the soils with higher cement contents. Furthermore, as shown in Figure 5.17, for stress paths plotted based on the prediction sphere C (PSC) situated at 2 $a_f$ (refer to Figure 5.7 (a))the failure envelopes of cemented sands were not yet reached during the adopted cavity expansion and obviously expansion to larger cavity would have been required to see the stress path meeting the failure envelope. This is due to the fact that the bond breakage at the prediction sphere C, located farthest away from the cavity wall, was not as significant as the locations closer to the internal cavity (i.e. predication spheres A and B).

Indeed, the presence of the cementation bonds leads to the increase in cohesion intercept, leading to an enhanced shear and tensile strengths. In many constitutive models developed for cemented soils, this enhanced shear resistance due to cementation is captured. However, many of the developed models (e.g. structured Cam Clay model) consider a linear failure envelope parallel to that of reconstituted clay for the sake of simplicity (Liu et al. 2002; Horpibulsuk et al. 2010). However, observations in this study reported in Figure 5.17, confirm that the failure envelope of the cemented sand should be nonlinear and different from the failure envelope of the over consolidated soils since the cementation degradation occurring due to volumetric and shear strains would lead to the reduction in shear strength, and theoretically when all the cementation bonds are broken, the shear strength of cemented soil would be comparable with the uncemented soil. Therefore, the recognition of the cementation degradation during cavity expansion is essential when assessing the post-installation properties of the soil in the vicinity of the cavity.

### 5.5.5 Deviatoric Stress Variations

Figure 5.18 shows the variations of deviatoric stress during the cavity expansion based on the stresses and strains calculated from the prediction spheres situated at $0.5\,a_f$ (prediction sphere A), $1a_f$ (prediction sphere B) and $2a_f$ (prediction sphere C).

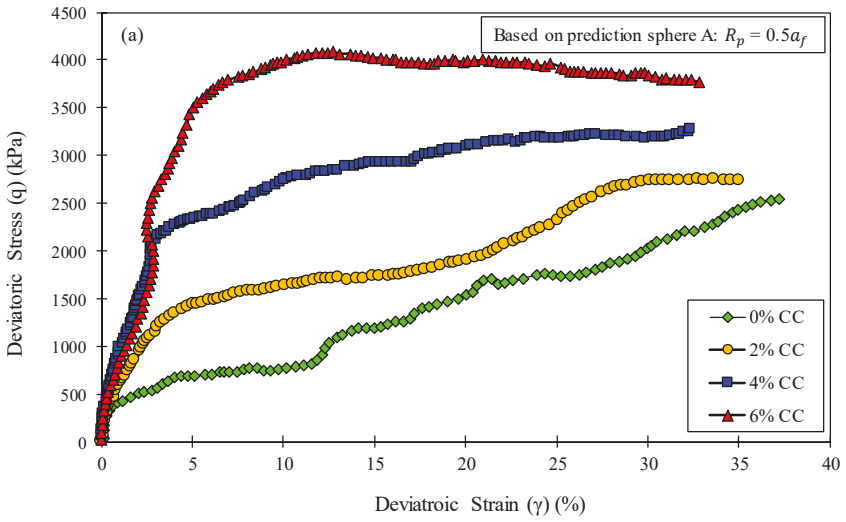
(a)
Based on prediction sphere A: $R_p = 0.5a_f$
0% CC
2% CC
4% CC
6% CC
Deviatoric Stress (q) (kPa)
Deviatroic Strain (γ) (%)
0
500
1000
1500
2000
2500
3000
3500
4000
4500
0
5
10
15
20
25
30
35
40

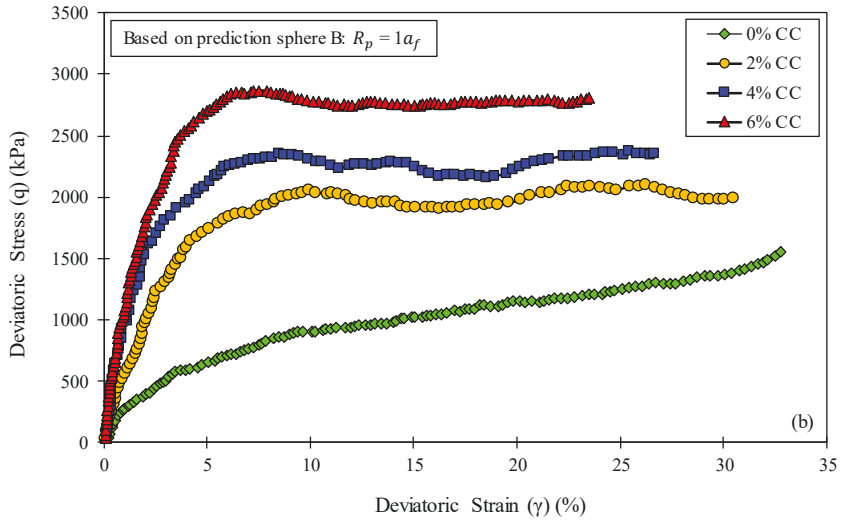
Based on prediction sphere B: $R_p = 1a_f$
0% CC
2% CC
4% CC
6% CC
(b)
Deviatoric Stress (q) (kPa)
Deviatoric Strain (γ) (%)
0
500
1000
1500
2000
2500
3000
3500
0
5
10
15
20
25
30
35

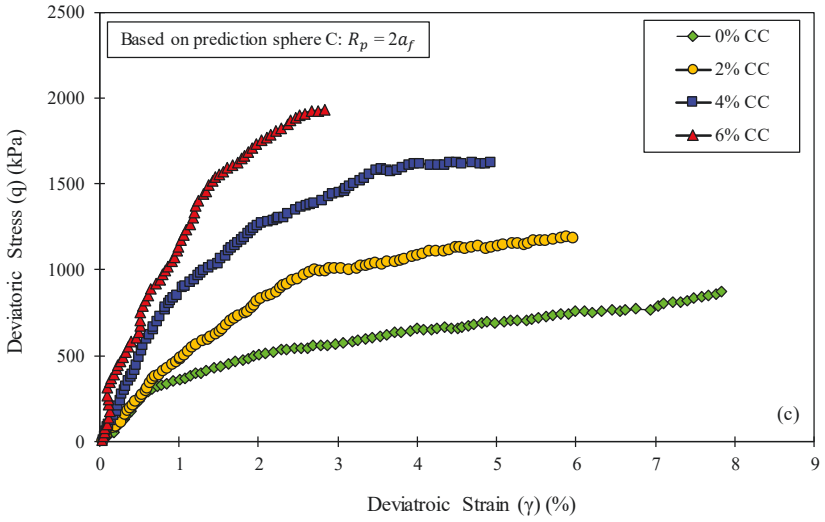


Figure 5.18 Deviatoric stress variations plotted based on different prediction spheres for cavity expansions in sand specimens with different level of cementations

It can be observed that during the cavity expansion, the specimen with the highest cement content (i.e. 6%) experienced the largest deviatoric stresses, for a given level of deviatoric strain. However, as evident in Figure 5.18, the addition of cement resulted in reduced level of deviatoric strains, with the uncemented sand experiencing the largest deviatoric strains during the cavity expansion. For instance, the deviatoric strain of the uncemented sand reaches 8% at the prediction sphere C (i.e. at $2a_f$), after the cavity was fully expanded, whereas a 3% deviatoric strain was predicted for sand with 6% cement. Indeed, since the sand with higher cement content had a higher shear resistance, and therefore expanded yield surface, the corresponding deviatoric strains experienced by the soil for a given size of cavity, were less.

It is interesting to notice that a peak in the deviatoric stress was observed during the cavity expansion in the sand with 6% cement, as depicted Figure 5.18 (a) and (b) in the vicinity of the cavity. In fact, in many laboratory experiments such as triaxial and direct shear tests reported by other researchers (Cornforth 1964; Green et al. 1975), a peak in deviatoric stress were observed in dense sand due to dilation. However, in cavity expansion, the peak in deviatoric stress is often suppressed due to the abrupt increase in mean effective stress (i.e. confining pressure) during the cavity expansion, especially in the plane strain condition. Due to the sharp increase in the mean effective stress during cavity expansion (see Figure 5.17) in uncemented sand, the shear strength of the sample continuously increased, and therefore the peak in the deviatoric stress did not appear; indeed the shear strength increase due to the increased confinement overweighed the corresponding decrease due to strain softening as a result of soil dilation. Similar findings were also reported by Manassero (1989) and Silvestri (2001) in studying the self-boring pressuremeter test. However, the evident peak in the deviatoric stress experienced by the sand with 6% cement shows that the impacts of the rate of the cementation degradation overweighed the rate at which the mean effective stress increased during the cavity expansion. In-situ tests such as CPT are often carried out in soils to derive the geotechnical parameters required for design of foundations such as piles and concrete injected columns. Authors' experience shows that in some circumstances on site, the pre-installation soil strength estimated from the CPT test surpass the post-installation values, which indicates the ground strength loss due to installation effects. The results reported in Figure 5.18 are in line with these field observations, which shows that structured soils

may experience degradation of cementation as a result of ground movements during installation (i.e. cavity expansion), which in turn contributes in the reduction of the soil strength. Hence, it is suggested that the choice of spacing between adjacent columnar inclusions (e.g. piles or CIC) should be deliberately considered by the design engineer to alleviate the adverse effects exerted due to installation in structured soils.

### 5.5.6 Variations of Volumetric Strains

The volumetric strain histories recorded during the cavity expansion were plotted in Figure 5.19.

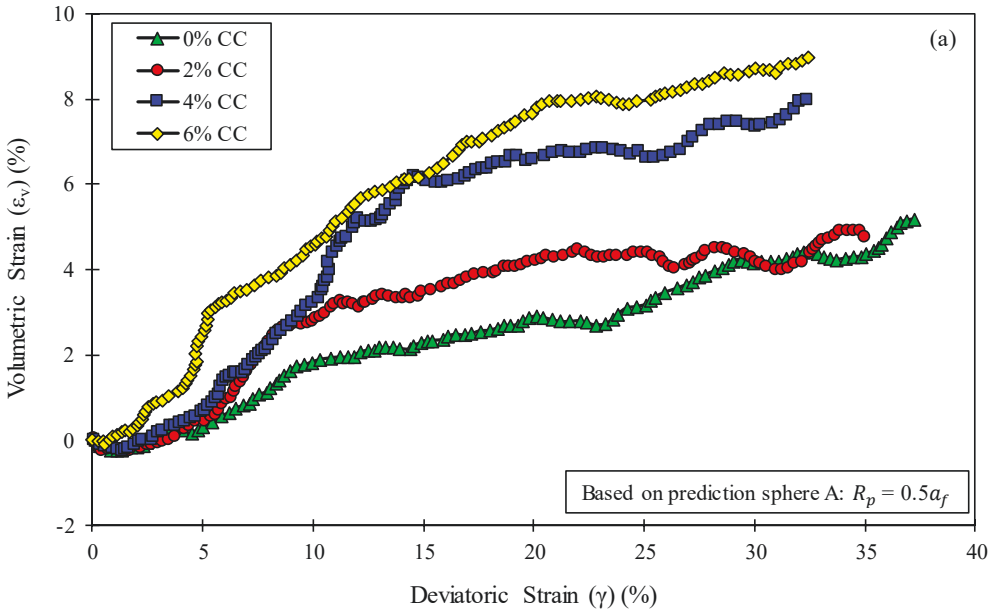

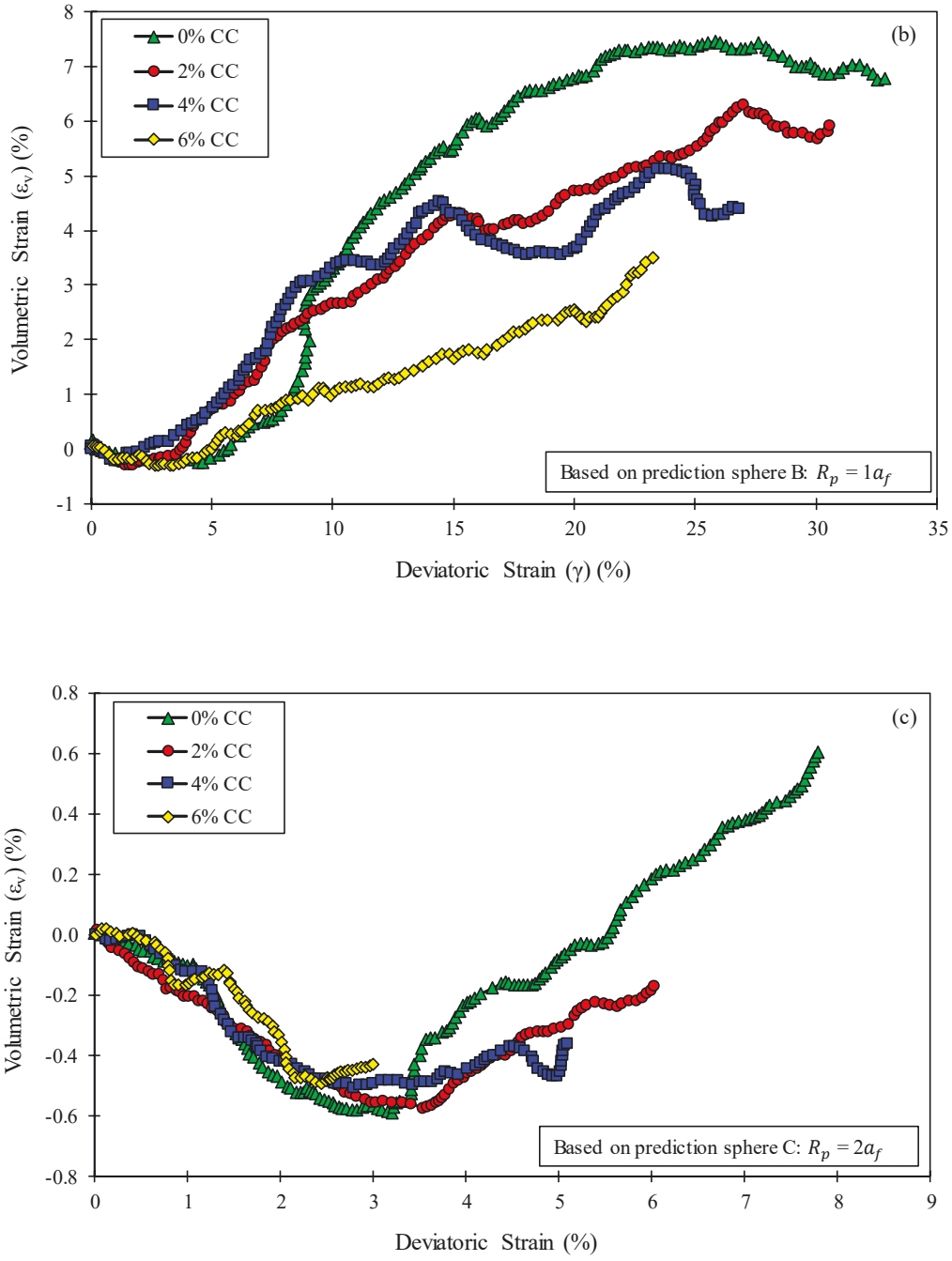


Figure 5.19 Volumetric strain variations plotted based on different prediction spheres for cavity expansions in sand specimens with different level of cementations

It must be clarified that the volumetric strain described in this section are localised volumetric strain computed based on different prediction spheres (see Figure 5.7(a)), and therefore it must be differentiated from the average volumetric strains of soil within the model boundaries reported earlier in Figure 5.15.

According to Figure 5.19, the predicted volumetric strains at radial distances of $0.5a_f$ (prediction sphere A) and $1a_f$ (prediction sphere B) reveal an overall dilative behaviour for the soil, especially where the measurements were taken in the vicinity of the internal cavity. For instance, the volumetric strain variations reported for the cavity expansion at $0.5a_f$ (prediction sphere A) in Figure 5.19 (a) shows a continuous and prompt dilation as soon as the expansion initiated. However, a slight contraction at the beginning of expansion was observed at the prediction sphere B located at the radial distance of $1a_f$, followed by a continuous dilation as the cavity expanded further. Farther away from the internal cavity (e.g. $r = 2a_f$), the dilation was only observed in uncemented sand (see Figure 5.19 (c)), with all cemented specimens exhibiting an overall contraction during the cavity expansion process.

However, the volumetric strain variations recorded based on the prediction sphere A location at $0.5a_f$ (i.e. Figure 5.19 (a)), showed an inverse relationship with the cement content, in contrast to the predictions at other measurement spheres B and C located farther away at $1a_f$ and $2a_f$ (i.e. Figure 5.19 (b) and (c)), correspondingly. Referring to Figure 5.19 (a), when the cavity expanded halfway through, the sand with 6% cement content resulted in the largest volumetric strains, whereas the uncemented sand

experienced the least. These findings bear a strong resemblance to the average volumetric strains within the model boundaries reported in Figure 5.15. Indeed, many triaxial tests conducted on the cemented sand by other researchers had indicated that the increase in the level of cementation led to the increase in dilatancy (Clough et al. 1981; Wang et al. 2008c). This is due to the fact that larger cemented clusters were formed after breakage of some of cementation bonds (see Figure 5.16) in the sand containing higher cement content, which intensified the interlocking between adjacent particle clumps and thus led to a higher volumetric change under shearing as observed in Figure 5.19 (a). However, as illustrated in Figure 5.13, the percentage of bond breakage farther away from the cavity wall (i.e. $1a_f$ and $2a_f$) was considerably less, which implied that there were a larger number of cementation bonds remaining intact, restricting the dilation between adjacent particles as explained earlier.

The findings presented in this study clearly shows that the response of lightly cemented sand to cavity expansion is controlled by the level of cementation. Indeed, in many geotechnical designs, ranging from shallow footings to deep foundations in lightly cemented sands, the cementation effect is often neglected and the design parameters are derived based on the uncemented sand characteristics (Lunne et al. 2002). Results of this study show that in the pile design for instance, analysis needs to be carried out to estimate the required force to open a cavity so the required driving force and the type and size of the equipment (e.g. piling rig, hammer) can be efficiently selected. Indeed, by choosing

the appropriate driving force, the installation of piles and inclusions to the required depth can be achieved without any risk of damage.

On the other hand, the potential effects of the cementation degradations should be deliberately considered by the design engineers to avoid overestimation of the shear strength. For instance, installation of inclusions in lightly cemented sand would inevitably lead to the breakage of cementation bonds in the surrounding soil, impacting the skin friction of the inclusion and settlement of the soil between inclusions. Indeed there are research studies showing that how the miscalculation of the skin friction can impact the axial capacity of the pile, especially when the bedrock is very deep and floating piles are adopted (McClelland 1974; Murff 1987; Ismael 1989, 1990). Additionally, when driven piles or concrete injected columns are utilised to improve the stability of slopes (Yang et al. 2011), the degradation of cementation in the soil induced by the installation effects should be accurately assessed for the sake of safety and reliability.

Furthermore, the results of this study show that when the in-situ soil is structured, the installation effects of piles and inclusions can be extended farther away from the external wall of the expanded cavity, and the soil dilation and subsequently ground heave in the vicinity of the expanded cavity are also more evident. Hence, extra care must be taken when assessing the installation effects of ground inclusions in the vicinity of existing underground structures such as pipelines in lightly cemented sands.

## 5.7 Summary

In the installation of displacement-based inclusions, the cementation level played an important role in determining the soil response. Increasing in cement content leads to the increase in the material strength through the increase in cohesion and tensile strength at the contacting interfaces, whereas the friction angle is not altered notably. Hence, the failure envelope of the cemented sand gradually merges with the critical state line due to the cementation degradation, particularly at a high confining pressure. In addition, with an increase in cement content, the soil dilation was more pronounced at points located at a closer radial distance to the internal cavity. However, with the increase in radial distance where the structure of the cementation remains intact, the dilation was impeded since the cementation led to a lower degree of freedom for particles overriding each other.

Hence, based on the studies carried out in lightly cemented sand, it is suggested that the softening behaviour of cemented soils during cavity expansion due to breakage of cementation bonds should be considered by design engineers when assessing the strength characteristics of the lightly cemented sands in the vicinity of an expanded cavity (e.g. installation piles or concrete injected columns). In addition, care must be taken by practicing engineers when piling in lightly cemented sand in the presence of neighbouring structures and facilities.

# Chapter 6 - Impact of Initial In-Situ Stress Field on Soil Response During Cavity Expansion Using Discrete Element Simulation

## 6.1 General

The installation of rigid inclusions in soils is influenced by the initial stress field in situ, however there is a very limited number of investigations conducted to study such effects on the soil response. Also, in discrete element modelling, the particle upscaling technique is often adopted to reduce the number of particles involved in a simulation in order to reduce the computational effort. However, the potential effects of this technique are not well recognised and understood.

Hence, in this chapter, a three-dimensional numerical analysis has been conducted using PFC$^{3D}$ to investigate the soil response under different initial stress conditions during cavity expansion. To examine the effects of the initial in-situ stresses, several cylindrical cavities were created and expanded gradually from an initial radius to a final radius, while stress and strain variations were monitored during the entire simulation. Besides the investigation on the impacts of initial stress field, a series of three-dimensional numerical models with different size scaling factors have been developed. Cavity pressure variations, stress-strain responses and radial displacement of gauge particles obtained from different simulations were discussed and compared. The results obtained confirmed that the initial

stress conditions have significant effects on the soil response during cavity expansion, and it is observed that the particle scaling factor beyond a certain limit can affect the soil response during cavity expansion.

## 6.2 Introduction

The recent advancement in computational technology has facilitated the application of discrete numerical analysis for many complex geotechnical problems. For instance, installation of driven pile or self-boring pressuremeter in cohesionless materials are often simulated using Distinct Element Method due to its merits in coping with problems involving large displacement (Jiang et al. 2006; Falagush et al. 2015). To interpret the installation mechanism of driven piles and self-boring pressuremeter, cylindrical cavity expansion modelling has been employed by many researchers (Gibson 1961; Carter et al. 1979b; Fahey 1986). Extensive research has been conducted to investigate cavity expansion mechanism in sandy soils adopting different techniques such as analytical solutions and numerical analysis based on continuum method (Carter et al. 1985; Collins et al. 1992). However, closed form solutions and many constitutive models adopted in numerical simulations have been obtained from a number of idealised material models and therefore may not capture the realistic behaviour of soil, particularly elastoplastic response (Carter et al. 1979b). Thus, the discrete element method may be an alternative to investigate the mechanical behaviour of granular materials at the microscopic level due to its discontinuous nature (Cundall et al. 1979). Despite the fact that there are studies conducted to investigate the soil behaviour during cavity expansion using DEM, the

impacts of initial stress filed is not well understood since there is a very limited number of investigations conducted to study such effects on the soil response. Besides this issue, when analysing the problems in a microscopic view adopting discrete element method, there are inherent constraints that impede its practicality in dealing with large-scale problems due to the significant computing requirements (O'Sullivan 2011). For instance, a laboratory scale triaxial test on a sand specimen with 30 mm diameter and 60 mm height would comprise approximately 4 million particles. Directly mapping such a huge number of particles into the simulation is unrealistic and computationally infeasible. Hence, only by reducing the number of particles, the analyses can become efficient and possible (O'Sullivan 2011). As a result, there are numerous approaches proposed to accelerate the simulation process (e.g. periodic cell boundaries, particle refinement), yet chief among these is the particle upscaling technique. It is to enlarge the particle size and therefore reduce the number of particles by multiplying a coefficient to the particle radius whereas maintaining the identical model size, void ratio and coordination number. Although this technique has been extensively adopted by many analysts, there is a lack of studies conducted on the effect of particle scaling on the simulation results (Jiang et al. 2006; Arroyo et al. 2011). As a matter of fact, without changing the model size, reducing the particle numbers by means of particle upscaling may enhance the efficiency of numerical analysis considerably; conversely, the results obtained may be unreliable and inaccurate if the upscaling factor selected is inappropriate (O'Sullivan 2011). Therefore, the purpose of this study is to investigate the effect of initial in-situ stress conditions and the effect of

particle upscaling on the soil response during the cylindrical cavity expansion in sandy soil using discrete element simulation.

## 6.3 Calibration Using Triaxial Test Results

Investigating the effect of initial stress state and particle upscaling cannot be validated if the constitutive contact behaviour of the soil adopted in the simulation is not realistic. Hence, the contact model adopted in this study was calibrated to mimic realistic behaviour of sandy soil by matching the results obtained from the numerical simulations of triaxial compression tests to existing laboratory results. In distinct element modelling, selecting the most appropriate contact model is of paramount importance. Despite the fact that classical theories believe that it is mainly the sliding that plays the dominant role in controlling the strength and dilatancy of sandy soil, (Oda et al. 1998) has observed that the effect of rolling is more prominent.

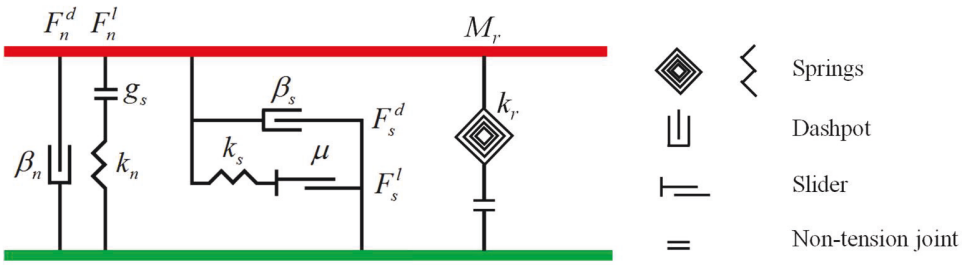


$K_n$, $K_s$ and $K_r$ are normal stiffness, shear stiffness and rolling stiffness, respectively
$\beta_n$ and $\beta_s$ are normal and shear dashpots, respectively
$M_r$ is rolling resistance moment
$F_n$ and $F_s$ are normal force and shear force, respectively
$\mu$ is friction coefficient

Figure 6.1 Rheological model for Rolling Resistance Contact Model

Therefore, The Rolling Resistance contact mode, illustrated in Figure 6.1 has been adopted due to its characteristics in capturing the rolling mechanism between sand particles, which is to incorporate a torque acting on the contacting pieces to counteract rolling motion (Iwashita et al. 1998). Experiment adopted for calibration was conducted by (Cornforth 1964) to obtain the drained strength of medium to fine grained sand under the plane strain condition. Considering the current computational power, it is not feasible to simulate the triaxial test following the true particle size distribution adopted by Cornforth (1964). Therefore, upscaling the grain size and hence reducing the number of particles becomes necessary. By trial and error, an upscaling factor of 16.5 has been adopted so that the same porosity as those reported in the experiment was achieved in the numerical simulation. Hence, the triaxial simulation comprised of 20,000 spherical particles, ranging from 1.25 to 24.50 mm after upscaling, and the setup of the triaxial test is shown in Figure 6.2.

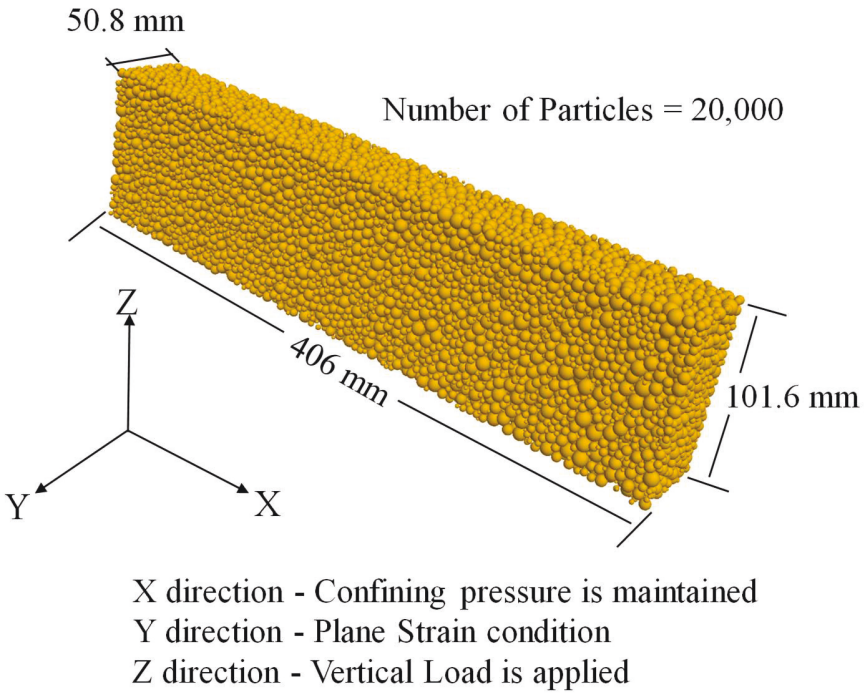


Figure 6.2 Triaxial compressive test in plane strain condition setup in PFC3D

Following the operational procedures given by (Cornforth 1964), isotropic stresses were applied to consolidate the sample to its desired initial stress state. Once the initial condition was established, the lateral stresses in X direction were maintained while the facets in the intermediate direction (Y direction) were fixed to simulate the plane strain condition, similar to the laboratory condition, and then axial load was applied on top of the specimen (Z direction) at a constant strain rate. Stress and strain variations as well as volumetric changes were continuously recorded in order to match the experimental results.

Calibrated results for stress-strain relationship as well as volumetric behaviour are plotted in Figure 6.3 and Figure 6.4 respectively.

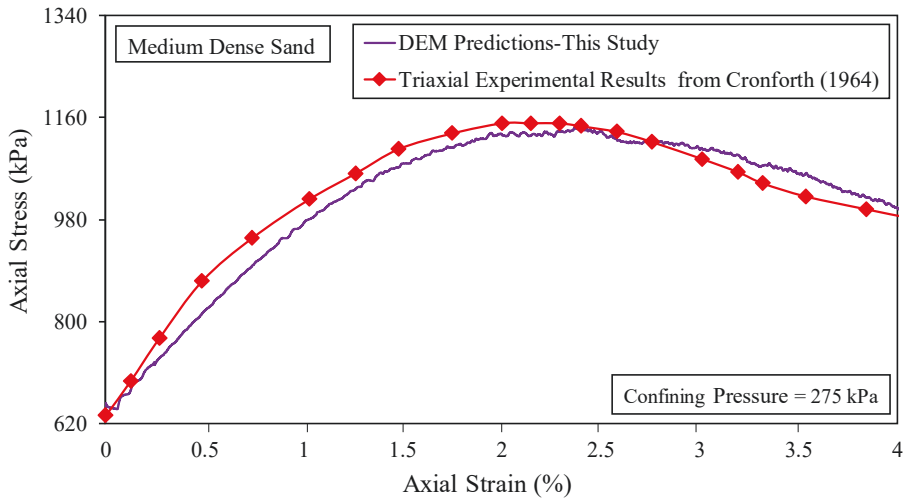


Figure 6.3 Variations of axial stress with axial strain (DEM predictions versus experimental measurement)

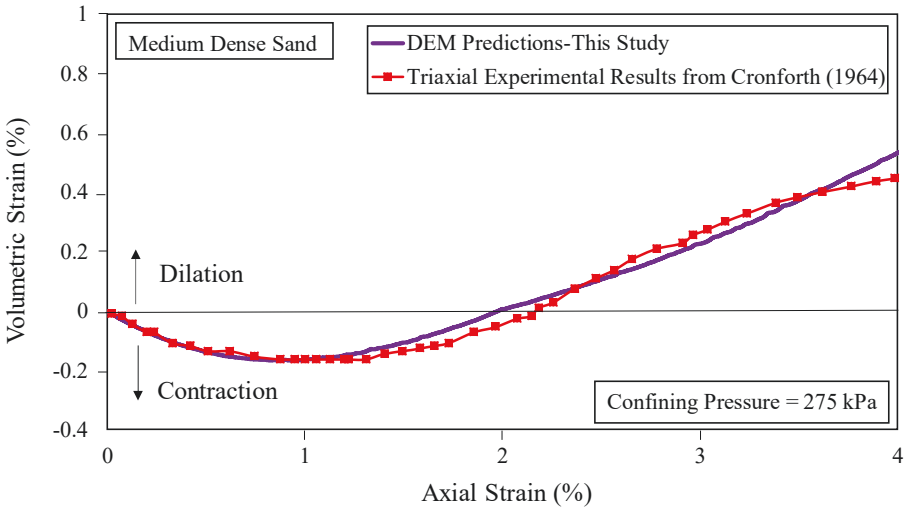


Figure 6.4 Variations of volumetric strain with axial strain (DEM predictions versus experimental measurements)

It is noteworthy to state that the numerical predictions have a good agreement with experimental data. The calibrated contact properties adopting rolling resistance contact model include the ratio between normal and shear stiffness, friction coefficient as well as rolling resistance coefficient, which are 1.75, 0.40 and 0.10, respectively.

## 6.4 Cavity Expansion Simulation

To study the effect of initial stress conditions on soil response subjected to cavity expansion, a large scale three-dimensional numerical model simulating the cylindrical cavity expansion has been proposed. Considering the fact that many cavity expansions related problems are in plane strain condition (Alshibli et al. 2000), and considering the axisymmetric geometry, only a quarter of geometry with plane strain condition has been simulated, as shown in Figure 6.5.

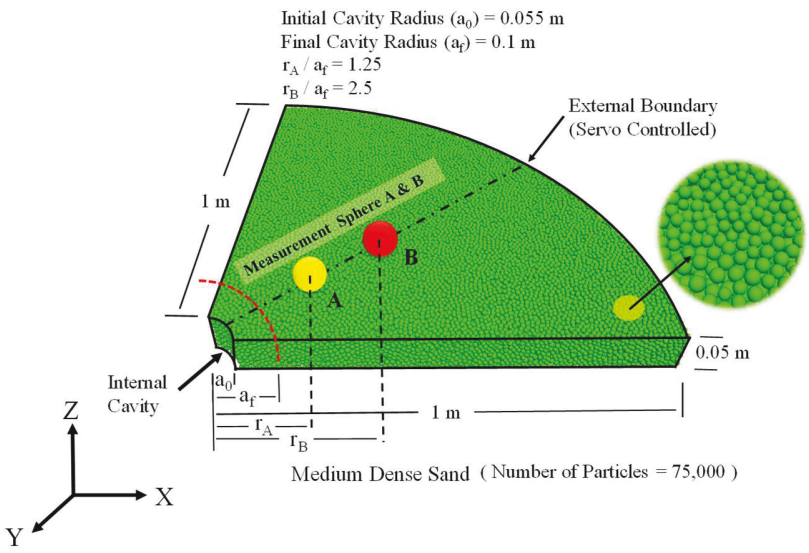


Figure 6.5 Cavity pressure variations during the cavity expansion

The model built contained 75,000 spherical particles following the particle size distribution adopted in the calibration and triaxial test in the laboratory. The model was generated using the radius expansion method, and the porosity and coordination numbers have been constantly monitored to ensure that the DEM sample has the identical properties to the soil in calibration exercise. The external boundary was located 1 m away from the centre of the initial cavity (Figure 6.5). The measured soil porosity was approximately 0.390, similar to the porosity of the medium dense sand specimen used for calibration and reported in Cornforth (1964). The ultimate objective of this study is to investigate the effect of the initial stress field on the soil response during cavity expansion. Hence, four different initial stress fields ($\sigma_{r_0} = \sigma_x = \sigma_y$) 62.5 kPa, 125 kPa, 250 kPa, and 500 kPa were adopted, respectively. In-situ stresses have been applied through the wall servo mechanism, ensuring that the radial stress ($\sigma_{r_0}$) is uniformed applied to the soil medium. After the initial conditions were satisfied, the cavity was expanded gradually from an initial cavity radius of 50 mm to a final cavity radius of 100 mm at a constant rate of 0.001 m/s to ensure the quasi-static loading, during which, the boundary pressure remained same as the initial stress. Cavity pressure is measured using coded subroutines by measuring the contact forces acting on the internal cavity wall and then divided by the corresponding contact area. Furthermore, stress and strain variations were continuously recorded using measurement spheres and subroutines at different radial distances from the cavity.

On the other hand, however, to study the effect of particle scaling on soil response subjected to cavity expansion, a series large scale three-dimensional numerical models simulating the cylindrical cavity expansion has been proposed. Axisymmetric and plane strain conditions were utilised to reduce the computational effort so that a quarter of cylindrical geometry with 1 m radius and 0.1m thickness was generated as illustrated in Figure 6.6.

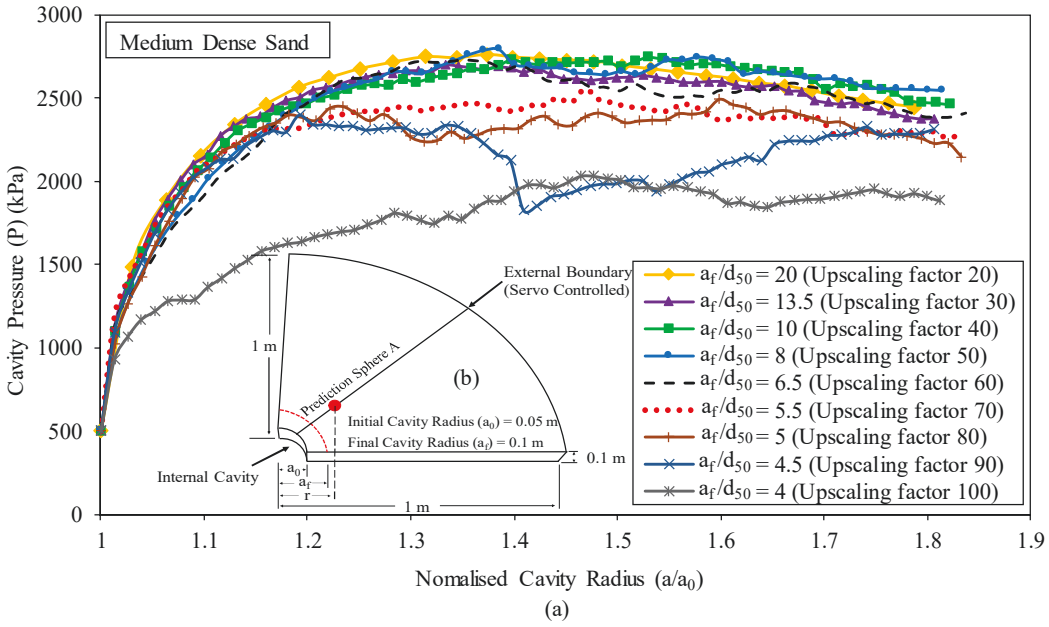


Figure 6.6 (a) Cavity pressure variations during the cavity expansion (b) DEM model setup

To study the effects of particle scaling and to find the maximum upscaling factor that can be applied without altering the sample property, a total of nine numerical analyses have been conducted, adopting different particle upscaling factors (USF) ranging from 20 to

100 times (as shown in Figure 6.7), based on the particle size distribution adopted in triaxial test reported by Cornforth (1964).

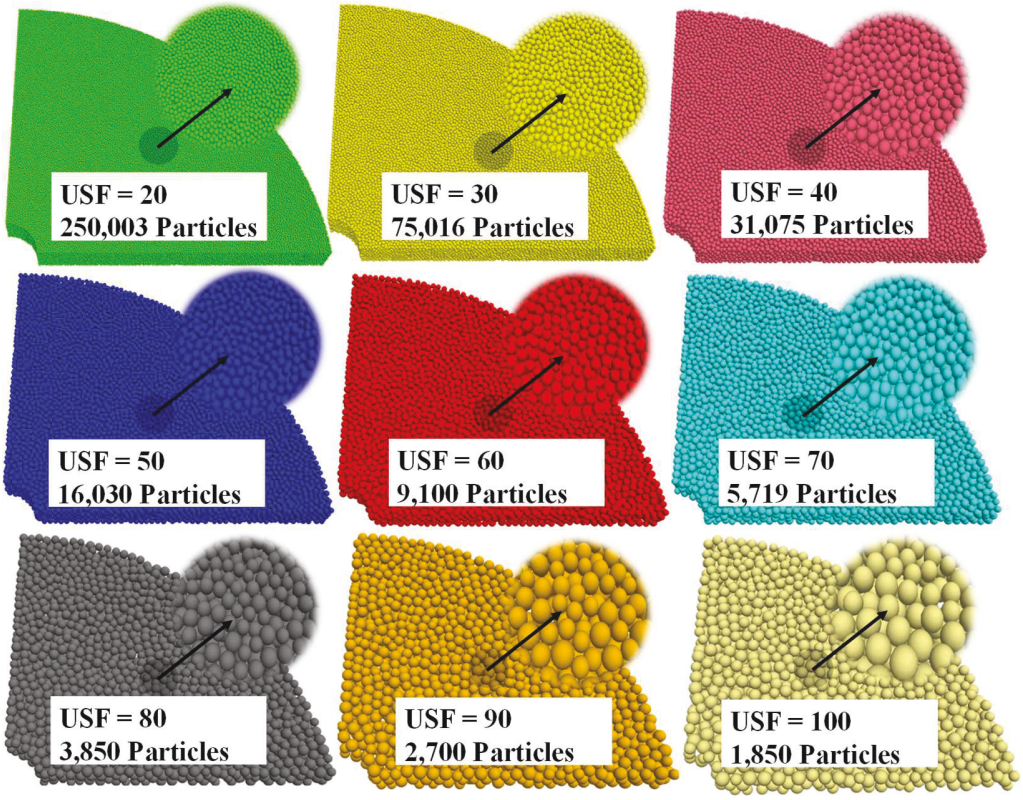


Figure 6.7 Particle size in DEM models after upscaling (USF- Upscaling Factor = $d_{DEM}$ / $d_{EXP}$)

As presented in Figure 6.7, nine generated sand specimens, after upscaling, comprise a wide range particle numbers, changing from the minimum of 1,850 (100 times upscaling) to the maximum of 250,003 (20 times upscaling), respectively. The sphere particles are used for all groups of analyses. Although it is acknowledged that the sand specimen used in the experiment has a certain level of angularity, the rolling resistance contact model can, by and large, mimic the rolling effects between particles with angular shape. These

simulations were conducted using calibrated contact parameters under the identical initial in-situ stress conditions. Additionally, the porosity as well as coordination number have been constantly monitored to ensure that all DEM samples have the identical properties to the soil in calibration exercise. In the coarsest grain case (i.e. USF = 100, the coordination number measured is approximately five, which is similar to the one predicated in the finest case. Hence, the prediction sphere is considered to be validated. However, when the particle size is further unscaled (i.e. USF > 100), the coordination number becomes too small and therefore inconsistent. Hence, it is not considered in this study in investigating the effects of particle upscaling. The measured initial porosity using prediction spheres was approximately 0.390 for all groups of simulations, similar to the porosity of the medium dense sand specimen used for calibration and reported in Cornforth (1964). After the initial conditions were satisfied, the cavity was expanded gradually from an initial cavity radius of $a_0$ = 50 mm to a final cavity radius of $a_f$ = 100 mm at a constant strain rate of 0.01 m/s to ensure the quasi-static loading, during which, the boundary pressure remained same as the initial stress (see Figure 6.6).

Cavity pressure is measured using coded subroutines by measuring the contact forces acting on the internal cavity wall divided by the corresponding contact area. The stress variations and the displacements of selected gauge particles are continuously monitored during the cavity expansion process.

Rolling Resistance contact model, developed to mimic the rolling effect between particles with angular shapes, has been employed for the model calibration. Hence, it is considered

as a more realistic contact constitutive model for granular materials where the rolling of particles is dominant in determining the strength. It should be noted that the contact parameters adopted in this study are calibrated based on the Linear Deformability Method available in PFC3D, which utilises the particle deformability at the contact interface between particles, as well as the stiffness ratio between normal and shear springs (as illustrated in Figure 6.8), adopting a set of equations reported in Equation (6-1).

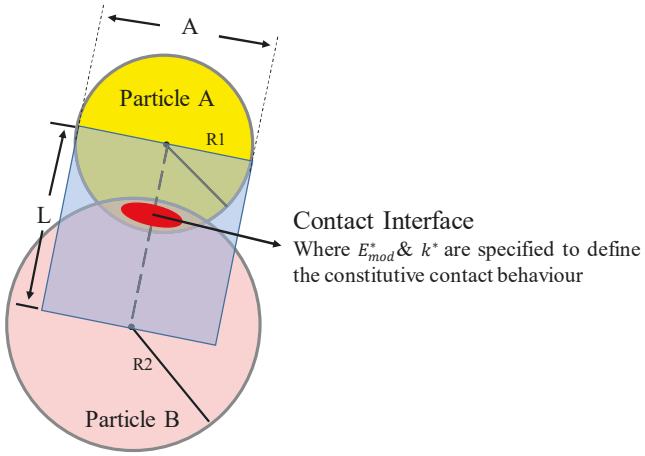


Figure 6.8 Illustration of the particle assembly in DEM

$$\begin{cases} k_n = AE^*_{mod}/L \\ k_s = k_n/k^* \\ A = 2R(2D) \; or \; A = \pi R^2(3D) \\ r = \min(R_1, R_2) \\ L = R_1 + R_2 \end{cases} \tag{6-1}$$

Where, $A$ is the contact area, $E^*_{mod}$ is the deformability, $k^*$is the ratio between the normal stiffness ($k_n$) and the shear stiffness ($k_s$) of the springs, $R$ is the particle radius, and L is the distance between the centre of two contacting particles (i.e. $R_1 + R_2$). The linear

model deformability method is employed in this analysis to control the normal and shear stiffness in real time by introducing the effective Young's modulus and the stiffness ratio of the normal and shear stiffness of the linear springs based on the equation 6-1. It can be concluded that the changes in particle size ($R$) will be automatically taken into account using the Linear Model Method in PFC$^{3D}$, where the normal stiffness ($k_n$) would be scaled-up with the increase in particle size ($R$) . In this case, it is no longer necessary to scale-up the microscopic contact parameters in respond to the upscaling of the particles. Besides this, the sample porosity and coordination number measured adopting measurement spheres are also continuously monitored to ensure the consistency between all specimens.

## 6.5 Results and Discussion

Variations of internal cavity pressure ($P$) during the cavity expansion process has been plotted against the normalised cavity radius ($\frac{a_0}{a_f}$) in Figure 6.9.

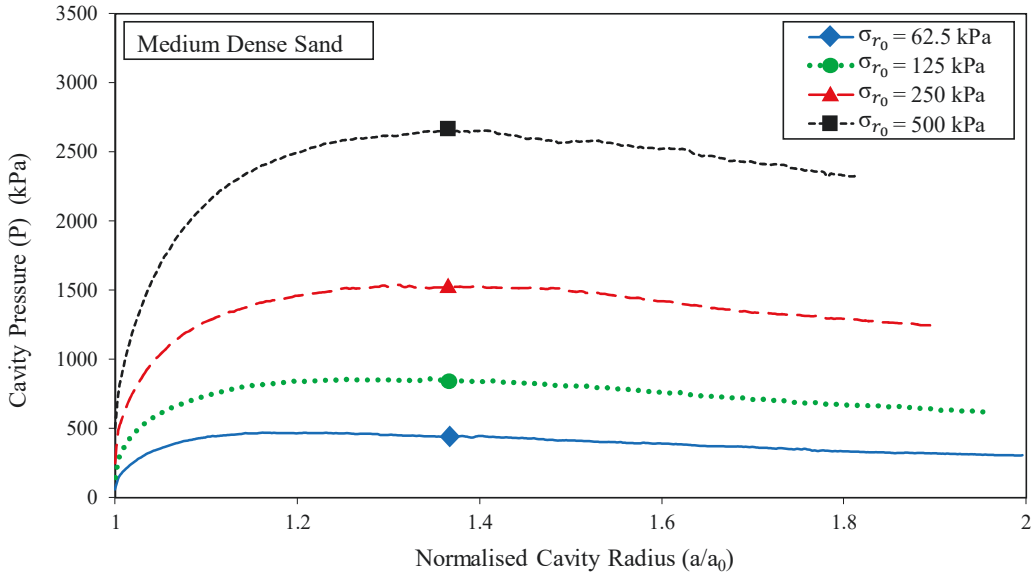


Figure 6.9 Cavity pressure variations during the cavity expansion

The results evidently reveal that an increase in the initial in-situ stress has contributed to escalation of the cavity pressure. For instance, the limit pressure ($P_{max}$) measured from the cavity expansion with $\sigma_{r_0}$ = 125 kPa is approximately 750 kPa, while the limit pressure corresponding to $\sigma_{r_0}$ = 500 kPa is $P_{max}$ = 2500 kPa. In other words, the pressure required to expand an existing cavity in the deeper ground is larger than the corresponding pressure in shallower ground. Indeed, similar results were reported by Arroyo et al. (2011) when interpreting cone penetration test results. As indicated by Arroyo et al. (2011), measured cone resistance was enhanced from 0.5 to 2.0 MPa when the confining pressure increased from 60 kPa to 300 kPa, respectively, demonstrating that the cone resistance measured was highly correlated to the in-situ stress conditions. Hence, it can be readily confirmed that the limit pressure is largely dependent on the soil initial

stress state, and such correlation may be used to evaluate the pile toe resistance during the pile driving process. Furthermore, comparisons were made on the deviatoric stress and the volumetric strain variations with the shear strain during the cavity expansion process. Prediction spheres A & B located along angular bisector (see Figure 6.5) were used to continuously record the variations of deviatoric stress, shear strain as well as volumetric strain during the cavity expansion process.

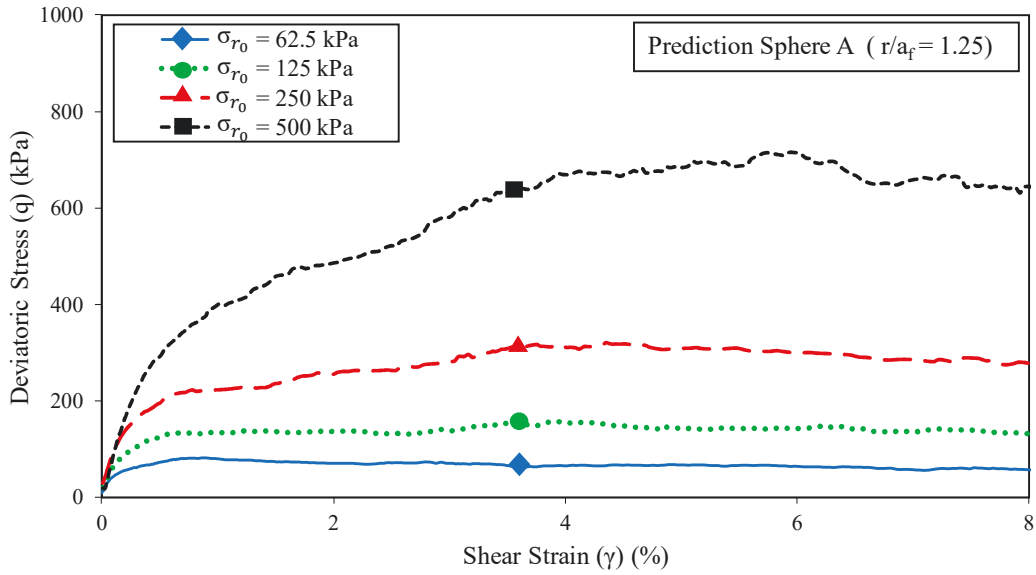


Figure 6.10 Deviatoric stress – shear strain relationship at prediction sphere A

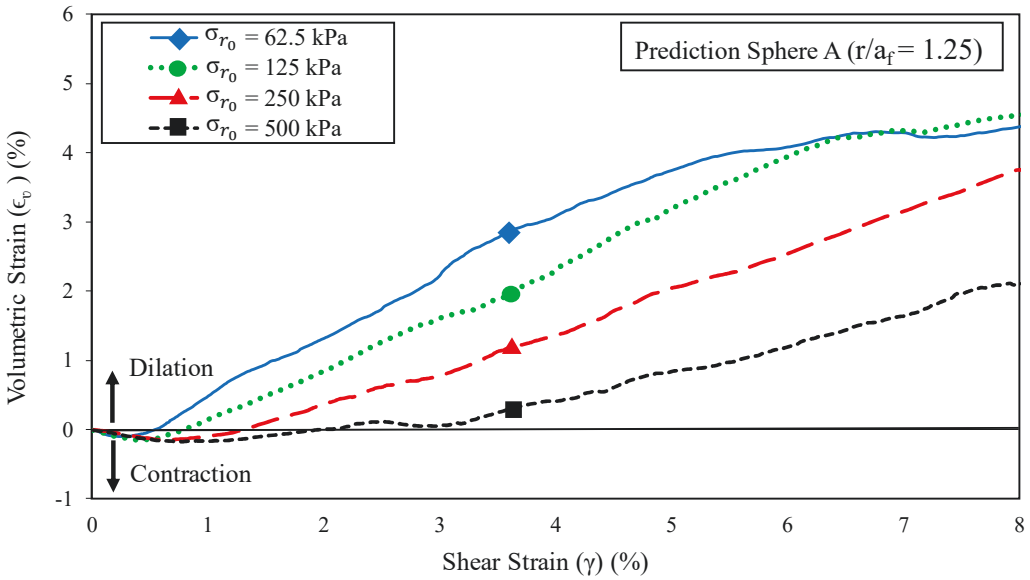


Figure 6.11 Volumetric strain – shear strain relationship at prediction sphere A

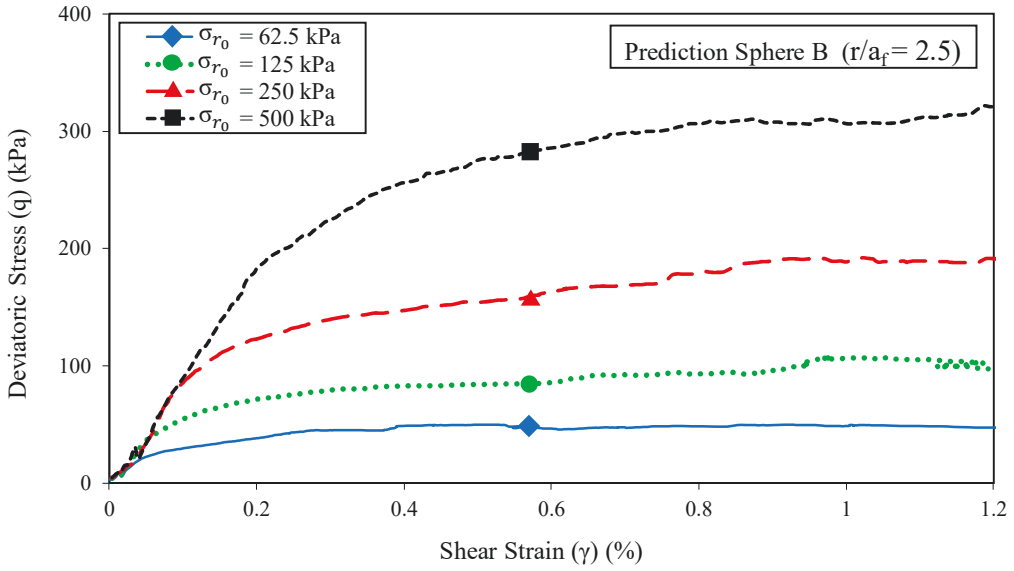


Figure 6.12 Deviatoric stress – shear strain relationship at prediction sphere B

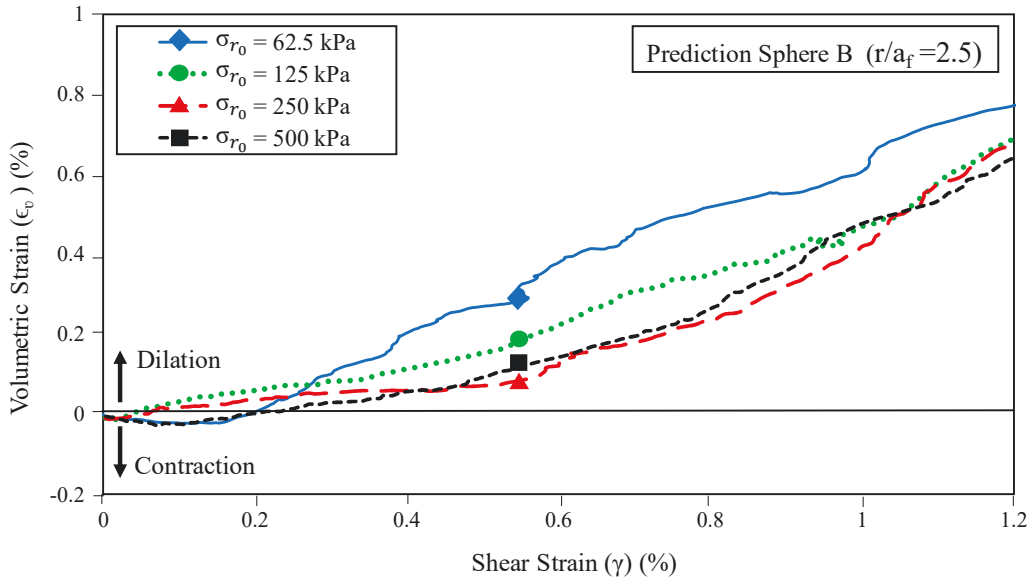


Figure 6.13 Volumetric strain – shear strain relationship at prediction sphere B

Figure 6.10 and Figure 6.12 present the results for $r/a_f$ = 1.25 and $r/a_f$ = 2.5, respectively (r being the radial distance from the centre of the cavity; $a_f$ being the final cavity radius). It can be concluded that given the same deviatoric strain, the magnitude of the deviatoric stress q is highly dependent on the initial stress state. For example, as the in-situ horizontal stress increases from 250 kPa to 500 kPa, the maximum deviatoric stresses ($g_{max}$) measured at $r/a_f$ = 1.25 and $r/a_f$ = 2.5 increased by 400 kPa and 150 kPa, respectively. As shown in Figures 6.11 and 6.13, with an increase in the initial in-situ stress, less significant volumetric strain changes are observed during the cavity expansion. This may explain the fact that the soil volume changes (expansion) during the pile installation are more evident near the ground surface, while the phenomenon becomes less pronounced at deeper soil layers, where initial in-situ stresses are larger.

Additionally, referring to Figure 6.11 and Figure 6.13 volumetric strain variations obtained for different initial in-situ stresses showed a slight contraction during the initial stage of cavity expansion and then dilation as cavity expanded further, confirming the medium dense state of the in-situ soil. Furthermore, referring to Figure 6.10 to Figure 6.13 comparisons can be made for the variations of the deviatoric stresses and volumetric strains at two different prediction locations (i.e. prediction spheres A & B shown in Figure 6.5). It can be evidently concluded that the soil close to the cavity (predication sphere A) experienced higher shear stresses and deformations compared to the soil further away from the cavity (prediction sphere B). Moreover, it is projected that the measured deviatoric stresses and volumetric strains would eventually approach zero for the points located far away from the cavity centre (i.e. $r = \infty$).

For the investigations conducted studying the effects of particle upscaling, Variations of the cavity pressure during the cavity expansion process have been plotted against the normalised cavity radius in Figure 6.6. It should be noted that the number of particles contacting with the internal cavity wall during the cavity expansion reduces with the increase in particle upscaling factors. Hence, it is believed that the ratio between the internal cavity radius and contacting particle radius that govern the accuracy of cavity pressure measurement. Therefore, the results are categorised in terms of the adopted particle scaling factors for each analysis and also the corresponding ratio between the radius of the internal cavity and the median particle diameter after upscaling (i.e. $a_f /d_{50}$). Referring to Figure 6.6, it is observed that the cavity pressure variations adopting different

particle upscaling factors follow the same pattern irrespective of the adopted upscaling factors when the final cavity radius is more than 8 times of the particle median size (i.e. $a_f/d_{50}$> 8 or particle upscaling factor < 50). However, as observed in Figure 4, the peak cavity pressure ($P_{max}$) decreases immensely and the patterns become unascertainable when excessively large upscaling factor is adopted (i.e. $a_f/d_{50}$< 5.5 or upscaling factor > 70). Additionally, as illustrated in Figure 6.6 with less number of particles contacting with the internal cavity wall during cavity expansion ($a_f/d_{50}$< 8 or upscaling factor >50), the results obtained manifested more impulsive oscillation.

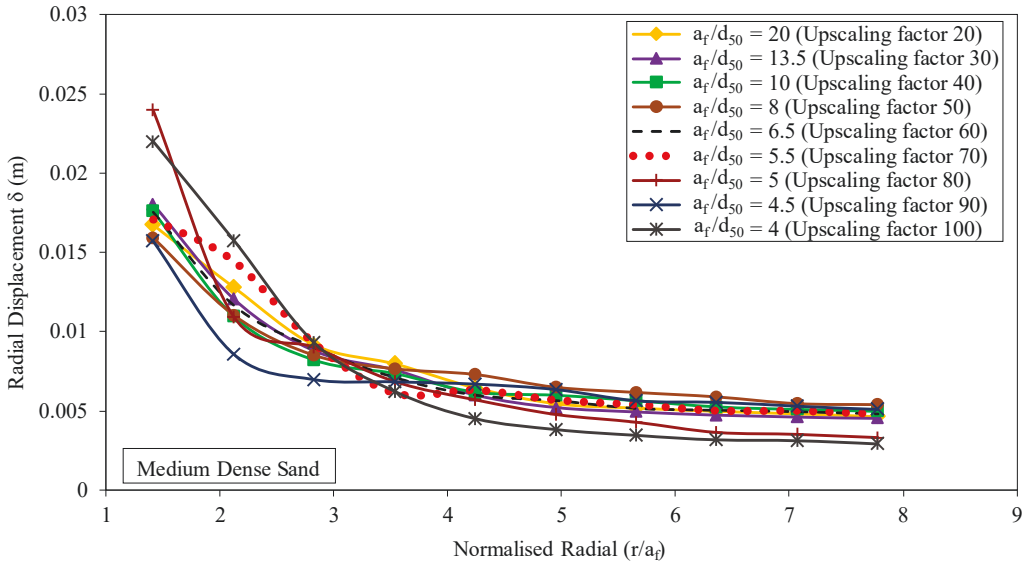


Figure 6.14 Radial displacement of ten equally spaced gauge particles during the cavity expansion

Figure 6.14 presents the soil movement in radial direction due to cavity expansion. The results depict the total displacement of ten equally spaced gauge particles from the beginning of the cavity expansion (i.e. $a = a_0$) till the end ($a_f$ = 0.1 m). As expected,

particles situated closer to the internal cavity experience a larger radial movement, while less radial displacement is experienced by those particles located further away. Furthermore, it is observed that the total radial displacement reduces dramatically when the normalised radius ($r/a_f$) is less than 4, while the changes become less pronounced when the normalised cavity radius is larger than 5. Furthermore, referring to Figure 6.14, it can be concluded that the radial displacements obtained from different upscaling factors reveal a very similar trend when the upscaling factors are less than 60, whereas greater errors are observed with higher upscaling factors.

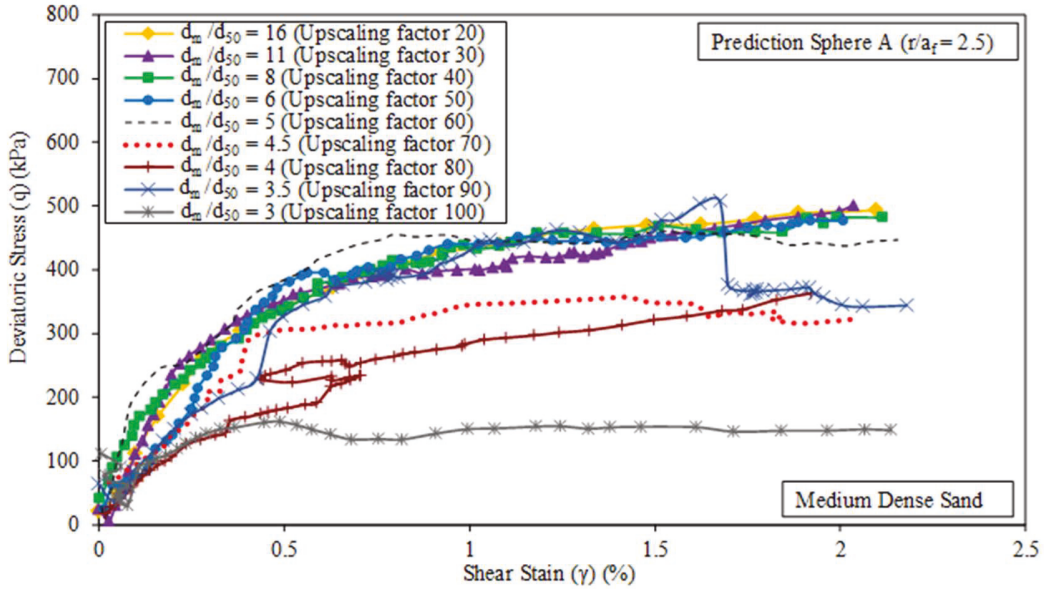


Figure 6.15 Deviatoric stress – shear strain relationship at prediction sphere A

Figure 6.15 illustrates the deviatoric stress variations with the shear strain obtained by the prediction sphere A ($r/a_f$ = 2.5, r being the radial distance) during the cavity expansion. Since the diameter of the predication sphere ($D_m$) adopted is constantly 0.08 m for all

analyses, the number of particles comprised in the predication sphere reduces with the increase in particle upscaling factors. In this case, investigating the effects of particle upscaling can be correlated to the ratio between the size of the predication sphere and the median particle diameter after upscaling ($D_m/d_{50}$). It can be clearly observed that the deviatoric stress variations obtained reveal a similar trend when there are an adequate number of particles in the prediction sphere (i.e. $D_m/d_{50} > 6$ or particle upscaling factor < 50), while greater disparities are noticed when the upscaling factors adopted exceeds 50 (i.e. $D_m /d_{50} < 5$ or particle upscaling factor > 60). In addition, severe oscillations are also observed, when there are fewer particles contributing to the computation of stresses and strains within the predication sphere.

## 6.6 Summary

In this study, the effects of initial in-situ stresses on the soil response during cylindrical cavity expansion have been studied using a three-dimensional discrete element simulation. Numerical results confirmed that the initial stress field plays a significant role in determining the soil response during the cavity expansion. Cavity pressures and deviatoric stresses showed a direct correlation with the value of the in-situ stresses, whereas the volumetric strain reduced as the in-situ stress increased. Furthermore, it was observed that soil close to the internal cavity experienced larger shear stresses and volumetric strains (dilation) compared to corresponding points locates further away from the cavity.

Besides this, the influence of particle upscaling technique adopted in discrete element simulation of cavity expansion was also studied. Given a constant model size, the cavity pressure measured on the internal cavity adopting different particle upscaling factors is highly correlated to the size effects between the internal cavity and the median particle size (i.e. $a_f$ / $d_{50}$). In addition, the deviatoric stress variations obtained adopting prediction spheres reveal that the upscaling factor selected plays a significant role in affecting the accuracy of the stress and strain predictions. It should be noted that the size of prediction spheres has to be relatively small when measuring the variations of stresses and strains at a particular point of interest. Furthermore, despite the fact that the upscaling of particles leads to less impact on the soil radial displacement, it is firmly believed that the predictions will be unreliable if the particles are upscaled excessively and consequently leads to insufficient number particles in numerical analysis. Therefore, it can be concluded that the particle upscaling adopting an appropriate factor can be efficient to reduce the computational effort while achieving a reasonable level of accuracy.

# Chapter 7 - Conclusions and Recommendations

## 7.1 General Conclusions

This research study has adopted discrete element method to investigate the installation effects of displacement based rigid inclusions in cohesionless and lightly cemented soils through cylindrical cavity expansion simulations. True scale three-dimensional models considering realistic initial stress fields and boundary conditions in-situ were carefully selected. The microscopic contact constitutive laws describing the behaviour between adjacent soil particles at their contacting interfaces were calibrated against experimental testing results, and the calibration was attained by matching the experimental macroscopic stress - strain curves with that obtained from numerical simulations. The outcomes of this research study are potentially beneficial for the piling contractors, practicing engineers as well as future researchers by providing a better understanding of the soil response during the cavity expansion in a microscopic view. Discrete element simulations can largely offer practicing engineers and pilling contractors an alternative to investigate the installation effects numerically. Therefore, assessing the pile installation effects will no longer solely rely on the empirical correlations or relevant theoretical analyses. It is expected that the results obtained will encourage the use of three-dimensional numerical models to accurately assess the installation effects rather than restricting its application to solely qualitative analysis.

## 7.2 Influence of Particle Contact Models on Soil Response of Poorly Graded Sand during Cavity Expansion in Discrete Element

The numerical model simulating the cylindrical cavity expansion subjected to cavity expansion in sandy soils considering three different contact constitutive models, namely Linear, Rolling Resistance and Hertz contact models was proposed. The simulations with different contact models have been calibrated adopting the experimental results obtained from a triaxial test in plane stain condition on a poorly graded medium dense sand. The calibration process calibrating the microscopic contact parameters including the methodology adopted and parametric studies carried out was expounded. In addition, micro-mechanical formulations based on the contact forces have been developed explaining the soil dilation and strain softening in a microscopic point of view.

The numerical predictions indicated that these calibrated contact models produced similar results in terms of cavity pressure variations, radial stress distributions, deviatoric stress and volumetric strain variations as well as soil radial movement, confirming that the soil response during the cavity expansion is highly correlated to its behaviour during the triaxial test used for the model calibration. Additionally, strain-softening behaviour due to the dilatancy of medium dense specimen has been captured during the cavity expansion, and the volumetric strain predicted shows an initial slight contraction followed by dilation at larger shear strains. However, it should be highlighted that if the soil particles are highly angular (e.g. ballast particles), modelling adopting simplified Linear contact model may result in inaccurate predictions. Furthermore, according to the results reported in this

study, at a radial distance beyond $11a_f$ and $8a_f$ ($a_f$ being the final cavity radius), soil displacement and radial stress variations would be insignificant, respectively. Thus, the effects of soil displacement due to installation of displacement-based inclusions (such as driven piles and vertical drains used in ground improvement) on nearby structures should be considered carefully by practicing engineers when piling in similar ground conditions.

## 7.3 Three-Dimensional Discrete Element Simulation of Cylindrical Cavity Expansion from Zero Initial Radius in Sand

A realistic scale discrete element model was developed investigating the influence of the choice of the initial cavity radius on the soil response during cavity expansion for a given expansion volume. The results obtained confirmed that the choice of initial cavity radius could significantly influence the soil response at the earlier stages of the cavity expansion. By adopting zero or a small initial cavity size, the cavity pressure measured during expansion in dense sand showed a massive increase to the peak, followed by a continuous decrease to a constant pressure. However, the maximum predicted cavity pressure changed inversely with the initial cavity radius, while the ultimate cavity pressure was not sensitive to the choice of the initial cavity radius. In other words, for a given expansion volume, creating a cylindrical cavity (i.e. $a_0 = 0$, $a_0$ is the initial cavity radius) induces larger stresses in the soil compared to expanding existing cavities in the same soil medium, while the pressure needed to maintain an already expanded cavity is not sensitive to the choice of the initial cavity radius. In general, the variations of the internal cavity pressure during the expansion process in both loose and dense sands followed the same trend,

while the magnitudes of the peak and ultimate pressures were significantly lower in loose sand. However, it is recommended that practicing engineers should consider the difference in cavity pressure induced by different initial radii when assessing the variations of stress path, volumetric strain and deviatoric stress in coarse grained soils. Given the same expansion percentage, creating a cavity (i.e. $a_0$= 0), in general, resulted in the largest deviatoric stresses, mean stresses, and shear strains in the soil, whereas the cavity expansion with the largest initial radius considered in this study (i.e. $a_0$ is the initial cavity radius =1/4$R_c$, $R_c$ is the radius of column), led to the lowest corresponding values. In addition, adopting cylindrical cavity expansion in plane strain condition, the loose sand experienced a dilative behaviour when the cavity expansion started from infinitesimal initial radii (i.e. $a_0$ = 0 and ($a_0$ =1/16 $R_c$).

Furthermore, both radial and hoop stresses decreased dramatically with the radial distance, and the radial pressure eventually reached the initial stress field when the measurements were taken at large radial distances (i.e. $\frac{r}{a_f} > 10$) for loose sand and $\frac{r}{a_f} > 20$ for dense sand); where, $r$ is the radial distance measured from the centre of the cavity, and $a_f$ is the final cavity radius determined based on the constant volume theory.

Moreover, the radial soil displacement showed a significant decrease with the radial distance. The influence zone induced by the cavity expansion in loose sand was approximately 25 $a_f$, while a larger influence zone (approximately 30 $a_f$) must be considered in the dense sand to eliminate the boundary effects. Hence, practicing engineers may use the above criteria to eliminate the adverse effects of lateral soil

movement to adjacent structures when installing the displacement-based inclusions in granular materials.

## 7.4 Discrete Element Simulation of Cavity Expansion in Lightly Cemented Sands Considering Cementation Degradation

A three-dimensional discrete element simulation investigating the effects of cementation on the response of lightly cemented sands during cavity expansion was carried out. The results confirmed that the cementation level played an important role in determining the soil response, in the installation of displacement-based inclusions. With an increase in cement content, the soil dilation was more pronounced at points located at a closer radial distance to the internal cavity. However, with the increase in radial distance where the structure of the cementation remains intact, the dilation was impeded since the cementation led to a lower degree of freedom for particles overriding each other. In addition, a slight offset was observed between the maximum dilatancy and the peak cavity pressure, which was attributed to the hindering effects induced by the cementation between particles.

Regarding the cementation degradation characteristics, the peak cavity pressure was reached when the breakage of the cementation bonds reached its maximum value, and the bond breakage slowed down as the cavity expanded further. It was found that for a given expansion volume, structured sand with higher cement content experienced less deviatoric strains due to the additional shear resistance stemming from the cementation

bonds between aggregates. Given the cemented sand considered in this study, the failure mode of the lightly cemented sand was mainly controlled by the shear rather than tensile strength at the contacting interfaces. The failure envelope of the cemented sand was nonlinear and gradually merged with the critical state line with the increase in the volumetric and shear strains inducing the cementation degradation. The softening behaviour of cemented soils during cavity expansion due to breakage of cementation bonds should be considered by design engineers when assessing the strength characteristics of the lightly cemented sands in the vicinity of an expanded cavity (e.g. installation piles or concrete injected columns). In addition, the influence zone in terms of cementation bond breakage induced by cavity expansion was found to be approximately $4a_f$ ($a_f$ being the final cavity radius).

The radial soil displacements induced by the cavity expansion showed inconspicuous difference regardless of the cement content when the radial distance from the cavity was less than $4a_f$. However, as the radial distance extended beyond $4a_f$, soils with higher cement content experienced a larger radial displacement, confirming that the influence zone in terms of lateral displacement is highly dependent on the level of cementation. Hence, care must be taken by practicing engineers when piling in lightly cemented sand in the presence of neighbouring structures and facilities.

## 7.5 Impact of Initial In-Situ Stress Field and Particle Scaling on Soil Response during Cavity Expansion Using Discrete Element Simulation

The developed three-dimensional model was also adopted in studying the effects of in-situ stress field and particle scaling on the soil response. Numerical results confirmed that the initial stress field plays a significant role in determining the soil response during the cavity expansion. Cavity pressures and deviatoric stresses showed a direct correlation with the value of the in-situ stresses, whereas the volumetric strain reduced as the in-situ stress increased. In other words, the pressure required to expand an existing cavity in the deeper ground is larger than the corresponding pressure in shallower ground, while the induced volume changes become less evident with the increase in soil depth.

Besides the in-situ stress field, the impact of particle upscaling technique commonly adopted to reduce the computational effort was also studied. It was found that given a constant model size, the cavity pressure measured on the internal cavity adopting different particle upscaling factors is highly correlated to the size effects between the internal cavity and the median particle size (i.e. $a_f/d_{50}$). It can be concluded $a_f/d_{50} > 8$ is a prerequisite to obtain reliable results using discrete element cavity expansion simulations. In addition, the deviatoric stress variations obtained adopting prediction spheres reveal that the upscaling factor selected plays a significant role in affecting the accuracy of the stress and strain predictions. It should be noted that the size of prediction spheres has to be relatively small when measuring the variations of stresses and strains at a particular point of interest. Therefore, given a constant size of the prediction sphere ($D_m$), it is

highly recommended to adopt a relatively smaller particle upscaling factor (i.e. upscaling factor < 50) to ensure that a sufficient number of particles are included within the prediction sphere (i.e. $D_m/d_{50} > 6$) to obtain reliable results. Furthermore, despite the fact that the upscaling of particles leads to less impact on the soil radial displacement, it is firmly believed that the predictions will be unreliable if the particles are upscaled excessively and consequently leads to insufficient number particles in numerical analysis. Therefore, it can be concluded that the particle upscaling adopting an appropriate factor can be efficient to reduce the computational effort while achieving a reasonable level of accuracy.

## 7.6 Recommendations for Future Research

The current study concentrated on developing a discrete element model to investigate the installation effects of rigid inclusions (e.g. driven piles, controlled modulus columns), particularly focusing on the stress-strain, strength, deformation and displacement characteristics of the surrounding soil during the installation process in both clean sand and lightly cemented sand. To further expand this research study, the following recommendations can be made:

- The simulation of the actual auger boring or penetration process may be incorporated in the numerical model considering the realistic shape and dimensions such as continuous flight auger (CFA) or controlled modulus columns (CMC).

- The effects of particle crushing and angularities (i.e. shape) may be considered, and the model can be furtherly enlarged to account for the vertical soil movement in assessing such installation effects of displacement-based inclusions.
- The installation effects can be extended to heavily cemented soils, in which a user defined contact model may be developed considering the cementation at the voids.
- Moreover, the DEM simulations considering the pore water effect through a coupling analysis with the computational fluid solver may be considered for cavity expansion in saturated soils.

# References


Abdulla, A.A. 1992, 'Testing and constitutive modeling of cemented soils', The Univerity of Arizona.

Abdulla, A.A. & Kiousis, P.D. 1997, 'Behavior of cemented sands—I. Testing', *International Journal for Numerical and Analytical Methods in Geomechanics*, vol. 21, no. 8, 533-47.

Acar, Y.B. & El-Tahir, E.-T.A. 1986, 'Low strain dynamic properties of artificially cemented sand', *Journal of Geotechnical Engineering*, vol. 112, no. 11, 1001-15.

Agnolin, I. & Roux, J.-N. 2007, 'Internal states of model isotropic granular packings. I. Assembling process, geometry, and contact networks', *Physical Review E*, vol. 76, no. 6, 061302.

Ai, J., Chen, J.-F., Rotter, J.M. & Ooi, J.Y. 2011, 'Assessment of rolling resistance models in discrete element simulations', *Powder Technology*, vol. 206, no. 3, 269-82.

Airey, D. 1993, 'Triaxial testing of naturally cemented carbonate soil', *Journal of Geotechnical Engineering*, vol. 119, no. 9, 1379-98.

Al-Thawadi, S., Cord-Ruwisch, R. & Bououdina, M. 2012, 'Consolidation of sand particles by nanoparticles of calcite after concentrating ureolytic bacteria in situ', *International Journal of Green Nanotechnology*, vol. 4, no. 1, 28-36.

Alfaro, M. & Pathak, Y. 2005, 'Dilatant stresses at the interface of granular fills and geogrid strip reinforcements', *Geosynthetics International*, vol. 12, no. 5, 239-52.

Alshibli, K.A. & Sture, S. 2000, 'Shear band formation in plane strain experiments of sand', *Journal of Geotechnical and Geoenvironmental Engineering*, vol. 126, no. 6, 495-503.

Arora, K. 1992, *Soil Mechanics and Foundation Engineering in SI Units*, Standard publishers distributors.

Arroyo, M., Butlanska, J., Gens, A., Calvetti, F. & Jamiolkowski, M. 2011, 'Cone penetration tests in a virtual calibration chamber', *Géotechnique*, vol. 61, no. 6, 525-31.

AS, A.S. 1995, 'Piling Design and Installation', *Standards Australia Limited*.

Atkinson, J.H. & Bransby, P. 1977, *The mechanics of soils, an introduction to critical state soil mechanics*, 0042-3114.

Australia, I. 2016, 'Australian infrastructure plan'.

Azari, B., Fatahi, B. & Khabbaz, H. 2014, 'Assessment of the elastic-viscoplastic behavior of soft soils improved with vertical drains capturing reduced shear strength of a disturbed zone', *International Journal of Geomechanics*, vol. 16, no. 1, B4014001.

Baligh, M.M. 1985, 'Strain path method', *Journal of Geotechnical Engineering*, vol. 111, no. 9, 1108-36.

Bardenhagen, S., Brackbill, J. & Sulsky, D. 2000, 'The material-point method for granular materials', *Computer methods in applied mechanics and engineering*, vol. 187, no. 3-4, 529-41.

Bareither, C.A., Edil, T.B., Benson, C.H. & Mickelson, D.M. 2008, 'Geological and physical factors affecting the friction angle of compacted sands', *Journal of Geotechnical and Geoenvironmental Engineering*, vol. 134, no. 10, 1476-89.

Been, K. & Jefferies, M.G. 1985, 'A state parameter for sands', *Géotechnique*, vol. 35, no. 2, 99-112.

Bishop, A.W. & Green, G.E. 1965, 'The influence of end restraint on the compression strength of a cohesionless soil', *Geotechnique*, vol. 15, no. 3, 243-66.

Bishop, R., Hill, R. & Mott, N. 1945, 'The theory of indentation and hardness tests', *Proceedings of the Physical Society*, vol. 57, no. 3, 147.
Bolton, M. 1986, 'The strength and dilatancy of sands', *Geotechnique*, vol. 36, no. 1, 65-78.
Bolton, M., Nakata, Y. & Cheng, Y. 2008, 'Micro-and macro-mechanical behaviour of DEM crushable materials', *Géotechnique*, vol. 58, no. 6, 471-80.
Bolton, M.D., Gui, M.-W., Garnier, J., Corte, J.F., Bagge, G., Laue, J. & Renzi, R. 1999, 'Centrifuge cone penetration tests in sand', *Géotechnique*, vol. 49, no. 4, 543-52.
Budhu, M. 2008, *Soil Mechanics and Foundations*, John Wiley & Sons.
Butlanska, J., Arroyo, M., Gens, A. & O'Sullivan, C. 2013, 'Multi-scale analysis of cone penetration test (CPT) in a virtual calibration chamber', *Canadian geotechnical journal*, vol. 51, no. 1, 51-66.
Byrne, P.M., Cheung, H. & Yan, L. 1987, 'Soil parameters for deformation analysis of sand masses', *Canadian Geotechnical Journal*, vol. 24, no. 3, 366-76.
Camusso, M. & Barla, M. 2009, 'Microparameters calibration for loose and cemented soil when using particle methods', *international Journal of Geomechanics*, vol. 9, no. 5, 217-29.
Carter, J. 1978, *CAMFE, a computer program for the analysis of a cylindrical cavity expansion in soil*, University of Cambridge, Department of Engineering.
Carter, J., Booker, J. & Small, J. 1979a, 'The analysis of finite elasto-plastic consolidation', *International Journal for Numerical and Analytical Methods in Geomechanics*, vol. 3, no. 2, 107-29.
Carter, J., Booker, J.R. & Yeung, S. 1986, 'Cavity expansion in cohesive frictional soils', *Geotechnique*, vol. 36, no. 3, 349-58.
Carter, J., Randolph, M. & Wroth, C. 1980, 'Some aspects of the performance of open-and closed-ended piles', *Numerical methods in offshore piling*, Thomas Telford Publishing, pp. 165-70.
Carter, J.P., Randolph, M. & Wroth, C. 1979b, 'Stress and pore pressure changes in clay during and after the expansion of a cylindrical cavity', *International Journal for Numerical and Analytical Methods in Geomechanics*, vol. 3, no. 4, 305-22.
Carter, J.P., Randolph, M.F. & Wroth, C.P. 1979c, 'Stress and pore pressure changes in clay during and after the expansion of a cylindrical cavity', *Int. J. for Numerical and Analytical Methods in Geomechanics*, vol. 3, no. 4, 305-22.
Carter, J.P. & Yeung, S. 1985, 'Analysis of cylindrical cavity expansion in a strain weakening material', *Computers and Geotechnics*, vol. 1, no. 3, 161-80.
Ceccato, F., Beuth, L., Vermeer, P.A. & Simonini, P. 2016, 'Two-phase material point method applied to the study of cone penetration', *Computers and Geotechnics*, vol. 80, 440-52.
Chadwick, P. 1959, 'The quasi-static expansion of a spherical cavity in metals and ideal soils', *The Quarterly Journal of Mechanics and Applied Mathematics*, vol. 12, no. 1, 52-71.
Chareyre, B., Briançon, L. & Villard, P. 2002, 'Theoretical versus experimental modeling of the anchorage capacity of geotextiles in trenches', *Geosynthetics International*, vol. 9, no. 2, 97-123.
Chen, P.-y. 2017, 'Effects of microparameters on macroparameters of flat-jointed bonded-particle materials and suggestions on trial-and-error method', *Geotechnical and Geological Engineering*, vol. 35, no. 2, 663-77.
Chen, R., Tang, L., Ling, D. & Chen, Y. 2011, 'Face stability analysis of shallow shield tunnels in dry sandy ground using the discrete element method', *Computers and Geotechnics*, vol. 38, no. 2, 187-95.

Cheng, K., Wang, Y., Yang, Q., Mo, Y. & Guo, Y. 2017, 'Determination of microscopic parameters of quartz sand through tri-axial test using the discrete element method', *Computers and Geotechnics*, vol. 92, 22-40.
Cheng, L., Cord-Ruwisch, R. & Shahin, M.A. 2013, 'Cementation of sand soil by microbially induced calcite precipitation at various degrees of saturation', *Canadian Geotechnical Journal*, vol. 50, no. 1, 81-90.
Chow, Y. & Teh, C. 1990, 'A theoretical study of pile heave', *Geotechnique*, vol. 40, no. 1, 1-14.
Christoffersen, J., Mehrabadi, M.M. & Nemat-Nasser, S. 1981, 'A micromechanical description of granular material behavior'.
Ciantia, M., Arroyo Alvarez de Toledo, M., Calvetti, F. & Gens Solé, A. 2015, 'An approach to enhance efficiency of DEM modelling of soils with crushable grains', *Géotechnique*, vol. 65, no. 2, 91-110.
Ciantia, M.O., Arroyo, M., Butlanska, J. & Gens, A. 2016, 'DEM modelling of cone penetration tests in a double-porosity crushable granular material', *Computers and Geotechnics*, vol. 73, 109-27.
Clough, G.W., Sitar, N., Bachus, R.C. & Rad, N.S. 1981, 'Cemented sands under static loading', *Journal of Geotechnical and Geoenvironmental engineering*, vol. 107, no. ASCE 16319 Proceeding.
Collins, I., Pender, M. & Yan, W. 1992, 'Cavity expansion in sands under drained loading conditions', *International Journal for Numerical and Analytical Methods in Geomechanics*, vol. 16, no. 1, 3-23.
Collins, I. & Stimpson, J. 1994, 'Similarity solutions for drained a undrained cavity expansions in soils', *Geotechnique*, vol. 44, no. 1, 21-34.
Collins, I.F. & Yan, W. 1990, *Similarity solutions for the quasi-static expansion of cavities in frictional materials*, Department of Engineering Science, University of Auckland.
Collins, I.F. & Yu, H. 1996a, 'Undrained cavity expansions in critical state soils', *International journal for numerical and analytical methods in geomechanics*, vol. 20, no. 7, 489-516.
Collins, I.F. & Yu, H.S. 1996b, 'Undrained cavity expansions in critical state soils', *International Journal for Numerical and Analytical Methods in Geomechanics*, vol. 20, no. 7, 489-516.
Consoli, N., Cruz, R.C., Consoli, B. & Maghous, S. 2012, 'Failure envelope of artificially cemented sand', *Géotechnique*, vol. 62, no. 6, 543.
Consoli, N., Rotta, G. & Prietto, P. 2000, 'Influence of curing under stress on the triaxial response of cemented soils', *Geotechnique*, vol. 50, no. 1, 99-105.
Consoli, N., Rotta, G. & Prietto, P. 2006, 'Yielding–compressibility–strength relationship for an artificially cemented soil cured under stress', *Geotechnique*, vol. 56, no. 1, 69-72.
Consoli, N.C., Cruz, R.C., Da Fonseca, A.V. & Coop, M.R. 2011, 'Influence of cement-voids ratio on stress-dilatancy behavior of artificially cemented sand', *Journal of Geotechnical and Geoenvironmental Engineering*, vol. 138, no. 1, 100-9.
Consoli, N.C., Cruz, R.C. & Floss, M.F. 2010, 'Variables controlling strength of artificially cemented sand: Influence of curing time', *Journal of Materials in Civil Engineering*, vol. 23, no. 5, 692-6.
Consoli, N.C., Cruz, R.C., Floss, M.F. & Festugato, L. 2009, 'Parameters controlling tensile and compressive strength of artificially cemented sand', *Journal of Geotechnical and Geoenvironmental Engineering*, vol. 136, no. 5, 759-63.
Consoli, N.C., Prietto, P.D. & Ulbrich, L.A. 1998, 'Influence of fiber and cement addition on behavior of sandy soil', *Journal of Geotechnical and Geoenvironmental Engineering*, vol. 124, no. 12, 1211-4.

Cooke, R., Price, G. & Tarr, K. 1979, 'Jacked piles in London Clay: a study of load transfer and settlement under working conditions', *Geotechnique*, vol. 29, no. 2, 113-47.
Coop, M. 2005, 'On the mechanics of reconstituted and natural sands', *Deformation characteristics of geomaterials*, CRC Press, pp. 31-60.
Coop, M. & Atkinson, J. 1993, 'The mechanics of cemented carbonate sands', *Geotechnique*, vol. 43, no. 1, 53-67.
Coop, M. & Wroth, C. 1989, *Field studies of an instrumented model pile in clay*, University of Oxford, Department of Engineering Science.
Cornforth, D.H. 1964, 'Some experiments on the influence of strain conditions on the strength of sand', *Geotechnique*, vol. 14, no. 2, 143-67.
Cuccovillo, T. & Coop, M. 1997, 'Yielding and pre-failure deformation of structured sands', *Geotechnique*, vol. 47, no. 3, 491-508.
Cuccovillo, T. & Coop, M. 1999, 'On the mechanics of structured sands', *Géotechnique*, vol. 49, no. 6, 741-60.
Cudmani, R. & Osinov, V. 2001, 'The cavity expansion problem for the interpretation of cone penetration and pressuremeter tests', *Canadian Geotechnical Journal*, vol. 38, no. 3, 622-38.
Cui, M.-J., Zheng, J.-J., Zhang, R.-J., Lai, H.-J. & Zhang, J. 2017, 'Influence of cementation level on the strength behaviour of bio-cemented sand', *Acta Geotechnica*, vol. 12, no. 5, 971-86.
Cundall, P.A. & Hart, R.D. 1992, 'Numerical modelling of discontinua', *Engineering computations*, vol. 9, no. 2, 101-13.
Cundall, P.A. & Strack, O.D. 1979, 'A discrete numerical model for granular assemblies', *geotechnique*, vol. 29, no. 1, 47-65.
de Bono, J., McDowell, G. & Wanatowski, D. 2015, 'Investigating the micro mechanics of cemented sand using DEM', *International Journal for Numerical and Analytical Methods in Geomechanics*, vol. 39, no. 6, 655-75.
de Bono, J.P. & McDowell, G.R. 2014a, 'Discrete element modelling of one-dimensional compression of cemented sand', *Granular Matter*, vol. 16, no. 1, 79-90.
de Bono, J.P., McDowell, G.R. & Wanatowski, D. 2014b, 'DEM of triaxial tests on crushable cemented sand', *Granular Matter*, vol. 16, no. 4, 563-72.
DeJong, J.T., Fritzges, M.B. & Nüsslein, K. 2006, 'Microbially induced cementation to control sand response to undrained shear', *Journal of Geotechnical and Geoenvironmental Engineering*, vol. 132, no. 11, 1381-92.
Ding, X., Zhang, L., Zhu, H. & Zhang, Q. 2014, 'Effect of model scale and particle size distribution on PFC3D simulation results', *Rock mechanics and rock engineering*, vol. 47, no. 6, 2139-56.
Dong, Y., Fatahi, B. & Khabbaz, H. 2020, 'Three dimensional discrete element simulation of cylindrical cavity expansion from zero initial radius in sand', *Computers and Geotechnics*, vol. 117, no. 1, 103230.
Dong, Y., Fatahi, B., Khabbaz, H. & Kamruzzaman, A. 2018, 'Investigating Effects of Particle Scaling for Cavity Expansion Simulation Using Discrete Element Method', *GeoShanghai International Conference*, Springer, pp. 938-46.
Duan, N., Cheng, Y.P. & Liu, J.W. 2018, 'DEM analysis of pile installation effect: comparing a bored and a driven pile', *Granular Matter*, vol. 20, no. 3, 36.

Duncan, J., Wong, K.S. & Mabry, P. 1980, 'Strength, stress-strain and bulk modulus parameters for finite element analyses of stresses and movements in soil masses', *Geotechnical engineering*, University of California.
Durban, D. & Baruch, M. 1976, 'On the problem of a spherical cavity in an infinite elasto-plastic medium', *Journal of Applied Mechanics*, vol. 43, no. 4, 633-8.
Dutta, S., Hawlader, B. & Phillips, R. 2014, 'Finite element modeling of partially embedded pipelines in clay seabed using Coupled Eulerian–Lagrangian method', *Canadian Geotechnical Journal*, vol. 52, no. 1, 58-72.
Enomoto, T., Koseki, J., Tatsuoka, F. & Sato, T. 2015, 'Creep failure of sands exhibiting various viscosity types and its simulation', *Soils and Foundations*, vol. 55, no. 6, 1346-63.
Fahey, M. 1986, 'Expansion of a thick cylinder of sand: a laboratory simulation of the pressuremeter test', *Geotechnique*, vol. 36, no. 3, 397-424.
Falagush, O., McDowell, G.R., Yu, H.-S. & de Bono, J.P. 2015, 'Discrete element modelling and cavity expansion analysis of cone penetration testing', *Granular Matter*, vol. 17, no. 4, 483-95.
Feng, K., Montoya, B. & Evans, T. 2017, 'Discrete element method simulations of bio-cemented sands', *Computers and Geotechnics*, vol. 85, no. 1, 139-50.
Fu, R., Hu, X. & Zhou, B. 2017, 'Discrete element modeling of crushable sands considering realistic particle shape effect', *Computers and Geotechnics*, vol. 91, 179-91.
Gao, Z. & Zhao, J. 2012, 'Constitutive modeling of artificially cemented sand by considering fabric anisotropy', *Computers and Geotechnics*, vol. 41, no. 1, 57-69.
Geng, Y. 2010, 'Discrete element modelling of cavity expansion in granular materials', University of Nottingham.
Geng, Y., Yu, H. & McDowell, G. 2013, 'Discrete element modelling of cavity expansion and pressuremeter test', *Geomechanics and Geoengineering*, vol. 8, no. 3, 179-90.
Gibson, R. 1961, 'In situ measurement of soil properties with the pressuremeter', *Civil Engrg. and Pub. Wks. Rev*, vol. 56, no. 568, 615-8.
Green, G. & Reades, D. 1975, 'Boundary conditions, anisotropy and sample shape effects onthe stress-strain behaviour of sand in triaxial compression and plane strain', *Geotechnique*, vol. 25, no. 2, 333-56.
Gu, X. & Yang, J. 2013, 'A discrete element analysis of elastic properties of granular materials', *Granular Matter*, vol. 15, no. 2, 139-47.
Haeri, S.M., Hamidi, A. & Tabatabaee, N. 2005, 'The effect of gypsum cementation on the mechanical behavior of gravely sands', *Geotechnical Testing Journal*, vol. 28, no. 4, 380-90.
Hagerty, D.J. & Peck, R.B. 1971, 'Heave and lateral movements due to pile driving', *Journal of Soil Mechanics & Foundations Div*.
Hardin, B.O. 1978, 'The nature of stress-strain behavior for soils', *From Volume I of Earthquake Engineering and Soil Dynamics--Proceedings of the ASCE Geotechnical Engineering Division Specialty Conference, June 19-21, 1978, Pasadena, California. Sponsored by Geotechnical Engineering Division of ASCE in cooperation with:*.
Hardin, B.O. & Drnevich, V.P. 1972, 'Shear modulus and damping in soils: design equations and curves', *Journal of Soil Mechanics & Foundations Div*, vol. 98, no. sm7.
Henke, S. 2010, 'Influence of pile installation on adjacent structures', *International journal for numerical and analytical methods in geomechanics*, vol. 34, no. 11, 1191-210.

Herle, I. & Gudehus, G. 1999, 'Determination of parameters of a hypoplastic constitutive model from properties of grain assemblies', *Mechanics of Cohesive-frictional Materials*, vol. 4, no. 5, 461-86.
Hill, R. 1950, 'The mathematical theory of plasticity'.
Hirsch, T., Lowery, L., Coyle, H.M. & Samson Jr, C. 1970, 'Pile-driving analysis by one-dimensional wave theory: State of the art'.
Holt, R., Kjølaas, J., Larsen, I., Li, L., Pillitteri, A.G. & Sønstebø, E. 2005, 'Comparison between controlled laboratory experiments and discrete particle simulations of the mechanical behaviour of rock', *International Journal of Rock Mechanics and Mining Sciences*, vol. 42, no. 7, 985-95.
Horn, H. & Deere, D. 1962, 'Frictional characteristics of minerals', *Geotechnique*, vol. 12, no. 4, 319-35.
Horpibulsuk, S., Liu, M.D., Liyanapathirana, D.S. & Suebsuk, J. 2010, 'Behaviour of cemented clay simulated via the theoretical framework of the structured cam clay model', *Computers and Geotechnics*, vol. 37, no. 1-2, 1-9.
Hosn, R.A., Sibille, L., Benahmed, N. & Chareyre, B. 2017, 'Discrete numerical modeling of loose soil with spherical particles and interparticle rolling friction', *Granular Matter*, vol. 19, no. 1, 4.
Huang, A.-B. & Ma, M.Y. 1994, 'An analytical study of cone penetration tests in granular material', *Canadian Geotechnical Journal*, vol. 31, no. 1, 91-103.
Huang, J. & Airey, D. 1998, 'Properties of artificially cemented carbonate sand', *Journal of Geotechnical and Geoenvironmental Engineering*, vol. 124, no. 6, 492-9.
Huang, X., Hanley, K.J., O'Sullivan, C. & Kwok, C.Y. 2014, 'Exploring the influence of interparticle friction on critical state behaviour using DEM', *International Journal for Numerical and Analytical Methods in Geomechanics*, vol. 38, no. 12, 1276-97.
Irazábal, J., Salazar, F. & Oñate, E. 2017, 'Numerical modelling of granular materials with spherical discrete particles and the bounded rolling friction model. Application to railway ballast', *Computers and Geotechnics*, vol. 85, 220-9.
Ismael, N.F. 1989, 'Skin friction of driven piles in calcareous sands', *Journal of Geotechnical Engineering*, vol. 115, no. 1, 135-9.
Ismael, N.F. 1990, 'Behavior of laterally loaded bored piles in cemented sands', *Journal of Geotechnical Engineering*, vol. 116, no. 11, 1678-99.
Ismael, N.F. 2001, 'Axial load tests on bored piles and pile groups in cemented sands', *Journal of geotechnical and geoenvironmental engineering*, vol. 127, no. 9, 766-73.
Ismail, M. 2005, 'Performance of cement-stabilized retaining walls', *Canadian geotechnical journal*, vol. 42, no. 3, 876-91.
Ismail, M., Joer, H. & Randolph, M. 2000, 'Sample preparation technique for artificially cemented soils', *Geotechnical Testing Journal*, vol. 23, no. 2, 171-7.
Ismail, M., Joer, H., Randolph, M. & Meritt, A. 2002, 'Cementation of porous materials using calcite', *Geotechnique*, vol. 52, no. 5, 313-24.
Itasca 2016, 'PFC 5.0 (Particle flow code in 2 and 3 dimensions), Version 5.0 [User's manual]', Minneapolis.
Iwashita, K. & Oda, M. 1998, 'Rolling resistance at contacts in simulation of shear band development by DEM', *Journal of engineering mechanics*, vol. 124, no. 3, 285-92.
Janbu, N. 1963, 'Soil compressibility as determined by odometer and triaxial tests', *Proc. Europ. Conf. SMFE*, vol. 1, pp. 19-25.

Jenck, O., Dias, D. & Kastner, R. 2009, 'Discrete element modelling of a granular platform supported by piles in soft soil–Validation on a small scale model test and comparison to a numerical analysis in a continuum', *Computers and Geotechnics*, vol. 36, no. 6, 917-27.
Jiang, M., Konrad, J. & Leroueil, S. 2003, 'An efficient technique for generating homogeneous specimens for DEM studies', *Computers and Geotechnics*, vol. 30, no. 7, 579-97.
Jiang, M., Yan, H., Zhu, H. & Utili, S. 2011, 'Modeling shear behavior and strain localization in cemented sands by two-dimensional distinct element method analyses', *Computers and Geotechnics*, vol. 38, no. 1, 14-29.
Jiang, M., Yu, H.-S. & Harris, D. 2005, 'A novel discrete model for granular material incorporating rolling resistance', *Computers and Geotechnics*, vol. 32, no. 5, 340-57.
Jiang, M., Yu, H.S. & Harris, D. 2006, 'Discrete element modelling of deep penetration in granular soils', *International Journal for Numerical and Analytical Methods in Geomechanics*, vol. 30, no. 4, 335-61.
Jiang, M., Zhang, W., Sun, Y. & Utili, S. 2013, 'An investigation on loose cemented granular materials via DEM analyses', *Granular Matter*, vol. 15, no. 1, 65-84.
Jing, X.Y., Zhou, W.H., Zhu, H.X., Yin, Z.Y. & Li, Y. 2018, 'Analysis of soil - structural interface behavior using three - dimensional DEM simulations', *International Journal for Numerical and Analytical Methods in Geomechanics*, vol. 42, no. 2, 339-57.
Kirkpatrick, W. 1965, 'Effects of grain size and grading on the shearing behaviour of granular materials', *Proceedings of the sixth International Conference on Soil Mechanics and Foundation Engineering*, pp. 273-7.
Klotz, E. & Coop, M. 2001, 'An investigation of the effect of soil state on the capacity of driven piles in sands', *Géotechnique*, vol. 51, no. 9, 733-51.
Kolbuszewski, J. 1948, 'An experimental study of the maximum and minimum porosities of sands', *Proceedings of the Second International Conference on Soil Mechanics and Foundation Engineering*, vol. 1, pp. 158-65.
Kuwano, R. & Jardine, R.J. 2002, 'On measuring creep behaviour in granular materials through triaxial testing', *Canadian Geotechnical Journal*, vol. 39, no. 5, 1061-74.
Lackenby, J., Indraratna, B., McDowell, G. & Christie, D. 2007, 'Effect of confining pressure on ballast degradation and deformation under cyclic triaxial loading'.
Ladanyi, B. & Foriero, A. 1998, 'A numerical solution of cavity expansion problem in sand based directly on experimental stress-strain curves', *Canadian Geotechnical Journal*, vol. 35, no. 4, 541-59.
Lade, P.V. & Overton, D.D. 1989, 'Cementation effects in frictional materials', *Journal of Geotechnical Engineering*, vol. 115, no. 10, 1373-87.
Lade, P.V., Yamamuro, J.A. & Bopp, P.A. 1996, 'Significance of particle crushing in granular materials', *Journal of Geotechnical Engineering*, vol. 122, no. 4, 309-16.
Lagioia, R. & Nova, R. 1995, 'An experimental and theoretical study of the behaviour of a calcarenite in triaxial compression', *Géotechnique*, vol. 45, no. 4, 633-48.
Lai, H.-J., Zheng, J.-J., Zhang, J., Zhang, R.-J. & Cui, L. 2014, 'DEM analysis of "soil"-arching within geogrid-reinforced and unreinforced pile-supported embankments', *Computers and Geotechnics*, vol. 61, 13-23.
Lehane, B.M. & White, D.J. 2005, 'Lateral stress changes and shaft friction for model displacement piles in sand', *Canadian geotechnical journal*, vol. 42, no. 4, 1039-52.
Leroueil, S. & Vaughan, P. 2009, 'The general and congruent effects of structure in natural soils and weak rocks', *Selected papers on geotechnical engineering by PR Vaughan*, Thomas Telford Publishing, pp. 235-56.

Leslie, D. 1969, 'Relationship between shear strength, gradation and index properties', *Proceedings of the 7th International Conference on Soil Mechanics and Foundation Engineering*, pp. 212-22.
Li, L., Li, J., Sun, D.a. & Gong, W. 2017, 'Unified solution to drained expansion of a spherical cavity in clay and sand', *International Journal of Geomechanics*, vol. 17, no. 8, 04017028.
Liu, G., Rong, G., Peng, J. & Zhou, C. 2015, 'Numerical simulation on undrained triaxial behavior of saturated soil by a fluid coupled-DEM model', *Engineering geology*, vol. 193, 256-66.
Liu, M. & Carter, J. 2002, 'A structured Cam Clay model', *Canadian Geotechnical Journal*, vol. 39, no. 6, 1313-32.
Lobo-Guerrero, S. & Vallejo, L. 2005, 'DEM analysis of crushing around driven piles in granular materials', *Géotechnique*, vol. 55, no. 8, 617-23.
Lunne, T., Powell, J.J. & Robertson, P.K. 2002, *Cone penetration testing in geotechnical practice*, CRC Press.
Manassero, M. 1989, 'Stress-strain relationships from drained self-boring pressuremeter tests in sand', *Geotechnique*, vol. 39, no. 2, 293-307.
Marri, A., Wanatowski, D. & Yu, H. 2012, 'Drained behaviour of cemented sand in high pressure triaxial compression tests', *Geomechanics and Geoengineering*, vol. 7, no. 3, 159-74.
Marschi, N.D., Chan, C.K. & Seed, H.B. 1972, 'Evaluation of properties of rockfill materials', *Journal of the Soil Mechanics and Foundations Division*, vol. 98, no. 1, 95-114.
Marshall, A.M. 2012, 'Tunnel-pile interaction analysis using cavity expansion methods', *Journal of Geotechnical and Geoenvironmental Engineering*, vol. 138, no. 10, 1237-46.
McClelland, B. 1974, 'Design of deep penetration piles for ocean structures', *Journal of Geotechnical and Geoenvironmental Engineering*, vol. 100, no. Proc Paper 10064.
Mindlin, R.D. 1953, 'Elastic spheres in contact under varying oblique forces', *Journal of Applied Mechanics*, vol. 20, 327-44.
Mitchell, J.K. & Soga, K. 2005, 'Fundamentals of soil behavior'.
Miura, N., Murata, H. & Yasufuku, N. 1984, 'Stress-strain characteristics of sand in a particle-crushing region', *Soils and Foundations*, vol. 24, no. 1, 77-89.
Mo, P.Q., Marshall, A.M. & Yu, H.S. 2014, 'Elastic-plastic solutions for expanding cavities embedded in two different cohesive-frictional materials', *International Journal for Numerical and Analytical Methods in Geomechanics*, vol. 38, no. 9, 961-77.
Murff, J.D. 1987, 'Pile capacity in calcareous sands: State if the art', *Journal of Geotechnical Engineering*, vol. 113, no. 5, 490-507.
Nagashima, T., Omoto, Y. & Tani, S. 2003, 'Stress intensity factor analysis of interface cracks using X-FEM', *International Journal for Numerical Methods in Engineering*, vol. 56, no. 8, 1151-73.
Nasr, A.M. 2014, 'Behavior of strip footing on fiber-reinforced cemented sand adjacent to sheet pile wall', *Geotextiles and geomembranes*, vol. 42, no. 6, 599-610.
Negussey, D., Wijewickreme, W. & Vaid, Y. 1988, 'Constant-volume friction angle of granular materials', *Canadian Geotechnical Journal*, vol. 25, no. 1, 50-5.
Ng, T.-T. & Meyers, R. 2015, 'Side resistance of drilled shafts in granular soils investigated by DEM', *Computers and Geotechnics*, vol. 68, 161-8.
Nguyen, H.H., Khabbaz, H. & Fatahi, B. 2019, 'A numerical comparison of installation sequences of plain concrete rigid inclusions', *Computers and Geotechnics*, vol. 105, 1-26.
Nguyen, L., Fatahi, B. & Khabbaz, H. 2017, 'Development of a constitutive model to predict the behavior of cement-treated clay during cementation degradation: C3 model', *International Journal of Geomechanics*, vol. 17, no. 7, 04017010.

Ni, Q., Hird, C. & Guymer, I. 2009, 'Physical modelling of pile penetration in clay using transparent soil and particle image velocimetry', *Geotechnique*, vol. 60, no. 2, 121-32.
Niemunis, A. & Herle, I. 1997, 'Hypoplastic model for cohesionless soils with elastic strain range', *Mechanics of Cohesive-frictional Materials: An International Journal on Experiments, Modelling and Computation of Materials and Structures*, vol. 2, no. 4, 279-99.
Ning, Z., Khoubani, A. & Evans, T. 2015, 'Shear wave propagation in granular assemblies', *Computers and Geotechnics*, vol. 69, 615-26.
O'Sullivan, C. 2011, *Particulate discrete element modelling: a geomechanics perspective*, Taylor and Francis.
Obermayr, M., Dressler, K., Vrettos, C. & Eberhard, P. 2011, 'Prediction of draft forces in cohesionless soil with the Discrete Element Method', *Journal of Terramechanics*, vol. 48, no. 5, 347-58.
Obermayr, M., Dressler, K., Vrettos, C. & Eberhard, P. 2013, 'A bonded-particle model for cemented sand', *Computers and Geotechnics*, vol. 49, no. 1, 299-313.
Oda, M. & Kazama, H. 1998, 'Microstructure of shear bands and its relation to the mechanisms of dilatancy and failure of dense granular soils', *Geotechnique*, vol. 48, no. 4, 465-81.
Palmer, A.C. 1971, *Undrained plane-strain expansion of a cylindrical cavity in clay: a simple interpretation of the pressuremeter test*, ARPA E78, Division of Engineering, Brown University Providence, R.I.
Park, S.-S. 2010, 'Effect of wetting on unconfined compressive strength of cemented sands', *Journal of geotechnical and geoenvironmental engineering*, vol. 136, no. 12, 1713-20.
Parsa-Pajouh, A., Fatahi, B. & Khabbaz, H. 2015, 'Experimental and numerical investigations to evaluate two-dimensional modeling of vertical drain–assisted preloading', *International Journal of Geomechanics*, vol. 16, no. 1, B4015003.
Pham Van Bang, D., Di Benedetto, H., Duttine, A. & Ezaoui, A. 2007, 'Viscous behaviour of dry sand', *International Journal for Numerical and Analytical Methods in Geomechanics*, vol. 31, no. 15, 1631-58.
Phillips, R. & Valsangkar, A. 1987, *An experimental investigation of factors affecting penetration resistance in granular soils in centrifuge modelling*, University of Cambridge Department of Engineering.
Phuong, N., Van Tol, A., Elkadi, A. & Rohe, A. 2016, 'Numerical investigation of pile installation effects in sand using material point method', *Computers and Geotechnics*, vol. 73, 58-71.
Plassiard, J.-P., Belheine, N. & Donzé, F.-V. 2009, 'A spherical discrete element model: calibration procedure and incremental response', *Granular Matter*, vol. 11, no. 5, 293-306.
Plomteux, C., Porbaha, A. & Spaulding, C. 2004, 'CMC foundation system for embankment support—A case history', *GeoSupport 2004: Drilled Shafts, Micropiling, Deep Mixing, Remedial Methods, and Specialty Foundation Systems*, pp. 980-92.
Potyondy, D. 2012, 'A flat-jointed bonded-particle material for hard rock', *46th US rock mechanics/geomechanics symposium*, American Rock Mechanics Association.
Potyondy, D. & Cundall, P. 2004, 'A bonded-particle model for rock', *International journal of rock mechanics and mining sciences*, vol. 41, no. 8, 1329-64.
Potyondy, D.O. 2015, 'The bonded-particle model as a tool for rock mechanics research and application: current trends and future directions', *Geosystem Engineering*, vol. 18, no. 1, 1-28.
Poulos, H. 1994, 'Effect of pile driving on adjacent piles in clay', *Canadian geotechnical journal*, vol. 31, no. 6, 856-67.

Poulos, H.G. & Davis, E.H. 1980, *Pile foundation analysis and design*.
Pucker, T. & Grabe, J. 2012, 'Numerical simulation of the installation process of full displacement piles', *Computers and geotechnics*, vol. 45, 93-106.
Puebla, H., Byrne, P.M. & Phillips, R. 1997, 'Analysis of CANLEX liquefaction embankments: prototype and centrifuge models', *Canadian Geotechnical Journal*, vol. 34, no. 5, 641-57.
Rahimi, M., Chan, D. & Nouri, A. 2015, 'Bounding surface constitutive model for cemented sand under monotonic loading', *International Journal of Geomechanics*, vol. 16, no. 2, 04015049.
Rajapakse, R.A. 2016, *Pile design and construction rules of thumb*, Butterworth-Heinemann.
Randolph, M. 2003, 'Science and empiricism in pile foundation design', *Geotechnique*, vol. 53, no. 10, 847-76.
Randolph, M.F. & Wroth, C. 1979, 'An analytical solution for the consolidation around a driven pile', *International Journal for Numerical and Analytical Methods in Geomechanics*, vol. 3, no. 3, 217-29.
Reddy, K.R. & Saxena, S.K. 1993, 'Effects of cementation on stress-strain and strength characteristics of sands', *Soils and Foundations*, vol. 33, no. 4, 121-34.
Robinsky, E. & Morrison, C. 1964, 'Sand displacement and compaction around model friction piles', *Canadian Geotechnical Journal*, vol. 1, no. 2, 81-93.
Rowe, P.W. 1962, 'The stress-dilatancy relation for static equilibrium of an assembly of particles in contact', *Proc. R. Soc. Lond. A*, vol. 269, no. 1339, 500-27.
Sagaseta, C. 1987, 'Analysis of undraind soil deformation due to ground loss', *Geotechnique*, vol. 37, no. 3, 301-20.
Sagaseta, C. & Whittle, A. 2001a, 'Prediction of Ground Movements due to Pile Driving in Clay', *Journal of Geotechnical and Geoenvironmental Engineering*, vol. 127, no. 1, 55-66.
Sagaseta, C. & Whittle, A.J. 2001b, 'Prediction of ground movements due to pile driving in clay', *Journal of Geotechnical and Geoenvironmental Engineering*, vol. 127, no. 1, 55-66.
Sagaseta, C., Whittle, A.J. & Santagata, M. 1997, 'Deformation analysis of shallow penetration in clay', *International Journal for Numerical and Analytical Methods in Geomechanics*, vol. 21, no. 10, 687-719.
Salgado, R., Mitchell, J. & Jamiolkowski, M. 1997, 'Cavity expansion and penetration resistance in sand', *Journal of Geotechnical and Geoenvironmental Engineering*, vol. 123, no. 4, 344-54.
Salgado, R. & Prezzi, M. 2007, 'Computation of cavity expansion pressure and penetration resistance in sands', *International Journal of Geomechanics*, vol. 7, no. 4, 251-65.
Salgado, R. & Randolph, M. 2001, 'Analysis of cavity expansion in sand', *International Journal of Geomechanics*, vol. 1, no. 2, 175-92.
Sandeep, C. & Senetakis, K. 2018, 'Grain-scale mechanics of quartz sand under normal and tangential loading', *Tribology International*, vol. 117, 261-71.
Sandeep, C.S. & Senetakis, K. 2017, 'Exploring the Micromechanical Sliding Behavior of Typical Quartz Grains and Completely Decomposed Volcanic Granules Subjected to Repeating Shearing', *Energies*, vol. 10, no. 3, 370.
Saxena, S.K., Avramidis, A.S. & Reddy, K.R. 1988a, 'Dynamic moduli and damping ratios for cemented sands at low strains', *Canadian Geotechnical Journal*, vol. 25, no. 2, 353-68.
Saxena, S.K. & Lastrico, R.M. 1978, 'Static properties of lightly cemented sand', *Journal of Geotechnical and Geoenvironmental Engineering*, vol. 104, no. ASCE 14259.

Saxena, S.K., Reddy, K.R. & Avramidis, A.S. 1988b, 'Liquefaction resistance of artificially cemented sand', *Journal of Geotechnical Engineering*, vol. 114, no. 12, 1395-413.
Schanz, T. & Vermeer, P. 1996, 'Angles of friction and dilatancy of sand', *Géotechnique*, vol. 46, no. 1, 145-52.
Schnaid, F., Prietto, P.D. & Consoli, N.C. 2001, 'Characterization of cemented sand in triaxial compression', *Journal of Geotechnical and Geoenvironmental Engineering*, vol. 127, no. 10, 857-68.
Schofield, A. & Wroth, P. 1968, *Critical state soil mechanics*, vol. 310, McGraw-Hill London.
Senetakis, K. & Coop, M. 2014, 'The development of a new micro-mechanical inter-particle loading apparatus'.
Senetakis, K., Coop, M.R. & Todisco, M. 2013, 'Tangential load–deflection behaviour at the contacts of soil particles', *Géotechnique Letters*, vol. 3, no. 2, 59-66.
Sharma, J. & Xiao, D. 2001, 'Determination of smear zone around vertical drains', *Soft Ground Technology*, pp. 270-9.
Shen, C., Liu, S. & Wang, Y. 2017, 'Microscopic interpretation of one-dimensional compressibility of granular materials', *Computers and Geotechnics*, vol. 91, 161-8.
Shen, Z., Jiang, M. & Thornton, C. 2016, 'DEM simulation of bonded granular material. Part I: contact model and application to cemented sand', *Computers and Geotechnics*, vol. 75, no. 1, 192-209.
Sheng, D., Eigenbrod, K.D. & Wriggers, P. 2005, 'Finite element analysis of pile installation using large-slip frictional contact', *Computers and geotechnics*, vol. 32, no. 1, 17-26.
Silvestri, V. 2001, 'Interpretation of pressuremeter tests in sand', *Canadian geotechnical journal*, vol. 38, no. 6, 1155-65.
Sitar, N., Clough, G.W. & Bachus, R.C. 1980, 'Behavior of weakly cemented soil slopes under static and seismic loading', *Stanford University*.
Smith, E.A. 1962, 'Pile-driving analysis by the wave equation', *American Society of Civil Engineers Transactions*.
Suleiman, M.T., Ni, L., Davis, C., Lin, H. & Xiao, S. 2015, 'Installation Effects of Controlled Modulus Column Ground Improvement Piles on Surrounding Soil', *J of Geotechnical and Geoenvironmental Eng.*, vol. 10.1061/(ASCE)GT.1943-5606.0001384 , 04015059.
Sulsky, D., Chen, Z. & Schreyer, H.L. 1994, 'A particle method for history-dependent materials', *Computer methods in applied mechanics and engineering*, vol. 118, no. 1-2, 179-96.
Susila, E. & Hryciw, R.D. 2003, 'Large displacement FEM modelling of the cone penetration test (CPT) in normally consolidated sand', *International Journal for Numerical and Analytical methods in geomechanics*, vol. 27, no. 7, 585-602.
Thornton, C. 2000, 'Numerical simulations of deviatoric shear deformation of granular media', *Géotechnique*, vol. 50, no. 1, 43-53.
Timoshenko, S. & Goodier, J. 1970, *Theory of Elasticity*, 3rd edn, McGraw-Hill, New York, NY.
Tolooiyan, A. & Gavin, K. 2011, 'Modelling the cone penetration test in sand using cavity expansion and arbitrary Lagrangian Eulerian finite element methods', *Computers and Geotechnics*, vol. 38, no. 4, 482-90.
Tomlinson, M. & Woodward, J. 2014, *Pile design and construction practice*, CRC Press.
Tong, A.-T., Catalano, E. & Chareyre, B. 2012, 'Pore-scale flow simulations: model predictions compared with experiments on bi-dispersed granular assemblies', *Oil and Gas Science and Technology–Revue d'IFP Energies nouvelles*, vol. 67, no. 5, 743-52.

Tordesillas, A. & Walsh, D.S. 2002, 'Incorporating rolling resistance and contact anisotropy in micromechanical models of granular media', *Powder Technology*, vol. 124, no. 1, 106-11.
Tran, Q.A., Chevalier, B. & Breul, P. 2016, 'Discrete modeling of penetration tests in constant velocity and impact conditions', *Computers and Geotechnics*, vol. 71, 12-8.
Tsao, C.C. & Hocheng, H. 2003, 'The effect of chisel length and associated pilot hole on delamination when drilling composite materials', *International journal of machine tools and manufacture*, vol. 43, no. 11, 1087-92.
Tsuji, Y., Tanaka, T. & Ishida, T. 1992, 'Lagrangian numerical simulation of plug flow of cohesionless particles in a horizontal pipe', *Powder technology*, vol. 71, no. 3, 239-50.
Vesic, A.S. 1972, 'Expansion of cavities in infinite soil mass', *Journal of Soil Mechanics & Foundations Div*, vol. 98, no. sm3.
Von Wolffersdorff, P.A. 1996, 'A hypoplastic relation for granular materials with a predefined limit state surface', *Mechanics of Cohesive - frictional Materials: An International Journal on Experiments, Modelling and Computation of Materials and Structures*, vol. 1, no. 3, 251-71.
Wang, Y.-H. & Leung, S.-C. 2008a, 'A particulate-scale investigation of cemented sand behavior', *Canadian Geotechnical Journal*, vol. 45, no. 1, 29-44.
Wang, Y.-H., Xu, D. & Tsui, K.Y. 2008b, 'Discrete element modeling of contact creep and aging in sand', *Journal of Geotechnical and Geoenvironmental Engineering*, vol. 134, no. 9, 1407-11.
Wang, Y. & Leung, S. 2008c, 'Characterization of cemented sand by experimental and numerical investigations', *Journal of geotechnical and geoenvironmental engineering*, vol. 134, no. 7, 992-1004.
Wang, Z., Jacobs, F. & Ziegler, M. 2014, 'Visualization of load transfer behaviour between geogrid and sand using PFC 2D', *Geotextiles and Geomembranes*, vol. 42, no. 2, 83-90.
Wensrich, C. & Katterfeld, A. 2012, 'Rolling friction as a technique for modelling particle shape in DEM', *Powder Technology*, vol. 217, no. 1, 409-17.
Wroth, C. & Windle, D. 1975, 'Analysis of the pressuremeter test allowing for volume change', *Geotechnique*, vol. 25, no. 3.
Wu, Y., Yamamoto, H., Cui, J. & Cheng, H. 2020, 'Influence of load mode on particle crushing characteristics of silica sand at high stresses', *International Journal of Geomechanics*, vol. 20, no. 3, 04019194.
Yan, G., Yu, H.-s. & McDowell, G. 2009, 'Simulation of granular material behaviour using DEM', *Procedia Earth and Planetary Science*, vol. 1, no. 1, 598-605.
Yang, J., Tham, L.G., Lee, P.K.K., Chan, S. & Yu, F. 2006, 'Behaviour of jacked and driven piles in sandy soil', *Géotechnique*, vol. 56, no. 4, 245-59.
Yang, S., Ren, X. & Zhang, J. 2011, 'Study on embedded length of piles for slope reinforced with one row of piles', *Journal of Rock Mechanics and Geotechnical Engineering*, vol. 3, no. 2, 167-78.
Yang, X.-X. & Qiao, W.-G. 2018, 'Numerical investigation of the shear behavior of granite materials containing discontinuous joints by utilizing the flat-joint model', *Computers and Geotechnics*, vol. 104, 69-80.
Yang, Z., Yang, J. & Wang, L. 2012, 'On the influence of inter-particle friction and dilatancy in granular materials: a numerical analysis', *Granular Matter*, vol. 14, no. 3, 433.
Yi, J., Goh, S. & Lee, F. 2013, 'Effect of sand compaction pile installation on strength of soft clay', *Geotechnique*, vol. 63, no. 12, 1029-41.

Yu, F. 2017, 'Particle breakage and the drained shear behavior of sands', *International Journal of Geomechanics*, vol. 17, no. 8, 04017041.
Yu, H.-S. 1990, 'Cavity expansion theory and its application to the analysis of pressuremeters', University of Oxford.
Yu, H.-S. 2013, *Cavity expansion methods in geomechanics*, Springer Science & Business Media.
Yu, H. 1992, 'Expansion of a thick cylinder of soils', *Computers and Geotechnics*, vol. 14, no. 1, 21-41.
Yu, H. 1993, 'Finite elastoplastic deformation of an internally pressurized hollow sphere', *Acta Mech Solida Sinica (English Edition)*, vol. 6, no. 1.
Yu, H., Tan, S. & Schnaid, F. 2007, 'A critical state framework for modelling bonded geomaterials', *Geomechanics and Geoengineering*, vol. 2, no. 1, 61-74.
Yu, P. & Richart, F. 1984, 'Stress ratio effects on shear modulus of dry sands', *Journal of Geotechnical Engineering*, vol. 110, no. 3, 331-45.
Zeghal, M. & Tsigginos, C. 2015, 'A micromechanical analysis of the effect of fabric on low-strain stiffness of granular soils', *Soil Dynamics and Earthquake Engineering*, vol. 70, 153-65.
Zhang, N., Arroyo, M., Ciantia, M.O., Gens, A. & Butlanska, J. 2019, 'Standard penetration testing in a virtual calibration chamber', *Computers and Geotechnics*, vol. 111, 277-89.
Zhang, X.-P. & Wong, L.N.Y. 2014, 'Choosing a proper loading rate for bonded-particle model of intact rock', *International Journal of Fracture*, vol. 189, no. 2, 163-79.
Zhao, S., Zhou, X. & Liu, W. 2015, 'Discrete element simulations of direct shear tests with particle angularity effect', *Granular Matter*, vol. 17, no. 6, 793-806.
Zhao, X. & Evans, T.M. 2009, 'Discrete simulations of laboratory loading conditions', *International journal of geomechanics*, vol. 9, no. 4, 169-78.
Zhou, J., Jian, Q.-w., Zhang, J. & Guo, J.-j. 2012, 'Coupled 3D discrete-continuum numerical modeling of pile penetration in sand', *Journal of Zhejiang University-Science A*, vol. 13, no. 1, 44-55.
Zhu, H., Zhou, W.-H. & Yin, Z.-Y. 2017, 'Deformation mechanism of strain localization in 2D numerical interface tests', *Acta Geotechnica*, 1-17.
Zhuang, P. & Yu, H.-S. 2018, 'Uplift resistance of horizontal strip anchors in sand: a cavity expansion approach', *Géotechnique Letters*, vol. 8, no. 4, 1-18.